

**University of Sheffield**

**Department of Civil and Structural Engineering**

**Shear Strength and Volume Change**

**Behaviour of Unsaturated Soils**

**Volume 1**

**Thesis :Chapter 1 to 5**

**by**

**Mohd.Jamaludin bin Md.Noor**

**A thesis submitted to**

**The University of Sheffield**

**Department of Civil and Structural Engineering**

**for the degree of Doctor of Philosophy**

**July 2006**

## SUMMARY

Over the last 30 years there has been increasing interest in the mechanical behaviour (i.e. the shear strength and volume change behaviour) of unsaturated soils. However, there is still a lack of a good representative and comprehensive shear strength analytical model. Researchers have been trying to link the volume change behaviour to the shear strength; however there are still shortcomings in the existing frameworks.

Following a review of the literature, a new shear strength model and a hypothetical volume change framework that link volume change and mobilized shear strength have been proposed specifically for coarse-grained soils at low stress levels. They have been developed from the standpoint of stress-strain behaviour.

The shear strength model takes the form of a warped-surface envelope in  $\tau : (\sigma - u_a) : (u_a - u_w)$  space known as the extended Mohr Coulomb space and defined by seven shear strength parameters. The model is divided into four distinct zones and each zone is represented by a shear strength equation. Initially the applicability of the shear strength model was verified using data reported in the literature and a fuller verification has been performed by carrying out series of consolidated drained triaxial tests on saturated and unsaturated specimens of diameter 150 mm and 375 mm height. The test equipment involved a conventional and a double-walled triaxial cell, and the test material was 10 mm nominal size limestone gravel. The results underlined the shear strength behaviour of the test material with respect to net stress and suction and showed a good match with the proposed shear strength model.

The proposed hypothetical volume change framework is intended to explain the volume change behaviour due to load increase and inundation under low stress levels within the same framework. These modes of failure are referred as loading and wetting collapse respectively. The framework is based on the interaction between mobilized shear strength and the soil state of stress represented graphically by the mobilized shear strength envelope and the Mohr stress circle respectively. Soil compression is triggered whenever the Mohr stress circle extends above the mobilized shear strength envelope to indicate a state of stress imbalance. This will cause the compression of the soil structure which in turn increases or mobilizes the shear

strength to enable the soil to carry the applied stresses. The increase in the mobilized shear strength is marked by the rotation of the mobilized shear strength envelope about the suction axis due to the increase in the mobilized friction angle,  $\phi'_{mob}$ . When the rotation stops it indicates that the soil compression has ceased and stress equilibrium is reinstated. At this point the mobilized shear strength envelope is at the point of engaging contact with the Mohr stress circle.

When there is no particle breakage, failure at different net confining stress is assumed to occur at the same value of axial strain. This produces a unique relationship between effective mobilized minimum friction angle,  $\phi'_{min_{mob}}$ , and axial strain,  $\epsilon_a$ , irrespective of the net confining stresses. The angle  $\phi'_{min_{mob}}$  signifies the inclination of the linear section of the mobilized shear strength envelope from the horizontal. The existence of a unique relationship of  $\phi'_{min_{mob}} - \epsilon_a$  would justify the mobilized shear strength envelope as the yield surface representing identical axial strain irrespective of the net confining stresses. Therefore the rotation of the yield surface is reflecting the increase in the axial strain and correspondingly signifies the volume change through the relationship of  $\phi'_{min_{mob}} - \epsilon_a$  and  $\epsilon_v - \epsilon_a$ . The results of the triaxial tests on saturated and unsaturated specimens showed the existence of this unique relationship of  $\phi'_{min_{mob}} - \epsilon_a$  under loading collapse stress conditions and thus verifying the applicability of the hypothetical framework for this mode of collapse. Further work is required to prove the applicability of the framework for wetting collapse stress conditions. Another advantage of the framework is its ability to predict the stress-strain curve at any net confining stress provided the shear strength envelope at failure and its unique relationship of  $\phi'_{min_{mob}} - \epsilon_a$  are known.

It has been found that particle breakage caused the variation of the graph of  $\phi'_{min_{mob}} - \epsilon_a$  for different net confining stress and thus the mobilized shear strength envelope could no longer be regarded as the yield surface and thence limits the applicability of the proposed hypothetical volume change framework.

## ACKNOWLEDGEMENTS

I would like first of all to express my sincere gratitude to my supervisor Professor William F. Anderson for his guidance and suggestions during the development of the theoretical model and framework, experimental work and writing up this thesis. Without him this thesis may never have been completed.

The quality of the technical support in the Geotechnics Laboratories at Sheffield University is second to none. I would like to thank all the technical staff especially Paul Osborne and Mark Foster for all of their expertise and help in the experimental work. Their input does not go unrecognised.

I am very grateful to the University Technology MARA, Malaysia for giving me the study leave and opportunity to do a Ph.D course in geotechnics in the University of Sheffield, United Kingdom. I am also very grateful to the Department of Public Service under the Prime Minister Office of Malaysia for providing me with a scholarship during the course of the study.

Finally, I would like to thank my wife, Suhariah binti Ali and all my seven children ; Hanani, Ahmad Zaki, Ahmad Ridzwan, Syakirah, Ahmad Zaid, Ahmad Ismail and Ahmad Yusof for all the encouragement and support they showed throughout this work.

## Table of Contents

Summary		
Acknowledgements		
List of Tables		
List of Plates		
List of Figures		
List of Symbols		
List of Definitions		
Chapter 1	Introduction	1-1
Chapter 2	Literature Review: Shear Strength and Volume Change Behaviour of Unsaturated Soils	2-1
	2.1 Independent Stress State Variables used for Unsaturated Soils	2-1
	2.2 Soil-Moisture Characteristic Curve and Residual Suction	2-3
	2.3 Behaviour of Coarse-grained Soils	2-3
	2.3.1 Stress, Strain and Volume Change Behaviour	2-4
	2.3.2 Mohr Stress Circle and Mobilized Friction Angle, $\phi'_{mob}$	2-7
	2.3.3 Effect of Particle Breakage on Stress-Strain and Volume Change Behaviour	2-8
	2.3.4 Collapse Volume Change Behaviour	2-12
	2.3.5 Non-linear Shear Strength Behaviour With Respect to Effective Stress	2-15
	2.3.6 Non-linear Shear Strength Behaviour With Respect to Suction	2-16
	2.4 Existing Shear Strength Equations for Unsaturated Soils	2-17
	2.4.1 Early Attempts to a Define a Shear Strength Equation for Unsaturated Soils	2-18
	2.4.2 Equations for Linear Behaviour of Shear Strength with respect to Suction	2-18
	2.4.3 Equation for Non-linear Behaviour of Shear Strength with respect to Suction	2-19
	2.5 Existing Volume Change Models for Unsaturated Soils	2-20
	2.5.1 Volume Change Model Based on Two Independent Stress State Variables	2-21
	2.5.2 Critical State Volume Change Frameworks	2-24
	2.5.3 Elasto-Plastic Stress-Strain Frameworks	2-31
	2.6 Limitations of Critical State Frameworks	2-33
Chapter 3	Proposed Shear Strength Model and Hypothetical Shear Strength-Volume Change Framework	3-1
	3.1 Mohr Stress Diagram in Extended Mohr-Coulomb Space	3-1
	3.2 Proposed Shear Strength Model	3-4
	3.2.1 Model General Characteristics and Anticipated Form.	3-5
	3.2.2 Shear Strength Behaviour Relative to Suction	3-5
	3.2.3 Shear Strength Behaviour Relative to Effective Stress	3-10
	3.2.4 Shear Strength Equations to Represent the Surface Envelope	3-12
	3.2.5 Determination of the Seven Soil Shear Strength Parameters	3-14
	3.2.6 Procedure for Drawing the Shear Strength Contours of the Shear Strength Surface Envelope in $\tau - s$ Space	3-16
	3.3 Validation of Proposed Shear Strength Equations	3-17
	3.3.1 Validation of Shear Strength Behaviour with respect to Suction	3-17
	3.3.2 Validation of Shear Strength Behaviour with respect to Effective Stress at Saturation	3-18
	3.4 Proposed Hypothetical Shear Strength-Volume Change Framework	3-18
	3.4.1 Framework General Characteristics	3-20
	3.4.2 Framework Principle Concept	3-21
	3.4.3 Framework Structure	3-25
	3.4.4 Qualitative Simulation of Loading Collapse	3-29
	3.4.5 Qualitative Simulation of Wetting and Drying Collapse	3-30
	3.4.6 Relationship between Mobilized Minimum Friction Angle and Axial Strain	3-31

	3.4.7	Yield Surface Envelope According to the Proposed Hypothetical Volume Change Framework	3-32
	3.4.8	Framework Prediction of the Stress-strain Curve for a Triaxial Compression Test	3-35
	3.5	Summary	3-37
Chapter 4		Test Material and Equipment, Test Procedures and Test Programme	
	4.1	Introduction	4-1
	4.2	Choice of Test Material	4-1
	4.2.1	Sample Preparation and Grading Tests	4-2
	4.2.2	Compaction Test	4-3
	4.3	Test Equipment	4-3
	4.3.1	Volumetric Pressure Plate Extractor Apparatus	4-4
	4.3.2	Conventional Triaxial Cell	4-4
	4.3.3	Double-walled Triaxial Cell	4-5
	4.3.4	Rowe Consolidation Cell	4-9
	4.4	Instrumentation and Calibration	4-9
	4.4.1	Measuring Devices	4-10
	4.4.2	Calibration	4-11
	4.4.2.1	Displacement Transducers	4-11
	4.4.2.2	Volume Change Units	4-12
	4.4.2.3	Load Cell	4-13
	4.4.2.4	Pressure Transducers	4-13
	4.4.2.5	Pressure Gauges	4-13
	4.4.3	Corrections	4-14
	4.4.4	Data Acquisition System	4-15
	4.5	Test Procedures	4-16
	4.5.1	Determination of the Soil-moisture Characteristic Curve Using the Pressure Plate Extractor Apparatus	4-16
	4.5.2	Conventional Triaxial Cell	4-18
	4.5.2.1	Preparatory Stage	4-18
	4.5.2.2	Specimen Compaction Procedure	4-18
	4.5.2.3	Specimen Placement	4-19
	4.5.2.4	Cell Assembly	4-20
	4.5.2.5	Saturation Stage	4-20
	4.5.2.6	Consolidation and Shearing Stages	4-21
	4.5.2.7	Multistage and Single Stage Triaxial Tests	4-21
	4.5.3	Double-wall Triaxial Cell	4-23
	4.5.3.1	Preparatory Stage	4-23
	4.5.3.2	Specimen Placement and Measurement of Specimen Dimensions	4-24
	4.5.3.3	Installation of the Local Displacement Transducers	4-26
	4.5.3.4	Multistage Consolidation and Shearing	4-28
	4.5.4	Suction Controlled Compression Test Using a Modified Rowe Cell	4-29
	4.5.4.1	Specimen Placement and Cell Assembly	4-30
	4.5.4.2	Equalisation Stage	4-30
	4.5.4.3	Compression Stage	4-31
	4.6	Test Programmes and Objectives	4-31
	4.6.1	Test Series A: Determination of the Soil-Moisture Characteristic Curve	4-32
	4.6.2	Test Series B: Determination of the Saturated Shear Strength Behaviour with respect to Effective Stress	4-32
	4.6.3	Test Series C: Determination of the Unsaturated Shear Strength Behaviour with respect to Suction	4-33
	4.6.4	Test Series D: Determination of the Effect of Particle Size Distribution on the Shear Strength Surface Envelope	4-34

	4.6.5 Test Series E: Determination of the 1-D Volume Change Characteristics of the Test Material under Different Suctions	4-34
Chapter 5	Test Results	5-1
	5.1 Results of Test Series A	5-1
	5.2 Results of Test Series B	5-2
	5.2.1 Specimen Consistency	5-2
	5.2.2 Saturation Stage	5-2
	5.2.3 Consolidation Stage	5-3
	5.2.4 Shearing Stage	5-5
	5.3 Results of Test Series C	5-8
	5.3.1 Specimen Consistency	5-8
	5.3.2 Equalisation Stage	5-8
	5.3.3 Consolidation Stage	5-9
	5.3.4 Shearing Stage	5-11
	5.4 Results of Test Series D	5-13
	5.5 Results of Test Series E	5-13
	5.5.1 Specimen Consistency	5-13
	5.5.2 Equalisation Stage	5-14
	5.5.3 Determination of Friction between Cell Wall and Top Platen	5-14
5.5.4 Compression Stage	5-15	
Chapter 6	Discussion	6-1
	6.1 Specimen Consistency	6-1
	6.2 Test Repeatability	6-2
	6.3 Comparability between Single Stage and Multistage Triaxial Tests	6-3
	6.4 Membrane Penetration	6-4
	6.5 Stress, Strain and Volume Change Behaviour of Triaxial Specimens	6-5
	6.5.1 Detection of Particle Breakage on the Graphs of Mobilized Friction Angle, $\phi'_{mob}$ , Versus Void Ratio, $e$	6-7
	6.5.2 Effect of Particle Breakage on Definition of Failure	6-10
	6.6 Effect of Grading on the Shear Strength	6-10
	6.7 Shear Strength of the Test Material	6-11
	6.7.1 Saturated Shear Strength	6-12
	6.7.2 Unsaturated Shear Strength	6-13
	6.7.3 Warped-surface Shear Strength Envelope	6-14
	6.8 Prediction of Soil Response by the Shear Strength-Volume Change Framework	6-17
	6.8.1 Interpretation of Yield Surface	6-20
	6.8.2 Unique Relationship Between $\phi'_{min_{mob}}$ and $\epsilon_a$	6-21
	6.8.3 Influence of Particle Breakage on the Applicability of the Framework	6-22
6.8.4 Framework Prediction of the Stress-strain Curve from a Triaxial Compression Test	6-24	
6.8.5 Volume Change Behaviour under Loading and Wetting Collapse from Rowe Cell Compression Tests	6-26	
Chapter 7	Conclusions and Recommendations for Future Work	7-1
	7.1 Conclusions	7-1
	7.2 Recommendations for Further Work	7-3
References		
Appendix 1	Labview Calibration Program for the Double-wall Triaxial Cell.	
Appendix 2	Labview Data Acquisition Program for the Double-wall Triaxial Cell.	
Appendix 3	Assembly and Dismantling Procedure for the Double-wall Triaxial Cell.	

## List of Tables

	Chapter 2	Page no.
2.1	Comparison between experimental values of $\phi'$ and $\phi^b$ .	2-35
2.2	The data for the drained triaxial tests on saturated specimens of limestone coarse-grained soil obtained from the same quarry with similar properties to the test material (Salman, 1995).	2-35
	Chapter 3	
3.1	Summary of the shear strength behaviour in the four distinct zones on the constitutive shear strength surface.	3-38
3.2	Shear strength parameters used in Equations 3.4 and 3.7 in the validation work.	3-39
3.3	Constants used in Equation 3.13 and 3.14 in their validation against the experimental data by Charles and Watts (1980).	3-39
	Chapter 4	
4.1	Chemical composition of test material (Goodwin, 1991).	4-36
4.2	Transducers used in the Conventional Triaxial Cell Tests.	4-36
4.3	Purposes of the transducers used with the Conventional Triaxial Cell.	4-37
4.4	Transducers used in Double-wall Triaxial Cell Tests.	4-37
4.5	Purposes of the transducers used with the Double-wall Triaxial Cell.	4-38
4.6	Transducers used in the Rowe Consolidation Cell.	4-39
4.7	Purposes of the transducers used with the Rowe Consolidation Cell.	4-39
4.8	Calibration factors and drift for displacement transducers (LVDTs).	4-40
4.9	Calibration factors, drift and corrected calibration factors for volume change units.	
	(a) Calibration factors and drift for volume change units.	4-41
	(b) Corrected calibration factors for 100 cc Imperial College volume change unit used with the conventional triaxial cell due to significant drift.	4-41
4.10	Calibration factors and drift for load cells.	4-42
4.11	Calibration factors and drift for pressure transducers.	4-42
4.12	List of consolidated drained triaxial tests on saturated specimens for test series B.	4-43
4.13	List of consolidated drained triaxial tests on unsaturated specimens for test series C.	4-43
4.14	List of consolidated drained triaxial tests on saturated specimens for test series D.	4-44
4.15	List of Rowe cell compression tests for test series E.	4-44
	Chapter 5	
5.1	Results of pressure plate test on the test material (i.e. no fine content).	5-17
5.2	Initial specimen dimensions and dry density for the test series B.	5-17
5.3	Skempton's B value, effective stress, deviator stress, cell pressure, pore water pressure and back pressure for all consolidated drained triaxial tests on saturated specimens in test series B.	5-18
5.4	Volume of membrane penetration at the start of the consolidation stage in test series B.	5-19
5.5	Initial specimen dimensions and dry densities for triaxial tests on unsaturated specimens for test series C.	5-19
5.6	Volume of membrane penetration at the start of the consolidation stage and the leak correction made to the consolidation and shearing in test series C	5-20
5.7	Net stress, deviator stress, cell pressure, pore water pressure and pore air pressure at failure for all consolidated drained triaxial tests on unsaturated specimens in test series C.	5-20
5.8	Central height radial displacements at the point of specimen dilation during the shearing stage in unsaturated consolidated drained triaxial tests in test series C.	5-21
5.9	Initial specimen dimensions and dry densities for the test series D.	5-21
5.10	Skempton's B values, effective stress, deviator stress, cell pressure and pore water pressure at failure during shearing for triaxial tests on saturated specimen in test series D.	5-21
5.11	Specimen and cell properties in Rowe cell compression tests under constant suction in test series E.	5-22
	Chapter 6	
6.1	Previous strain rates that have been applied by researchers in shearing of coarse grain unsaturated specimens.	6-29

## List of Tables (continued)

6.2	Apparent and total shear strength at respective suctions and net stresses obtained from unsaturated triaxial tests.	6-29
6.3	The seven shear strength parameters of the test material according to the warped-surface extended Mohr-Coulomb envelope.	6-30
6.4	Parameters used to plot the Mohr circles corresponding to effective mobilized minimum friction angle of 10, 20, 30 and 34 degrees for saturated triaxial specimens compacted at 8% moisture content shown in Figure 6.18.	6-30
6.5	Parameters used to plot the yield surfaces using Equation 3.13 and 3.14 for saturated triaxial specimens compacted at 8% moisture content shown in Figures 6.18, 6.34, 6.35 and 6.36.	6-31
6.6	Parameters used to plot the Mohr circles corresponding to effective mobilized minimum friction angle of 10, 20, 30 and 34 degrees for saturated triaxial specimens compacted at 4% moisture content shown in Figure 6.18.	6-31
6.7	Parameters used to plot the yield surface corresponding to effective mobilized minimum friction angle of 10, 20, 30 and 34 degrees using Equation 3.13 and 3.14 for saturated triaxial specimens compacted at 4% moisture content shown in Figure 6.21.	6-32
6.8	Parameters used to plot the Mohr circles corresponding to effective mobilized minimum friction angle of 10, 20, 30 and 34 degrees for saturated triaxial specimens compacted at 6% moisture content shown in Figure 6.22.	6-32
6.9	Parameters used to plot the yield surfaces using Equation 3.13 and 3.14 for saturated triaxial specimens compacted at 6% moisture content shown in Figures 6.22, 6.39, 6.40 and 6.41.	6-33
6.10	Parameters used to plot the Mohr circles corresponding to $\phi'_{min\ mob}$ of 10, 20, 30 and 34 degrees for unsaturated triaxial specimens of suction 25 kPa shown in Figure 6.23.	6-33
6.11	Parameters used to plot the mobilized shear strength envelope corresponding to effective mobilized minimum friction angle of 10, 20, 30 and 34 degrees using Equation 3.13 and 3.14 for unsaturated triaxial specimens of suction 25 kpa compacted at 4% moisture content shown in Figure 6.23.	6-34
6.12	Parameters used to plot the Mohr circles corresponding to mobilized minimum friction angle of 10, 20, 30 and 34 degrees for unsaturated triaxial specimens of suction 50 kpa compacted at 4% moisture content shown in Figure 6.24.	6-34
6.13	Parameters used to plot the mobilized shear strength envelope corresponding to effective mobilized minimum friction angle of 10, 20, 30 and 34 degrees using Equation 3.13 and 3.14 for unsaturated triaxial specimens of suction 50 kpa compacted at 4% moisture content shown in Figure 6.24.	6-35
6.14	The deduced values for the unique relationship of $\phi'_{min\ mob} - \epsilon_a$ for triaxial tests on saturated specimens compacted at 8% moisture content plotted in Figure 6.33.	6-35
6.15	The predicted major principal net stresses and the deviator stresses corresponding to the yield surfaces and the represented axial strain during triaxial tests on saturated specimens compacted at 8% moisture content at effective stresses of 100, 200 and 300 kPa.	6-36
6.16	The deduced values for the unique relationship of $\phi'_{min\ mob} - \epsilon_a$ for triaxial tests on saturated specimens compacted at 6% moisture content plotted in Figure 6.38.	6-36
6.17	The predicted major principal stresses and the deviator stresses corresponding to the yield surfaces and the represented axial strain during triaxial tests on saturated specimens compacted at 6% moisture content at effective stresses of 105, 199 and 245 kPa.	6-37
6.18	The deduced values for the unique relationship of $\phi'_{min\ mob} - \epsilon_a$ for triaxial tests on unsaturated specimens of suction 25 kPa plotted in Figure 6.38.	6-37
6.19	The predicted major principal stresses and the deviator stresses corresponding to the yield surfaces and the represented axial strain during triaxial tests on unsaturated specimens of suction 25 kPa at net stresses of 100, 200 and 300 kPa.	6-38
6.20	Parameters used to plot the Mohr stress circles and the corresponding mobilized shear strength envelope in Figure 6.50.	6-38

## List of Plates

Chapter 4		Page no.
4.1	Initial preparation of soil samples.	
	(a) The soil sample after being ground for 10 minutes to crush down the soft particles of shale.	4-45
	(b) Washed sample freshly removed from the oven to be cooled down before carrying out the specimen compaction.	4-45
4.2	Hammer held vertically and vibrated under its own weight as a standard compaction procedure for the triaxial test specimens.	4-46
4.3	Kango hammer and transformer used to compact saturated and unsaturated specimens for triaxial tests.	4-46
4.4	Pressure plate extractor apparatus and the prepared specimens.	
	(a) Test material contained in circular rings and compacted by tapping lightly with a hammer placed directly on the 3-bar ceramic disc.	4-47
	(b) Specimens placed in plate extractor apparatus.	4-47
	(c) Pressure plate extractor connected to a burette to collect excess water during equalization.	4-47
4.5	The overall set up for the conventional triaxial cell for testing a specimen of diameter 150 mm and height 375 mm.	4-48
4.6	Double-walled triaxial cell for testing unsaturated coarse grain soil (Salman, 1995) and the large volume change unit (Fair, 2004) connected to the inner cell to measure specimen volume change during testing.	4-48
4.7	Float improvement for the 1770cc volume change unit.	
	(a) Algae grow on the white coloured float causing it to tilt and stick to the wall of the volume change unit.	4-49
	(b) New improved dark coloured hollow float of smaller diameter.	4-49
4.8	Quick Log data logging system for the conventional triaxial cell and the Rowe consolidation cell.	4-50
4.9	Data logging system for the double-wall triaxial cell.	4-50
4.10	Sliding technique for specimen placement onto the cell base pedestal (Salman, 1995).	
	(a) Mould containing the compacted specimen placed with its base level with the porous disc sitting directly on top of the triaxial cell pedestal.	4-51
	(b) Three tie rods outside the mould are removed and the mould is slid horizontally to sit over the pedestal.	4-51
4.11	Improved specimen placement technique for the saturated shear strength test in the conventional triaxial cell.	
	(a) The base disc is placed on top of the specimen before the whole unit is turned upside down by holding to the porous disc.	4-52
	(b) The upside down unit is placed directly on to the pedestal.	4-52
4.12	Guide beam spanning between the two loading machine uprights with the centre pointing needle helping to align the specimen vertically.	
	(a) Top view showing the guide beam and the specimen aligned.	4-53
	(b) Side view showing the centre pointing needle aligned at the centre of the top cap.	4-53
4.13	Split rings of diameter 170 mm and width 30 mm used to stretch the O-rings and the second membrane.	
	(a) New improved split ring system with special connectors used to stretch O-rings and the second membrane during the setting up of saturated and unsaturated triaxial test specimens.	4-54
	(b) Vacuum applied, mould removed, and the two O-rings and the second membrane stretched around the split rings ready to be installed.	4-54
4.14	Overall view of the double-wall triaxial cell.	4-55
4.15	The sequence of specimen placement onto the base pedestal of the double-wall triaxial cell.	
	(a) Mould is turned upside down to sit on a rigid plate.	4-56

## List of Plates (continued)

		Page no.
	(b) Base plate is removed.	4-56
	(c) The mould is slid onto the pedestal by pushing the rigid plate.	4-57
	(d) The clamp system is assembled to hold the mould rigidly in place before the plate is pulled out.	4-57
4.16	Clamp components and a rigid sliding plate for the specimen placement.	4-58
4.17	Two O-rings and the second membrane stretched around the split rings ready to be installed after the application of a vacuum and subsequent mould removal.	4-58
4.18	Calliper for measuring specimen diameter in the conventional and double-wall triaxial cell tests.	
	(a) Gauge calliper used to measure specimen diameter.	4-59
	(b) Measuring the mid height specimen diameter using the fabricated gauge calliper with the aid of the electronic vernier scale ruler.	4-59
4.19	Lowering the second membrane after silicon grease is uniformly applied onto the first membrane.	4-60
4.20	Three stand system to ease installation of the top and bottom Perspex curves transducer holders.	
	(a) Taller stand system for installing top Perspex curve system.	4-61
	(b) Shorter stand system for installing bottom Perspex curve system.	4-61
4.21	Screw type jack system used to install and remove the Rowe cell top platen.	4-62

## List of Figures

	Chapter 2	Page no.
2.1	Volume change in terms of void ratio against net stress, $\sigma'$ , and suction, $(u_a - u_w)$ (Bishop and Blight, 1963).	2-36
2.2	Warped surface representing the volume change behaviour of a mixture of flint (80%) and kaolin (20%) under isotropic stress conditions (Matyas and Radhakrishna, 1968).	2-36
2.3	Soil-moisture characteristic curves and graphical illustration for the definition of residual suction and residual water content	
	(a) Soil-moisture characteristic curves for some Dutch soils (Koorevaar <i>et al.</i> , 1983).	2-37
	(b) Soil-moisture characteristic curve illustrating the residual suction and residual water content (Fredlund and Xing, 1994).	2-37
2.4	Typical shear stress, shear strain and volume change behaviour from a shear box test on dense and loose sand (Powrie 1997): (a) $\tau$ versus $\gamma$ (b) $\epsilon_{vol}$ versus $\gamma$ (c) $V$ versus $\gamma$ .	2-38
2.5	Stress-strain curves showing either a well defined peak or a kink.	
	(a) Well defined peak in the stress-strain curve for decomposed granite (Jovicic and Coop, 1997).	2-39
	(b) Well defined peak in the stress-strain curve for over-consolidated London clay (Atkinson, 1975).	2-39
	(c) A kink in the stress-strain curve for normally consolidated clay (Callisto and Calabresi, 1998).	2-39
2.6	Mohr circles representing different mobilized shear strengths under the same mobilized shear strength envelope or the yield envelope.	2-40
2.7	Stress-strain and volume change relationships for drained plane strain tests on loose and dense Brasted sand (Bishop 1972).	2-41
2.8	Stress-strain and volume change relationships for drained triaxial tests on saturated Ham River sand at normal and elevated net confining pressures (Bishop 1966) (Note : 1 lb/sq.inch = 6.896 kN/m <sup>2</sup> ). (a) loose (b) dense	2-42
2.9	Change in grading resulting from shear at different net confining pressures (Bishop 1966).	2-42
2.10	Principal effective stress ratio, strain and volume change relationships for drained triaxial compression tests on saturated Ham River sand at normal and elevated stress levels (Bishop 1972) (Note : 1 lb/sq.inch. = 6.896 kN/m <sup>2</sup> ).	2-43
2.11	Stress-strain and volume change relationship for drained triaxial tests on crushed anthracite demonstrating that axial strain at failure does not go on increasing indefinitely with particle breakage (Billam 1972).	2-44
2.12	Stress-strain and volume change behaviour of greywacke rockfill in large-scale triaxial testing Indraratna <i>et al.</i> (1993).	2-44
2.13	Stress-strain and volume change behaviour during consolidated drained triaxial tests on unsaturated specimens of similar limestone gravels as the test material of this research (Salman 1995).	
	(a) Deviator stress versus axial strain.	2-45
	(b) Specimen volumetric strain versus internal axial strain.	2-45
2.14	Sign of particle breakage even at low stress levels (<300 kPa) (Indraratna and Salim, 2001).	2-46
2.15	Constant suction triaxial tests performed on gneiss rock residual soil at horizon B (Futai and Almeida 2005).	
	(a), (b) Suction = 100 kPa.	2-47
	(c), (d) Suction = 300 kPa.	2-47
	(e), (f) Air dried.	2-47
2.16	Constant suction triaxial tests performed on gneiss rock residual soil at horizon C (Futai and Almeida 2005).	
	(a), (b) Suction = 100 kPa.	2-47
	(c), (d) Suction = 300 kPa.	2-47
	(e), (f) Air dried.	2-47
2.17	Electron micrographs of kaolin showing void spaces indicated by the dark coloured areas (Penumadu and Dean, 2000).	2-48
2.18	Significant 1-D compression of coarse-grained soils due to inundation indicated by the last two data points on the graphs (Goodwin 1991).	2-48

## List of Figures (continued)

		Page no.
2.19	Volume changes versus time during inundation of a compacted specimen of Indian Head silty sand (Tadepalli <i>et al.</i> , 1992).	2-49
2.20	Three-dimensional representation of void ratio change with compaction air voids and vertical stress at inundation (Blanchfield and Anderson, 2000).	2-49
2.21	$K_o$ -compression test with three different stress paths under each increment of net normal stress (Rahardjo and Fredlund, 2003).	
	(a) Stress paths, M, CW and C.	2-50
	(b) Reduction in volume represented by $V_v/V_o$ resulting from the stress paths in (a).	2-50
2.22	The curvilinear type of Mohr-Coulomb envelope base on data by Salman (1995) as shown in Table 2.2.	2-50
2.23	Reported curvilinear type of Mohr-Coulomb envelope for coarse-grained soils.	
	(a) Mohr-Coulomb envelopes for loose and dense sand (Bishop, 1966)	2-51
	(b) Mohr-Coulomb envelope for granular soils of minimum particle size of 38mm (Charles and Watts, 1980).	2-51
2.24	Mohr-Coulomb envelopes showing non-linear behaviour of shear strength at low effective stress for saturated greywacke rockfill material Indraratna <i>et al.</i> (1993).	
	(a) gradation A.	2-52
	(b) gradation B.	2-52
2.25	Predicted shear strength according to the proposed shear strength equation.	
	(a) Predicted shear strength represented by the line graph according to Equation 2.8 (Fredlund <i>et al.</i> , 1995).	2-53
	(b) Best-fit predicted shear strength represented by the dotted line according to Equation 2.10 (Vanapalli <i>et al.</i> , 1996).	2-53
	(c) Best-fit predicted shear strength represented by the dotted line for suction of 3000 kPa according to Equation 2.11 (Vanapalli <i>et al.</i> , 1996).	2-53
2.26	Non-linear behaviour of shear strength at suction lower than residual suction and remaining constant beyond that.	
	(a) Madrid clayey sand (Escario and Juca, 1989).	2-54
	(b) Fine ash tuff (Gan and Fredlund, 1996).	2-54
	(c) Sandy silt (Rassam and Williams, 1999).	2-54
	(d) Bukit Timah residual soil, Singapore (Toll <i>et al.</i> , 2000).	2-54
	(e) Jurong residual soil, Singapore (Toll <i>et al.</i> , 2000).	2-54
2.27	Behaviour of unsaturated shear strength with reference to the soil-water characteristic curve (Vanapalli <i>et al.</i> , 1996).	
	(a) Soil-water characteristic curve.	2-55
	(b) Corresponding non-linear shear strength behaviour with respect to suction.	2-55
2.28	A three-dimensional plane surface for the extended Mohr-Coulomb failure envelope for unsaturated soil (Fredlund <i>et al.</i> , 1978).	2-55
2.29	Variation of settlements with various constant vertical pressures and decreasing negative pore water pressures at different degree of compaction (Escario and Saez, 1973) with Proctor optimum moisture content of 11%.	
	(a) Compaction m.c. 3%.	2-56
	(b) Compaction m.c. 6%.	2-56
	(c) Compaction m.c. 8%.	2-56
2.30	Three-dimensional void ratio constitutive surface for unsaturated soil based on the two independent stress state variables, $(\sigma - u_a)$ and $(u_a - u_w)$ (Fredlund and Morgenstern, 1976).	2-56
2.31	Void ratio constitutive surface for Madrid grey clay (Sabbagh, 2000).	2-57
2.32	Planar constitutive surface for void ratio proposed by Fredlund (1979).	2-57
2.33	State surface for void ratio of Pinolen clayey sand under isotropic compression (Lloret and Alonso, 1985).	2-58

## List of Figures (continued)

		Page no.
2.34	Isotropic normal compression line and loading collapse yield curve in the elasto-plastic critical state framework of Alonso <i>et al.</i> (1990).	
	(a) Normal compression curve for saturated and unsaturated soil.	2-58
	(b) Loading collapse yield curve in the $s: p'$ plane.	2-58
2.35	Three-dimensional elasto-plastic critical state framework in $(p, q, s)$ stress space (Alonso <i>et al.</i> , 1990).	
	(a) Three-dimensional yield surfaces and four types of stress paths that can lead to failure.	2-59
	(b) Critical state line (CSL) in $q - p'$ space.	2-59
2.36	Various responses of specific volume with mean net stress, $p'$ , under wetting and drying stress paths (Alonso <i>et al.</i> , 1990).	
	(a) Increments of net mean stress and increasing suction (drying).	2-60
	(b) Decreasing suction (wetting) at increasing net mean stress.	2-60
	(c) Increments of net mean stress and decreasing suction.	2-61
2.37	Introduction of the Neutral Line (NL) yield curve for highly expansive soils to complement the LC and the SI yield curves (Gens and Alonso, 1992).	2-61
2.38	Critical state constitutive surfaces for Kinyu gravel (Toll, 1990).	
	(a) Deviator stress critical state surface.	2-62
	(b) Specific volume critical state surface.	2-62
2.39	Variation of specific volume during ramped consolidation of compacted speswhite kaolin at various values of suction (Wheeler and Sivakumar, 1995).	2-62
2.40	Critical state lines for deviator stress and specific volume (Wheeler and Sivakumar, 1995).	
	(a) Deviator stress versus mean net stress.	2-63
	(b) Specific volume versus mean net stress.	2-63
2.41	A constant suction yield curve in relation to the normal compression line and CSL (Wheeler and Sivakumar, 1995).	2-63
2.42	Shear strength surface in $q-s$ space (Delage and Graham, 1995).	2-64
2.43	State boundary surface of the "closure" type critical state framework for unsaturated soil (Tang and Graham, 2002).	2-64
2.44	Framework prediction for wetting and drying cycles under an isotropic net stress of 10 kPa (Gallipolli <i>et al.</i> , 2003) based on the experimental data of Sharma (1998).	
	(a) Change of void ratio.	2-65
	(b) Stress path.	2-65
2.45	Elasto-plastic framework proposed by Wheeler <i>et al.</i> (2003).	2-65
2.46	Volume reductions under wetting and drying stress paths.	
	(a) Alonso <i>et al.</i> (1995).	2-66
	(b) Sharma (1998).	2-66
2.47	Superimposition of the wetting followed by the drying path onto the elasto-plastic framework of Wheeler and Sivakumar (1995) as reported by Alonso <i>et al.</i> (1995) in Figure 2.45(a).	2-66
	Chapter 3	
3.1	Unsaturated triaxial stress state.	
	(a) Stress state in an unsaturated triaxial specimen.	3-40
	(b) Stress state in a saturated triaxial specimen.	3-40
	(c) Representation of unsaturated stress state by Mohr circle 1 and the saturated stress state by Mohr circle 2 in extended Mohr-Coulomb space.	3-40
3.2	New proposed semi-empirical soil shear strength model.	3-41
3.3	Validation of Equations 3.4 and 3.7 using experimental data from Gan and Fredlund (1996) and Toll <i>et al.</i> (2000). The lines represent the analytical form and the data points are the reported data.	3-42
3.4	The validation of Equations 3.4 and 3.7 using experimental data from Escario and Juca (1989). The lines represent the analytical form and the data points are the reported data.	3-42
3.5	The validation of Equations 3.13 and 3.14 using experimental results from Charles and Watts (1980). The lines represent the analytical form and the data points are the reported data.	3-43

## List of Figures (continued)

		Page no.
3.6	Mobilized minimum friction angle, $\phi'_{\min_{mob}}$ describes the position of the current yield envelope. All the points on the yield envelope represent the same axial strain irrespective of the net confining stress or suction.	3-43
3.7	Typical stress-strain behaviour from triaxial compression test.	3-44
3.8	The rotation of the yield surface envelope as the deviator stress increases from $q_{mob1}$ to $q_{mob2}$ and the assumption that $\Delta\phi'_{\min_{mob}} = \Delta\phi'_{mob}$ .	3-44
3.9	Rotation of the yield envelope to the shear strength envelope at failure and the assumption that $\phi'_{mob_f} - \phi'_{mob} = \phi'_{\min_f} - \phi'_{\min_{mob}}$ .	3-45
3.10	Modelling loading collapse in the Multiple Rotational Yield Surface Framework.	
	(a) Rotated mobilized shear strength envelopes at the point of engaging contact with the corresponding enlarged Mohr circles at stress equilibrium..	3-46
	(b) The rotated mobilized shear strength envelopes about the suction axis that correspond to their curvilinear lines in (a).	3-46
3.11	Modelling wetting and drying collapse in the Multiple Rotational Yield Surface Framework.	
	(a) Proportionate rotation of the curvilinear tangent line on the surface envelope when Mohr circles retreat towards lower suction.	3-47
	(b) The shear surface envelopes rotated about the suction axis that correspond to the curvilinear tangent lines in (a).	3-47
3.12	Process of predicting the stress-strain curve by the Rotational Multiple Yield Surface Framework.	
	(a) Predetermined unique relationship of $\phi'_{\min_{mob}} - \varepsilon_a$ .	3-48
	(b) Construction of the different inclination of the yield surfaces base on the shape of the shear strength envelope at failure and the drawing of the corresponding Mohr stress circles for saturated conditions.	3-48
3.12	(c) Construction of the different inclination of the yield surfaces base on the shape of the shear strength envelope at failure and the drawing of the corresponding Mohr stress circles for unsaturated conditions.	3-49
	(d) Predicted stress-strain curve of the soil at a net confining pressure.	3-49
Chapter 4		
4.1	Grading curves for the test material.	4-63
4.2	Specimen compaction mould.	4-64
4.3	Compaction curves for washed and unwashed samples.	4-65
4.4	Pressure plate extractor apparatus illustrating the flow of excess water during the equalization process with the specimen initially flooded with de-ionised and de-aired water.	4-65
4.5	Plumbing system for the conventional triaxial cell (Salman 1995).	4-66
4.6	Double-wall triaxial cell for testing unsaturated soils after Salman (1995).	4-67
4.7	Plan view of the Perspex curves mounting system for the axial LVDTs used for the specimen internal axial strain measurements (Salman, 1995).	4-68
4.8	Plumbing system for the double-walled triaxial cell (Salman 1995).	4-69
4.9	Large (1770cc) volume change unit (Fair, 2004).	4-70
4.10	Rowe compression cell and its plumbing system used to obtain volume change characteristics for different vertical normal stresses under constant suction.	4-70
4.11	Five high air-entry ceramic discs in a locking ring for the Rowe compression cell.	4-71
4.12	General assembly of the base platen of the Rowe consolidation cell.	4-72
4.13	Initial and final calibration lines for the 0 – 50mm LVDT (Serial No. HS50/4017).	4-73
4.14	Initial and final calibration lines for the 0 – 10mm immersible type LVDT (Serial No. DS200W – 50953).	4-73
4.15	Initial and final calibration lines for the 0 – 25mm immersible type LVDT (Serial No. DS500W – 50956).	4-74

## List of Figures (continued)

		Page no.
4.16	Initial and final calibration lines for Imperial College 100cc type volume change unit (Serial No. LVDT 6015).	4-74
4.17	Calibration lines for 1770cc volume change unit fabricated in house.	4-75
4.18	Initial and final calibration lines for the load cell (Serial No. 8903979).	4-75
4.19	Typical initial and final calibration lines for a pressure transducer (Serial No. 334923).	4-76
4.20	Saturation set up for the high air-entry ceramic disc to be used in the Double-wall Triaxial Cell.	4-76
4.21	The Perspex curves joint system used by Salman (1995).	4-77
4.22	New double guide rod joint in the three Perspex curved system for the internal axial transducer and target holder.	4-77
Chapter 5		
5.1	Soil-moisture characteristic curve and residual suction of 15 kPa of the test material.	5-23
5.2	Soil moisture characteristic curve of the test material relative to finer materials.	5-23
5.3	Consolidation curves for specimens compacted at 4% moisture content (Test series B).	5-24
5.4	Consolidation curves for specimens compacted at 6% moisture content (Test series B).	5-24
5.5	Consolidation curves for specimens compacted at 8% moisture content (Test series B).	5-25
5.6	Consolidation curves for specimens prepared with loose poured dry soil (Test series B).	5-25
5.7	The typical enlarged consolidation curve to determine the volume of membrane penetration for effective stress 100kPa (Test no.1 in Test series B).	5-26
5.8	The typical enlarged consolidation curve to determine the volume of membrane penetration for effective stress 200kPa (Test no.5 in Test series B).	5-26
5.9	The typical enlarged consolidation curve to determine the volume of membrane penetration for effective stress 300kPa (Test no.9 in Test series B).	5-27
5.10	The typical enlarged consolidation curves to determine the volume of membrane penetration for multistage triaxial tests at effective stress of 100kPa (Test no.14(a) in test series B).	5-27
5.11	The typical enlarged consolidation curves to determine the volume of membrane penetration for multistage triaxial tests at effective stress of 200kPa (Test no.14(b) in test series B).	5-28
5.12	The typical enlarged consolidation curves to determine the volume of membrane penetration for multistage triaxial tests at effective stress of 300kPa (Test no.14(c) in test series B).	5-28
5.13	Curves of deviator stress versus axial strain for specimens compacted at 4% moisture content (Test series B).	5-29
5.14	Curves of deviator stress versus axial strain for specimens compacted at 6% moisture content (Test series B).	5-29
5.15	Curves of deviator stress versus axial strain for specimens compacted at 8% moisture content (Test series B).	5-30
5.16	Curves of deviator stress versus axial strain for specimens prepared with loose poured dry soil (Test series B).	5-30
5.17	Curves of deviator stress versus axial strain for the multistage shear strength test on saturated specimens compacted at 4% moisture content (Test series B).	5-31
5.18	Curves of deviator stress versus axial strain for the multistage shear strength test on a saturated specimens compacted at 12% moisture content (Test series B).	5-31
5.19	Curves of volumetric strain versus axial strain during the shearing stage for specimens compacted at 4% moisture content (Test series B).	5-32
5.20	Curves of volumetric strain versus axial strain during the shearing stage for specimens compacted at 6% moisture content (Test series B).	5-32
5.21	Curves of volumetric strain versus axial strain during the shearing stage for specimens compacted at 8% moisture content (Test series B).	5-33
5.22	Curves of volumetric strain versus axial strain during the shearing stage for specimens prepared by loose poured dry soil (Test series B).	5-33
5.23	Curves of volumetric strain versus axial strain during multistage shearing stage for specimens compacted at 4% moisture content (Test series B).	5-34
5.24	Curves of volumetric strain versus axial strain during multistage shearing stage for a specimen compacted at 12% moisture content (Test series B).	5-34

## List of Figures (continued)

		Page no.
5.25	Specimen water volume change during the equalisation process for the triaxial tests on unsaturated specimens.	5-35
5.26	Consolidation curves for net stresses of 100, 200 and 300kPa at suction of 25 kPa (Test series C).	5-35
5.27	Consolidation curves for net stresses of 100, 200 and 300kPa at suction of 50 kPa (Test series C).	5-36
5.28	Consolidation curves for net stresses of 100, 200 and 300kPa at suction of 60 kPa (Test series C).	5-36
5.29	Consolidation curves for net stresses of 100, 200 and 300kPa at suction of 90 kPa (Test series C).	5-37
5.30	The typical enlarged curves of volume change and specimen radial contraction versus time during consolidation of an unsaturated specimen at a net stress 100kPa to determine the membrane penetration value (Test series C: USSuc25NS100).	5-37
5.31	The typical enlarged curves of volume change and specimen radial contraction versus time during consolidation of an unsaturated specimen at a net stress 200kPa to determine the membrane penetration value (Test series C: USSuc25NS200)	5-38
5.32	The typical enlarged curves of volume change and specimen radial contraction versus time during consolidation of an unsaturated specimen at a net stress 300kPa to determine the membrane penetration value (Test series C: USSuc25NS300).	5-38
5.33	Graph of deviator stress versus internal axial strain during shearing for the multistage triaxial test on an unsaturated specimen at a suction of 25kPa (Test series C).	5-39
5.34	Graph of deviator stress versus internal axial strain during shearing for the multistage triaxial test on an unsaturated specimen at a suction of 50kPa (Test series C).	5-39
5.35	Graph of deviator stress versus internal axial strain during shearing for the multistage triaxial test on an unsaturated specimen at a suction of 60kPa (Test series C).	5-40
5.36	Graph of deviator stress versus internal axial strain during shearing for the multistage triaxial test on an unsaturated specimen at a suction of 90kPa (Test series C).	5-40
5.37	Graphs of volumetric strain and specimen water volume change versus internal axial strain during shearing for the multistage triaxial test on an unsaturated specimen at suction of 25kPa (Test series C).	5-41
5.38	Graphs of volumetric strain and specimen water volume change versus internal axial strain during shearing for the multistage triaxial test on an unsaturated specimen at suction of 50kPa (Test series C).	5-41
5.39	Graphs of volumetric strain and specimen water volume change versus internal axial strain during shearing for the multistage triaxial test on an unsaturated specimen at suction of 60kPa (Test series C).	5-42
5.40	Graphs of volumetric strain and specimen water volume change versus internal axial strain during shearing for the multistage triaxial test on an unsaturated specimen at suction of 90kPa (Test series C).	5-42
5.41	Graph of average radial contraction versus internal axial strain during shearing for the multistage triaxial test on an unsaturated specimen at suction of 25kPa (Test series C).	5-43
5.42	Graph of average radial contraction versus internal axial strain during shearing for the multistage triaxial test on an unsaturated specimen at suction of 50kPa (Test series C).	5-43
5.43	Graph of average radial contraction versus internal axial strain during shearing for the multistage triaxial test on an unsaturated specimen at suction of 60kPa (Test series C).	5-44
5.44	Graph of average radial contraction versus internal axial strain during shearing for the multistage triaxial test on an unsaturated specimen at suction of 90kPa (Test series C).	5-44
5.45	Consolidation curves at effective stresses of 100 and 200kPa for the specimens of minimum particle size of 5mm used in test series D.	5-45
5.46	Graphs of deviator stress versus axial strain during the shearing stage of the soil samples used in test series D.	5-45
5.47	Graphs of volumetric strain versus axial strain during the shearing stage of the soil samples used in test series D.	5-46
5.48	Specimen water content during equalisation for 1-D compression tests at suctions of 25 and 50kPa in test series E.	5-46

## List of Figures (continued)

		Page no.
5.49	Graph of axial displacement transducer reading against net stress to determine the friction between the piston and the cell wall for the compression test at a suction of 25kPa in test series E.	5-47
5.50	Graph of axial displacement transducer reading against net stress to determine the friction between the piston and the cell wall for the compression test at a suction of 50kPa in test series E.	5-47
5.51	Graph of axial displacement transducer reading against effective stress for the compression test on saturated specimen in test series E.	5-48
5.52	Graph of net stress and axial displacement against time for the compression test at a suction of 25kPa in test series E.	5-48
5.53	Graph of net stress and axial displacement against time for the compression test at a suction of 50kPa in test series E.	5-49
5.54	Graph of net stress and axial displacement against time for the compression test at saturation in test series E.	5-49
5.55	Stepped-graph of net stress against axial displacement for the compression test at a suction of 25kPa in test series E. The red line represents the states at stress equilibrium condition.	5-50
5.56	Stepped-graph of net stress against axial displacement for the compression test at a suction of 50kPa in test series E. The red line represents the states at stress equilibrium condition.	5-50
5.57	Stepped-graph of axial displacement versus effective stress for the compression test on saturated specimen in test series E. The red line represents the states at stress equilibrium condition.	5-51
Chapter 6		
6.1	Lower shear strength envelope for S4%MST1 due to the reduction of the cell and pore water pressure by more than 150kPa after the saturation stage.	6-39
6.2	Volumetric strain versus axial strain during the third shearing stage for a multistage triaxial test on an unsaturated specimen.	
	(a) Suction of 25 kPa.	6-40
	(b) Suction of 50 kPa.	6-40
	(c) Suction of 60 kPa.	6-41
	(d) Suction of 90 kPa.	6-41
6.3	Graph of mobilized friction angle, $\phi'_{mob}$ , versus void ratio, $e$ during shearing stage in triaxial tests on saturated and unsaturated specimens.	
	(a) Graph of mobilized friction angle, $\phi'_{mob}$ , versus void ratio, $e$ , for triaxial tests on saturated specimens in test series B.	6-42
	(b) Lines of identical gradient, $\frac{\Delta\phi'_{mob}}{\Delta e}$ , for shearing of saturated and unsaturated triaxial test specimens at an effective or net stress of 100kPa.	6-43
6.4	Plots of mobilized friction angle versus void ratio to indicate the breakage and "no breakage" conditions.	
	(a) Plot of mobilized friction angle versus void ratio.	6-44
	(b) Plot of S8%SSES300.	6-44
6.5	Graphs of deviator stress, cell pressure, pore water pressure and specimen volume change versus strain for S8%SSES300.	6-45
6.6	Mohr Coulomb envelopes for loose specimens of different gradings.	6-45
6.7	Saturated shear strength behaviour of test material with respect to effective stress and the corresponding shear strength parameters.	
	(a) Mohr Coulomb envelope for saturated conditions obtained from Mohr circles for shear strength tests on saturated specimens according to the data listed in Table 5.3.	6-46
	(b) The Mohr-Coulomb envelope is obtained using Equations 3.13 and 3.14 with transition effective stress of 200 kPa, transition shear strength of 230 kPa, and the minimum internal friction angle, $\phi'_{min}$ , of 34°.	6-46

## List of Figures (continued)

		Page no.
6.8	Comparison of the shear strength envelopes for loosely prepared specimens and compacted specimens.	6-47
6.9	Mohr circles for unsaturated consolidated drained triaxial tests at suction 25kPa compared to the saturated shear strength envelope.	6-47
6.10	Mohr circles for unsaturated consolidated drained triaxial tests at suction 50kPa compared to the saturated shear strength envelope.	6-48
6.11	Mohr circles for unsaturated consolidated drained triaxial tests at suction 60kPa compared to the saturated shear strength envelope	6-48
6.12	Mohr circles for unsaturated consolidated drained triaxial tests at suction 90kPa compared to the saturated shear strength envelope.	6-49
6.13	The variation of apparent shear strength with respect to suction using Equations 3.4 and 3.7 excluding the saturated shear strength..	6-49
6.14	The assumed linear variation of ultimate suction with respect to effective stress from the data in Figure 6.13.	6-50
6.15	Analytical contours for the warped-surface extended Mohr-Coulomb envelope of the test material. Data points are the experimental data.	6-50
6.16	Perspective view of the warped-surface extended Mohr-Coulomb envelope of the test material showing the four shear strength equations and their represented zones, and the seven parameters required to define the surface envelope.	6-51
6.17	Perspective view from underneath the warped-surface extended Mohr-Coulomb envelope of the test material showing the shear strength parameters and the dimensions they represent.	6-51
6.18	Rotation of the mobilized shear strength envelope during triaxial compression test on saturated specimens compacted at 8% moisture content.	6-52
6.19	Plots of effective mobilized friction angle, $\phi'_{mob}$ , versus axial strain for triaxial tests on saturated specimens compacted at 8% moisture content.	6-52
6.20	Unique graphs of $\phi'_{min_{mob}} - \epsilon_a$ for triaxial tests on saturated specimens compacted at 8% moisture content and sheared at effective stresses of 100, 200 and 300 kPa.	6-53
6.21	Rotation of the mobilized shear strength envelope during triaxial compression test on saturated specimens compacted at 4% moisture content.	6-53
6.22	Rotation of the mobilized shear strength envelope during triaxial compression test on saturated specimens compacted at 6% moisture content.	6-54
6.23	Rotation of the mobilized shear strength envelope during triaxial compression test on unsaturated specimens of suction 25 kPa.	6-54
6.24	Rotation of the mobilized shear strength envelope during triaxial compression test on unsaturated specimens of suction 50 kPa.	6-55
6.25	Plots of mobilized friction angle versus axial strain for triaxial compression tests on saturated specimens compacted at 4% moisture content.	6-55
6.26	The dispersion on the graphs of $\phi'_{min_{mob}} - \epsilon_a$ for triaxial compression tests on saturated specimens compacted at 4% moisture content and sheared at effective stresses of 100, 200 and 300 kPa.	6-56
6.27	Plots of mobilized friction angle versus axial strain for triaxial tests on saturated specimens compacted at 6% moisture content.	6-56
6.28	The dispersion on the graphs of $\phi'_{min_{mob}} - \epsilon_a$ for triaxial compression tests on saturated specimens compacted at 6% moisture content and sheared at effective stresses of 100, 200 and 300 kPa.	6-57
6.29	Graphs of mobilized friction angle versus axial strain for triaxial tests on unsaturated specimens of suction 25 kPa compacted at 4% moisture content and sheared at net stresses of 100, 200 and 300 kPa.	6-57
6.30	The slight dispersion on the graphs of $\phi'_{min_{mob}} - \epsilon_a$ for triaxial compression tests on unsaturated specimens of suction 25 kPa compacted at 4% moisture content and sheared at effective stresses of 100, 200 and 300 kPa.	6-58

## List of Figures (continued)

		Page no.
6.31	Graphs of mobilized friction angle versus axial strain for triaxial tests on unsaturated specimens of suction 25 kPa compacted at 4% moisture content and sheared at net stresses of 100, 200 and 300 kPa.	6-58
6.32	The slight dispersion on the graphs of $\phi'_{\min_{mob}} - \epsilon_a$ for triaxial compression tests on unsaturated specimens of suction 50 kPa compacted at 4% moisture content and sheared at effective stresses of 100, 200 and 300 kPa.	6-59
6.33	Deduced unique relationship of $\phi'_{\min_{mob}} - \epsilon_a$ for triaxial compression tests on saturated specimens compacted at 8% moisture content.	6-59
6.34	Prediction of major principal net stresses during yielding in triaxial compression test at effective stress 100 kPa in order to obtain the corresponding deviator stress.	6-60
6.35	Prediction of major principal net stresses during yielding in triaxial compression test at effective stress 200 kPa in order to obtain the corresponding deviator stress.	6-60
6.36	Prediction of major principal net stresses during yielding in triaxial compression test at effective stress 300 kPa in order to obtain the corresponding deviator stress.	6-61
6.37	Prediction of the stress-strain behaviour up to failure point for triaxial tests on saturated specimens compacted at 8% moisture content at effective stresses of 105, 200 and 304 kPa.	6-61
6.38	Deduced unique relationship of $\phi'_{\min_{mob}} - \epsilon_a$ for triaxial compression tests on saturated specimens compacted at 6% moisture content.	6-62
6.39	Prediction of major principal stresses during yielding in triaxial compression test at effective stress 105 kPa for specimen compacted at 6% moisture content.	6-62
6.40	Prediction of major principal stresses during yielding in triaxial compression test at effective stress 199 kPa for specimen compacted at 6% moisture content.	6-63
6.41	Prediction of major principal stresses during yielding in triaxial compression test at effective stress 245 kPa for specimen compacted at 6% moisture content.	6-63
6.42	Prediction of the stress-strain behaviour up to failure point for triaxial test on saturated specimens compacted at 6% moisture content at effective stresses of 105, 199 and 304 kPa.	6-64
6.43	Deduced unique relationship of $\phi'_{\min_{mob}} - \epsilon_a$ for triaxial compression tests on unsaturated specimens at suction of 25 kPa.	6-64
6.44	Prediction of major principal stresses during yielding in triaxial compression test on unsaturated specimen of suction 25 kPa at net stress of 100 kPa.	6-65
6.45	Prediction of major principal stresses during yielding in triaxial compression test on unsaturated specimen of suction 25 kPa at net stress of 200 kPa.	6-65
6.46	Prediction of major principal stresses during yielding in triaxial compression test on unsaturated specimen of suction 25 kPa at net stress of 300 kPa.	6-66
6.47	Prediction of the stress-strain behaviour up to failure point for triaxial test on unsaturated specimens of suction 25 kPa at net stresses of 100, 200 and 300 kPa.	6-66
6.48	Effective stress and net stress versus void ratio for saturated and unsaturated specimens respectively in Rowe cell compression tests in test series E.	6-67
6.49	The relationship between net normal stress and axial strain during Rowe cell compression tests on saturated and unsaturated specimens.	6-67

## List of Symbols

$c'$	Effective cohesion.
$c_s$	Apparent cohesion.
$c_s^{\max}$	Maximum apparent cohesion.
$e$	Void ratio.
$e_0$ or $e_i$	Initial void ratio.
$e_i'$	Intercept of the extrapolated linear section of $e-\sigma'$ curve with void ratio axis at saturation.
$e_f$	Final void ratio.
$m_1^s$	Coefficient of soil volume change with respect to a change in net normal stress.
$m_2^s$	Coefficient of soil volume change with respect to a change in suction.
$n$	Porosity.
$p$	Isotropic stress.
$p'$	Net mean stress.
$p_o'(s)$	Yielding stress for a given suction taken as the kink in the normal compression line that represents the change in stiffness.
$p^c$	Value of net mean stress at which the yield stress $p_o'$ is independent of suction.
$p_{at}$	Atmospheric pressure (100kPa).
$p_x$	Critical state value of $p$ .
$p^*$ or $p''$ or $\sigma_{hk}'$	Bishop (1959) effective stress or inter-particle stress.
$s^*$	Modified suction.
$t$	Time.
$v$	Specific volume.
$w$	Moisture content.
$C_t$	Compressibility coefficient with respect to net mean stress.
$C_m$	Compressibility coefficient with respect to suction.
$F_R$	Coulomb friction.
$F_N$	Normal force.
$K$	Soils shear strength parameter dependent on soil type.
$K_o$	Coefficient of earth pressure at rest.
$M$ or $M(s)$ or $M_s$ or $M_\theta$	Critical state stress ratio or slope of critical state line in $q-p$ plot.
$M_w$ or $k$ or $\mu(s)$	Critical state suction ratio or intersection of the critical state line, CSL with the ordinate in a $q-p$ plot.
$M_*$	The critical state elliptical yield surface aspect ratio.
$N$	A constant that makes the gradient at the end of the curved section of shear strength behaviour with respect to effective stress equal to the gradient of the linear section.
$N(0)$	Value of $N(s)$ at zero suction.
$N(s)$	Intercept of the normal compression line in a $v-\ln(p'/p_{at})$ or $v-\ln(p'/p^c)$ plot.
$S_r$	Degree of saturation at residual condition.
$S$	Degree of saturation.
$V$	Total volume.
$V_i$	Initial specimen volume.
$V_v$	Volume of soil voids.
$V_o$	Initial total volume of soil.
$\phi'$	Effective angle of internal friction.
$\phi'_{mob}$	Effective mobilized friction angle.
$\phi'_{min\ mob}$	Effective mobilized minimum friction angle.
$\phi'_{min f}$	Effective minimum friction angle at failure.
$\phi^b$	Angle indicating the rate of increase in shear strength related to suction.
$\mu$	Coefficient of friction.
$\lambda(0)$	Value of $\lambda(s)$ at zero suction.
$\lambda(s)$	Slope of the normal compression line in a $v-\ln(p'/p_{at})$ or $v-\ln(p'/p^c)$ plot.

## List of Symbols (continued)

$\lambda_a$	Slope of the critical state plane in $v:p-u_a:u_a-u_w$ space with respect to net stress.
$\lambda_w$	Slope of the critical state plane in $v:p-u_a:u_a-u_w$ space with respect to suction.
$\kappa_s$	Elastic swelling index with respect to $s$ .
$\kappa$	Elastic swelling index with respect to $p'$ .
$\sigma$	Normal stress.
$\sigma'$ or $(\sigma - u_w)$	Effective normal stress.
$(\sigma_1 - u_w)$	Effective major principal stress.
$(\sigma_3 - u_w)$	Effective minor principal stress.
$\sigma'_x$	Arbitrary effective stress.
$u_a$	Pore-air pressure.
$u_w$	Pore-water pressure.
$(u_a - u_w)$ or $s$	Suction.
$(u_a - u_w)_r$ or $s_r$	Residual suction.
$(u_a - u_w)_u$	Ultimate suction.
$(u_a - u_w)_u^{\sigma'=0}$	Ultimate suction when net stress is zero.
$\sigma_1$	Major principal stress.
$\sigma_3$	Minor principal stress.
$\sigma'_1$ or $(\sigma_1 - u_a)$	Net major principal stress
$\sigma'_3$ or $(\sigma_3 - u_a)$	Net minor principal stress.
$(\sigma - u_a)$	Net normal stress.
$(\sigma - u_w)_t$	Transition effective stress.
$\chi$	Effective stress parameter (Bishop, 1959).
$(p - u_a)$ or $p'$	Net mean stress.
$q$ or $(\sigma_1 - \sigma_3)$	Deviator stress.
$\epsilon_a$	Axial strain.
$\epsilon_v$	Volumetric strain
$\gamma_w$	Unit weight of water.
$\gamma_{dry}$	Dry unit weight of soil.
$(\sigma_3 - u_a)$	Net cell pressure.
$(\sigma_3 - u_w)$	Effective cell pressure.
$\tau$	Shear strength.
$\tau_t$	Transition shear strength.
$\zeta$	Rate of increase in ultimate suction with respect to net stress.
$\tau_m$	Mobilized shear stress.
$\theta$	Volumetric moisture content.
$\theta_s$	Volumetric water content at saturation.
$\theta_r$	Volumetric water content at residual condition.
$\Gamma_s$	Specific volume in saturated state.
$\Gamma_{aw}$	Specific volume when $p-u_a$ and $u_a - u_w$ equal unity.
$\Psi_s$	Slope of critical state line in $v - \ln p$ plot.

## List of Symbols (continued)

$\eta_s$	Stress ratio s/p.
$\xi$	Second type of suction as a function of degree of saturation.
$\Delta e$	Change in void ratio.
$\Delta \phi'$	Change in friction angle.
$\Delta s$	Change in suction
$\Delta \sigma'$	Change in effective stress
$\Delta V$	Change in total volume.
$\Theta$	Normalised volumetric moisture content.

## List of Definitions

Angle of dilation, $\psi$	If the shearing distance $dx$ along a horizontal shear plane produces an upward movement of $dy$ , then the angle of dilation is given by $\psi = \tan^{-1}(dy/dx)$ .
Collapse failure	Soil compression due to yielding which occurs when the soil state of stress exceeds the mobilized shear strength through either wetting or loading collapse.
Critical state condition	The state of shearing where unlimited shear strain can be applied without further changes in specific volume, $v$ , shear stress, $\tau$ , and effective normal stress, $\sigma'$ .
Critical state friction angle, $\phi'_{crit}$	The slope of the line $\tau = \sigma' \tan \phi'_{crit}$ that passes through the origin and is tangential to Mohr circles of stress representing the stress condition at critical state.
Critical state line (CSL)	The line representing critical states condition where soil deforms at constant deviator stress and constant specific volume.
Dilation	Increase in total volume due to the increase in the volume of voids as the soil particles slide over one another during shear.
Dilation point	The point where the volume change behaviour changes from contraction to dilation and this is represented by the point of minimum volumetric strain by a specimen that exhibits dilation.
Direct strain, $\epsilon$	Change in length divided by the original length.
Effective angle of internal friction, $\phi'$	The slope of the line representing shear strength in terms of effective normal stress on the failure surface. In the proposed hypothetical shear strength model, $\phi'$ is the slope of the linear section of the failure envelope.
Effective minimum friction angle at failure, $\phi'_{min}$	The slope of the linear section of the shear strength envelope at failure.
Effective mobilized friction angle, $\phi'_{mob}$	Friction angle that describes the stress ratio, $\tau/\sigma'$ at any stage of a shear box or triaxial test. ( $\phi'_{mob} = \tan^{-1}(\tau/\sigma')$ ). In the proposed hypothetical shear strength model, $\phi'_{mob}$ is the slope of the tangent to the Mohr stress circle which passes through the origin at any stage of the shearing in a triaxial compression test.
Effective mobilized minimum friction angle, $\phi'_{min\ mob}$	The slope of the linear section of the mobilized shear strength envelope.
Effective stress	The component of the normal stress transmitted through the soil skeleton. The higher the effective stress the greater is the shear stress that can be applied before relative slip between particles starts to occur.
Failure	Significant movement on the shear plane when the maximum shear stress of the soil is exceeded.
Limiting stress state	Stress state at failure where the Mohr circle of stress touches the yield envelope.
Loading collapse	Soil compression due to load increase.
Mobilized shear strength envelope	In the extended Mohr Coulomb space, it is the locus of the mobilized shear strength with respect to net confining stress and suction to represent all limiting stress states above which the soil will be compressed.
Mobilized shear strength or mobilized shear stress, $\tau_m$	The shear resistance developed in the soil mass or mobilized to enable the soil to carry the applied stresses.
Mohr circle of effective stress	A circle plotted on a graph of shear stress, $\tau$ , against effective normal stress, $\sigma'$ , having centre at $s' = \frac{1}{2}(\sigma'_1 + \sigma'_3)$ and radius $r = \frac{1}{2}(\sigma'_1 - \sigma'_3)$ .

## List of Definitions (continued)

Net stress or net normal stress	The difference between the normal stress and the pore air pressure.
Peak strength	Maximum shear stress when the soil is failing.
Normal compression line (NCL)	A straight line in $v$ - $\ln p'$ space representing a unique relationship between specific volume, $v$ and the mean normal effective stress $p'$ when the soil is subjected to isotropic compression for first time.
Point of maximum rate of dilation	The point of steepest gradient on the graph of volumetric strain versus axial or shear strain when the soil is dilating.
Shear strain, $\gamma$	Specimen lateral displacement divided by height.
Shear strength	The ability of the soil to resist shear.
Shear strength envelope or failure envelope	The locus of the shear strength with respect to net stress and suction to represent all possible stress states at failure.
Specific volume	Actual volume of soil containing a unit volume of solid.
Strain hardening or work hardening or volumetric hardening	The increased capacity of the material to sustain an increasing stress with increasing plastic strain between yield and failure.
Suction	The difference between the pore air and the pore water pressures acting on the contractile skin present between particles of a partly saturated soil.
Wetting collapse	Soil compression induced by inundation or suction decrease.
Yield point	The point when the stress-strain behaviour ceases to be purely elastic, i.e. the deformation stops being recoverable on unloading.
Yield strength	Shear stress corresponding to the yield point.
Yield surface envelope or yield surface	(a) In the extended Mohr Coulomb space for unsaturated soil, i.e. $\tau : (\sigma - u_a) : (u_a - u_w)$ , it is the surface that represents identical axial strain according to the proposed Rotational Multiple Yield Surface Framework. It is in contact with the Mohr stress circles representing the soil current stress state which is lower than the stress state at peak strength. (b) In critical state model for unsaturated soil it is the combination of $q$ , $p'$ and $(u_a - u_w)$ that causes the soil to yield.
Yielding	Soil compression which causes relative slip between particles and results in the rearrangement of the particles to a denser state of packing whenever the stress state exceeds the current yield strength.

## Chapter 1

### Introduction

The mechanics of unsaturated soil behaviour are more complex than those of saturated soils due to the presence of negative pore water pressure or suction within the soil mass. The difficulties in finding a single value effective stress equation has resulted in the use of two independent stress state variables namely net stress,  $(\sigma - u_a)$  where  $\sigma$  is the total stress and  $u_a$  is the pore air pressure and suction,  $(u_a - u_w)$  where  $u_w$  is the pore water pressure in assessing the mechanical behaviour of unsaturated soils. Currently there is still a need for a comprehensive and representative shear strength model with respect to net stress and suction. This is very significant for explaining the soil behaviour at low stress and suction levels in situations like collapse failure due to inundation and shallow slope failures due to rainfall infiltration. There is also the need for a volume change framework that can explain both the volume change behaviour due to inundation (i.e. wetting collapse) and the increase in vertical stress (i.e. loading collapse) from the standpoint of shear strength. The aims of this research are to understand the shear strength behaviour and how it influences the volume change behaviour in the context of saturated and unsaturated coarse-grained soils.

Researchers like Wheeler *et al.* (2003) and Gallipoli *et al.* (2003) have been working on the volume change framework for fine-grained soils, and have tried to incorporate degree of saturation in the stress state variables since the effect of suction on soil behaviour does not increase indefinitely. It seems to be dependent on soil and water contact area. This alternative step was taken after the realisation by Wheeler *et al.* (2003) that the existing critical state model of Alonso (1990) developed for unsaturated fine grain soils has failed to model the volume change behaviour due to alternate wetting and drying as reported by Alonso (1995) and Sharma (1998). It is anticipated that there is inadequacy in the definition of yielding based purely on the changes of suction,  $(u_a - u_w)$ , without incorporating the contribution by the principal stresses. Applying the same approach for coarse-grained soils is anticipated to encounter the same problem. In order to consider yielding as a collective effect of the principal stresses and suction a hypothetical volume change framework is proposed

based on the concept of Mohr stress circles and the mobilized shear strength,  $\tau_m$ , envelope.

The following objectives were formulated to achieve this aim.

1. To propose a semi-empirical unsaturated shear strength model for fine and coarse-grained soils based on the shear strength behaviour with respect to net stress and suction reported in the literature.
2. To propose a qualitative shear strength-volume change framework for coarse-grained soils based on the relevant volume change characteristics of fine and coarse-grained soils reported in the literature.
3. To conduct pressure plate extractor tests on coarse-grained soil to obtain its soil-moisture characteristic curve and to determine its magnitude of residual suction.
4. To conduct triaxial compression tests on saturated and unsaturated specimens of coarse-grained soils.
5. To check whether the test results in objective (4) support the proposed semi-empirical shear strength model.
6. To check whether the test results in objective (4) support the application of the proposed hypothetical volume change framework in explaining the modes of loading and wetting collapse in coarse-grained soils.
7. To investigate the effect of particle breakage on the proposed hypothetical shear strength-volume change framework.
8. To conduct 1-D compression tests in a Rowe cell under saturated conditions and under different suctions in order to examine the one-dimensional volume change behaviour of the test material.

Chapter 2 presents a review of literature relating to past work on shear strength and volume change behaviour of unsaturated soils. By and large this chapter is showing that there is still a lack of a good representative extended Mohr Coulomb shear strength model, and that the existing critical state frameworks cannot comprehensively explain the wetting and drying collapse volume change behaviour.

In Chapter 3 the physical shape of the semi-empirical shear strength model is formulated based on shear strength behaviour reported in the literature. It takes the

form of a single warped-surface envelope in  $\tau : (\sigma - u_a) : (u_a - u_w)$  space known as extended Mohr-Coulomb and this is followed by the formulation of the representative analytical form. They were then validated against reported data. This is followed by the formulation of the hypothetical shear strength-volume change framework starting from the development of the conceptual model. Collapse failure is based on the availability of space for particle rearrangement and is taken as particle densification by the combination of their shear and vertical movement driven by shear and net vertical stresses respectively which move them to any available space. Based on the reported volume change behaviour in the literature the general characteristics of the hypothetical framework are recognised and applied to construct the structure and the principal concept. This is followed by the qualitative evaluation of the framework.

Chapter 4 begins with a discussion on the selection of the test material followed by the description of its properties. Then the equipment involved in this research is described, followed by the instrumentation and the calibration of the measuring devices. The chapter gives details of the test procedures for each type of test. The chapter concludes with a description of the laboratory test programme outlined as test series A, B, C, D and E.

Test results of the test series A, B, C, D and E are presented in Chapter 5. In Chapter 6 the shear strength parameters according to the proposed shear strength model are interpreted from the test results. The correlation between the analytical and the experimental data was obtained in order to check the applicability of the proposed model to the shear strength behaviour of coarse-grained material. Then the rotation of the mobilized shear strength envelope about the suction axis towards the soil shear strength envelope at failure according to the proposed Rotational Multiple Yield Surface Framework, was plotted. The existence of unique graphs of  $\phi'_{\min, \text{mob}} - \epsilon_a$  proved that a mobilized shear strength envelope is representing identical axial strain and therefore can be regarded as a yield surface. The existence of this unique relationship for loading collapse stress conditions was addressed. Finally in Chapter 7 conclusions are drawn and a number of recommendations are made for future research.

## Chapter 2

### Literature Review: Shear Strength and Volume Change Behaviour of Unsaturated Soils

This chapter begins with a discussion on the choice of appropriate stress state variables for unsaturated soils and the various soil-moisture characteristic curves for soils of different particle sizes, and highlights the importance of this curve in connection with the shear strength behaviour. Then it reviews behaviour of coarse-grained soils and the influence of particle breakage on that behaviour. It also covers the shear strength and volume change behaviour of the soils under saturated and unsaturated conditions. This includes a review of the shear strength behaviour with respect to suction and net stress. This leads on to the description of the various published volume change models which mostly were developed based on the behaviour of fine grain soils. It includes the various elasto-plastic critical state frameworks that have been introduced to explain the volume change behaviour of the fine grain unsaturated soils from the standpoint of deviator stress, net mean stress and suction. The models' strengths and weaknesses act as a guide for the development of an appropriate model for coarse-grained soils. Then the chapter describes the problem faced by the critical state frameworks in simulating the reported alternate wetting and drying volume change behaviour. Finally it emphasises on the need for a more representative shear strength model and an alternative shear strength-volume change framework for coarse-grained soils.

#### 2.1 Independent Stress State Variables used for Unsaturated Soils.

Bishop (1959) was the first to use the two independent stress state variables, net stress,  $(\sigma - u_a)$  and suction,  $(u_a - u_w)$  for unsaturated soils in his tentative suggestion for unsaturated soil effective stress equation as in Equation 2.1,

$$\sigma' = (\sigma - u_a) + \chi(u_a - u_w) \quad \text{Equation 2.1}$$

where  $\chi$  is the weighting factor related to degree of saturation and takes a value of 1.0 for full saturation and zero when dry.

In an attempt to validate the Bishop (1959) effective stress equation Bishop *et al.* (1960) substituted the effective stress equation into Terzaghi's (1936) shear strength

equation for saturated soil as in Equation 2.2 to produce a tentative shear strength equation for unsaturated soil as in Equation 2.3;

$$\tau = c' + (\sigma - u_w) \tan \phi' \quad \text{Equation 2.2}$$

where  $c'$  is the effective cohesion and  $\phi'$  is the effective internal friction angle.

$$\tau = c' + [(\sigma - u_a) + \chi(u_a - u_w)] \tan \phi' \quad \text{Equation 2.3}$$

This was followed by Bishop and Blight (1963) in another attempt to restate the Bishop (1959) effective stress equation where a graphical illustration for volume change behaviour of unsaturated soil was expressed in the form of the two independent stress state variables as shown in Figure 2.1. This further reinforced the use of the two stress state variables. Burland (1964 and 1965) further questioned the validity of the Bishop (1959) effective stress equation but insisted that the use of those stress state variables in formulating the mechanical behaviour of unsaturated soil is inevitable. This was then followed by Matyas and Radhakrishna (1968) who described the volume change behaviour of unsaturated soil in the form of a three-dimensional surface with respect to the two independent stress state variables as shown in Figure 2.2. Barden *et al.* (1969) came up with the same idea as Burland (1964, 1965) in the use of the two independent stress state variables in accessing volume change behaviour. Brackely (1971) studied the application of the effective stress principle to the volume change behaviour of unsaturated soil and concluded that the use of a single-valued effective stress equation i.e. Equation 2.1 is limited. Since then the application of the two independent stress state variables in accessing the mechanical behaviour of unsaturated soil has intensified and they were used to formulate constitutive equations for shear strength and volume change behaviour of unsaturated soils. Subsequently, Fredlund and Morgenstern (1976) and Fredlund *et al.* (1978) have come up with a semi-empirical volume change, and shear strength equation, for unsaturated soil using the two independent stress state variables.

The application of critical state theory to unsaturated soils starts the use of the three-dimensional stress invariants; average principal effective stress or net mean stress  $p'$ , deviator stress,  $q$ , and suction,  $s$ . At any point within the body of unsaturated soil, there will be three principal net stresses acting, which are  $(\sigma_1 - u_a)$ ,  $(\sigma_2 - u_a)$  and  $(\sigma_3 - u_a)$  where  $\sigma_1$  is the total major principal stress and  $\sigma_2$  and  $\sigma_3$  are two

perpendicular stresses. Therefore, in the three-dimensional case there will be a total of four stress parameters required to fully define the stress condition at that specific point:  $(\sigma_1 - u_a)$ ,  $(\sigma_2 - u_a)$ ,  $(\sigma_3 - u_a)$  and  $(u_a - u_w)$ . For an axi-symmetric condition where  $\sigma_2$  equals  $\sigma_3$ , then the critical state stress invariants  $p'$ ,  $q$  and  $s$  are as defined in Equations 2.4, 2.5 and 2.6 respectively.

$$p' = \left( \frac{\sigma_1 + 2\sigma_3}{3} \right) - u_a \quad \text{Equation 2.4}$$

$$q = (\sigma_1 - \sigma_3) \quad \text{Equation 2.5}$$

$$s = (u_a - u_w) \quad \text{Equation 2.6}$$

## 2.2 Soil-moisture Characteristic Curve and Residual Suction.

The soil-moisture characteristic curve, which is also known as water retention curve, gives the relationship between water content and suction of a soil. The variation of the soil-moisture characteristic curves for soil types ranging from sand to clay is illustrated in Figure 2.3(a) for some Dutch soils (Koorevaar *et al.* 1983).

Residual suction,  $(u_a - u_w)_r$ , is defined as the suction at the water content below which a large suction change is required to remove additional water from the soil, or in other words a small change in the moisture content produces a vast change in suction (Fredlund and Xing 1994). In the soil-moisture characteristic curve, water content that corresponds to residual suction is referred as residual water content,  $\theta_r$ . A graphical method of drawing tangent lines at the mid and tail sections of the volumetric water content versus matric suction graph in order to obtain these two parameters is illustrated in Figure 2.3(b). Based on this method the residual suction for dune sand (Koorevaar *et al.* 1983) is about 100kPa (refer to Figure 2.3(a)) and the value increases as the soil particles get finer. The different paths taken by the same soil for drying (desorption) and wetting (adsorption), as illustrated in Figure 2.3(b), is called hysteresis.

## 2.3 Behaviour of Coarse-grained Soils.

Most of the shear strength tests on coarse-grained soils have concentrated on testing the soils either saturated or dry at higher stress levels ( $> 100\text{kPa}$ ). Then from the

1980's onwards triaxial testing of unsaturated soils has mostly involved clayey sand and silty sand involving residual soils, gold tailings and glacial tills like the work of Ho and Fredlund (1982), Gan *et al.* (1988), Gan and Fredlund (1988, 1996), Escario and Juca (1989), Rahardjo and Fredlund (1993), Mahalinga-Iyer and Williams (1995), Rassam and Williams (1999) and Toll *et al.* (2000). Little work has been done to study the shear strength behaviour of granular soils bigger than sand size with respect to suction except the works of Toll (1990) and Anderson *et al.* (1997). This may be due to the small value of suction available in this type of soil compared to that in clay soils and thus its influence was thought to be less pronounced. However, when dealing with unsaturated coarse-grained soil at low ( $< 100\text{kPa}$ ) stress levels, the value of the suction may be of the same order of magnitude as the applied stresses and thus be significant. Moreover the massive compression collapse near saturation upon inundation usually involved coarse-grained backfilled material (Goodwin 1991, Blanchfield and Anderson 2000) and this type of behaviour is still not fully understood. This volume change behaviour was taking place under low confining pressure since it occurred near the ground surface under low suction since it was close to saturation. Thus in order to understand the phenomenon of volume change in this type of soil from the standpoint of shear strength, it is essential to know the shear strength behaviour under these low stress conditions.

Quite an extensive amount of work has been performed to determine the shear strength behaviour of clayey sand (e.g. Escario and Juca, 1989; Rassam and Williams, 1999 and Toll *et al.*, 2000) with respect to suction and the rapid drop in shear strength as suction approaches zero has become very apparent. However, the shear strength behaviour at high values of suction is still unclear and more work is still required. The limitation of working at the high range of suction in clayey soils is the difficulty of achieving the suction during tests, which required a very fine high air-entry disc and this leads to a lengthy equalisation period. This could be one of the reasons why the current shear strength behaviour in the higher suction range at different confining pressures is not fully understood.

### 2.3.1 Stress, Strain and Volume Change Behaviour.

Consider the typical results from shear box tests on dense and loose specimens of sand under a constant and uniform normal stress,  $\sigma$ , as shown in Figure 2.4(a) – (c). Figure 2.4(a) shows the relationship between shear stress,  $\tau$  and shear strain,  $\gamma$ , Figure 2.4(b) shows the relationship between volumetric strain,  $\varepsilon_v$  and shear strain and Figure 2.4(c) shows the relationship between the specimen's volume,  $V$ , and shear strain. In the test, the shear stress gradually increases with shear strain up to point Y. Within this range (O – Y) the behaviour is elastic; as shear stress increases the soil structure distorts. The distortion is proportional to the applied stress and if the stress is removed the distortions are recovered. The distortions are probably associated with the elastic compression of the particles or the elastic rotations at the particle contacts without any particle slippage taking place.

However, as the shear stress increases beyond point Y, which is known as the yield point, elastic and plastic shear strains occur simultaneously. At this stage the plastic deformation is attributed to the rearrangement of the particle locations through contact point slippage and the plastic components will not be recovered. Beyond the yield point the plastic straining occurs as a non-linear stress-strain behaviour. Since plastic straining results in an increase in shear stress between the grains, which in turn increases the shear strength, this characteristic is known as strain hardening or work hardening. This is because for the case of a dense specimen extra work is required to overcome an increasing shear stress due to the expansion (dilatancy) of the soil skeletal structure as strain increase. At the beginning of shear a dense specimen may undergo a very small compression before it starts to dilate (Figure 2.4(b) and a loose specimen will continually undergoing volumetric compression. For a dense specimen, the gradient of the curve  $\varepsilon_v$  versus  $\gamma$  becomes steeper indicating that the rate of dilation increases and become steepest at point p. The shear stress increases to a peak at point P also known as shear strength at failure (Figure 2.4(a)) which corresponds to the maximum rate of dilation at point p in Figure 2.4(b).

If at point A (Figure 2.4(a)) the stress is removed the strain recovered is the elastic strain BD while the plastic strain OB is irrecoverable. Increasing the stress from B

will recover the elastic strain BD at A and when the stress exceeds the mobilized shear strength,  $\tau_m$ , developed between the soil grains at A, which is achieved from the previous strain hardening, the soil will continue to compress plastically. The mobilized shear strength is a function of the applied effective major principal stress and the soil mobilized friction angle,  $\phi'_{mob}$ , according to Equation 2.7.

$$\tau_m = \sigma' \tan \phi'_{mob} \quad \text{Equation 2.7}$$

Equation 2.7 defines the mobilized shear strength envelope or yield surface envelope. The variation of mobilized friction angle is representing the change in stress ratio  $\tau_m / \sigma'$  at any stage of the shear box or triaxial test and will be discussed further in Section 2.3.2.

After reaching a peak shear stress the shearing resistance decreases and this is described as strain softening or work softening. Eventually, a steady state at C (Figure 2.4(a)) is reached where the curve become horizontal after quite a large strain has taken place.

Similarly in the context of a triaxial test, shear strength at failure is taken as the maximum shear stress developed, which corresponds to the maximum deviator stress. As the deviator stress falls towards a steady state at C, the curve of  $\varepsilon_v$  versus  $\gamma$  also become horizontal which means  $d\varepsilon_v / d\gamma$  is zero indicating that dilation has ceased and correspondingly Figure 2.4(c) indicate the achievement of the critical specific volume,  $v_{crit}$ . This is the onset of a critical state condition whereby deformation is taking place under constant stress and volume irrespective of the initially dense or loose specimen. In an undrained triaxial test the volumetric strain is given by,

$$\varepsilon_v = \varepsilon_a + 2\varepsilon_r = 0 \quad \text{Equation 2.8}$$

$$\varepsilon_r = \left(-\frac{1}{2}\right)\varepsilon_a \quad \text{Equation 2.9}$$

In a drained triaxial test the volumetric strain is non zero,

$$\varepsilon_r = \left(\frac{1}{2}\right)(\varepsilon_v - \varepsilon_a) \quad \text{Equation 2.10}$$

At critical state condition, there is zero volume change or zero volumetric strain ( $\varepsilon_v = 0$ ). Therefore the relationship between radial and axial strain is reduced to Equation 2.9.

The point that represent the shear strength at failure during shearing is indicated by the point F in the stress-strain curves for dense coarse-grained soils (Jovicic and Coop, 1997) and over-consolidated London clay (Atkinson, 1975) as shown in Figures 2.5(a) and (b) respectively, with point Y being their yield point. However, for soils that do not exhibit a peak on the stress-strain curve even at large strains the shear strength at failure is taken at an arbitrary strain or at the kink of the stress-strain curve marked by point F, like shown in Figure 2.5(c) for natural soft clay found at Pisa, Italy (Callisto and Calabresi, 1998). The stress-strain curve in Figure 2.5(c) is indicating the occurrence of strain hardening even after the failure point as the typical stress-strain behaviour for normally consolidated clay.

### 2.3.2 Mohr Stress Circle and Mobilized Friction Angle, $\phi'_{mob}$ .

The deviator stress versus axial strain and the volume change behaviour in a conventional triaxial compression test is similar to the shear stress- shear strain and volume change behaviour discussed for the shear box (plane strain) test in the Section 2.3.1. Initially as the deviator stress,  $q$  is increased from zero to the deviator stress correspond to point A,  $q_A$  shown in Figure 2.4(a) the Mohr stress circle starts growing up to Mohr circle 1 in Figure 2.6. At this point the effective minor principal stress is equal to  $\sigma'_{3_A} = \sigma_{3_A} - u$  and the effective major principal stress is equal to  $\sigma'_{1_A} = \sigma_{3_A} + q_A - u$ . The maximum stress ratio at this point is  $\tau_m / \sigma'$  and the mobilized shear stress,  $\tau_m$  in the specimen is given by Equation 2.7 which is the function of the effective major principal stress,  $\sigma'$  and the mobilized friction angle,  $\phi'_{mob}$ . The Mohr stress circle and the mobilized friction angle corresponding to point A in Figure 2.4(a) are represented by Mohr stress circle 1 in Figure 2.6 and the mobilized friction angle,  $\phi'_{mob}$  can be determined according to Equations 2.11 – 2.14.

$$\sin \phi'_{mob} = \frac{(\sigma'_{1_A} - \sigma'_{3_A})}{(\sigma'_{1_A} + \sigma'_{3_A})} \quad \text{Equation 2.11}$$

$$\sin \phi'_{mob} = \frac{(\sigma_{3,A} + q_A - u - \sigma_{3,A} + u)}{(\sigma_{3,A} + q_A - u + \sigma_{3,A} - u)} \quad \text{Equation 2.12}$$

$$\sin \phi'_{mob} = \frac{q_A}{(2\sigma_{3,A} + q_A - 2u)} \quad \text{Equation 2.13}$$

$$\phi'_{mob} = \sin^{-1} \left( \frac{q_A}{(2\sigma_{3,A} + q_A - 2u)} \right) \quad \text{Equation 2.14}$$

Note that the specimen would only undergo plastic yielding whenever the applied stress state is higher than the mobilized shear strength represented by the Mohr stress circle 1 (Figure 2.6) that represents the stress state in the specimen corresponding to yield point A (Figure 2.4(a)). When the reloading path travels along BA in Figure 2.4(a) the behaviour is elastic until the stress exceeds the yield stress at A. The Mohr circle 2 in Figure 2.6 represents the higher mobilized shear strength under a higher effective stress that would produce the same irrecoverable volume change on the specimen as the Mohr circle 1, therefore they touch the same yield envelope or the mobilized shear strength envelope.

### 2.3.3 Effect of Particle Breakage on Stress-Strain and Volume Change Behaviour.

The stress, strain and volume change graphs for triaxial tests would differ for tests with and without particle breakage. The notable effect of particle breakage on the properties of granular materials has been summarized by Billam (1972) as follows:

1. Principal effective stress ratio at failure decreases with increasing confining pressure due to the suppression of dilatancy that give rise to particle breakage and the stress ratio tends towards a lower limiting constant value.
2. Large volume reductions occur, especially during shear.
3. The axial strain required to reach failure increases.

Bishop (1972) presented typical stress, strain and volume change behaviour as discussed in Section 2.3.1 for the drained plane strain tests on dense and loose saturated Brasted sand as shown in Figure 2.7. The results show the achievement of the peak deviator stress corresponding to the maximum rate of dilation. This type of volume change behaviour can act as a reference for cases with pure specimen dilation during shear without the occurrence of particle breakage. Particle breakage suppresses the specimen from dilating. Bishop (1966) reported the results of drained triaxial

compression tests at different confining pressures on loose and dense saturated Ham River sand as shown in Figure 2.8(a) and (b) respectively. This was to study the effect of grain crushing on stress, strain and volume change behaviour of coarse grained soils. Bishop (1966) also plotted the soil's grading curves before and after tests (Figure 2.9) and showed that shearing at effective cell pressure higher than 1000 lb/sq. inch. ( $6896\text{kN/m}^2$ ) is causing particle breakage. In fact the shearing at effective cell pressure of higher than 100 lb/sq. inch. shows failure at higher axial strain, which is a sign of particle breakage according to Billam (1972). The occurrence of particle breakage is marked by the steep volume reduction shown by the curves of volumetric strain versus axial strain no. 21 and 25 in Figure 2.8(b).

Bishop (1972) again presented the results of drained triaxial compression tests at different confining pressures on saturated Ham River sand as shown in Figure 2.10. The figure indicates that the principal effective stress ratio at failure decreased with increasing confining pressure. This evidence is suggesting that the curvature of the shear strength envelope discussed in Section 2.3.5 is the result of particle breakage. Furthermore, the stress-strain behaviours shown in both Figures 2.8 and 2.10 are indicating that the axial strain at failure increases at high (more than 990 lb/sq. inch. or  $6827\text{kN/m}^2$ ) confining pressures. However, Billam (1972) has presented results of drained triaxial test on crushed anthracite (Figure 2.11) that show that axial strain at failure does not go on increasing indefinitely. At very high pressures the crushing which took place during consolidation creates a dense mass which is able to resist shearing without further major crushing of the test material.

A series of large scale triaxial tests on specimens of 300 mm diameter and 600 mm high were conducted by Indraratna *et al.* (1993) on greywacke rockfill material used for dam construction in Southern Thailand. Two material gradations, A and B, with maximum particle sizes of 38.1 mm and 25.4 mm respectively were tested at confining net cell pressures of 100, 200, 300, 400, 500 and 600 kPa, and the stress-strain and volume change behaviour are presented in Figures 2.12(a) and (b) respectively. The axial strain at failure increases with the net confining pressure for both soil gradations. This is suggesting the occurrence of particle breakage similar to the reports by Bishop (1966, 1972) and Billam (1972). Also the volumetric strain steeply decreases as the deviator stress was initially applied for net confining

pressures of 300 kPa and higher and levels off at higher axial strains. This is typical specimen volume change behaviour indicating the occurrence of particle breakage.

Salman (1995) has conducted constant suction drained triaxial tests on limestone gravel of maximum particle size of 6.3mm. The material is similar to the test material used in this research except that the latter has a uniform grading while the former has a wider grading. The typical results of the stress, strain and volume change behaviour of the material are shown in Figures 2.13(a) and (b). The tests were conducted under low confining net cell pressures of minimum 31.7 kPa and maximum of 114.2 kPa. The results generally show that the tests exhibit peak deviator stress and typical dilation behaviour during shearing due to the effect of interlocking similar to the results for saturated drained triaxial tests on dense granular or over-consolidated clay soils. The specimen volume first decreased which corresponds to the elastic behaviour of the stress path and then increased before the failure strain was reached, and continued to increase after failure. The latter corresponds to the plastic behaviour after yielding. The tests show typical volume change behaviour during shear for no significant breakage condition similar to the results of the plane strain tests presented by Bishop (1972) as shown in Figure 2.7.

Indraratna and Salim (2001) have conducted a series of large scale consolidated drained triaxial tests on fresh ballast under relatively low stress levels ( $\leq 300$  kPa). The dimensions of the specimens were 300 mm in diameter and 600 mm in height and the maximum ballast particle size was 63.0 mm. Figure 2.14 indicates that at low net confining pressure ( $\leq 100$  kPa) a peak deviator stress is evident and the specimen exhibited dilation during shearing while at higher net confining pressure the overall volumetric strain tended towards contraction. The latter is attributed to the suppression of dilatancy where the specimen continues to contract at a decreasing rate as the shear strain increases. Since they have also confirmed that the breakage of ballast increased with increasing confining pressure then the contraction of the specimens at this level of confinement must be attributed to particle breakage. Therefore the tests result indicate that particle breakage is evident even at low stress levels ( $\leq 300$  kPa).

Futai and Almeida (2005) have conducted constant suction and air-dried triaxial tests on gneiss rock residual soil at horizons B and C. Horizon B was found at the first 2m thick from the surface while the depth of horizon C may reach up to 40m. Both soils have the same proportion of quartz sand of about 50% and the rest is clay and silt. The amount of clay was greater in horizon B than C. Figures 2.15 and 2.16 show the stress, strain and volume change behaviour of the soil at low and high confining pressures. Under low confining pressures the specimens show a well defined dilation associated with the approaching of the peak deviator stress, similar to the typical specimen volume change during drained plane strain tests on saturated Brasted sand presented by Bishop (1972) as shown in Figure 2.7. Irrespective of the confining pressure, when the graphs of deviator stress versus axial strain show peak stress the graphs of volumetric strain versus axial strain indicate specimen dilation. However, when the deviator stress is continuously increasing with respect to axial strain the graphs of volumetric strain decrease steeply and tend to level off at higher strains. This type of volume change behaviour is supporting the proposition that grain crushing is suppressing dilation.

By and large particle crushing is producing a greater axial strain at failure and a continuous volume reduction during shear. The graphs of deviator stress versus axial strain that show the existence of a well define peak stress would exhibit a point of dilation in the graph of volumetric strain versus axial strain. But again if the axial strain at failure is higher than those at low stress levels then the occurrence of particle breakage is evident. Graphs that show a continuously increasing deviator stress give a continuous decrease in the volumetric strain. In certain cases the deviator stress increases and levels off at higher strain while the volumetric strain decreases steeply and becomes constant at higher strain. These are typical behaviours for shearing at high confining pressures which suggest a strong association with particle breakage. The asymptotic behaviour of the deviator stress and the volumetric strain in relation to particle breakage is similar to the onset of the critical state condition and the only difference is that the deviator stress usually drops off gradually after the peak strength due to strain softening before arriving at the critical state condition. Moreover, some evidence is still required in order to confirm that the behaviour is purely due to particle breakage and not the onset of a critical state condition.

The absence of a well-defined peak deviator stress is typical behaviour for normally consolidated clay soils. The clay has a fabric structure consisting of agglomerates of micro platelets as shown in Figure 2.17. The agglomerates are weakly bonded by charge distribution with open voids in between indicated by the dark areas. The kink in the stress-strain curve shown in Figure 2.5(c) could be due to the collapsing of the micro structure or the break up of the agglomerates of micro platelets, which resembles particle breakage in coarse-grained soils. Therefore a similar shape of the stress-strain curve for coarse-grained soils could indicate particle breakage during shearing. Similarly in over-consolidated clays the break up of these agglomerates has already occurred during the pre-consolidation process and therefore its stress-strain behaviour for the existing state would be a well defined peak as shown in Figure 2.5(b). Therefore, if the stress-strain curve for coarse-grained soils has a kink like the graphs in Figure 2.5(c) then this is strongly indicating the occurrence of particle breakage during the shearing.

Furthermore Ueng and Chen (2000) have studied the effect of particle breakage on the shear strength of sand based on the energy consumption due to particle breakage. A stress-dilatancy relationship based on principal stress ratio for sand under triaxial loading conditions was developed. They concluded that the energy consumption due to particle breakage during shearing resulted in a higher shear strength.

#### **2.3.4 Collapse Volume Change Behaviour.**

The major cause of collapse compression in unsaturated soils is the reduction in suction upon inundation, whether it is a fine or coarse-grained soil (Matyas and Radhakrishna 1968; Escario and Saez 1973; Cox, 1978; Lloret and Alonso, 1980; Maswoswe, 1985, Blanchfield and Anderson 2000). The unique massive volume change near saturation is a phenomenon in both fine and coarse grained soils. The former is as reported by Alonso *et al.* (1990) for clay soils and the latter is reported by Goodwin (1991), Tadepalli *et al.* (1992) and Blanchfield and Anderson (2000).

Goodwin (1991) carried out 1-D inundated compression tests in the same Rowe cell used in this research on coarse-grained soil of well distributed particle size between 37.5mm and 63 $\mu$ m. The specimen was 254mm in diameter and had a thickness of

about 110mm. Suctions were measured at the bottom and top of the specimens. On achieving equalization the specimens were subjected to monotonic incremental vertical net stress up to a maximum of 120 kPa. Between each loading stage, the incremental stress was maintained until equilibrium in terms of suction and axial strain were established before proceeding to the next incremental stress. At the end of the final loading stage the specimen was inundated. Figure 2.18 shows typical graphs of total axial strain and the vertical net stress and the massive compression collapse upon inundation was apparent indicated by the last two points on the graphs.

Tadepalli *et al.* (1992) conducted collapse tests using Indian Head silty sand in an oedometer with three small-tip tensiometers installed along the side of the oedometer to measure suction during the test. Vertical pressure was applied under constant water content conditions. On achieving equilibrium the specimen was inundated. The result was as shown in Figure 2.19 where soil volume decreased progressively with the reduction in suction and ceased when the suction dropped to zero throughout the entire specimen.

Blanchfield and Anderson (2000) conducted one-dimensional consolidation tests using specimens of diameter 254mm with initial suction of 200 kPa in the study of collapse behaviour of opencast coalmine backfill when inundated. The specimens were inundated at vertical pressures of 10, 160 and 700 kPa in different series of tests. The next stage of the test was to apply increments of vertical pressures of 10, 20, 40, 80, 160, 200, 400 and 700 kPa every 24 hours to simulate the build-up of the overburden pressure on the backfill and the volume changes were recorded after each increment. The results are presented in Figure 2.20. The significant feature of the results is the linear behaviour of volume change with respect to the applied vertical pressures. This agrees with the findings of Cox (1978), Feda (1988), Brandon *et al.* (1990), Basma and Tuncer (1992) and Vilar (1995).

Rahardjo and Fredlund (2003) conducted a  $K_0$ -compression test on unsaturated silty sand with respect to various loading paths. The composition of sand, silt and clay for the soil was 52.5%, 37.5% and 10.0% respectively. The loading paths and the resultant volume change are shown in Figure 2.21(a) and (b) respectively. The loading paths are labelled as M for suction increase achieved by opening the pore water

pressure line and leaving the pore air pressure line closed, CW for constant water content achieved by opening air pressure line and closing the pore-water line and C for consolidation by opening both pore water and pore air lines. Therefore in the loading paths M and C suction increased due to the loss in pore-water pressure and in the path CW suction decreased due to the loss in pore-air pressure. For each load increment the stress paths taken were CW, C and finally M before the next load increment was applied. The results showed that volume decrease was encountered in each of the three different stress paths (M, CW and C) under each load increment. In this way the volume decrease under increasing suction (stress paths M and C) is ambiguous since the volume decrease could be due to the load increment as an equilibrium condition has not being achieved, or due to increased suction. In general the results indicate that the rate of volume decrease reduced as net normal stress and suction increased as represented by a line joining points F, M, P, S and T<sub>7</sub> in Figure 2.21(b). This sort of behaviour is expected as the settlement results in denser particle packing. It thereby increases the stiffness and thus becomes more resistant to volume change, and at the same time the shear strength also increases as indicated by the overall increase in suction as the test progresses. Nonetheless the results also indicate that at the end of each load increment a limiting equilibrium condition is achieved since the settlement momentarily stopped and started as soon as the subsequent load increment was applied.

Based on the above review the conclusions that can be drawn are summarized as follow:

1. Compressive volume change progress with reduction in suction.
2. Volume change stops when suction is zero.
3. Volume change varies linearly with vertical net stress.
4. As suction decreases with inundation it implies that collapse compression due to inundation is taking place under effective stress decrease.

The collapse compression behaviour must be taking place before the soil reaches the failure point or the maximum shear strength since beyond that the particles are fully interlocked and any further one-dimensional vertical settlement can only possibly be attributed to particle breakage. Therefore this is in accordance with the proposition by Atkinson (1975) that the interpretation of soil deformation in saturated or unsaturated

soils essentially requires the state of stress and strain behaviour prior to the failure point.

### 2.3.5 Non-linear Shear Strength Behaviour With Respect to Effective Stress.

The variation of shear strength with respect to effective stress for coarse-grained soils is not exactly linear as suggested by Terzaghi (1936) based on the linear variation with respect to total stress as formerly suggested by Coulomb (1776). Skermer and Hillis (1970), Marachi *et al.* (1972), Charles and Watts (1980), Al-Hussaini (1983) and Indraratna *et al.* (1993) have studied the effect of confining pressure on the soil shear strength of granular soils under high confining pressures. They showed that the angle of shearing resistance,  $\phi'$ , decreased at decreasing rate with increasing confining pressure and tended to flatten at very high values of confining pressure ( $> 4\text{Mpa}$ ). Apart from that, Skermer and Hillis (1970) and Al-Hussaini (1983) have shown that there was particle breakage at high confining pressures. For low values of confining pressures, Ponce and Bell (1971) and Fukushima and Tatsuoka (1984) conducted triaxial tests on saturated fine granular soils (sand) and showed that  $\phi'$  increased as the confining pressure decreased. Bishop (1966) has also reported a similar shear strength variation with respect to effective stress for cohesive soils. Salman (1995) has specifically conducted triaxial tests at low stress levels on saturated specimens of limestone coarse-grained soil from the same quarry and of similar properties as the test material of this research. The reported data is shown in Table 2.2 and the curvilinear type of Mohr-Coulomb envelope is apparent at low stress levels as interpreted in Figure 2.22.

Therefore it can be concluded that, shear strength steeply diminishes non-linearly towards zero, as the effective stress approaches zero for coarse-grained soils. The behaviour is thereby a combination of linear and non-linear behaviour as presented by Bishop (1966), Charles and Watts (1980) and Indraratna *et al.* (1993) as shown in Figure 2.23 and 2.24. Indraratna *et al.* (1993) have conducted large scale drained triaxial tests on greywacke rockfill and have quoted that at low confining stresses ( $<500\text{ kPa}$ ) the non-linearity of the failure envelope is pronounced and at high confining stress levels ( $>1.5\text{MPa}$ ) the assumption of the linear Mohr-coulomb criterion is acceptable. The consideration of this non-linearity in the shear strength

behaviour at low stress levels could shed some light on the behaviour of inundation volume change since it is a near surface phenomenon and involves similar stress levels. Nevertheless the present practice is to assume linear behaviour by drawing the best-fit straight line crossing the origin for cohesionless soils. Currently, no curvilinear type of shear strength equation with respect to effective stress has been proposed.

### **2.3.6 Non-linear Shear Strength Behaviour With Respect to Suction.**

Escario and Saez (1986) suggested that the behaviour of shear strength relative to suction was non-linear and later this type of behaviour was confirmed by several authors like Fredlund *et al.* (1987), Escario and Juca (1989), Gan *et al.* (1988), Gan and Fredlund (1988, 1996), Mahalinga-Iyer and Williams (1995), Rassam and Williams (1999), Nishimura and Fredlund (2000) and Toll *et al.* (2000). Some examples of the non-linear behaviour of shear strength with respect to suction are shown in Figures 2.25 and Figure 2.26. The angle  $\phi^b$  is no longer a constant but decreases non-linearly from the maximum value at saturation and becomes zero at residual suction. This suggests that the apparent shear strength attains the maximum value at residual suction. This is in accordance with the relationship between the apparent shear strength and degree of saturation suggested by Vanapalli *et al.* (1996) as shown in Figure 2.27 where maximum shear strength is attained at residual saturation, which corresponds to residual suction.

It was also reported that shear strength decreases slightly beyond residual suction under lower confining pressures (Escario and Juca, 1989, Mahalinga-Iyer and Williams, 1995, Gan and Fredlund, 1996 and Vanapalli *et al.*, 1998). At higher confining pressures, shear strength was reported to remain constant at suctions exceeding residual suction (Escario and Juca, 1989, Gan and Fredlund, 1996, Rassam and Williams, 1999, Nishimura and Fredlund, 2000 and Toll *et al.*, 2000). Nevertheless, there are also reports that under high confining pressure there is a slight drop in shear strength at high suction (Escario and Juca, 1989, Gan and Fredlund, 1996). These reports would imply that shear strength does decrease beyond residual suction and those reports that claim it remains constant are probably due to the

maximum suction applied being close to residual suction. At this locality the reduction in shear strength is not apparent and the curve is almost flat.

Thus, by and large, shear strength increases non-linearly up to residual suction and reduces at higher values of suction (Vanapalli *et al.* 1998). Perhaps the decrease of shear strength at this stage is getting more gradual as confining pressure increases. Ultimately the effect of suction on shear strength will cease at one point when the soil becomes totally dry. Perhaps the reduction in the apparent shear strength from the maximum value to zero is a gradual process. This is true even though the suction gets very high since the water contact area with the soil particles relative to the overall particle size would become infinitely small. This could be the reason why the same magnitude of suction is not giving the same apparent shear strength between soils with different grain sizes.

Furthermore, Nishimura and Fredlund (2000) and Gan and Fredlund (1996) reported that the angle  $\phi^b$  increases sharply towards  $\phi'$  at saturation. However in most reported cases the angle  $\phi^b$  is less than  $\phi'$  at zero suction as listed in Table 2.1. Therefore if there was to be a case that  $\phi^b$  equals  $\phi'$  at zero suction, it can be considered as a special case whereby in general the angle  $\phi^b$  is considered to be less than  $\phi'$  at zero suction.

#### **2.4 Existing Shear Strength Equations for Unsaturated Soils.**

The shear strength of saturated soil may be described using the Mohr-Coulomb failure criterion based on the effective stress concept. The shear strength equation defines the failure line obtained by plotting a series of Mohr circles corresponding to failure conditions plotted in  $\tau : (\sigma - u_w)$  space. In the case of unsaturated soil the Mohr circles are plotted in three-dimensional space,  $\tau : (\sigma - u_a) : (u_a - u_w)$ , with shear stress,  $\tau$  as the ordinate and the net stress,  $(\sigma - u_a)$  and suction,  $(u_a - u_w)$  as the abscissas. In this case the failure envelope is in the form of a surface, which is referred to as the extended Mohr-Coulomb failure envelope. The extended Mohr-Coulomb failure envelope was first thought to be a planar surface (Fredlund *et al.*, 1978) as shown in Figure 2.28 and later resolved to be a curvilinear surface (Escario and Saez, 1986, Fredlund *et al.*, 1987, Escario and Juca, 1989, Gan *et al.*, 1988, Gan and Fredlund,

1988 and 1996, Mahalinga-Iyer and Williams, 1995, Rassam and Williams, 1999, Nishimura and Fredlund, 2000 and Toll *et al.*, 2000). However, up to date there is still no complete shear strength model of this type in either the physical or analytical form.

#### 2.4.1 Early Attempts to a Define a Shear Strength Equation for Unsaturated Soils.

The shear strength equation for saturated soil based on the Mohr-Coulomb failure criterion and effective stress concept was introduced by Terzaghi (1936). This is the linear type Mohr-Coulomb failure line or failure envelope as defined by Equation 2.2.

Bishop (1959) introduced an effective stress equation for unsaturated soil conditions as in Equation 2.1. Following this, Bishop *et al.* (1960) substituted Equation 2.1 into Equation 2.2 to produce Equation 2.3 in an attempt to resolve the collapse volume change behavior of unsaturated soils. However no unique relationship between  $\chi$  and degree of saturation,  $S$  was found by doing back calculation for the value of  $\chi$  from drained and undrained triaxial tests. Jennings and Burland (1962) performed oedometer tests on silt and clay soils and no unique relationship between void ratio and effective stress was found and thus thereby questioned the validity of Bishop (1959) effective stress equation. This in turn affects the validity of Bishop *et al.* (1960) unsaturated shear strength equation (Equation 2.3).

#### 2.4.2 Equation for Linear Behaviour of Shear Strength with respect to Suction.

Fredlund *et al.* (1978) introduced an extended shear strength equation (Equation 2.15) for unsaturated soil based on the Mohr-Coulomb failure envelope using two independent stress state variables; net stress,  $(\sigma - u_a)$  and suction,  $(u_a - u_w)$ .

$$\tau = c' + (\sigma - u_a) \tan \phi' + (u_a - u_w) \tan \phi^b \quad \text{Equation 2.15}$$

where  $\phi^b$  is the angle indicating the rate of increase of shear strength with respect to suction.

The envelope is in the form of inclined plane as shown in Figure 2.28 where the variation of shear strength with respect to suction is linear with a constant slope angle value of  $\phi^b$ . Later in the thesis, this shear strength surface envelope plotted in the

space of  $\tau : (\sigma - u_a) : (u_a - u_w)$  will be referred to as the extended Mohr-Coulomb envelope.

### 2.4.3 Equations for Non-linear Behaviour of Shear Strength with respect to Suction.

Several shear strength equations have been proposed to match the reported non-linear shear strength behaviour with respect to suction. Equation 2.16 has been introduced by Fredlund *et al.* (1995) but does not produce a good approximation to experimental data as shown by the predicted curve in Figure 2.25(a);

$$\tau = c' + (\sigma - u_a) \tan \phi' + (u_a - u_w) \left[ \Theta (u_a - u_w) \right]^K \tan \phi' \quad \text{Equation 2.16}$$

where  $\Theta$  is the normalised volumetric moisture content given by,  $\Theta = \frac{\theta - \theta_r}{\theta_s - \theta_r}$ ,

$K$  is a soil parameter dependent on soil type

$\theta$  is volumetric water content

$\theta_s$  is volumetric water content at saturation

$\theta_r$  is volumetric water content at residual condition.

Based on the concept that the apparent shear strength of unsaturated soil is strongly related to the amount of water in the voids and thereby should bear a relationship to the soil-water characteristic curve, Vanapalli *et al.* (1996) redefined the normalised volumetric moisture content,  $\Theta$ , as in Equation 2.17 and proposed a shear strength equation based on this as in Equation 2.18 where  $\kappa$  is the fitting parameter. The performance of Equation 2.18 is still poor as shown by the best-fit curve in Figure 2.25(b).

$$\Theta = \frac{\theta}{\theta_s} \quad \text{Equation 2.17}$$

$$\tau = \left[ c' + (\sigma - u_a) \tan \phi' \right] + (u_a - u_w) \left[ \Theta^\kappa \tan \phi' \right] \quad \text{Equation 2.18}$$

By extending the same concepts, Vanapalli *et al.* (1996) simultaneously proposed another equation of shear strength (Equation 2.19) without using the fitting parameter,  $\kappa$ . Furthermore, an equivalent equation in terms of degree of saturation,  $S$  and degree of saturation at residual condition,  $S_r$  was also suggested as in Equation 2.20. Fitting

curves using Equation 2.19 for a variation of residual suction value are presented in Figure 2.25(c) and the best-fit curve representing residual suction of 3000kPa still could not match closely with the experimental results.

$$\tau = [c' + (\sigma - u_a) \tan \phi'] + (u_a - u_w) \left[ (\tan \phi') \left( \frac{\theta - \theta_r}{\theta_s - \theta_r} \right) \right] \quad \text{Equation 2.19}$$

$$\tau = [c' + (\sigma - u_a) \tan \phi'] + (u_a - u_w) \left[ (\tan \phi') \left( \frac{S - S_r}{100 - S_r} \right) \right] \quad \text{Equation 2.20}$$

The main limitation of Equations 2.19 and 2.20 is that the apparent shear strength represented by the last term becomes zero at residual conditions when the volumetric moisture content equals to the residual volumetric moisture content, whereas it should give the maximum value at this point.

## 2.5 Existing Volume Change Models for Unsaturated Soils.

Volume change in unsaturated soils involves expansion and contraction. On wetting expansive soil exhibits volume increase under low confining pressure whilst collapsible soil always exhibits volume decrease. Wetting reduces suction and causes subsequent decreases in effective stress. The normal type of collapse is due to load increase, which subsequently increases the effective stress and at a certain point triggers collapse. The occurrence of collapse due to both effective stress increase and decrease has made it difficult to formulate them under a single framework. This is the reason why volume change is the most difficult unsaturated soil behaviour to characterize (Fredlund, 2000). To make the situation even more complex, alternate wetting and drying has been reported to cause collapse (Alonso, 1995 and Sharma, 1998). Earlier studies of volume change behaviour in unsaturated soils are solely based on the influence of net stress and suction and the influence of shear strength was not incorporated until the critical state approach began (Alonso *et al.* 1987). Collapse produces closer packing of soil particles. The particles' movement is triggered when the friction between the particles is reduced as suction decreases upon wetting and the overburden pressure then mobilises the movement. Basically any soils compacted dry of optimum have low densities and often exhibit collapse behaviour upon wetting (Barden *et al.*, 1969).

### 2.5.1 Volume Change Model Based on Two Independent Stress State Variables.

The first attempt to explain the volume change behaviour of unsaturated soil based on two independent stress state variables was by Bishop (1959) with the widely quoted effective stress equation for unsaturated soil as in Equation 2.1. However a unique relationship between the weighting parameter,  $\chi$ , and volume change was not achieved. Then Jennings and Burland (1962) conducted oedometer one-dimensional compression tests on silt and clay soils and assessed the volume change behaviour using the Bishop (1959) effective stress equation, but no unique relationship between the effective stress and volume change was found. They thereby questioned the validity of Bishop (1959) effective stress equation. Normally volume reduction occurs under increasing effective stress such as settlement in the event of ground water table lowering but then collapse is encountered under effective stress decreasing in the case of the soil being inundated. The proposed effective stress equation thus failed to explain theoretically the mode of wetting collapse and also the massive volume change behaviour near saturation.

Bishop and Blight (1963) described the volume change behaviour of unsaturated soil under isotropic loading and expressed its path in void ratio,  $e$ , net stress,  $(\sigma - u_a)$  and suction,  $(u_a - u_w)$  space as shown in Figure 2.1. The figure indicates that wetting the soil at a low value of  $(\sigma - u_a)$  caused swelling of the soil along the path AD, while wetting the soil at a high value  $(\sigma - u_a)$  caused collapse of the soil along the paths BE and CF. For an unsaturated soil loaded at constant water content starting at point A the volume decreased and so did the suction as represented by path ABC. The path is moving towards full saturation as void ratio decreases when the line ABC is approaching the plane  $e$  versus  $(\sigma - u_a)$ .

Matyas and Radhakrishna (1968) carried out triaxial compression tests on a mixture of 80% flint and 20% kaolin. The tests were carried out in isotropic compression. Wetting tests were carried out by allowing the specimen to imbibe water, either under constant volume or under constant applied stress. The results were plotted in three-dimensional space of void ratio against net stress and suction as shown in Figure 2.2.

The results showed a steep drop in volume near saturation indicating collapse. Furthermore they noted that the collapse behaviour caused by suction reduction at high values of  $(\sigma - u_a)$  could not be explained by the principle of effective stress as suggested by Bishop (1959), as volume is decreasing (normally it swells) as effective stress decreases.

Barden *et al.* (1969) conducted a series of anisotropic consolidation tests in a modified Rowe cell using 150mm diameter by 25mm thick samples of compacted Westwater and Derwent clays. The specimens were initially consolidated at given values of suction and net stress and then taken through three different stress paths involving wetting at constant net stress, consolidation at constant suction and both consolidation and wetting at the same time. The results indicated that for specimens compacted dry of optimum, collapse occurred on wetting to zero suction under large  $p'$ . However, the higher the clay content, the smaller was the collapse. The smaller collapse is most probably caused by volume compensation due to the simultaneous swelling of the clay microstructure. However, specimens compacted close to optimum moisture content showed no collapse. This gives an indication that the degree of collapse depends on the availability of space for the soil particles to move. Therefore for coarse-grained soil the limit of collapse is when the particles have come to a fully interlocking position. It was also realised that the volume change behaviour of unsaturated soil is best analyzed in terms of the two independent stress tensors,  $(\sigma - u_a)$  and  $(u_a - u_w)$ .

Escario and Saez (1973) have noted that in one-dimensional compression under controlled suction, as negative pore water pressure decreases settlement increases and bigger settlement is achieved at a higher vertical pressure as illustrated in Figure 2.29. Compression settlement was thought to be strongly governed by the total net vertical stress,  $(\sigma - u_a)$  or the deviator stress,  $(\sigma_1 - \sigma_3)$  rather than the effective stress since effective stress was decreasing as negative pore water pressure was approaching zero while settlement increases. Furthermore, the settlement induced by the suction decrease process was not large until a relatively low suction value was attained which led to a bigger collapse. This is an important characteristic of collapse settlement, which ought not to be neglected in the development of a new shear strength-volume

change framework for unsaturated soil. In addition the collapse is plastic in behaviour since deformation is irrecoverable.

Fredlund and Morgenstern (1976) proposed a semi-empirical constitutive relation for unsaturated soil using the two independent stress state variables,  $(\sigma - u_a)$  and  $(u_a - u_w)$  as in Equation 2.21. However, physically the model is identical to the constitutive void ratio warped surface presented by Matyas and Radhakrishna (1968).

$$\frac{dV_v}{V_o} = m_1^s d(\sigma - u_a) + m_2^s d(u_a - u_w) \quad \text{Equation 2.21}$$

where :

$V_v$  = volume of voids

$V_o$  = initial total volume of soil.

$m_1^s$  = coefficient of soil volume change with respect to a change in net normal stress.

$m_2^s$  = coefficient of soil volume change with respect to a change in suction.

Equation 2.21 can be viewed as comprising of two parts; a part that is designated to the stress states (i.e.  $(\sigma - u_a)$  and  $(u_a - u_w)$ ) and a part that is designated to the soil properties (i.e.  $m_1^s$  and  $m_2^s$ ). The soil properties can be viewed as the slope of the void ratio constitutive surface as shown in Figure 2.30. The void ratio constitutive surface for a set of Madrid grey clay specimens subjected to monotonic loading and wetting paths is presented in Figure 2.31 (Sabbagh, 2000). The performance of Equation 2.21 is unique provided the loading is monotonic. However, stress paths that involve wetting and drying do not produce a unique constitutive surface, which appears to be associated with the problem of hysteresis. This suggests an irreversible type of behaviour, which required the use of the elastic-plastic form of constitutive framework.

Fredlund (1979) proposed that for a limited range of stresses the void ratio would vary linearly with the logarithm of both mean net stress and suction according to Equation 2.22.

$$e = e_o - C_l \log \frac{(p - u_a)_f}{(p - u_a)_o} - C_m \log \frac{(u_a - u_w)_f}{(u_a - u_w)_o} \quad \text{Equation 2.22}$$

$C_t$  and  $C_m$  are compressibility coefficients and subscripts 'o' and 'f' indicate initial and final states. This results in a planar constitutive void ratio surface as illustrated in Figure 2.32. The limitation of this framework is that it also cannot handle the alternate wetting and drying due to the problem of hysteresis.

With the concept of plotting the stress states on log scales, Lloret and Alonso (1985) have proposed a constitutive relation linking volume change and the stress states according to Equation 2.23 for suction greater than 1 kPa:

$$e = a + b \ln(p - u_a) + c \ln(u_a - u_w) + d \ln(p - u_a) \ln(u_a - u_w) \quad \text{Equation 2.23}$$

where a, b, c and d are constants. Equation 2.23 represents a warped surface and a typical state surface for Pinolen clayey sand is presented in Figure 2.33 (Lloret and Alonso 1985).

## 2.5.2 Critical State Volume Change Frameworks.

Section 2.5.1 described volume change behaviour of unsaturated soil with respect to the combination of either net normal stress, or net mean stress, and suction. In all cases the volume change behaviour was based solely on the variation of the two independent stress state variables and they were not linked to the shear strength. However, volume change occurs due to rearrangement of the soil particles and these involve the mobilisation of the inter-particle friction, which is essentially related to the shear strength. Inevitably the study of volume change behaviour must be associated with the shear strength and the application of this concept began when the critical state approach was first applied to unsaturated soils by Alonso *et al.* (1987).

Alonso *et al.* (1987) presented a qualitative description of an elasto-plastic critical state framework for unsaturated soil and the mathematical development of the framework was later proposed by Alonso *et al.* (1990). The proposal involved isotropic ( $q = 0$ ) and anisotropic stress states ( $q > 0$ ), where  $q$  is the principal stress difference.

For an isotropic stress state, Alonso *et al.* (1990) introduced isotropic normal compression lines for saturated and unsaturated states as in Equation 2.24 which is an

expression for the specific volume,  $v$ , under isotropic stress,  $p'$ , to virgin state at a given suction and is illustrated in Figure 2.34(a);

$$v = N(s) - \lambda(s) \ln \left( \frac{p'}{p^c} \right) \quad \text{Equation 2.24}$$

$N(s)$  is the value  $v$  at a reference  $p^c$  (defined below) or the intercept of the normal compression line in  $v-\ln(p/p^c)$  plot, and  $\lambda(s)$  is the stiffness parameter for changes in net mean stress towards the soil virgin state. Both  $N(s)$  and  $\lambda(s)$  decrease from a value of  $N(0)$  and  $\lambda(0)$  that corresponds to zero suction as suction increases.

Alonso *et al.* (1990) also introduced the concept of a yield curve in  $p' - s$  plane, which is named as the Loading-Collapse (LC) yield curve as shown in Figure 2.34(b). Yield stress,  $p_o'(s)$ , for a given suction,  $s$ , is taken as the kink in the normal compression line that represents the change in stiffness as illustrated in Figure 2.34(a). The shape of this yield curve is given by Equation 2.25,

$$\left( \frac{p_o'(s)}{p^c} \right) = \left( \frac{p_o'(0)}{p^c} \right)^{\left( \frac{\lambda(0)-\kappa}{\lambda(s)-\kappa} \right)} \quad \text{Equation 2.25}$$

where  $\kappa$  is the elastic swelling index for changes in mean net stress and  $p^c$  is the value of net mean stress at which the yield stress  $p_o'$  is independent of suction.

The suction-increased (SI) yield curve is introduced to represent the irreversible compression when suction is increased beyond the previous maximum as shown in Figure 2.34(b). This isotropic critical state framework is designed to model both swelling and collapse on wetting (suction decrease). Consider the stress path CDE in Figure 2.34(b). Decreasing the suction along CD results in elastic swelling, and further decrease in suction along DE results in irrecoverable (plastic) collapse and the collapse shifts the LC curve to a new LC yield curve on the right. The new yield stress at zero suction,  $p_o''(0)$  corresponds to the point E. This shows that under an isotropic stress condition collapse due to wetting involves multiple yield surfaces.

For an anisotropic stress state in a critical state condition, Alonso *et al.* (1990) came up with the expression in Equation 2.26 for the deviator stress,  $q$ , i.e. the critical state line (CSL).

$$q = Mp' + ks \quad \text{Equation 2.26}$$

where M is the critical state stress ratio for saturated soil and also represents the gradient of the CSL. M is assumed to be identical for different values of suction. The CSL at any given suction passes through the apex of the relevant elliptical yield curve as shown in Figure 2.35(b). The constant k, is the intersection of the CSL with the ordinate and s, is suction.

Equation 2.26 is equivalent to Equation 2.15 proposed by Fredlund *et al.* (1978) where no account is taken for the non-linearity behaviour of strength with respect to suction, as illustrated in Figure 2.28.

The expression for specific volume,  $v$ , at critical state is as in Equation 2.27 which is based on the results of isotropic compression tests under wetting and drying stress paths as shown in Figure 2.36 (Alonso *et al.* 1990).

$$v = N(s) - \{\lambda(s) - \kappa\} \ln \left\{ 2 + \frac{ks}{p'} \right\} - \lambda(s) \ln \left( \frac{p'}{p^c} \right) \quad \text{Equation 2.27}$$

Alonso *et al.* (1990), extended the LC yield curve into a three-dimensional space of  $q$ : $p'$ : $s$  to form an elliptical yield surface as shown in Figure 2.35(a). The elliptical shape of this LC yield surface at a constant suction is give by Equation 2.28,

$$q^2 - M^2(p' + p'_o)(p'_o - p') = 0 \quad \text{Equation 2.28}$$

Referring to Figure 2.35(a), consider a soil initially at stress state A inside the current position of the yield surface. Yield can be produced by an increase of  $p'$  (isotropic loading path ABC), an increase of  $q$  (shearing path ADE), a reduction in suction,  $s$  (wetting path AFG) and an increase in suction (drying path AHI), which move the stress state to points B, D, F and H located on the yield surface respectively. Changing  $p'$ ,  $q$  and  $s$  simultaneously in any fashion, as long as the path meets the yield surface, can also produce yield. The yielding is in the form of irrecoverable volume change, which will produce the expansion of the yield surface.

Extending the elasto-plastic framework proposed by Alonso *et al.* (1990), Josa *et al.* (1992) introduced the concept of maximum collapse from a wetting path whereby the

LC yield curve does not diverge indefinitely on increasing  $p'$ , but instead converges to a limit of maximum compression. This is because the scope for collapse is getting less as the soil become denser after every collapse.

Then, Gens and Alonso (1992) presented an extended version of the earlier framework of Alonso *et al.* (1990) to accommodate the irreversible swelling on first wetting behaviour of highly expansive clays at macro-structural level but at the micro-structural level they were still assumed to be reversible. The earlier framework assumed the swelling on wetting was purely elastic which is a reversible behaviour. Gens and Alonso (1992) introduced the Neutral Line (NL) to complement with the LC and SI yield curve. The NL is assumed to be inclined at  $45^\circ$  in  $(p', s)$  space as shown in Figure 2.37 and it represents the neutral loading paths where the value of  $(s + p')$  remains constant and no micro-structural deformation takes place along this line. Reduction in suction or pressure (stress paths OC and OD) will lead to micro-structural irreversible expansion, whereas an increase in suction or pressure (stress paths OE and OF) will results in a reversible micro-structural compression. Thereby the zone bounded by the NL, SI and LC lines is considered as the elastic zone.

Toll (1990) conducted standard displacement controlled triaxial tests on lateritic Kinyu gravel (9% clay). The specimens were compacted in a 100mm diameter and 200mm high mould using either static or drop hammer compaction. Pore-water pressures were measured at the base of the specimen using 500kPa air entry ceramics and at mid-height using a pore-water pressure probe. The specimens were sheared under constant water content using strain rates of 0.016% per minute and 0.8% per minute. Toll (1990) also noted that a critical state was difficult to achieve in granular soils due to specimen tilting at high strain; nevertheless a critical state framework for unsaturated soil with the critical states expressions for deviator stress,  $q$  and specific volume,  $v$  given by Equations 2.29, 2.30 and 2.31 was proposed;

$$q = M_a(p - u_a) + M_w(u_a - u_w) \quad \text{Equation 2.29}$$

$$v = \Gamma_{aw} - \lambda_a \ln(p - u_a) - \lambda_w \ln(u_a - u_w) \quad \text{Equation 2.30}$$

$$\Gamma_{aw} = 1 + \frac{\Gamma_s - 1}{S} \quad \text{Equation 2.31}$$

where  $M_a$  is the critical state stress ratio with respect to net stress,  $M_w$  is the critical state ratio with respect to suction,  $\Gamma_{cv}$  is the specific volume when  $p-u_a$  and  $u_a - u_w$  equals unity,  $\Gamma_s$  is the saturated critical state parameter, and  $\lambda_a$  and  $\lambda_w$  are the slopes of the critical state plane with respect to net stress and suction respectively.  $M_a$ ,  $M_w$ ,  $\lambda_a$  and  $\lambda_w$  were shown to vary with degree of saturation,  $S$ . The constitutive critical state surfaces for unsaturated Kinyu gravel are shown in Figure 2.38.

Referring to the  $q - (u_a - u_w)$  plane in Figure 2.38(a), there is no indication of a steep drop in  $q$  near saturation. This is very significant shear strength behaviour of unsaturated soil that needs to be considered in assessing the volume change behaviour. Therefore this critical state framework has again failed to account for the non-linear behaviour of shear strength at suctions less than the residual value. Because of this, since the collapse is highly influenced by the shear strength, then the main feature of collapse i.e. massive volume change near saturation will never be achieved as plotted in the plane  $v - (u_a - u_w)$  in Figure 2.38(b).

Wheeler and Sivakumar (1993) have suggested that the volumetric state of unsaturated soil needs to be defined by a second volume change parameter apart from specific volume,  $v$ , such as degree of saturation,  $S$  or water content,  $w$ , in order to fully define the volumetric state of unsaturated soil. This is because the occurrence of hysteresis in the water retention curve during wetting and drying means that two identical samples subjected to the same suction can be at significantly different values of  $S$ , if one is on a drying path and the other is on a wetting path. Therefore the degree of saturation,  $S$ , is also important in explaining the soil mechanical behaviour in addition to the net stress, suction and specific volume. This makes the problem more complex since it involves five-dimensional mathematical space with the five state variables (i.e.  $q$ ,  $p'$ ,  $s$ ,  $S$  and  $v$ ).

For an isotropic stress state Wheeler and Sivakumar (1993) suggested the requirement of three types of equation for the definition of the isotropic normal compression line, which are,

$$q = 0 \qquad \text{Equation 2.32}$$

$$v = f_1(p', s) \quad \text{Equation 2.33}$$

$$w = f_2(p', s) \quad \text{Equation 2.34}$$

For an anisotropic stress condition they suggested the use of another three types of equation for the definition of the critical state line,

$$q = f_3(p', s) \quad \text{Equation 2.35}$$

$$v = f_4(p', s) \quad \text{Equation 2.36}$$

$$w = f_5(p', s) \quad \text{Equation 2.37}$$

In addition, they suggested the requirement of two more equations to define the state boundary surface that links the normal compression line and the critical state line in the following form,

$$v = f_6(p', q, s) \quad \text{Equation 2.38}$$

$$w = f_7(p', q, s) \quad \text{Equation 2.39}$$

This would mean that Wheeler and Sivakumar (1993) have three more equations than those proposed by Alonso *et al.* (1990), i.e. Equations 2.34, 2.37 and 2.39.

The results of isotropic consolidation tests under constant suction are shown in Figure 2.39. Based on these data, Wheeler and Sivakumar (1995) suggested an expression for specific volume (i.e. equivalent to Equation 2.33) as follows;

$$v = N(s) - \lambda(s) \ln \left( \frac{p'}{p_{at}} \right) \quad \text{Equation 2.40}$$

where  $N(s)$  is the intercept of normal compression line in  $v-\ln(p'/p_{at})$  plot,  $\lambda(s)$  is the slope of normal compression line in  $v-\ln(p'/p_{at})$  plot and  $p_{at}$  is the atmospheric pressure (100kPa).

Equation 2.40 is slightly different from Equation 2.24 as proposed by Alonso *et al.* (1990) since  $p^c$  has been replaced by atmospheric pressure,  $p_{at}$ . This is because Wheeler and Sivakumar (1995) argued that the existence of  $p^c$  has never been validated experimentally. For the LC yield curve Wheeler and Sivakumar (1995) suggested the following expression,

$$(\lambda(s) - \kappa) \ln \left( \frac{p'_v}{p_{at}} \right) = (\lambda(0) - \kappa) \ln \left( \frac{p'_v(0)}{p_{at}} \right) + N(s) - N(0) + \kappa \ln \left[ \frac{s + p_{at}}{p_{at}} \right] \quad \text{Equation 2.41}$$

which is claimed to be easier to apply than Equation 2.25.

For an anisotropic stress condition, based on their data shown in Figure 2.40, Wheeler and Sivakumar (1995) suggested critical state equations for deviator stress and specific volume as in Equation 2.42 and 2.43 respectively;

$$q = M(s)p' + \mu(s) \quad \text{Equation 2.42}$$

$$v = \Gamma(s) - \psi(s) \ln\left(\frac{p'}{p_{at}}\right) \quad \text{Equation 2.43}$$

where  $M(s)$  is the gradient of the critical state line and seems to vary slightly with suction and the intercept  $\mu(s)$  shows a bigger gap between the critical state lines near saturation, as demonstrated in Figure 2.40(a). Equation 2.43 is different from Equation 2.27 as proposed by Alonso *et al.* (1990) since the latter assumes a linear increase in  $q$  with suction. This non-linear variation in  $\mu(s)$  according to Equation 2.42 is equivalent to the steep increase in  $\phi^b$  approaching saturation and this is in accordance to the non-linear variation of shear strength with respect to suction as reported by Escario and Saez (1986), Fredlund *et al.* (1987), Escario and Juca (1989), Gan *et al.* (1988), Gan and Fredlund (1988; 1996), Mahalinga-Iyer (1995), Rassam and Williams (1999), Nishimura and Fredlund (2000) and Toll *et al.* (2000).

For the anisotropic condition, Wheeler and Sivakumar (1995) proposed the elliptical shape of the LC yield surface at constant suction as follows,

$$q^2 = M_*^2 (p'_o - p') (p' + p'_o - 2p'_x) = 0 \quad \text{Equation 2.44}$$

where  $M_*$  is given by,

$$M_* = \left[ \frac{M(s)p'_x + \mu(s)}{p'_o - p'_x} \right] \quad \text{Equation 2.45}$$

Since  $M_*$  is a function of  $\mu(s)$  that has a steep drop in value near saturation as illustrated in Figure 2.40(a), then the LC yield surface given by Equation 2.44 has accounted for the non-linear behaviour of shear strength in the volume change equation as in Equation 2.43.

In this case the LC yield surface at constant suction is taken as passing through the yield isotropic stress ( $p'_o$ ) on the normal compression line and intersecting the critical state line (CSL) at isotropic stress  $p'_x$  (Figure 2.41).

Tang and Graham (2002) proposed a “closure” type of critical state yield envelope in q-p-s space for high-plasticity clayey soils and sand-clay mixtures. They incorporated a yield envelope of type OAs<sub>s</sub>B in q-s space that represents yielding stress q<sub>y</sub> varying with suction under zero isotropic stress, p, as shown in Figure 2.42 suggested by Delage and Graham (1995). Based on this shape of yield envelope, Tang and Graham (2002) suggested that the state boundary of the proposed framework for unsaturated soils in q-p-s space is as shown in Figure 2.43. M<sub>1</sub>, M<sub>2</sub> and M<sub>3</sub> are the critical state lines that correspond to suction c<sub>1</sub>, c<sub>2</sub> and c<sub>3</sub> and the elliptical yield envelopes y<sub>1</sub>, y<sub>2</sub> and y<sub>3</sub> respectively. The parameter η<sub>s</sub> represents the planes of constant stress ratio, η<sub>s</sub> = s/p. However a full constitutive framework is yet to be developed. This framework attempts to account for the interrelated influence of net mean stress and suction on the mechanical behaviour.

### 2.5.3 Elasto-Plastic Stress-Strain Frameworks.

Gallipolli *et al.* (2003) proposed an elasto-plastic stress-strain framework for unsaturated soil to account for the irreversible change of void ratio that occurs during drying, which failed to be modelled by the earlier frameworks. It is very difficult to explain the irreversible compression or collapse behaviour during wetting. To overcome this problem they introduced the concept of a second suction mechanism associated with slippage at the interface between soil particles. The possibility of slippage is believed to be partially reduced by the stabilising effect of the normal force exerted at the inter-particle contacts derived from the water meniscus. Subsequently an additional constitutive variable, ξ, is introduced as a measure of the second type of suction exerted by the inter-particle meniscus of water lenses given by,

$$\xi = f(s)(1 - S) \quad \text{Equation 2.46}$$

where the factor (1 - S) accounts for the number of water menisci per unit volume of solid fraction and f(s) is a function of suction, which varies between 1 and 1.5 for suction ranging between zero and infinity respectively. Also, the isotropic average skeleton stress, p'' or σ'<sub>hk</sub>, is introduced, which is equivalent to Bishop's (1959) effective stress equation as follows,

$$\sigma'_{hk} = \sigma_{hk} - \delta_{hk} [u_a - \chi(u_a - u_w)] \quad \text{Equation 2.47}$$

where is  $\sigma'_{hk}$  is Bishop's (1959) effective stress,  $\sigma_{hk}$  is the total stress and  $\delta_{hk}$  is the Kronecker's delta.

The equation for the isotropic stress state yield locus in the  $\xi - p''$  plane is proposed as,

$$\ln p''_o(\xi_1) = \frac{\lambda - \kappa}{\frac{e}{e_s}(\xi)\lambda - \kappa} \ln p''_o(0) + \frac{\left[ \frac{e}{e_s}(\xi) - 1 \right] (1 + N)}{\frac{e}{e_s}(\xi)\lambda - \kappa} \quad \text{Equation 2.48}$$

where  $p''_o(\xi_1)$  is the isotropic average skeleton stress on the unsaturated normal compression line corresponding to  $\xi$  equals  $\xi_1$ , N is the intercept of the saturated normal compression line at  $p''$  equals to 1kPa,  $\lambda$  is the slope of the saturated normal compression line,  $\kappa$  is the elastic swelling index,  $e$  is the void ratio under unsaturated conditions and  $e_s$  is the void ratio under saturated condition.

Therefore the irreversible compression due to suction increase is defined based on the magnitude of inter-particle bonding,  $\xi$  and the skeleton stress,  $p''$ . Figure 2.44(a) shows the variation of void ratio with respect to suction and the corresponding expansion of yield locus in the  $\xi - p''$  plane, as predicted by Equation 2.48, is shown in Figure 2.44(b). The first drying has expanded the yield locus to position A and the second drying pushed it further to position B.

The framework of Wheeler *et al.* (2003) takes into account hydraulic hysteresis in explaining the mechanical or volume change behaviour of unsaturated soils. It is claimed that, due to a different degree of saturation, the inter-particle contact forces transmitted through the soil skeleton would be different for the two samples. As a result two samples of the same specific volume,  $v$ , would show a different mechanical behaviour even though subjected to the same net stress and suction. The stress state variables employed in the framework are deviator stress, modified suction,  $s^*$  (suction multiplied by porosity), and Bishop's stress tensor which is referring to the inter-particle stress in the form of  $p^*$  defined as Equation 2.49;

$$p^* = p - S u_w - (1 - S) u_a \quad \text{Equation 2.49}$$

The proposed framework is shown in Figure 2.45 which presents the LC yield curve, suction decrease (SD) and suction increase (SI) as straight lines in  $s^*:p^*$  plane.

## 2.6 Limitations of Critical State Frameworks.

Collapse due to drying is triggered whenever suction exceeds the past maximum suction (Alonso *et al.*, 1990, Wheeler and Sivakumar, 1995 and Tang and Graham, 2002). But later, Wheeler *et al.* (2003) have noticed that this definition has failed to explain the collapse behaviour due to alternate wetting and drying based on the reports by Alonso *et al.* (1995) and Sharma (1998), as shown in Figure 2.46(a) and (b) respectively. This includes the “closed” type framework proposed by Tang and Graham (2002) since it applies the same definition of failure due to suction. In the first and second drying curves in Figure 2.46(a) and (b) the collapse is taking place even at suction lower than the past maximum suction indicated by point A in both figures. Furthermore, the critical state framework also claims that whenever the stress path is within the elastic zone (i.e. underneath the yield surface envelope) of the framework, the collapse will not be triggered. However, the corresponding alternate wetting and drying paths in Figure 2.46 are indicating otherwise. The path ABC in Figure 2.46(a) and (b) is correspondingly illustrated in  $p$ - $q$ - $s$  space in Figure 2.47, which shows the expansion of the yield envelope when the wetting path AB hits the inner loading collapse LC line along the way. Then the subsequent drying path BC is within the elastic zone and there should not be any collapse failure along this path. But the corresponding path showed in Figure 2.46(a) and (b) is indicating that plastic straining is taking place. This could be a problem of defining yield purely based on suction without considering the combined effect that it has with the major and minor principal stresses on the mobilized shear strength and the shear stress. Therefore the definition of failure purely based on suction increase through the SI yield line is not adequate. That is why some authors like Gallipoli *et al.* (2003) and Wheeler *et al.* (2003) have already switched from this type of yield definition, which is based solely on the limiting value of  $q$ ,  $p'$  and  $s$ , to defining yield based on inter-particle stress.

Nonetheless, the consideration of collapse compression based on the interaction between shear stress and mobilized shear strength would be an alternative approach in the search for a comprehensive framework. The shear stress and mobilized shear

strength must be derived from the combined effect of the principal stresses and suction. In order to link the volume change behaviour to the shear strength, a good representative shear strength model is required. The variation of the shear strength parameters in the model during soil compression will have a key role in governing the volume change behaviour. In addition, it is significant that the model concentrates on the shear strength behaviour at lower stress levels and at suction close to saturation since these are the real field conditions that trigger wetting collapse. The volume change framework must be able to account for the volume change behaviour due to alternate wetting and drying as reported by Alonso *et al.* (1995) and Sharma (1998). Most important of all, the proposed hypothetical volume change framework must also be able to model the unique massive volume reduction near saturation in wetting collapse.

Table 2.1 Comparison between experimental values of  $\phi'$  and  $\phi^b$ .

Soil Type	$c'$ (kPa)	$\phi'$ (degrees)	$\phi^b$ at zero suction (degrees)	Reference
Compacted shale	15.8	24.8	18.1	Bishop <i>et al.</i> , (1960)
Boulder clay	9.6	27.3	21.7	Bishop <i>et al.</i> , (1960)
Dhanauri clay	37.3	28.5	16.2	Satija (1978)
Dhanauri clay	20.3	29.0	12.6	Satija (1978)
Dhanauri clay	15.5	28.5	22.6	Satija (1978)
Dhanauri clay	11.3	29.0	16.5	Satija (1978)
Madrid grey clay	23.7	22.5	16.1	Escario (1980)
Undisturbed granitic residual soil	28.9	33.4	15.3	Ho and Fredlund (1982)
Undisturbed rhyolite residual soil	7.4	35.3	13.8	Ho and Fredlund (1982)
Tappen-Notch Hill silt	0	35.0	16.0	Krahn <i>et al.</i> , (1989)
Compacted glacial till	10	25.3	7 – 25.5	Gan <i>et al.</i> , (1988)
Bukit Timah residual soil, Singapore	10	32.0	28	Toll <i>et al.</i> , (2000)
Jurong residual soil, Singapore	10	51	< 51	Toll <i>et al.</i> , (2000)

Table 2.2 The data for the drained triaxial tests on saturated specimens of limestone coarse-grained soil obtained from the same quarry with similar properties to the test material (Salman, 1995).

Test no.	Effective cell pressure, $(\sigma_3 - u_w)$ (kPa)	Deviator stress at failure, $(\sigma_1 - \sigma_3)_f$ (kPa)
1	25.7	252.6
2	50.7	335.6
3	75.7	433.5
4	100.7	497.0
5	125.7	608.2

Note : All tests were conducted at pore water pressure of 540 kPa.

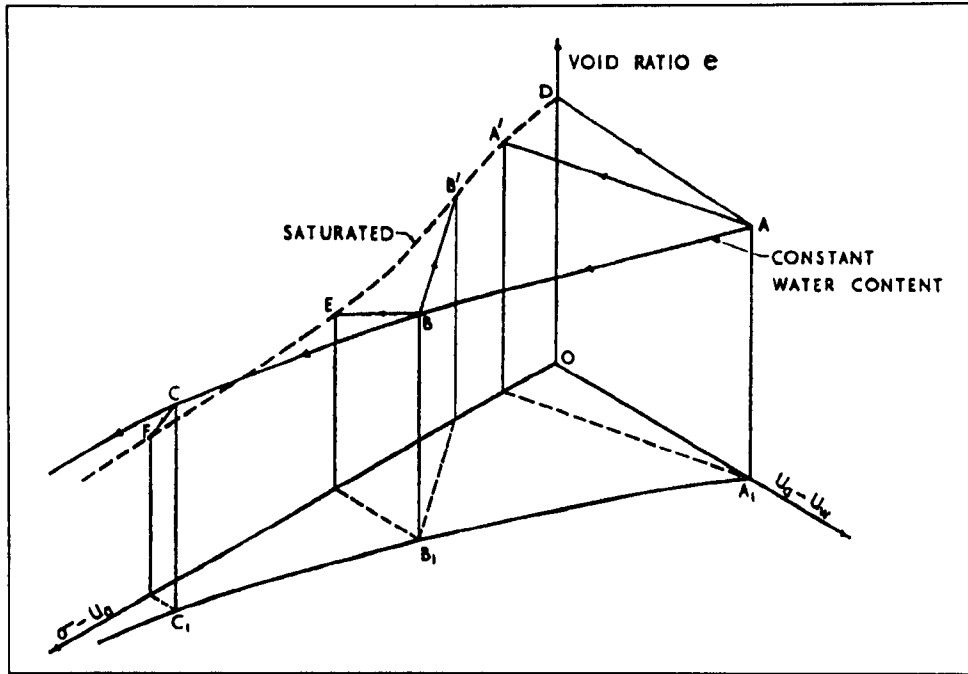


Figure 2.1 Volume change in terms of void ratio against net stress,  $\sigma'$ , and suction,  $(u_a - u_w)$  (Bishop and Blight, 1963).

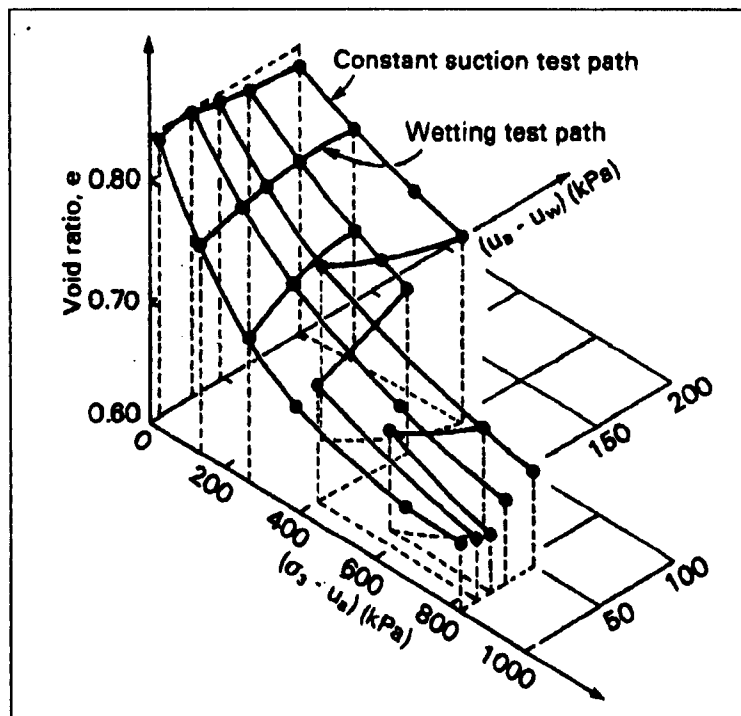
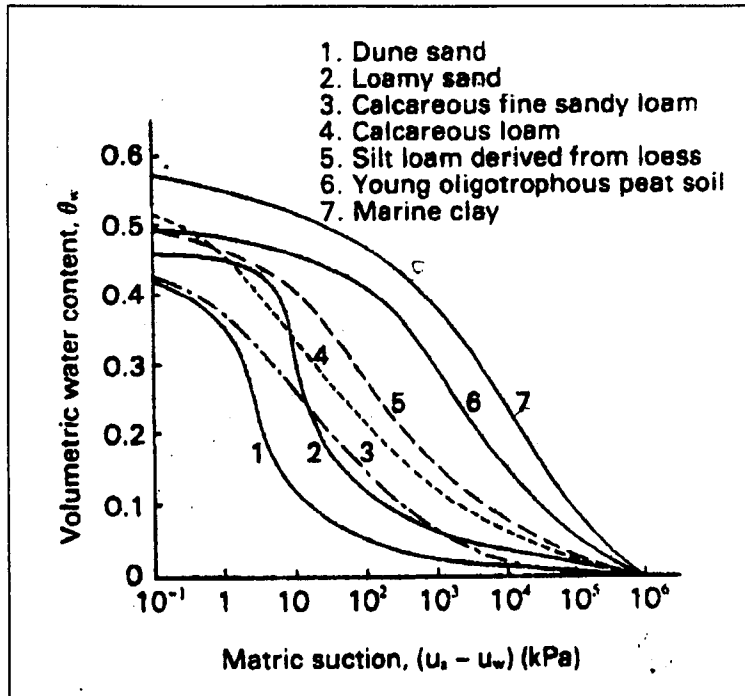
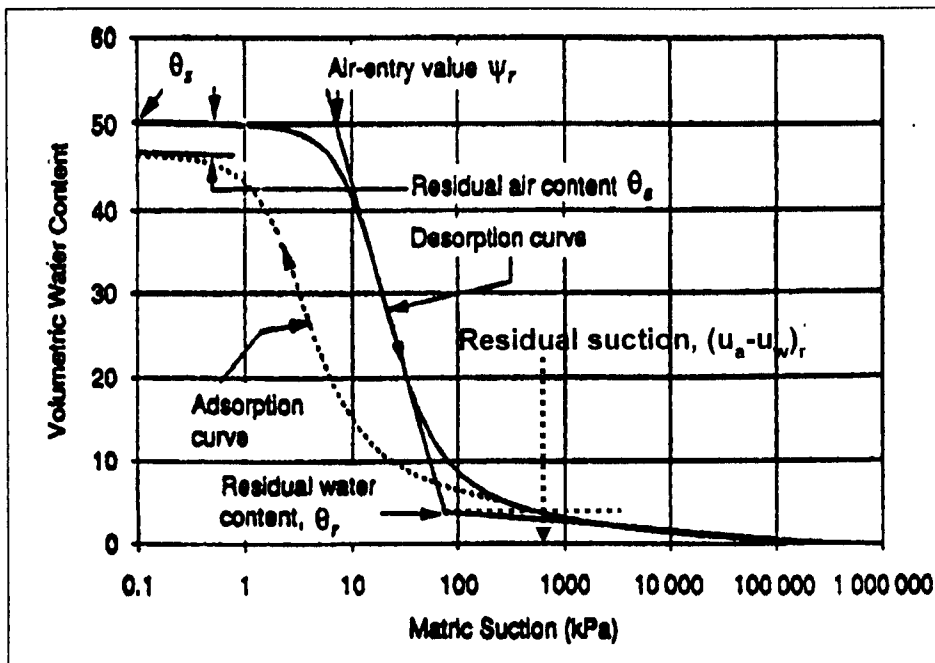


Figure 2.2 Warped surface representing the volume change behaviour of a mixture of flint (80%) and kaolin (20%) under isotropic stress conditions (Matyas and Radhakrishna, 1968).



(a) Soil-moisture characteristic curves for some Dutch soils (Koorevaar *et al.*, 1983).



(b) Soil-moisture characteristic curve illustrating the residual suction and residual water content (Fredlund and Xing, 1994).

Figure 2.3 Soil-moisture characteristic curves and graphical illustration for the definition of residual suction and residual water content.

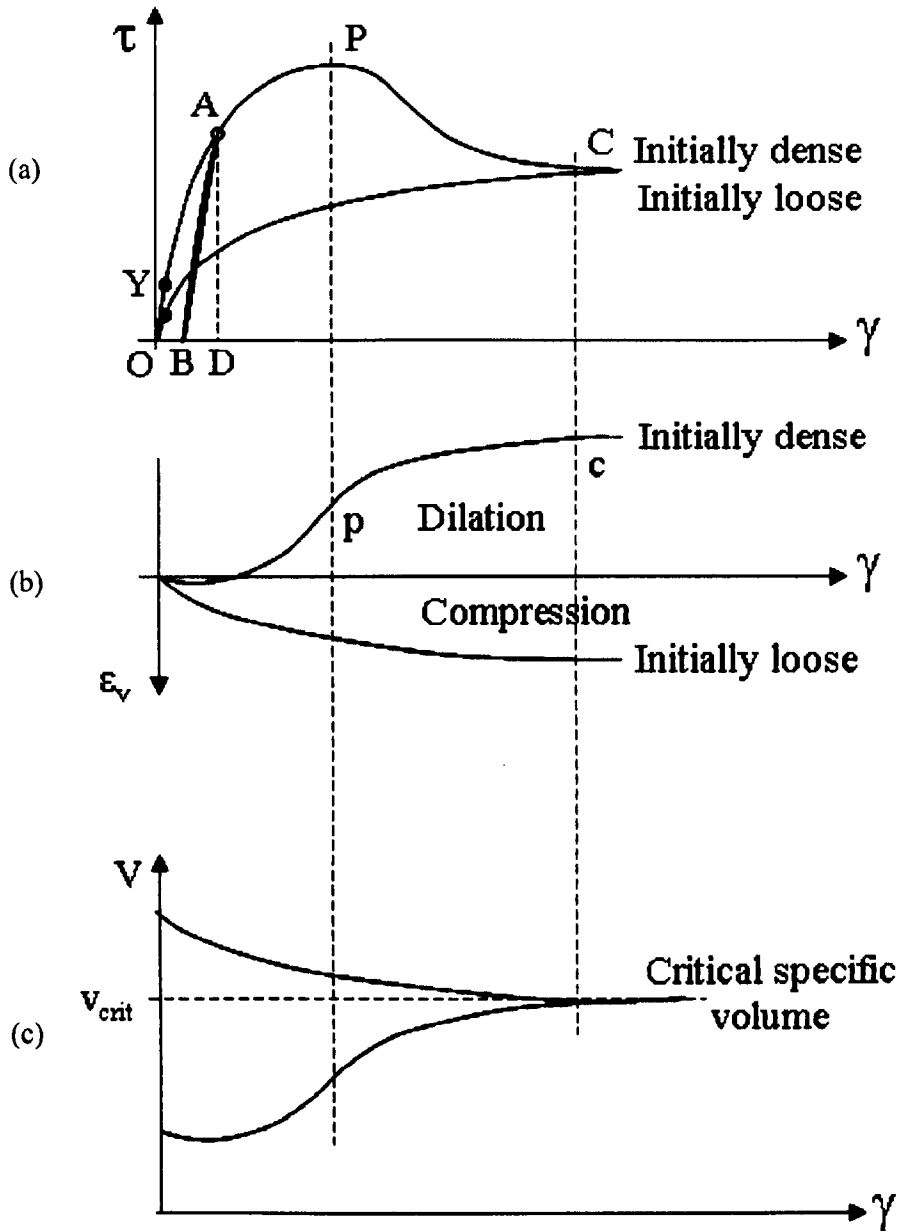
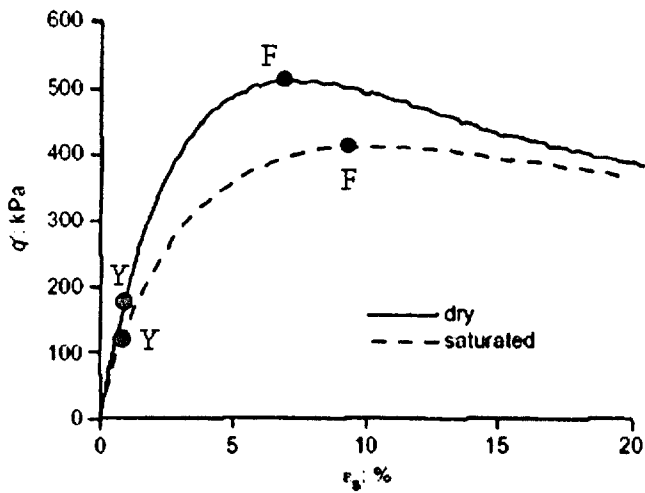
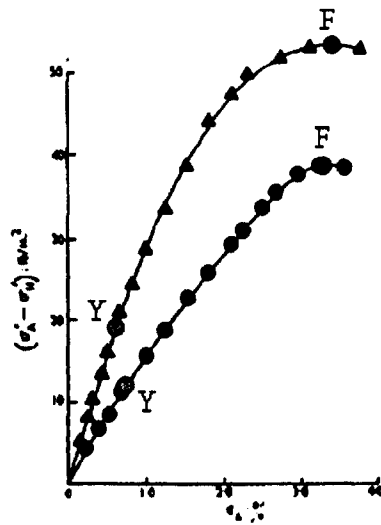


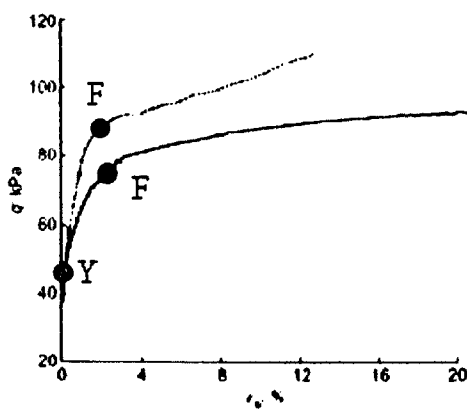
Figure 2.4 Typical shear stress, shear strain and volume change behaviour from a shear box test on dense and loose sand (Powrie 1997): (a)  $\tau$  versus  $\gamma$  (b)  $\epsilon_v$  versus  $\gamma$  (c)  $V$  versus  $\gamma$ .



(a) Well defined peak in the stress-strain curve for decomposed granite (Jovicic and Coop, 1997).



(b) Well defined peak in the stress-strain curve for over-consolidated London clay (Atkinson, 1975).



(c) A kink in the stress-strain curve for normally consolidated clay (Callisto and Calabresi, 1998).

Figure 2.5 Stress-strain curves showing either a well defined peak or a kink.

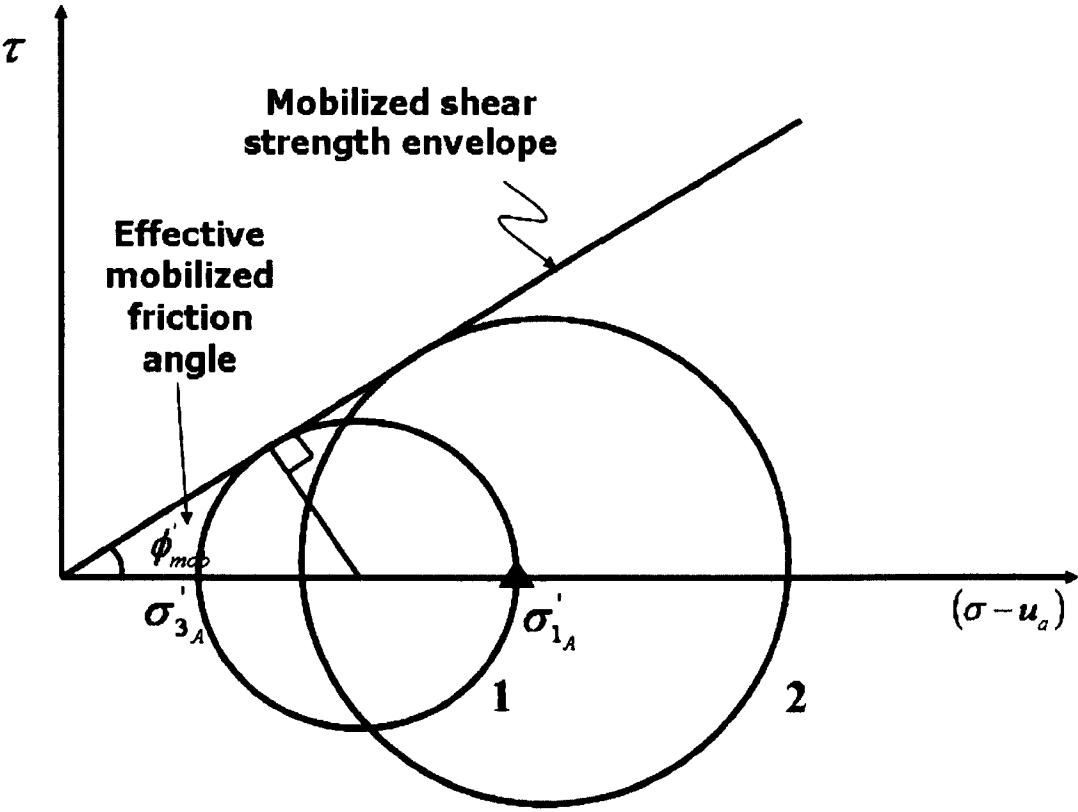


Figure 2.6 Mohr circles representing different mobilized shear strengths under the same mobilized shear strength envelope or the yield envelope.

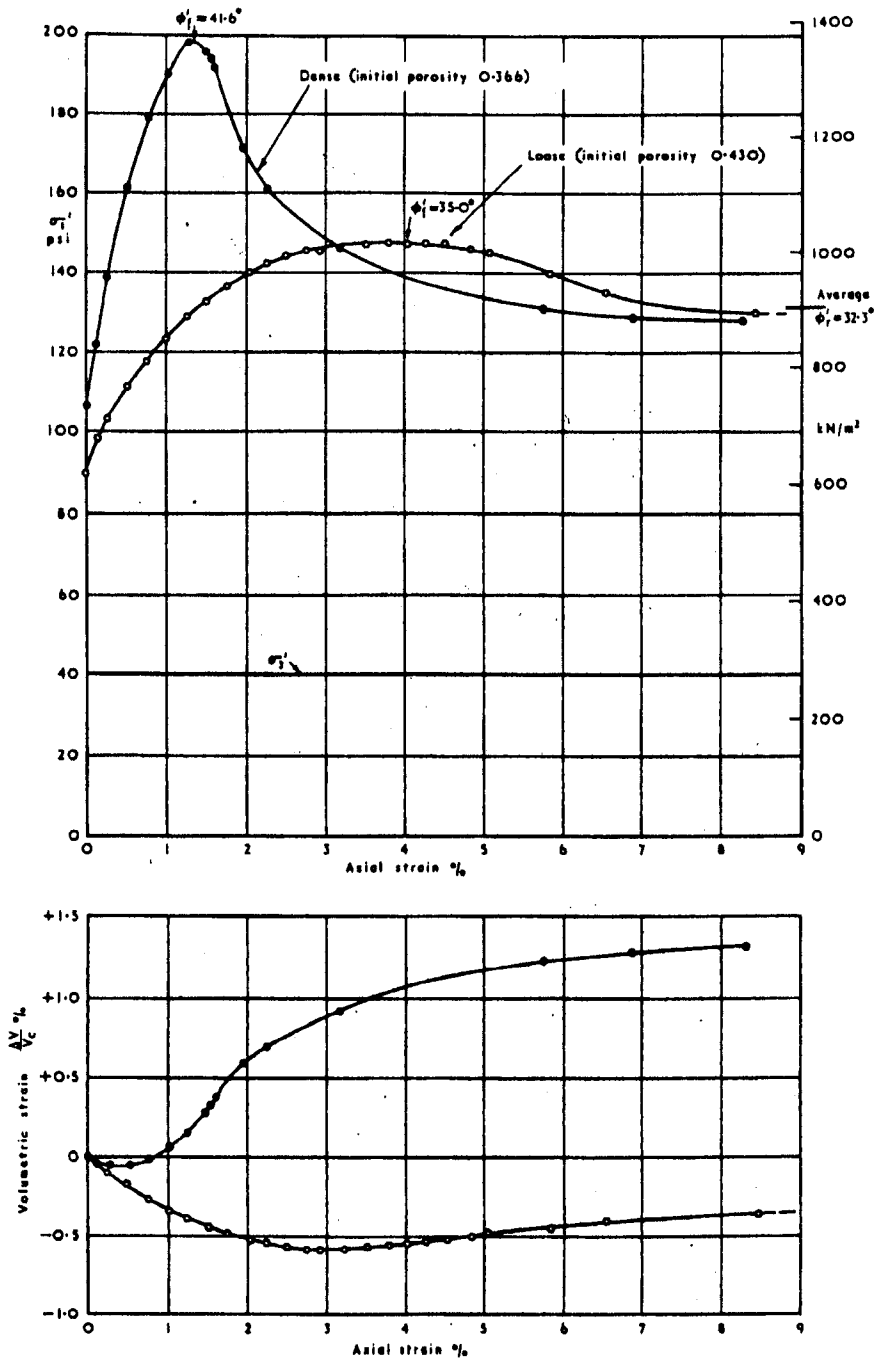
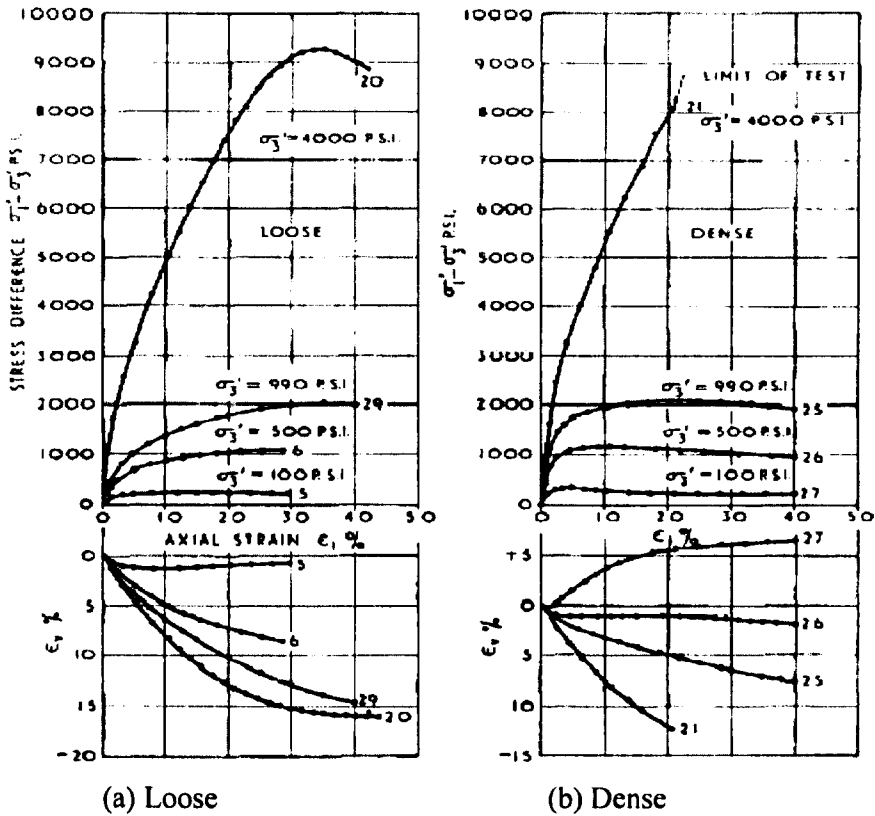


Figure 2.7 Stress-strain and volume change relationships for drained plane strain tests on loose and dense Brasted sand (Bishop 1972).



(a) Loose (b) Dense  
 Figure 2.8 Stress-strain and volume change relationships for drained triaxial tests on saturated Ham River sand at normal and elevated net confining pressures (Bishop 1966) (Note : 1 lb/sq.inch. = 6.896 kN/m<sup>2</sup>).

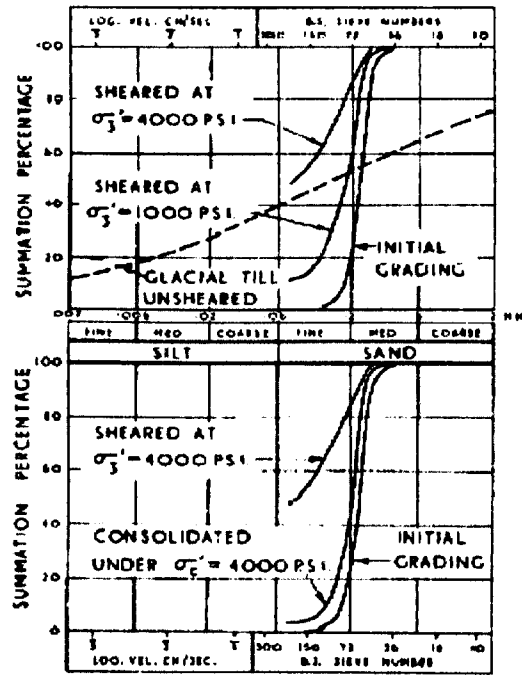


Figure 2.9 Change in grading resulting from shear at different net confining pressures (Bishop 1966).

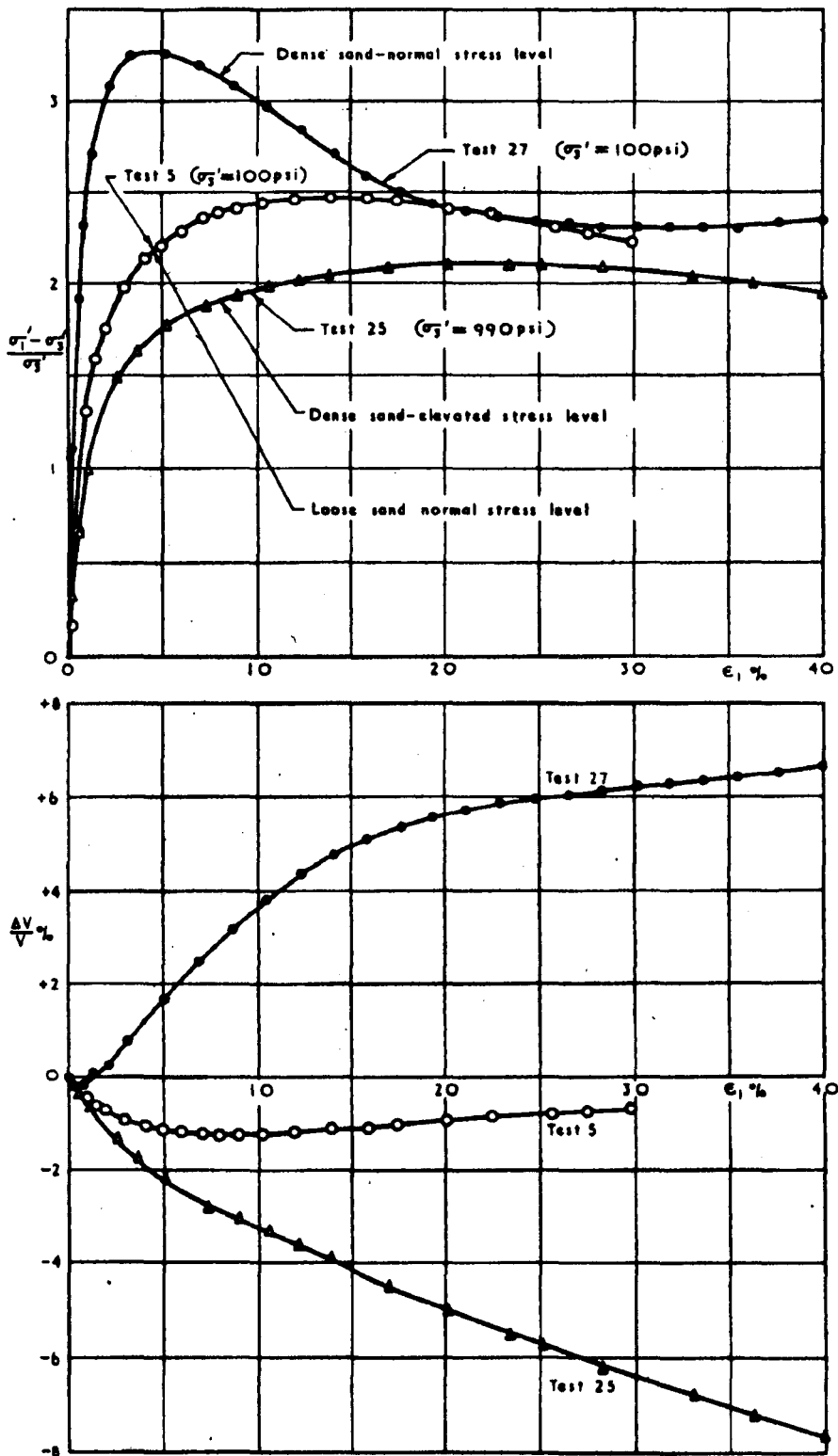


Figure 2.10 Principal effective stress ratio, strain and volume change relationships for drained triaxial compression tests on saturated Ham River sand at normal and elevated stress levels (Bishop 1972) (Note : 1 lb/sq.inch. = 6.896 kN/m<sup>2</sup>).

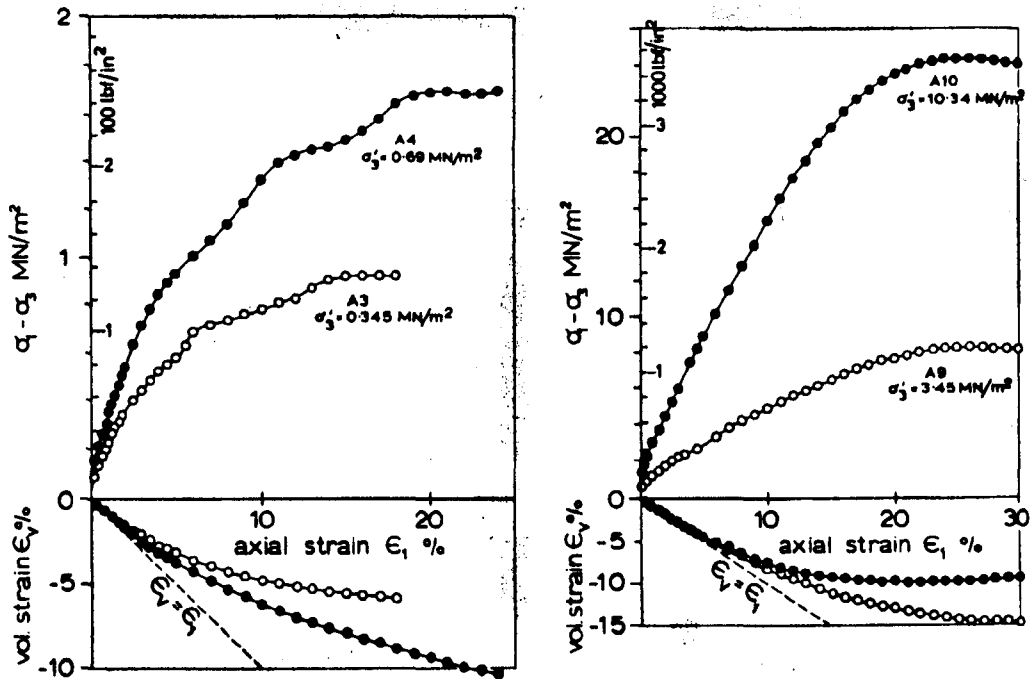
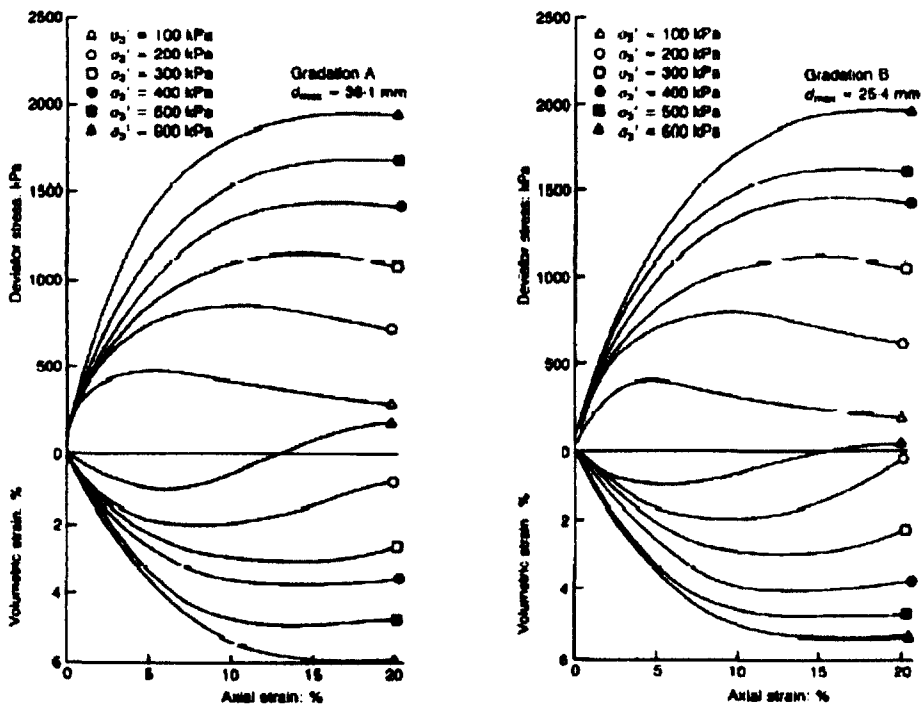


Figure 2.11 Stress-strain and volume change relationship for drained triaxial tests on crushed anthracite demonstrating that axial strain at failure does not go on increasing indefinitely with particle breakage (Billam 1972).



(a) Gradation A.

(b) Gradation B.

Figure 2.12 Stress-strain and volume change behaviour of greywacke rockfill in large-scale triaxial testing Indraratna *et al.* (1993).

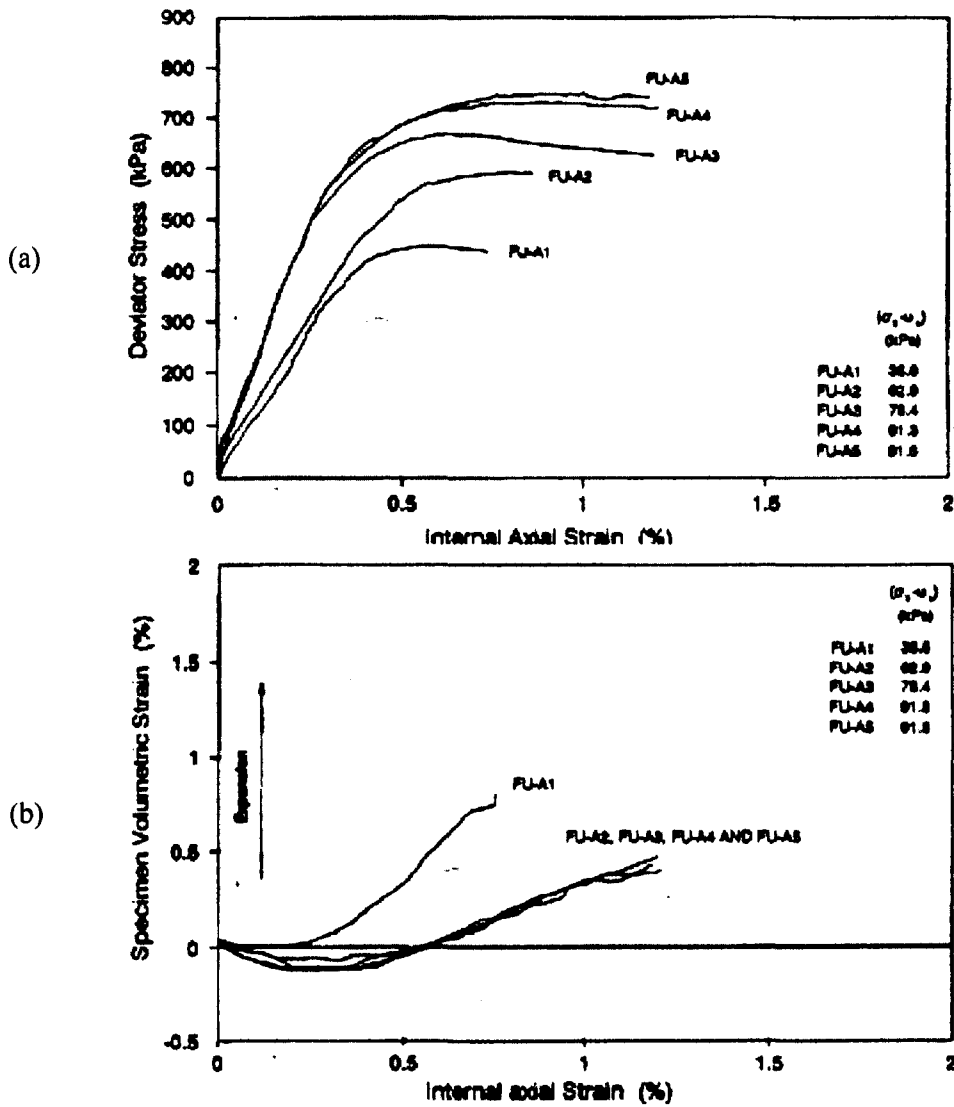


Figure 2.13 Stress-strain and volume change behaviour during consolidated drained triaxial tests on unsaturated specimens of similar limestone gravels as the test material of this research (Salman 1995) (a) deviator stress versus axial strain (b) specimen volumetric strain versus internal axial strain.

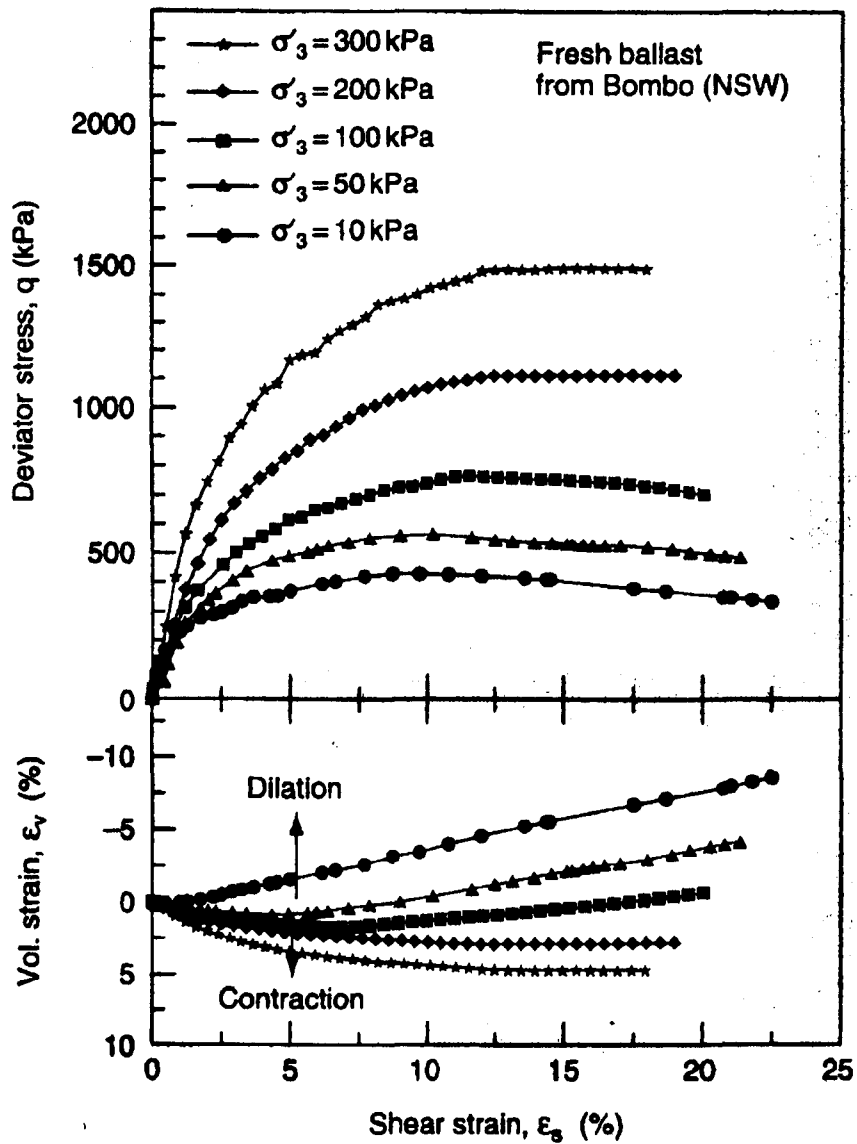


Figure 2.14 Sign of particle breakage even at low stress levels (<300 kPa) (Indraratna and Salim, 2001).

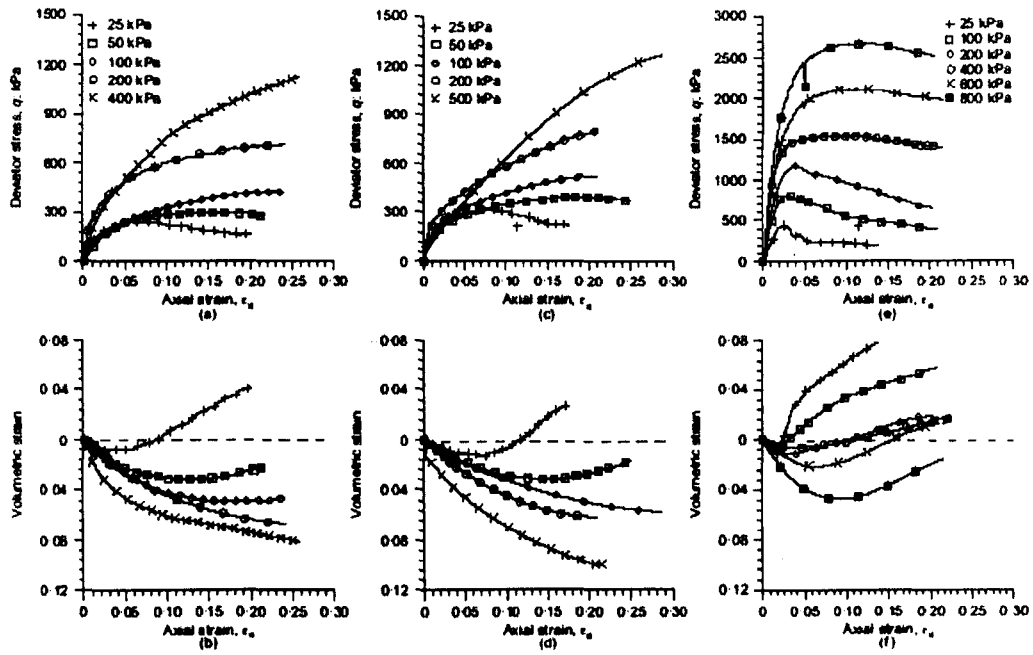


Figure 2.15 Constant suction triaxial tests performed on gneiss rock residual soil at horizon B (Futai and Almeida 2005) (a), (b) Suction = 100 kPa; (c), (d) Suction = 300 kPa; (e), (f) air dried.

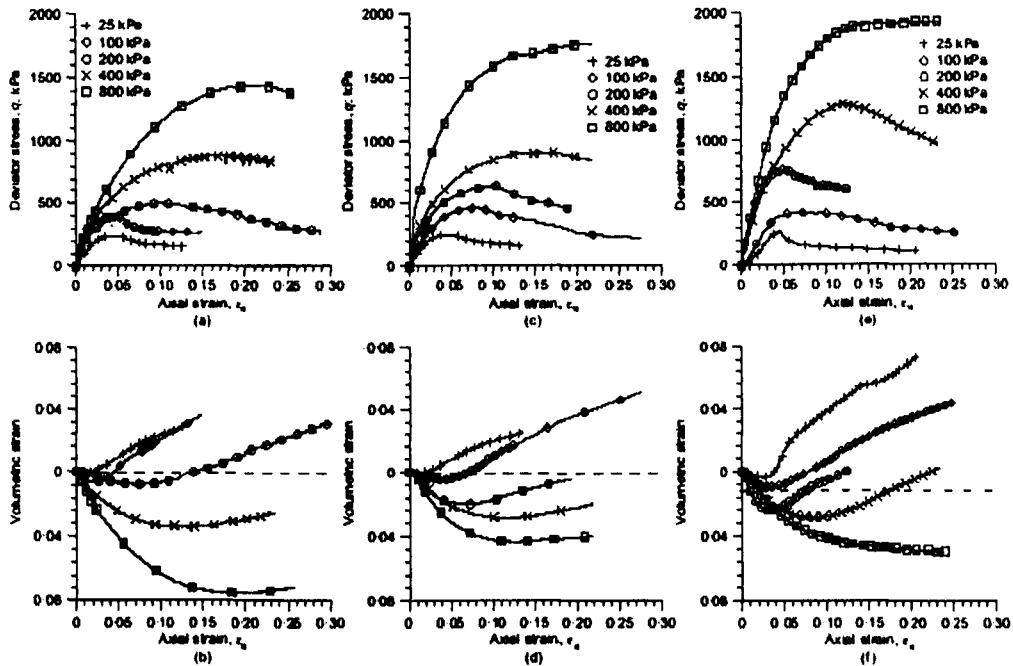


Figure 2.16 Constant suction triaxial tests performed on gneiss rock residual soil at horizon C (Futai and Almeida 2005) (a), (b) Suction = 100 kPa; (c), (d) Suction = 300 kPa; (e), (f) air dried.



Figure 2.17 Electron micrographs of kaolin showing void spaces indicated by the dark coloured areas (Penumadu and Dean, 2000).

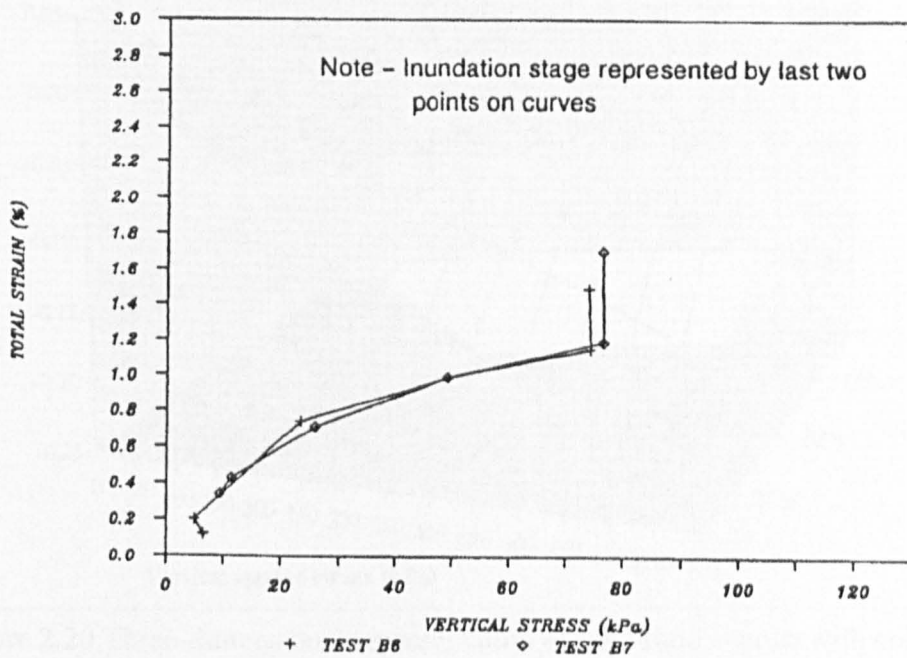


Figure 2.18 Significant 1-D compression of coarse-grained soils due to inundation indicated by the last two data points on the graphs (Goodwin 1991).

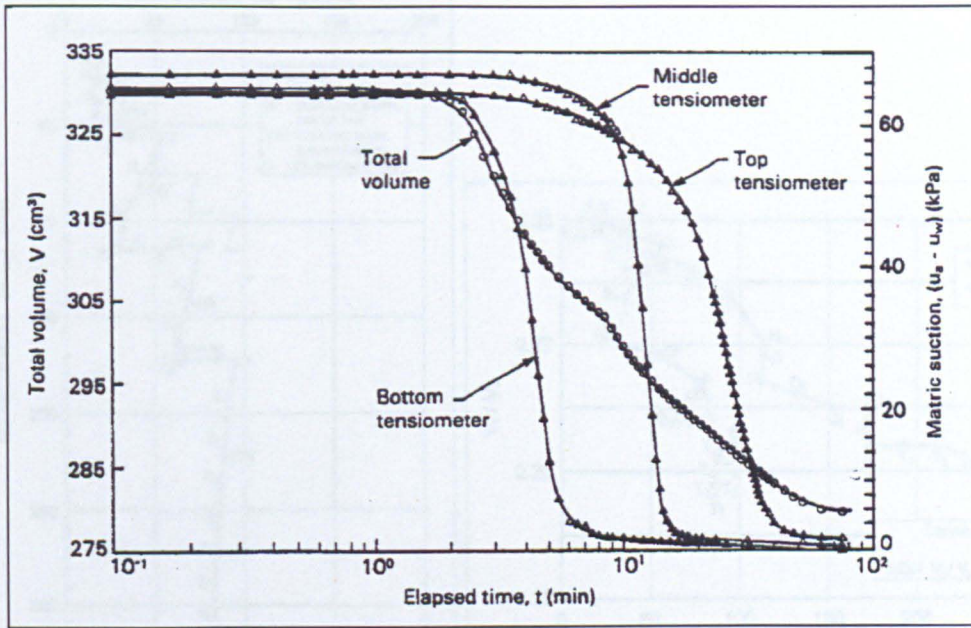


Figure 2.19 Volume changes versus time during inundation of a compacted specimen of Indian Head silty sand (Tadepalli *et al.*, 1992).

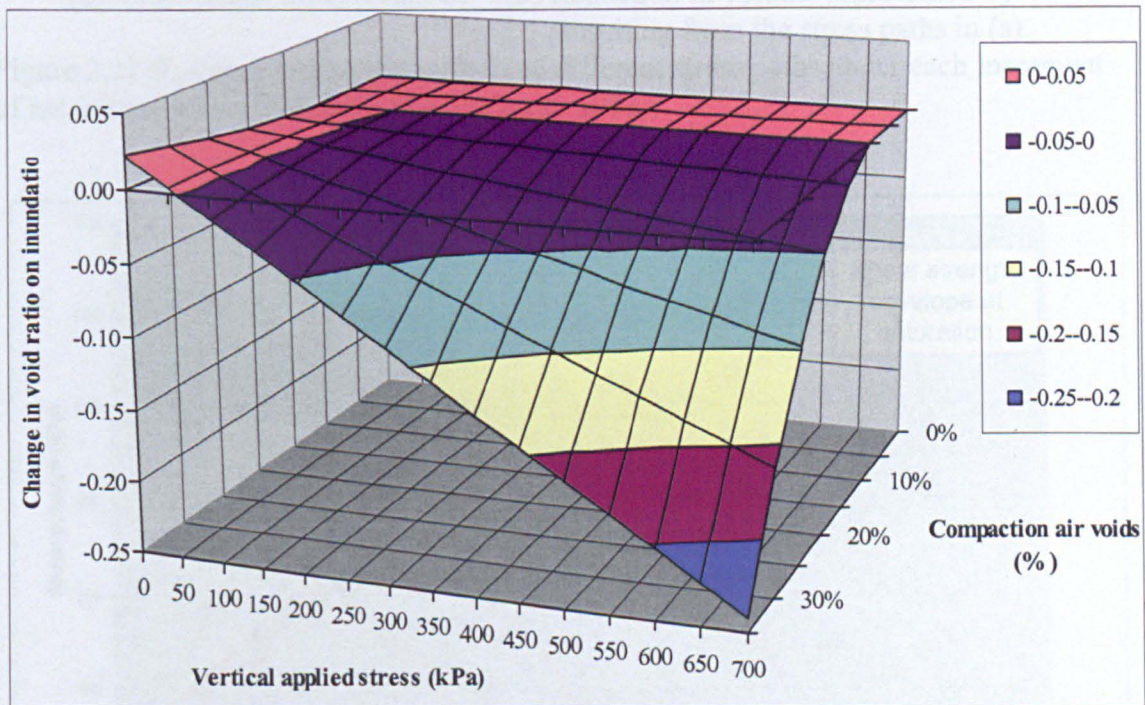
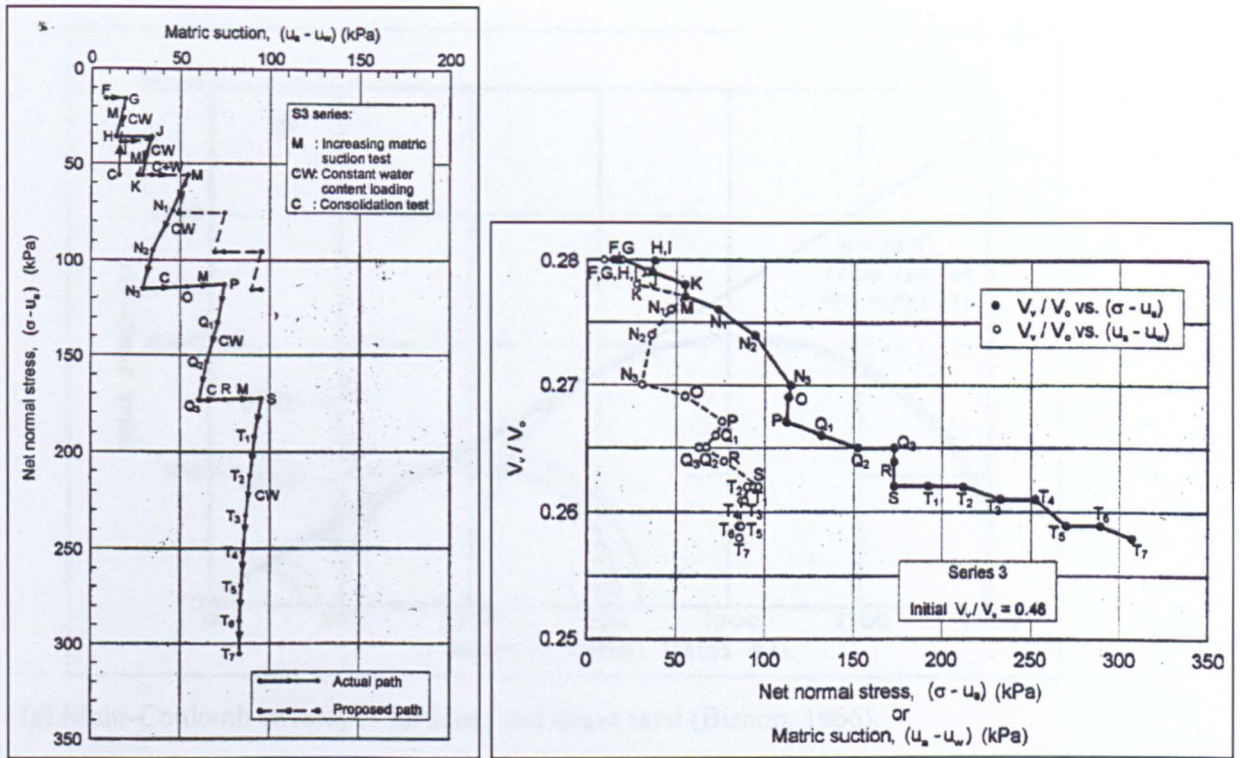


Figure 2.20 Three-dimensional representation of void ratio change with compaction air voids and vertical stress at inundation (Blanchfield and Anderson, 2000).



(a) Stress paths, M, CW and C. (b) Reduction in volume represented by  $V_v/V_o$  resulting from the stress paths in (a).

Figure 2.21  $K_0$ -compression test with three different stress paths under each increment of net normal stress (Rahardjo and Fredlund, 2003).

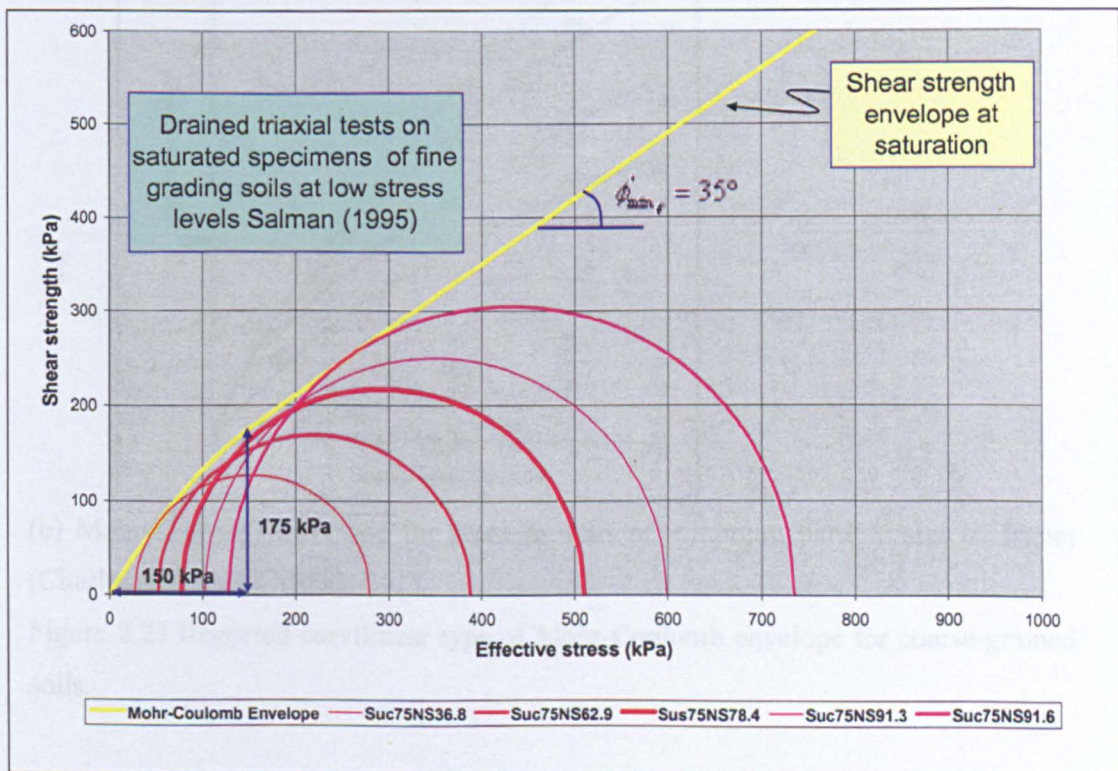
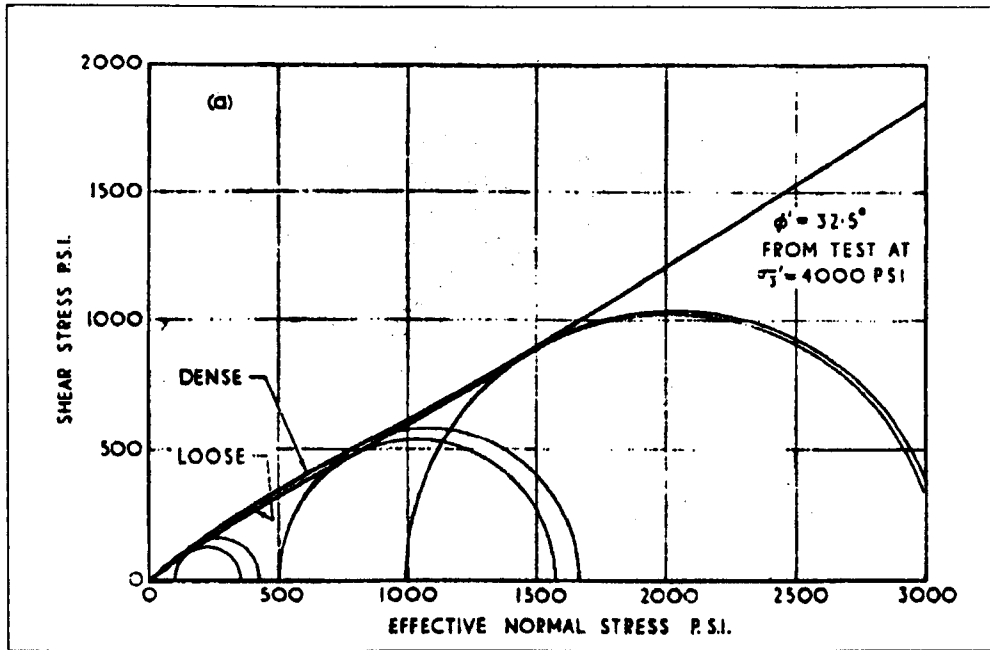
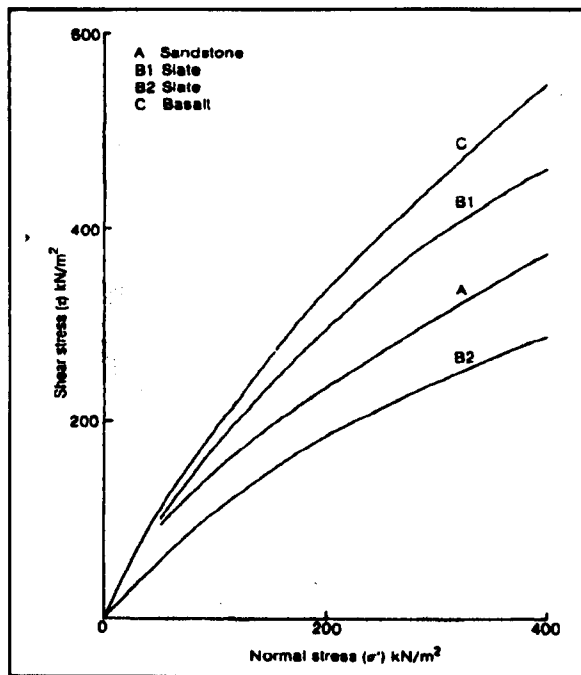


Figure 2.22 The curvilinear type of Mohr-Coulomb envelope base on data by Salman (1995) as shown in Table 2.2.



(a) Mohr-Coulomb envelopes for loose and dense sand (Bishop, 1966).



(b) Mohr-Coulomb envelope for granular soils of minimum particle size of 38mm (Charles and Watts, 1980).

Figure 2.23 Reported curvilinear type of Mohr-Coulomb envelope for coarse-grained soils.

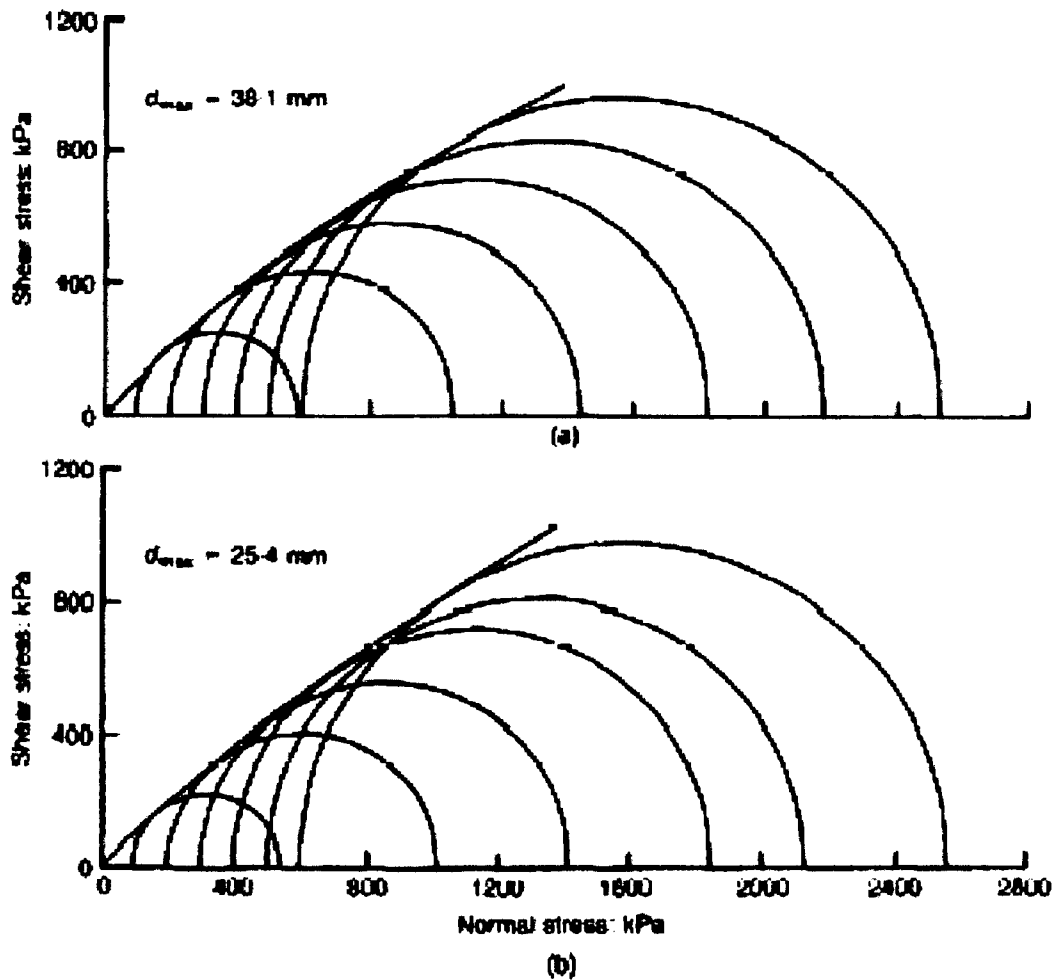
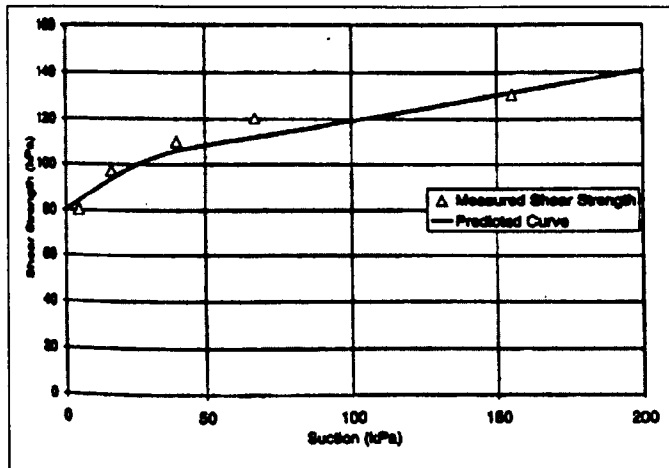
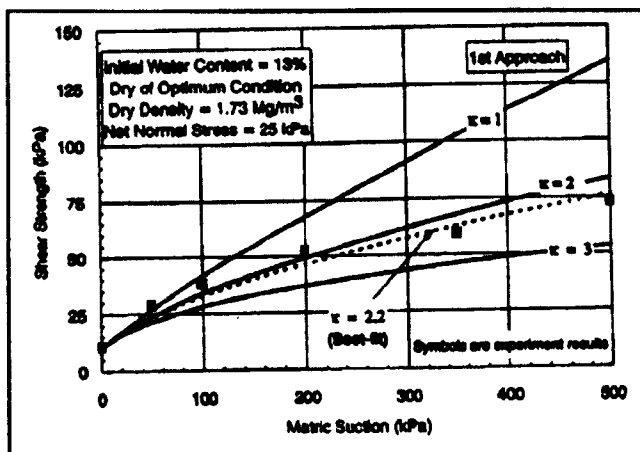


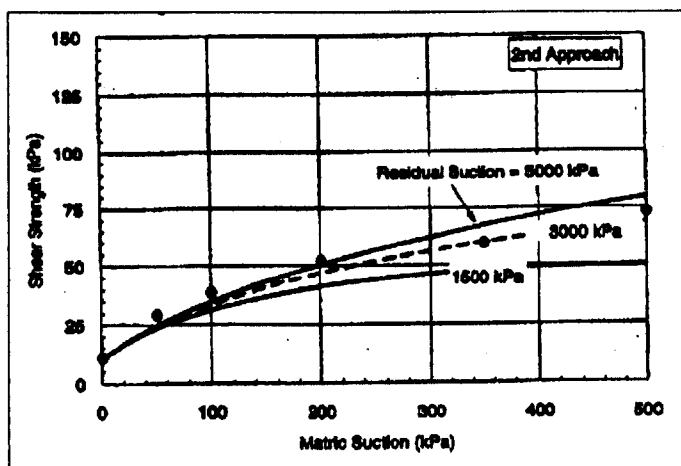
Figure 2.24 Mohr-Coulomb envelopes showing non-linear behaviour of shear strength at low effective stress for saturated greywacke rockfill material Indraratna *et al.* (1993) (a) gradation A (b) gradation B.



(a) Predicted shear strength represented by the line graph according to Equation 2.16 (Fredlund *et al.*, 1995).

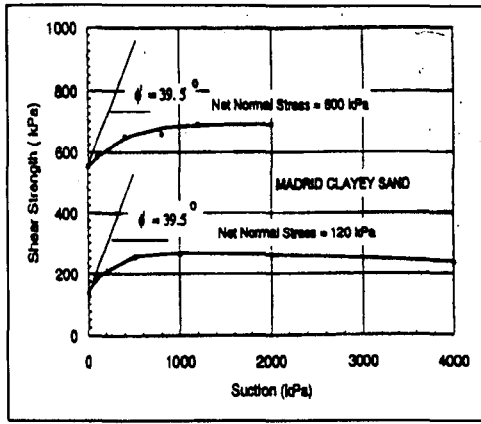


(b) Best-fit predicted shear strength represented by the dotted line according to Equation 2.18 (Vanapalli *et al.*, 1996).

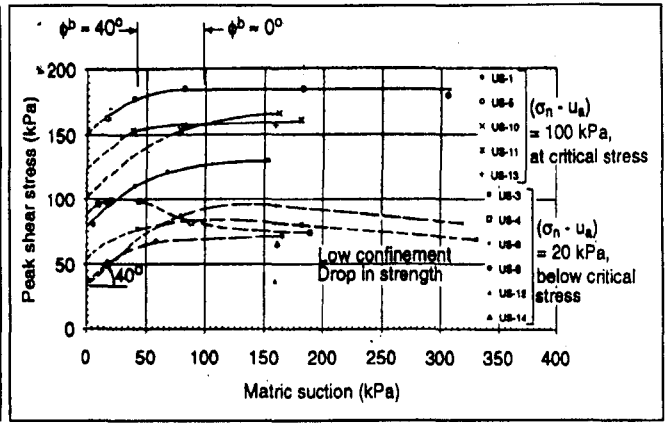


(c) Best-fit predicted shear strength represented by the dotted line for suction of 3000 kPa according to Equation 2.11 (Vanapalli *et al.*, 1996).

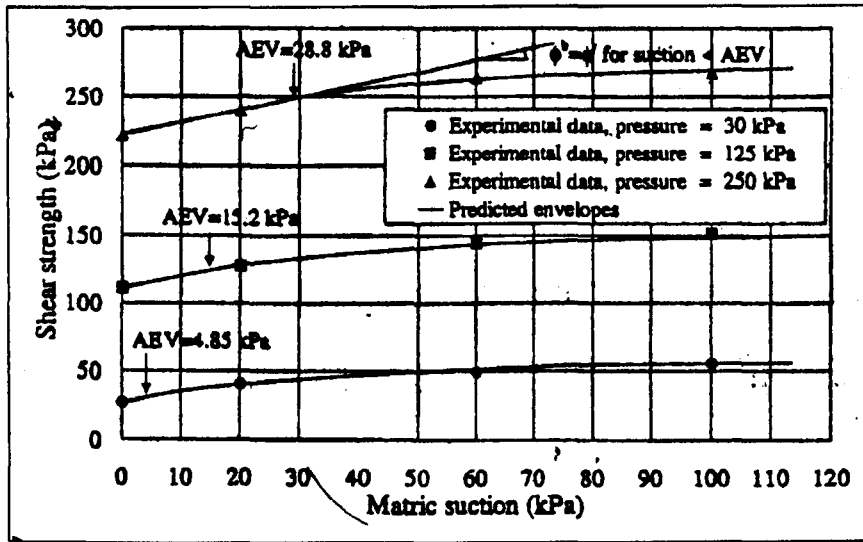
Figure 2.25 Predicted shear strength according to the proposed shear strength equation.



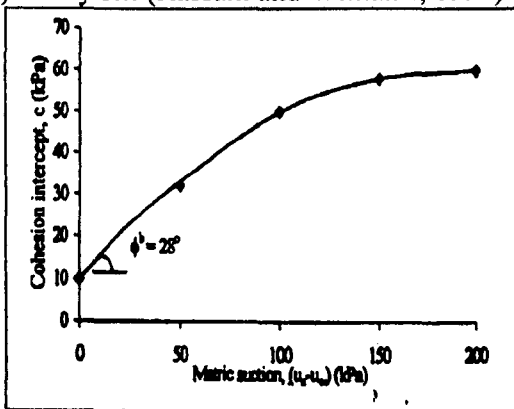
(a) Madrid clayey sand (Escario and Juca, 1989).



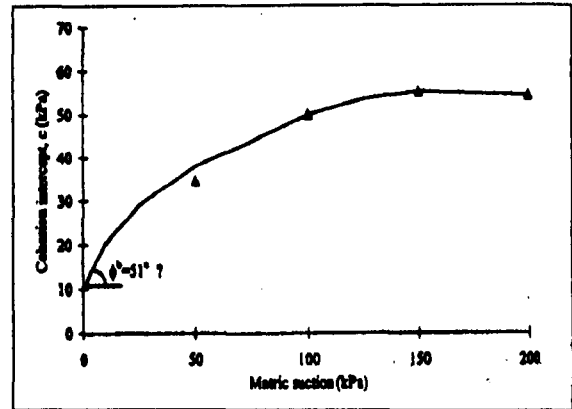
(b) Fine ash tuff (Gan and Fredlund, 1996).



(c) Sandy silt (Rassam and Williams, 1999).

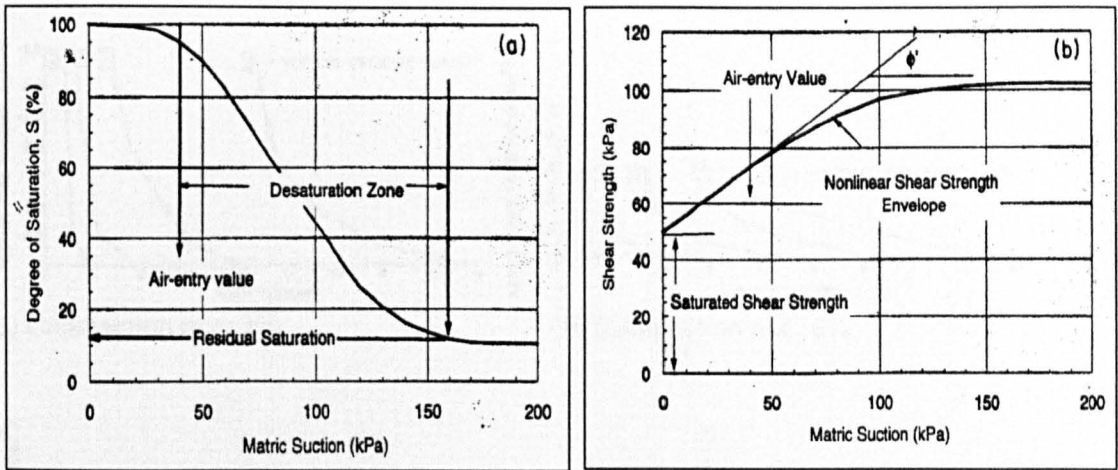


(d) Bukit Timah residual soil, Singapore (Toll *et al.*, 2000).



(e) Jurong residual soil, Singapore (Toll *et al.*, 2000).

Figure 2.26 Non-linear behaviour of shear strength at suction lower than residual suction and remaining constant beyond that.



(a) Soil-water characteristic curve.

(b) Corresponding non-linear shear strength behaviour with respect to suction.

Figure 2.27 Behaviour of unsaturated shear strength with reference to the soil-water characteristic curve (Vanapalli *et al.*, 1996).

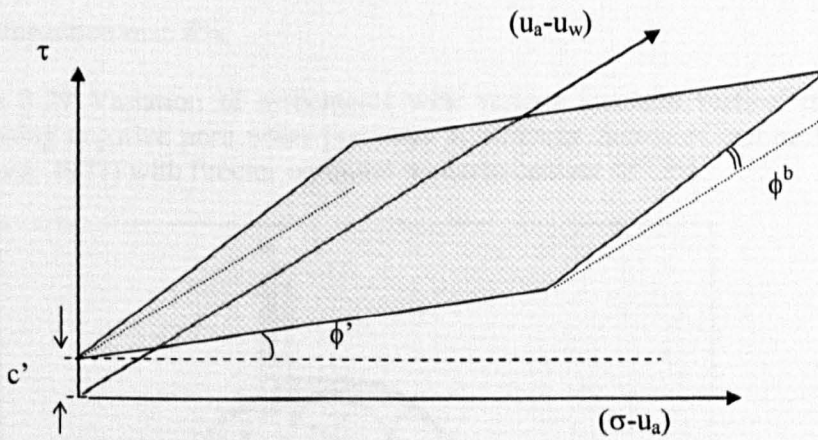


Figure 2.28 A three-dimensional plane surface for the extended Mohr-Coulomb failure envelope for unsaturated soil (Fredlund *et al.*, 1978).

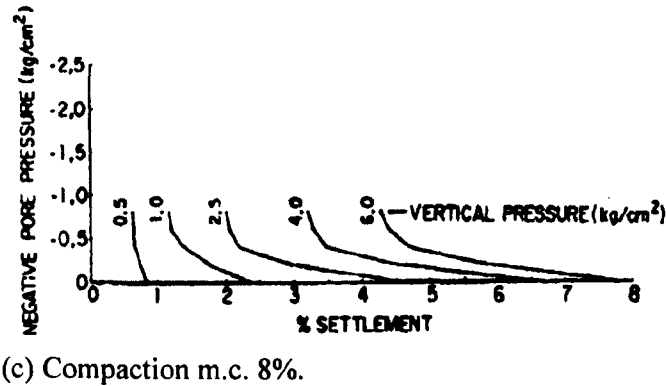
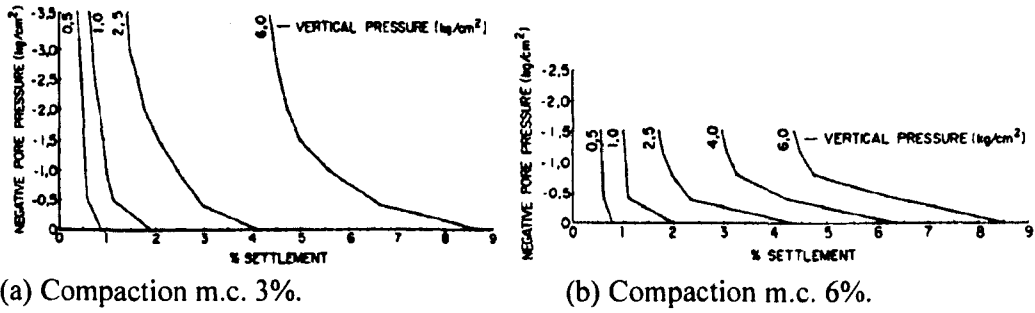


Figure 2.29 Variation of settlements with various constant vertical pressures and decreasing negative pore water pressures at different degree of compaction (Escario and Saez, 1973) with Proctor optimum moisture content of 11%.

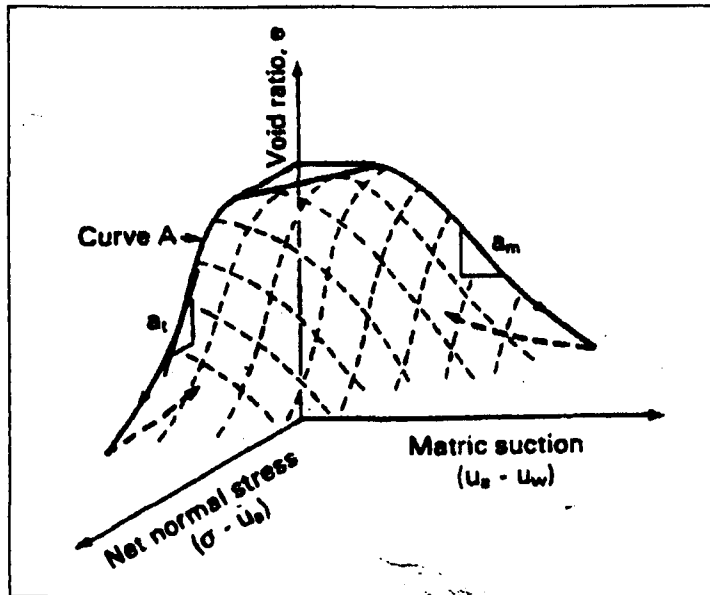


Figure 2.30 Three-dimensional void ratio constitutive surface for unsaturated soil based on the two independent stress state variables,  $(\sigma - u_a)$  and  $(u_a - u_w)$  (Fredlund and Morgenstern, 1976).

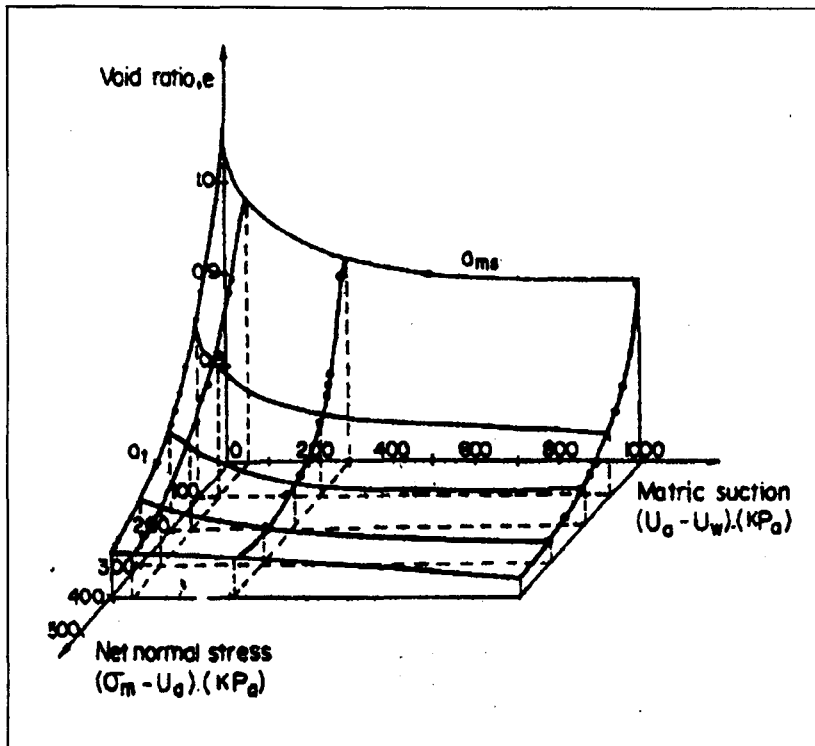


Figure 2.31 Void ratio constitutive surface for Madrid grey clay (Sabbagh, 2000).

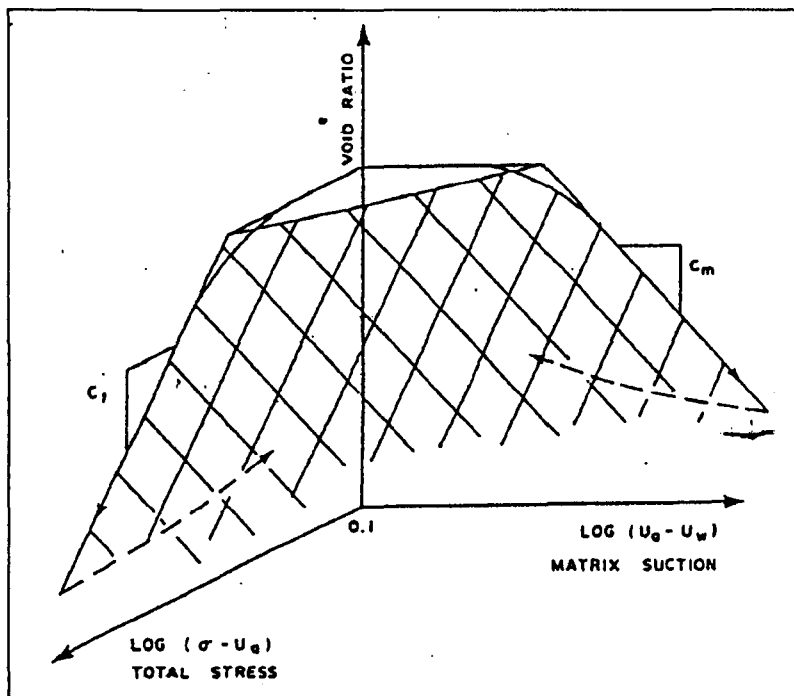


Figure 2.32 Planar constitutive surface for void ratio proposed by Fredlund (1979).

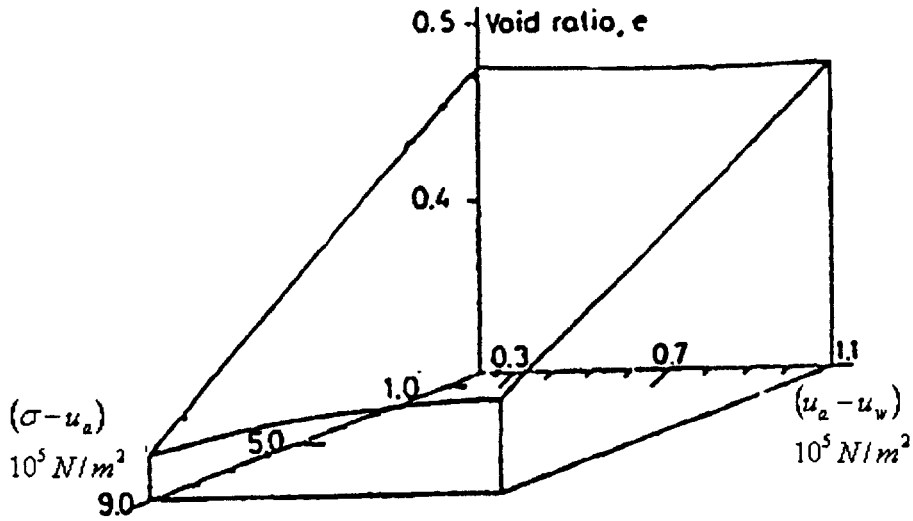
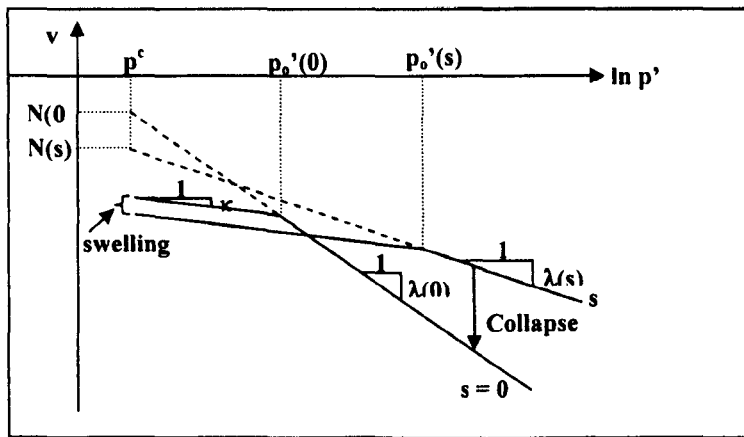
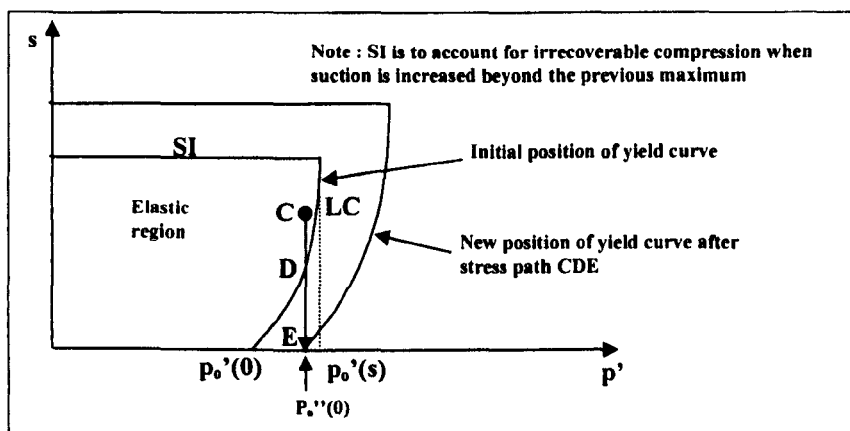


Figure 2.33 State surface for void ratio of Pinolen clayey sand under isotropic compression (Lloret and Alonso, 1985).

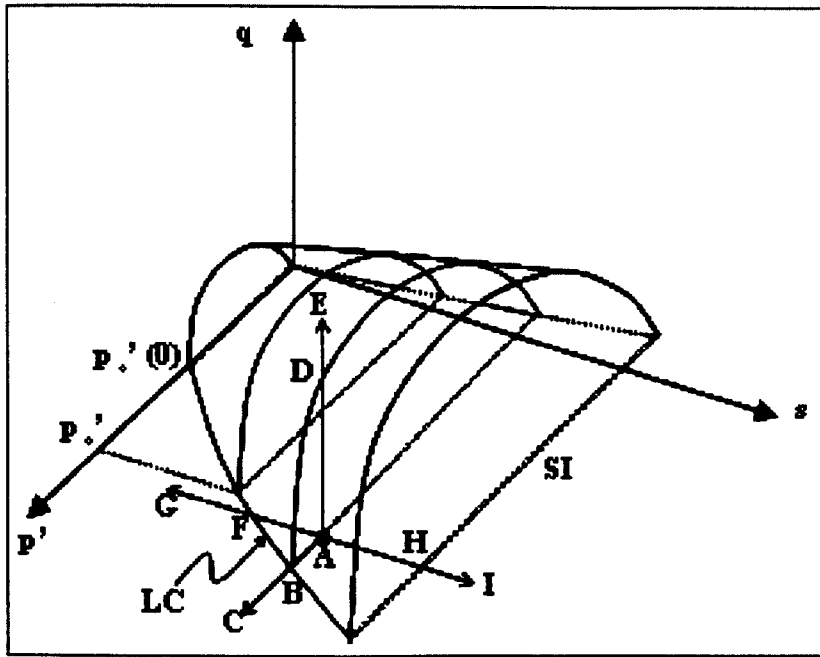


(a) Normal compression curve for saturated and unsaturated soil.

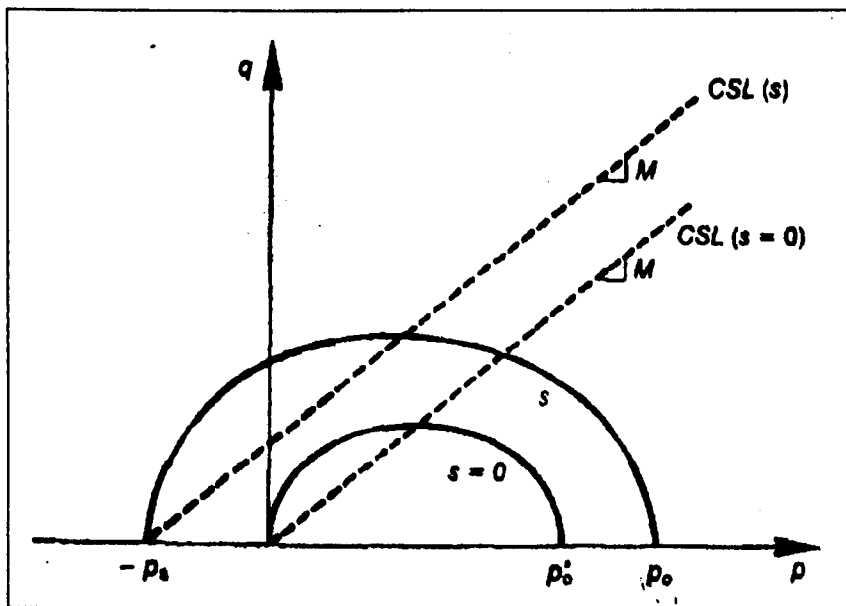


(b) Loading collapse yield curve in the  $s: p'$  plane.

Figure 2.34 Isotropic normal compression line and loading collapse yield curve in the elasto-plastic critical state framework of Alonso *et al.* (1990).

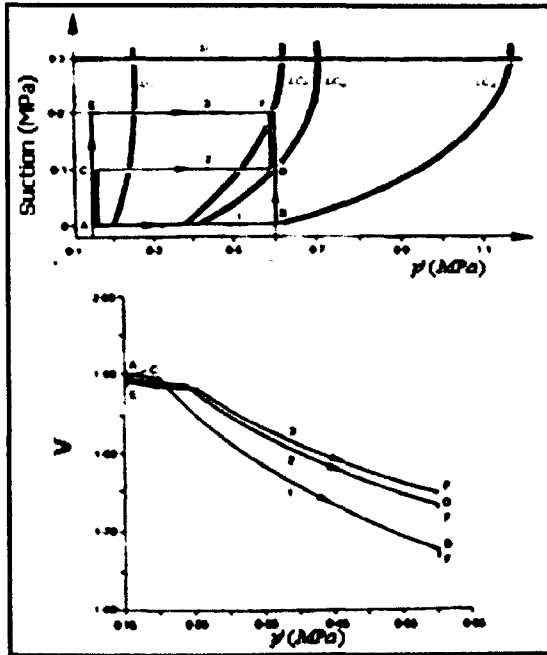


(a) Three-dimensional yield surfaces and four types of stress paths that can lead to failure.

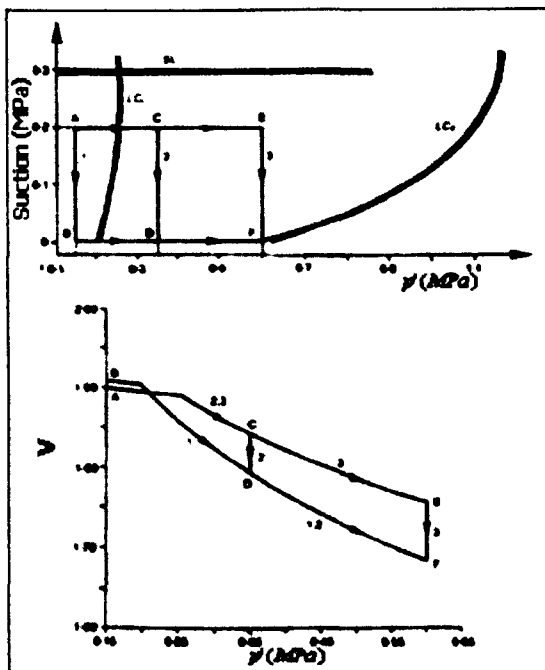


(b) Critical state line (CSL) in  $q - p'$  space.

Figure 2.35 Three-dimensional elasto-plastic critical state framework in  $(p, q, s)$  stress space (Alonso *et al.*, 1990).

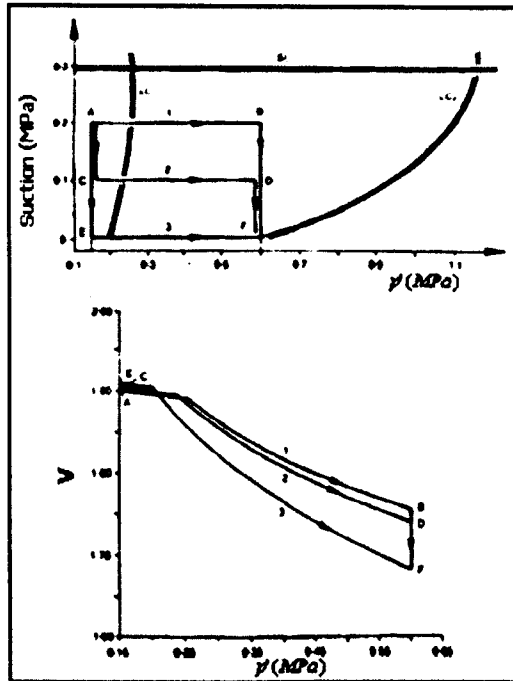


(a) Increments of net mean stress and increasing suction (drying).



(b) Decreasing suction (wetting) at increasing net mean stress.

Figure 2.36 Various responses of specific volume with mean net stress,  $p'$ , under wetting and drying stress paths (Alonso *et al.*, 1990).



(c) Increments of net mean stress and decreasing suction.

Figure 2.36 (continued) Various responses of specific volume with mean net stress,  $p'$ , under wetting and drying stress paths (Alonso *et al.*, 1990).

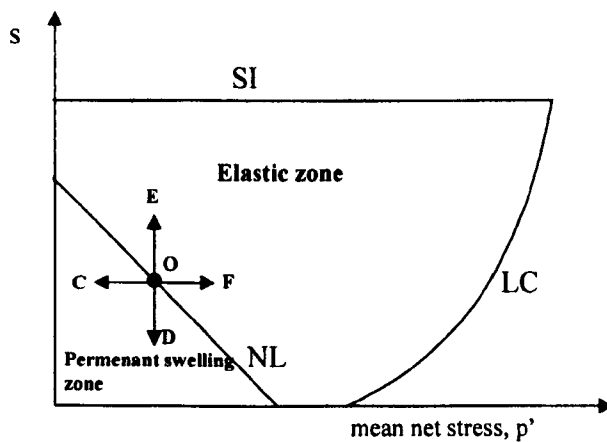
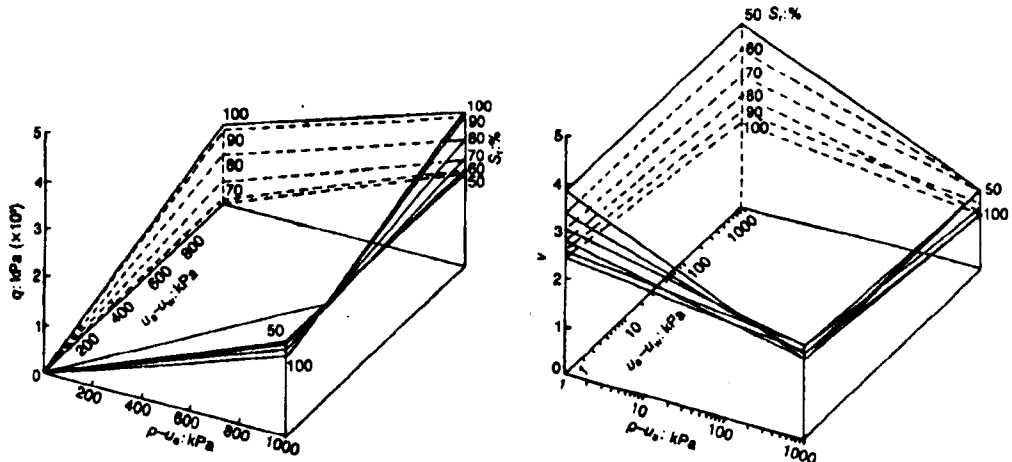


Figure 2.37 Introduction of the Neutral Line (NL) yield curve for highly expansive soils to complement the LC and the SI yield curves (Gens and Alonso, 1992).



(a) Deviator stress critical state surface.

(b) Specific volume critical state surface.

Figure 2.38 Critical state constitutive surfaces for Kinyu gravel (Toll, 1990).

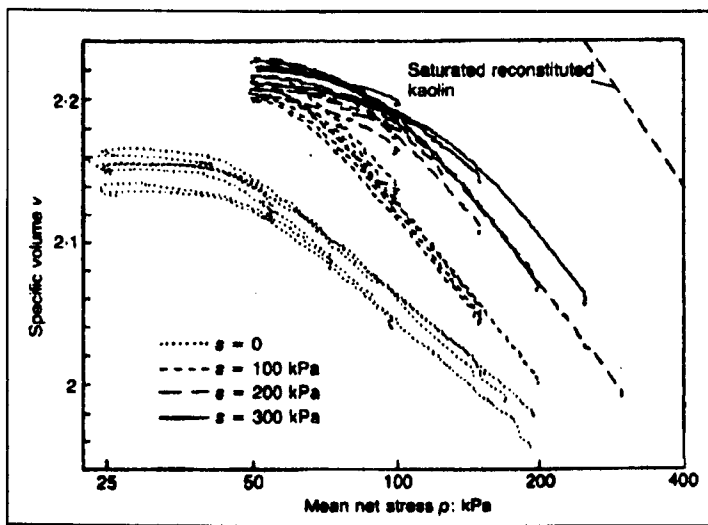
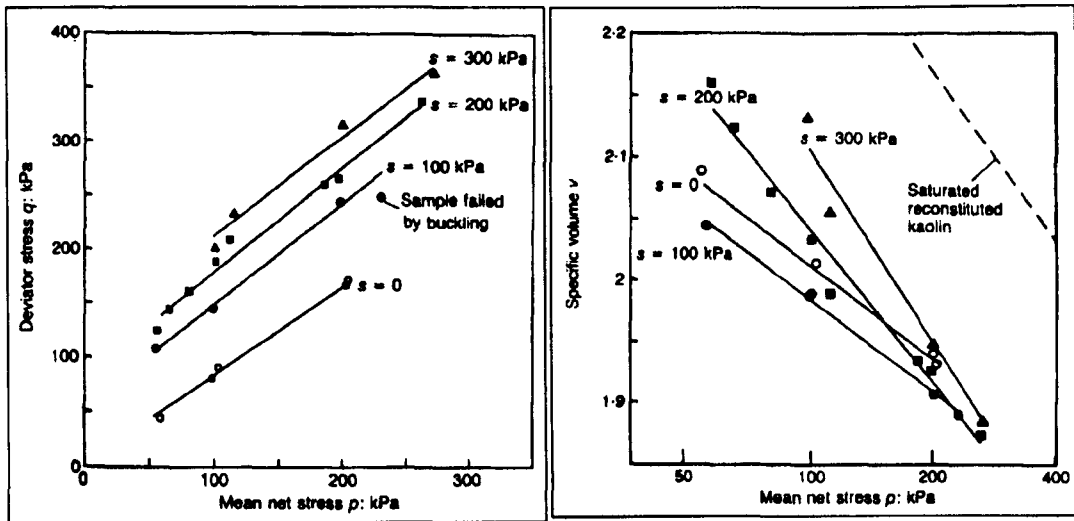


Figure 2.39 Variation of specific volume during ramped consolidation of compacted speswhite kaolin at various values of suction (Wheeler and Sivakumar, 1995).



(a) Deviator stress versus mean net stress. (b) Specific volume versus mean net stress.

Figure 2.40 Critical state lines for deviator stress and specific volume (Wheeler and Sivakumar, 1995).

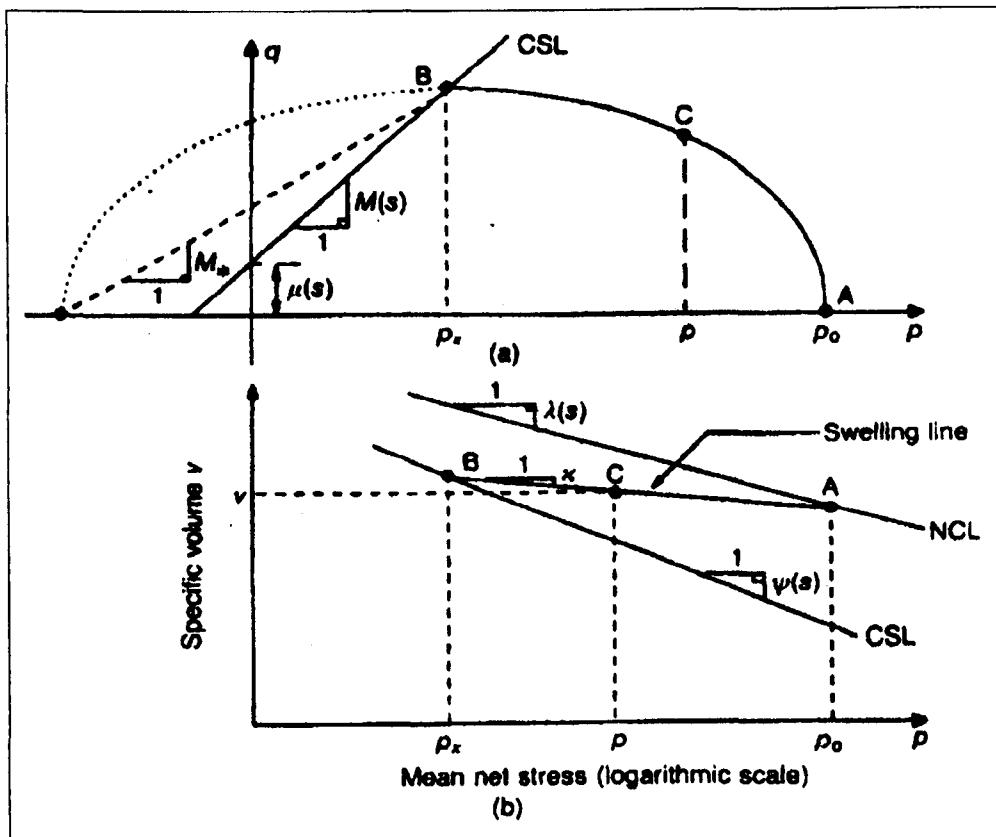


Figure 2.41 A constant suction yield curve in relation to the normal compression line and CSL (Wheeler and Sivakumar, 1995).

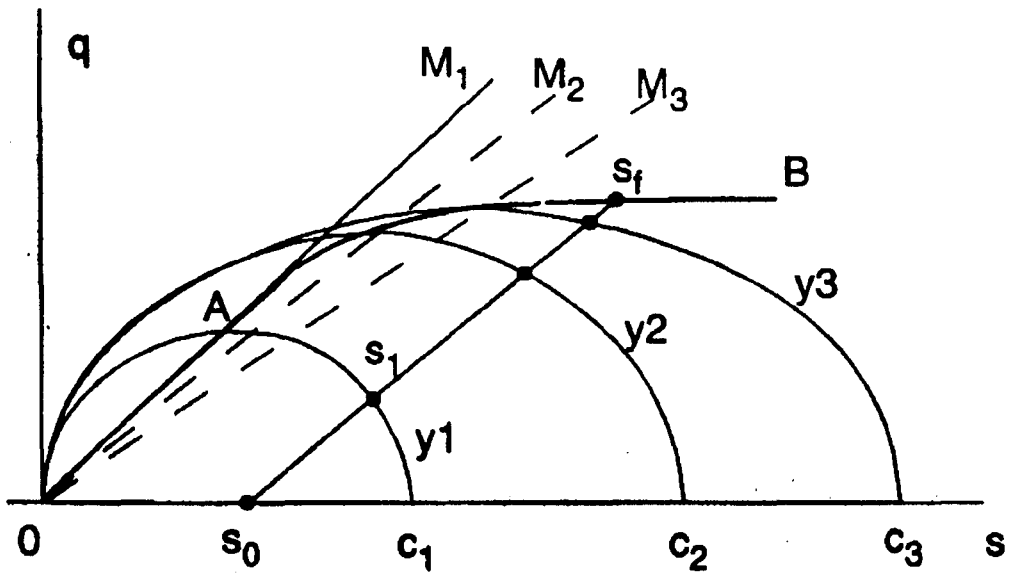


Figure 2.42 Shear strength surface in q-s space (Delage and Graham, 1995).

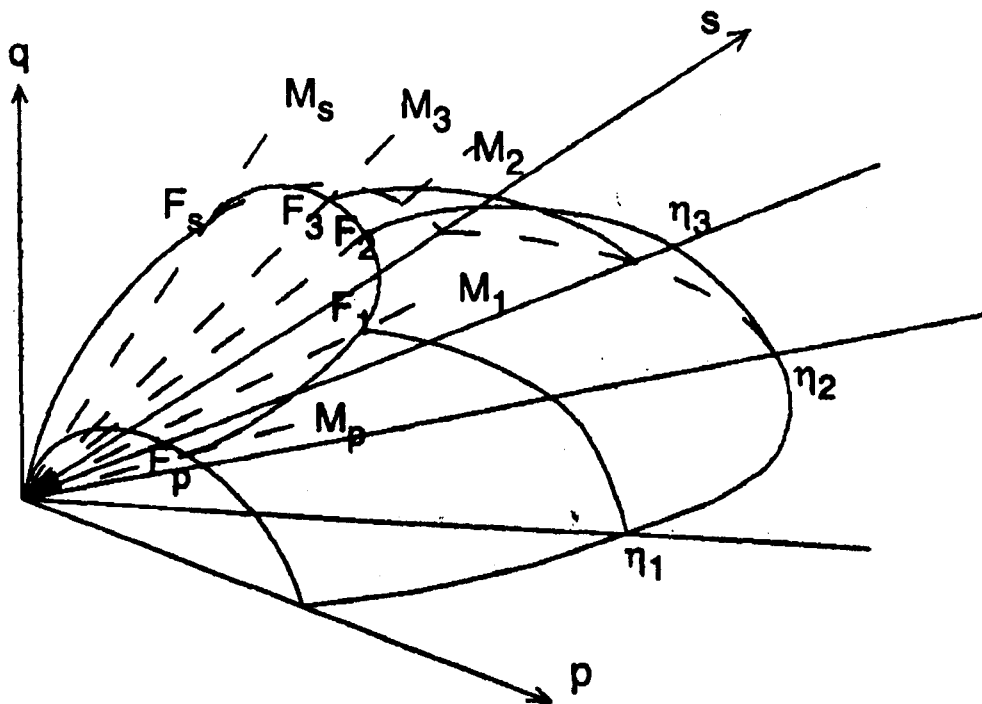
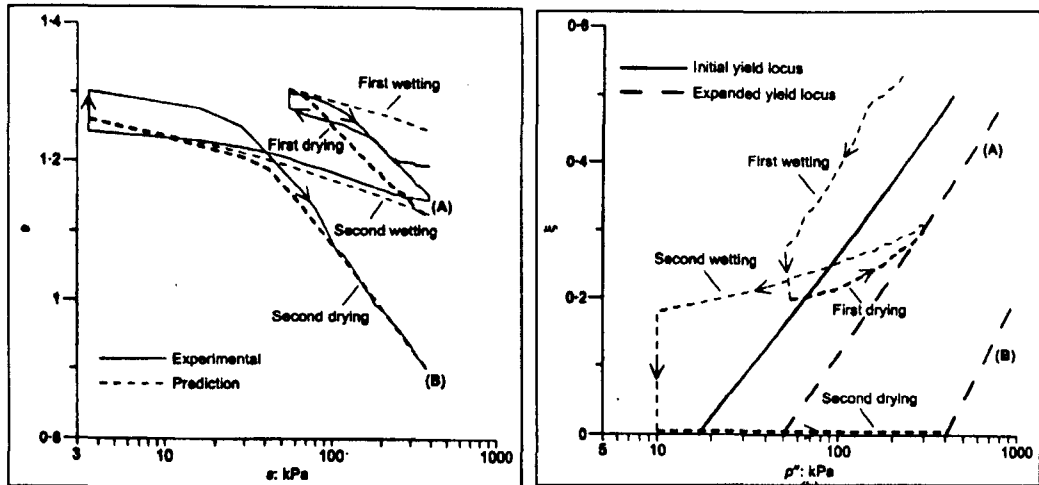


Figure 2.43 State boundary surface of the "closure" type critical state framework for unsaturated soil (Tang and Graham, 2002).



(a) Change of void ratio.

(b) Stress path.

Figure 2.44 Framework prediction for wetting and drying cycles under an isotropic net stress of 10 kPa (Gallipoli *et al.*, 2003) based on the experimental data of Sharma (1998).

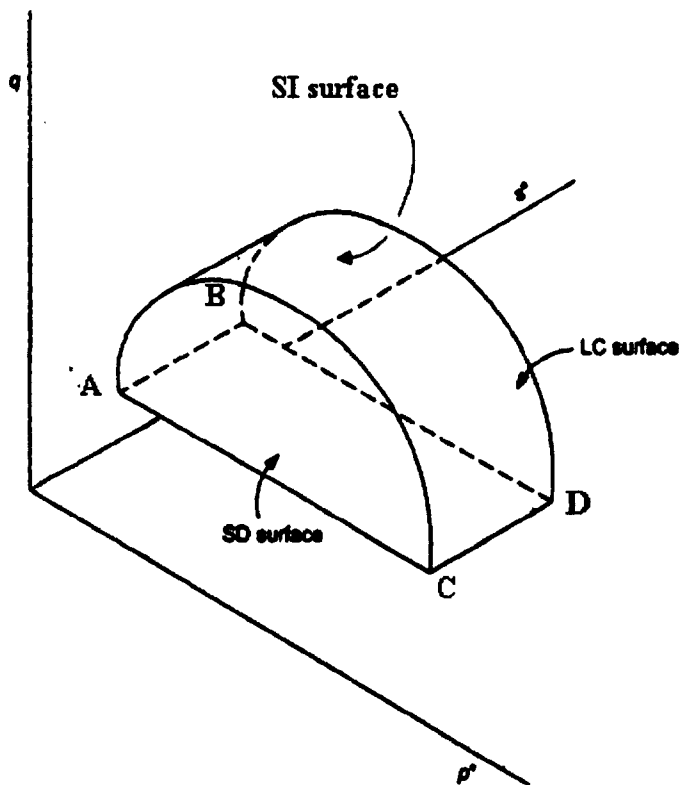
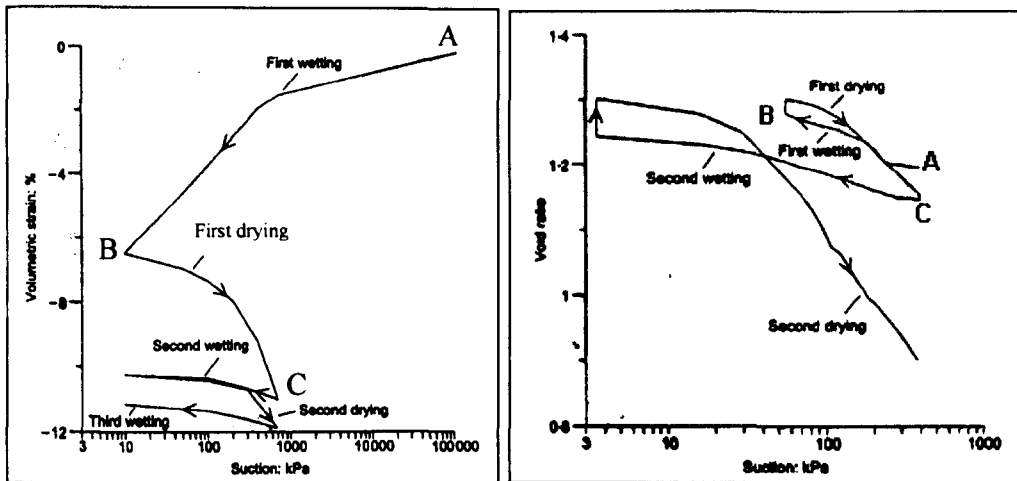


Figure 2.45 Elasto-plastic framework proposed by Wheeler *et al.* (2003).



(a) Alonso *et al.* (1995).

(b) Sharma (1998).

Figure 2.46 Volume reductions under wetting and drying stress paths.

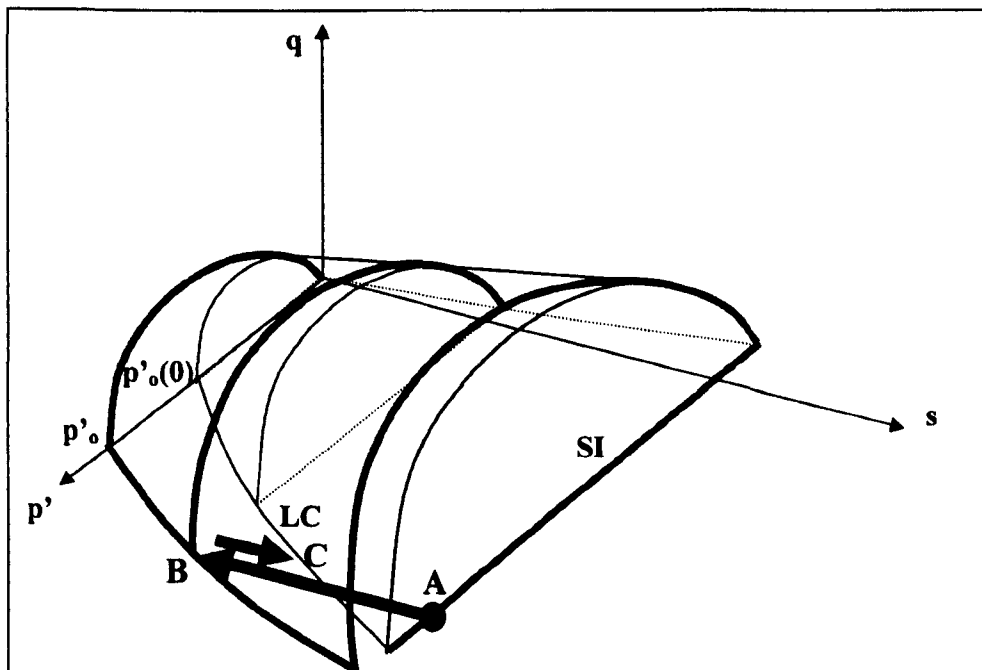


Figure 2.47 Superimposition of the wetting path followed by the drying path onto the elasto-plastic framework of Alonso *et al.* (1990) as reported by Alonso *et al.* (1995) in Figure 2.45(a).

## Chapter 3

### Proposed Shear Strength Model and Hypothetical Shear Strength-Volume Change Framework

The literature review in Chapter 2 revealed that there is a need for a comprehensive and a good representative shear strength model for unsaturated soils. Special attention is required to map the non-linear shear strength behaviour at low confining pressures and low suctions. Furthermore there is also the need for an alternative volume change framework for unsaturated soils that can model the volume change behaviour due to the increase in the vertical stress and inundation. This chapter starts by describing the application of Mohr stress diagram in the  $\tau : (\sigma - u_a) : (u_a - u_w)$  space according to Fredlund *et al.* (1978) which is referred as extended Mohr-Coulomb space in this thesis. It then presents the development of a proposed semi-empirical soil shear strength model based on the two independent stress state variables; net stress and suction. This is followed by the proposition and subsequently testing the model performance by comparing the analytical prediction with the reported behaviour. Then the chapter discusses the development of a proposed hypothetical shear strength-volume change framework that is based on shear stress and mobilized shear strength in characterising the volume change behaviour of coarse-grained unsaturated soils. The framework anticipates the existence of a unique relationship between effective mobilized minimum friction angle and the axial strain during the soil compression. Then a qualitative modelling of the loading, wetting and drying collapse is performed to test the applicability of the proposed hypothetical volume change framework. Finally the chapter describes how the framework can be used to predict the stress-strain curve from a triaxial test.

#### 3.1 Mohr Stress Diagram in Extended Mohr-Coulomb Space.

All proposed single-valued effective stress equations for unsaturated soil have incorporated a soil parameter (e.g. the work of Croney *et al.* (1958), Bishop (1959), Aitchison (1961), Bishop and Donald (1961), Jennings (1961), Bishop and Blight (1963), Burland (1965), Richard (1966), and Aitchison (1965, 1973)) like  $\chi$  in Bishop's (1959) effective stress equation to form an effective stress variable. They therefore have the constitutive behaviour in the stress variable. Normally, soil equilibrium considerations through stress state variables are linked to deformations

through constitutive behaviour and do not introduce constitutive behaviour directly into the stress variable (Morgenstern, 1979).

However, this may be inevitable since the effective stress equation based on net stress and suction is actually a constitutive equation itself. This is indicated by the non-linear behaviour of shear strength with respect to suction as discussed in Section 2.3.6, which is implying non-linear behaviour of effective stress with respect to suction. That is why in the latest development, researchers are trying to incorporate degree of saturation in the effective stress equation like the work of Wheeler *et al.* (2003) and Gallipoli *et al.* (2003) as discussed in Section 2.5.3. This is because it seems that the soil and water contact area is playing a key role in influencing the effective stress and the shear strength behaviour with respect to suction. It is also the likely factor that explains why shear strength does not increase indefinitely with suction.

The difficulty in finding a single value effective stress equation for unsaturated soils has made researchers resort to the use of the two independent stress state variables, net stress ( $\sigma - u_a$ ) and suction ( $u_a - u_w$ ) in assessing the shear strength and volume change behaviour of unsaturated soils. These stress state variables have then used to formulate constitutive equations for shear strength and volume change behaviour of unsaturated soils. The main advantage of assessing the mechanical behaviour of soils based on the two independent stress state variables is the availability of massive amount of data of this form in the literature. Furthermore this type of approach is able to avoid the incorporation of soil properties in the stress state.

In the extended Mohr-Coulomb space of  $\tau : (\sigma - u_a) : (u_a - u_w)$ , introduced by Fredlund *et al.* (1978), the influence of the two independent stress state variables on shear strength are considered separately through the net stress and suction axes. The same concept of Mohr stress diagram in the 3-D extended Mohr-Coulomb space will be applied in this thesis for the interpretation of the shear strength and volume change behaviour with respect to net stress and suction.

Consider an infinitely small element of soil within a soil mass subjected to triaxial stress state as shown in Figure 3.1(a). The element is subjected to major and minor principal net stresses (i.e.  $(\sigma_1 - u_a)$  and  $(\sigma_3 - u_a)$ ) in the vertical and the horizontal directions respectively. The suction,  $(u_a - u_w)$ , is considered as an isotropic tensor and thus it acts equally in all direction (Fredlund and Rahardjo, 1993). Let the net normal stress and shear stress on an inclined plane AC at an angle  $\alpha$  from the major principal plane AB be  $(\sigma_\alpha - u_a)$  and  $\tau_\alpha$  respectively. The expressions for the net normal stress and shear stress on the inclined plane are as in Equations 3.1 and 3.2.

$$(\sigma_\alpha - u_a) = \left( \frac{\sigma_1 + \sigma_3}{2} - u_a \right) + \left( \frac{\sigma_1 - \sigma_3}{2} \right) \cos 2\alpha \quad \text{Equation 3.1}$$

$$\tau_\alpha = \left( \frac{\sigma_1 - \sigma_3}{2} \right) \sin 2\alpha \quad \text{Equation 3.2}$$

When Equations 3.1 and 3.2 are squared and added, the resulting equation becomes the equation of a circle (Equation 3.3) which is known as the Mohr stress circle (Fredlund and Rahardjo, 1993).

$$\left[ (\sigma_\alpha - u_a) - \left( \frac{\sigma_1 + \sigma_3}{2} - u_a \right) \right]^2 + \tau_\alpha^2 = \left( \frac{\sigma_1 - \sigma_3}{2} \right)^2 \quad \text{Equation 3.3}$$

The Mohr stress circle forms a graphical method of presenting the state of net normal stress and shear stress at a point in a soil mass provided the inclination of the point from the principal planes is known. The Mohr stress circle is drawn on a plane with the net normal stress,  $(\sigma - u_a)$ , as the abscissa and the shear stress,  $\tau$ , as the ordinate.

The centre of the circle has the coordinate  $\left[ \left( \frac{\sigma_1 + \sigma_3}{2} - u_a \right), 0 \right]$  and the radius is  $\left( \frac{\sigma_1 - \sigma_3}{2} \right)$ .

The stress condition on a plane at an angle  $\alpha$  from major principal plane AB on the soil element as shown in Figure 3.1(a) is represented by the point Z at double the angle (i.e.  $2\alpha$ ) in the Mohr stress circle through the same course of rotation from the referred major principal plane OY as shown in Figure 3.1(c). The coordinate of the resultant point Z on the Mohr stress circle represents the stress state along the inclined

plane in the element. For unsaturated soils, the Mohr stress diagram uses a third orthogonal axis to represent suction since it must be included in the description of the stress state. The position of the circle along the suction axis is determined by the magnitude of the suction.

The corresponding extended Mohr diagram for the triaxial stress state shown in Figure 3.1(a) is presented at position 1 in Figure 3.1(c). In this case the plane of the Mohr circle is located at distance  $(u_a - u_w)_1$  from the net stress axis. When the condition becomes saturated and the suction becomes zero, while the net principal stresses remain constant like the triaxial stress state represented in Figure 3.1(b), the Mohr circle is shifted to position 2 in Figure 3.1(c), which sits exactly on the net stress axis. This is the way that the change in the stress state due to the change in suction is presented in the extended Mohr-Coulomb space. The Mohr stress circles from triaxial tests on unsaturated specimens at different suctions are plotted in this manner to obtain the curved-surface extended Mohr Coulomb shear strength envelope.

### **3.2 Proposed Shear Strength Model.**

The first and the most important task before the shear strength-volume change framework can be formulated is to develop a shear strength model based on the reported shear strength behaviour reviewed in Chapter 2. This is because it reflects the shape of the mobilized shear strength envelope which governs the soil deformation. The mobilized shear strength acts as the principal deformation resisting factor. The shear strength behavioural characteristics with respect to suction and net stress revealed in the literature review are summarised and from here the anticipated physical form of the model is deduced. The next step is to develop constitutive equations for the model that can closely map the anticipated physical shape. Then the analytical predictions of the model with respect to net stress and suction are tested independently. A fuller model prediction is carried out in Chapter 6 using the combination of the saturated and unsaturated shear strength data of the test material reported in Chapter 5.

### 3.2.1 Model General Characteristics and Anticipated Form.

This section summarizes the shear strength characteristics with respect to suction and net stress as described in the literature review (Section 2.3.5 and 2.3.6). The anticipated overall characteristics are presented three dimensionally in  $\tau : (\sigma - u_a) : (u_a - u_w)$  space as shown in Figure 3.2.

The shear strength increases non-linearly from zero at saturation to a maximum value at residual suction and it gradually diminishes to zero at ultimate suction. This decrease of shear strength towards zero after the residual suction becomes more gradual as the effective stress increases. In other words the value of ultimate suction increases with effective stress.

Along the effective stress axis, shear strength increases non-linearly from zero at an effective stress of zero to the transition shear strength that corresponds to the transition effective stress. The transition effective stress is the effective stress at which the shear strength behaviour changes from non-linear to linear when the stress is exceeded.

Using these two distinct shear strength behaviours with respect to each stress state variable, the surface envelope can be divided into four zones as illustrated in Figure 3.2. The shear strength behaviour in the four zones is summarised in Table 3.1. A good analytical form is required to represent the shear strength behaviour in each zone.

### 3.2.2 Shear Strength Behaviour Relative to Suction.

Additional shear strength that arises due to the presence of suction is termed apparent shear strength or apparent cohesion. It is termed as apparent since this additional strength will vanish when the conditions become saturated or dry. The shear strength at a fully saturated or dry condition is the basic minimum shear strength of the soil. The literature review on this shear strength behaviour in Section 2.3.6 has shown that along the suction axis apparent shear strength increases non-linearly up to the residual

suction and then undergoes a gradual decrease non-linearly to zero at the corresponding ultimate suction under the respective net stress.

Based on the shear strength behaviour with respect to suction outlined in Section 2.3.6, the shape of the curve in this direction under a constant effective stress should have the following characteristics;

1. At zero suction the apparent cohesion,  $c_s$ , should be zero.
2. At residual suction,  $(u_a - u_w)_r$ , the apparent cohesion or the apparent shear strength should be at its maximum value,  $c_s^{\max}$ .
3. The differentiation of the shear strength equation with respect to suction must give the tangent value of angle,  $\phi^b$ , which represents the gradient of the curve.
4. The angle  $\phi^b$  should be at a maximum value when the suction equals zero. It need not necessarily be equal to  $\phi'$  at this point.
5. The angle  $\phi^b$  should be zero when the suction equals the residual suction to support characteristic no. 2.
6. The shear strength should drop steeply near saturation; therefore the angle  $\phi^b$  must increase sharply as suction approaches zero.
7. When the residual suction is exceeded, the apparent cohesion should decrease non-linearly from  $c_s^{\max}$  at residual suction until it becomes zero at the corresponding ultimate suction,  $(u_a - u_w)_u$ , in a much more gradual manner than when it was increasing.
8. The gradient of the curve (i.e.  $\tan\phi^b$ ) that represents the shear strength beyond residual suction must be zero at residual suction  $(u_a - u_w)_r$ . This is to achieve a smooth transition of the curves before and after residual suction.
9. The dimension of the right hand side of the proposed shear strength equation must be those of stress, e.g.  $\text{kN/m}^2$ .

For values of suction ranging from zero to residual suction, as represented by the curve OF in Figure 3.2, the proposed shear strength equation is as Equation 3.4. This equation must satisfy the listed shape characteristics numbered 1 to 9 above.

$$c_s = \frac{(u_a - u_w)}{(u_a - u_w)_r} \left[ 1 + \frac{(u_a - u_w)_r - (u_a - u_w)}{(u_a - u_w)_r} \right] c_s^{\max} \quad \text{Equation 3.4}$$

where  $(u_a - u_w)_r$  is residual suction, which is the suction that corresponds to the maximum apparent shear strength, i.e. a zero value of angle  $\phi^b$  and  $c_s^{\max}$  is the maximum apparent cohesion.

When the suction is zero, Equation 3.4 produces zero apparent cohesion,  $c_s$ , which satisfies characteristic no.1, and when the suction equals the residual suction, Equation 3.4 indicates that the apparent cohesion,  $c_s$  becomes  $c_s^{\max}$ , which satisfies the characteristic no.2.

Then, applying the characteristic no.3 by differentiating Equation 3.4 with respect to suction should gives the tangent value of angle  $\phi^b$ , i.e.  $\tan \phi^b$ , which is the expression for the gradient of the curved surface, as follows;

$$\tan \phi^b = -\frac{2c_s^{\max}}{(u_a - u_w)_r^2} (u_a - u_w) + \frac{2c_s^{\max}}{(u_a - u_w)_r} \quad \text{Equation 3.5}$$

When the suction is zero, Equation 3.5 becomes,

$$\tan \phi^b = \frac{2c_s^{\max}}{(u_a - u_w)_r} \quad \text{Equation 3.6}$$

Equation 3.6 gives the value of the maximum gradient that occurs at zero suction and this is true since  $\tan \phi^b$  cannot be any bigger than the value on the right hand side of the Equation 3.6 since  $c_s^{\max}$  is the maximum possible value of the apparent cohesion. Therefore this satisfies the required shape characteristics no.3 and 4. When the suction equals the residual suction, Equation 3.5 gives a zero value of  $\tan \phi^b$ , which means that the tangent line has become horizontal indicating that the apparent shear strength is at its maximum value. This fulfils requirement no.5. Furthermore, the equation for the variation of the tangent to the curved surface, as given by Equation 3.5, is giving a non-linear increase as suction approaches zero and reaches the maximum value at suction equals zero as given by Equation 3.6. This satisfies the shape requirement no.6.

Above the residual suction up to the ultimate suction the shear strength criteria with respect to suction are as characteristics no. 7 and 8. This is represented by the curve FG in Figure 3.2 and the proposed equation for the apparent shear strength,  $c_s$  is as Equation 3.7,

$$c_s = c_s^{\max} \left[ \frac{(u_a - u_w)_u - (u_a - u_w)}{(u_a - u_w)_u - (u_a - u_w)_r} \right] \times \left[ 1 - \frac{(u_a - u_w)_r - (u_a - u_w)}{(u_a - u_w)_u - (u_a - u_w)_r} \right]$$

..... Equation 3.7

where  $(u_a - u_w)_u$  is the ultimate suction. The apparent shear strength totally vanishes for suction values greater than this, similar to the saturated condition. This is also equivalent to a completely dry condition.

When the suction equals the residual suction the apparent shear strength should be  $c_s^{\max}$  and this is achieved if the suction,  $(u_a - u_w)$  equals the residual suction,  $(u_a - u_w)_r$  in Equation 3.7, thus satisfying criterion no. 7.

For simplification let  $s = (u_a - u_w)$ ,  $s_{ult} = (u_a - u_w)_u$  and  $s_r = (u_a - u_w)_r$ .

Then Equation 3.7 is reduced to Equation 3.8.

$$c_s = c_s^{\max} \left[ \frac{s_{ult} - s}{s_{ult} - s_r} \right] \times \left[ 1 - \frac{s_r - s}{s_{ult} - s_r} \right]$$

..... Equation 3.8

Breaking up the square brackets Equation 3.8 become Equation 3.9,

$$c_s = \frac{c_s^{\max}}{s_{ult} - s_r} s_{ult} - \frac{c_s^{\max}}{s_{ult} - s_r} s - \frac{c_s^{\max}}{(s_{ult} - s_r)^2} [s_{ult} \times s_r - s_{ult} \times s - s \times s_r - s^2]$$

..... Equation 3.9

Differentiating Equation 3.9 with respect to suction,  $s$ ;

$$\frac{dc_s}{ds} = -\frac{c_s^{\max}}{s_{ult} - s_r} + \frac{c_s^{\max}}{(s_{ult} - s_r)^2} \cdot s_{ult} + \frac{c_s^{\max}}{(s_{ult} - s_r)^2} \cdot s_r - \frac{c_s^{\max}}{(s_{ult} - s_r)^2} \cdot 2s$$

..... Equation 3.10

Another requirement for the proposed Equation 3.7 to be valid is that,

$$\frac{dc_s}{ds} = 0 \text{ when } s = s_r \text{ or } \tan \phi^b = \left( \frac{dc_s}{ds} \right)_{s=s_r} = 0$$

This is checked by substituting,  $s = s_r$  into Equation 3.10, which gives  $\tan \phi^b$  or  $\frac{dc_s}{ds}$  a zero value as follows.

$$\begin{aligned} \left(\frac{dc_s}{ds}\right)_{s=s_r} &= -\frac{c_s^{\max}}{s_{ult} - s_r} + \frac{c_s^{\max}}{(s_{ult} - s_r)^2} \cdot s_{ult} + \frac{c_s^{\max}}{(s_{ult} - s_r)^2} \cdot s_r - 2 \frac{c_s^{\max}}{(s_{ult} - s_r)^2} \cdot s_r \\ \Rightarrow \left(\frac{dc_s}{ds}\right)_{s=s_r} &= -\frac{c_s^{\max}}{s_{ult} - s_r} + \frac{c_s^{\max}}{(s_{ult} - s_r)^2} \cdot s_{ult} - \frac{c_s^{\max}}{(s_{ult} - s_r)^2} \cdot s_r \\ \Rightarrow \left(\frac{dc_s}{ds}\right)_{s=s_r} &= -\frac{c_s^{\max}}{s_{ult} - s_r} + \frac{c_s^{\max}}{(s_{ult} - s_r)^2} \cdot (s_{ult} - s_r) \\ \Rightarrow \left(\frac{dc_s}{ds}\right)_{s=s_r} &= -\frac{c_s^{\max}}{s_{ult} - s_r} + \frac{c_s^{\max}}{s_{ult} - s_r} \\ \Rightarrow \left(\frac{dc_s}{ds}\right)_{s=s_r} &= 0 \qquad \dots\dots\dots \text{Equation 3.11} \end{aligned}$$

Therefore this satisfies criterion no.8. Finally the dimension of the right hand side of Equation 3.4 takes the dimension of  $c_s^{\max}$ , which is  $\text{kN/m}^2$ , and this is identical to the dimension for apparent shear strength,  $c_s$ , on the left hand side of the equation. Thus Equation 3.7 can be accepted as the equation for shear strength with respect to suction beyond the residual suction. The combination of Equations 3.4 and 3.7 comprehensively defines the shear strength behaviour along the suction axis.

It should be noted that Equation 3.7 assumes there is a gradual decrease in the apparent cohesion as the suction increases from residual suction as the soil dries up. This is a logical behaviour since the apparent cohesion must diminish towards zero, as is the case when the soil becomes totally dry. The experimental data from the literature (e.g. Escario and Juca, 1989 and Gan and Fredlund, 1996) is apparently indicating this type of behaviour at the lower confining pressures. However at higher confining pressures this effect is less obvious but the fading effect is still observable (e.g. Escario and Juca, 1989, Gan and Fredlund, 1996 and Toll *et al*, 2000). This implies that the ultimate suction must have been increasing with the confining pressure. Therefore there is a need to define the variation of ultimate suction with respect to net

confining stress. A linear variation is assumed and the proposed equation is as Equation 3.12.

$$(u_a - u_w)_u = \zeta(\sigma - u_a) + (u_a - u_w)_u^{\sigma'=0} \quad \text{Equation 3.12}$$

where

$\zeta$  is a constant which is the rate of change of ultimate suction with respect to net stress and

$(u_a - u_w)_u^{\sigma'=0}$  is the ultimate suction when net stress is zero.

### 3.2.3 Shear Strength Behaviour Relative to Effective Stress at Saturation.

The shear strength under saturated conditions is the soil minimum shear strength due to the absence of the water meniscus that provides suction forces and gives the extra apparent shear strength to the soil. Section 2.3.5 reviews the shear strength behaviour of coarse-grained soils with respect to effective stress under saturated conditions. Special attention is given to the behaviour at low stress levels in order to try to understand the modes of wetting collapse. The reviewed shear strength behaviour is summarized below. Along the effective stress axis, the shape of the curve OAB sketched in Figure 3.2 would have the following characteristics;

1. At zero net or effective stress the shear strength,  $\tau$ , should be zero.
2. The shear strength under saturated conditions should increase non-linearly from point O up to the transition effective stress,  $(\sigma - u_w)_t$ , represented by point A in Figure 3.2. Beyond point A it increases linearly as represented by the line AB.
3. The shear strength under saturated conditions that corresponds to the transition effective stress,  $(\sigma - u_w)_t$ , is named the transition shear strength,  $\tau_t$ .
4. The gradient of the curve (i.e.  $\tan \phi'$ ) at the transition effective stress,  $(\sigma - u_w)_t$ , which is at point A must equal to the gradient of the linear section AB (i.e.  $\tan \phi'_{\min}$ ) in order to achieve a smooth transition.

The saturated shear strength behaviour along the effective stress axis according to the above criteria is represented by Equations 3.13 and 3.14 for the curved line, OA, and the linear segment, AB, in Figure 3.2 respectively. Equation 3.15 gives the value of N in Equation 3.13.

$$\tau_{sat_f} = \frac{(\sigma - u_w)}{(\sigma - u_w)_t} \left[ 1 + \frac{(\sigma - u_w)_t - (\sigma - u_w)}{N(\sigma - u_w)_t} \right] \tau_t \quad \text{Equation 3.13}$$

$$\tau_{sat_f} = (\sigma - u_w) \tan \phi'_{min_f} + [\tau_t - (\sigma - u_w)_t \tan \phi'_{min_f}] \quad \text{Equation 3.14}$$

$$N = \frac{1}{1 - \left[ (\sigma - u_w)_t \frac{\tan \phi'_{min_f}}{\tau_t} \right]}, \quad \text{Equation 3.15}$$

where  $(\sigma - u_w)_t$  is the transition effective stress beyond which the shear strength is assumed to behave linearly,  $\tau_t$  is the transition shear strength that corresponds to transition effective stress,  $\tan \phi'_{min_f}$  is the gradient of the straight section of the graph, and N is a constant.

When the effective stress equals zero the shear strength given by Equation 3.13 becomes zero. This therefore satisfies criterion no.1. When the effective stress equals the transition effective stress the shear strength,  $\tau_{sat_f}$ , in Equation 3.13 and 3.14 is equal to the transition shear strength,  $\tau_t$ . This satisfies criterion no.3. Thus the linear and the non-linear segments of the graph will meet at point A with coordinates  $[(\sigma - u_w)_t, \tau_t]$  as shown in Figure 3.2. Therefore the combination of both Equations 3.13 and 3.14 is fulfilling criterion no. 2.

However, in order for Equation 3.13 to be valid at the transition effective stress,  $(\sigma - u_w)_t$ , its gradient must be equal to the gradient of the linear segment (i.e.  $\tan \phi'_{min}$ ). Expanding Equation 3.13 produces Equation 3.16;

$$\tau_{sat_f} = \frac{(\sigma - u_w)}{(\sigma - u_w)_t} \tau_t + \frac{(\sigma - u_w)}{N(\sigma - u_w)_t} \tau_t - \frac{(\sigma - u_w)^2}{N(\sigma - u_w)_t^2} \tau_t \quad \text{Equation 3.16}$$

Differentiating Equation 3.16 with respect to effective stress produces;

$$\frac{d\tau_{sat_f}}{d(\sigma - u_w)} = \frac{\tau_t}{(\sigma - u_w)_t} + \frac{\tau_t}{N(\sigma - u_w)_t} - \frac{2(\sigma - u_w)\tau_t}{N(\sigma - u_w)_t^2} \quad \text{Equation 3.17}$$

Note that  $\frac{d\tau_{sat_f}}{d(\sigma - u_w)} = \tan \phi'$  in the case of the curved segment, OA, in Figure 3.2.

The value of  $\phi'$  is a maximum at the origin when the net stress is zero.

When  $(\sigma - u_w) = (\sigma - u_w)_i$ ;  $\frac{d\tau_{sat_f}}{d(\sigma - u_w)}$  becomes;

$$\begin{aligned} \left[ \frac{d\tau_{sat_f}}{d(\sigma - u_w)} \right]_{(\sigma - u_w)_i} &= \frac{\tau_i}{(\sigma - u_w)_i} + \frac{\tau_i}{N(\sigma - u_w)_i} - \frac{2\tau_i}{N(\sigma - u_w)_i} \\ \Rightarrow \left[ \frac{d\tau_{sat_f}}{d(\sigma - u_w)} \right]_{(\sigma - u_w)_i} &= \frac{\tau_i}{(\sigma - u_w)_i} - \frac{\tau_i}{N(\sigma - u_w)_i} \end{aligned} \quad \text{Equation 3.18}$$

Substituting the expression for N, gives

$$\begin{aligned} \left[ \frac{d\tau_{sat_f}}{d(\sigma - u_w)} \right]_{(\sigma - u_w)_i} &= \frac{\tau_i}{(\sigma - u_w)_i} - \frac{\tau_i \left[ 1 - (\sigma - u_w)_i \frac{\tan \phi'_{min_f}}{\tau_i} \right]}{(\sigma - u_w)_i} \\ \Rightarrow \left[ \frac{d\tau_{sat_f}}{d(\sigma - u_w)} \right]_{(\sigma - u_w)_i} &= \frac{\tau_i}{(\sigma - u_w)_i} - \left[ \frac{\tau_i}{(\sigma - u_w)_i} - \tan \phi'_{min_f} \right] = \tan \phi'_{min_f} \end{aligned}$$

Equation 3.19

Therefore the gradient of the curve, OA, formed by Equation 3.13 equals  $\tan \phi'_{min_f}$ , when the effective stress equals the transition effective stress,  $(\sigma - u_w)_i$ . This satisfies criterion no. 4. Thence under saturated conditions there will be a smooth transition between the curve and the linear segments of the shear strength behaviour relative to the net stress or effective stress.

### 3.2.4 Shear Strength Equations to Represent the Surface Envelope.

The shear strength behaviour with respect to suction, defined by Equations 3.4 and 3.7, and with respect to effective stress in fully saturated conditions, defined by Equations 3.13 and 3.14, is represented by the lines indicated on the shear surface envelope shown in Figure 3.2. Note that the shear strength at saturation is the minimum shear strength. The presence of suction due to being unsaturated provides extra shear strength. Since this shear strength diminishes as suction decreases it is then referred to as apparent shear strength,  $c_s$ . Therefore the total shear strength at any point on the surface envelope under a specific net stress and suction is obtained by adding the shear strength under saturated condition,  $\tau_{sat_f}$  and the apparent shear strengths,  $c_s$ .

The shear surface envelope shown in Figure 3.2 consists of four distinct zones. The zones are divided at suction equals residual suction and net stress equals transition net stress. These are the points where the shear strength changes in behaviour with respect to the respective stress state variables. The shear strength equation to represent each zone is formed from the sum of the equations representing saturated and unsaturated conditions that represent the respective area. However the term effective stress,  $(\sigma - u_w)$ , in Equation 3.13 and 3.14 has to be changed to net normal stress,  $(\sigma - u_a)$ , in order to form a general representation of the model. But the term  $(\sigma - u_w)_i$  has to be maintained since it is a constant. In this manner, the shear strength equations representing Zone 1, 2, 3 and 4 are derived as Equation 3.20, 3.21, 3.22 and 3.23 respectively.

$$\tau_f = \frac{(\sigma - u_a)}{(\sigma - u_w)_i} \left[ 1 + \frac{(\sigma - u_w)_i - (\sigma - u_a)}{N(\sigma - u_w)_i} \right] \tau_i + \frac{(u_a - u_w)}{(u_a - u_w)_r} \left[ 1 + \frac{(u_a - u_w)_r - (u_a - u_w)}{(u_a - u_w)_r} \right] c_s^{\max}$$

.....Equation 3.20

Valid for Zone 1 where suction  $0 \geq (u_a - u_w) \leq (u_a - u_w)_r$  and net stress  $0 \geq (\sigma - u_a) \leq (\sigma - u_w)_i$ .

$$\tau_f = \frac{(\sigma - u_a)}{(\sigma - u_w)_i} \left[ 1 + \frac{(\sigma - u_w)_i - (\sigma - u_a)}{N(\sigma - u_w)_i} \right] \tau_i + c_s^{\max} \left[ \frac{(u_a - u_w)_u - (u_a - u_w)}{(u_a - u_w)_u - (u_a - u_w)_r} \right] \times \left[ 1 - \frac{(u_a - u_w)_r - (u_a - u_w)}{(u_a - u_w)_u - (u_a - u_w)_r} \right]$$

.....Equation 3.21

Valid for Zone 2 where suction  $(u_a - u_w)_r \geq (u_a - u_w) \leq (u_a - u_w)_u$  and net stress  $0 \geq (\sigma - u_a) \leq (\sigma - u_w)_i$ .

$$\tau_f = (\sigma - u_a) \tan \phi'_{\min} + [\tau_i - (\sigma - u_w)_i \tan \phi'_{\min}] + \frac{(u_a - u_w)}{(u_a - u_w)_r} \left[ 1 + \frac{(u_a - u_w)_r - (u_a - u_w)}{(u_a - u_w)_r} \right] c_s^{\max}$$

.....Equation 3.22

Valid for Zone 3 where suction  $0 \geq (u_a - u_w) \leq (u_a - u_w)_r$  and net stress  $(\sigma - u_a) \geq (\sigma - u_w)_i$ .

$$\tau_f = (\sigma - u_a) \tan \phi'_{\min} + [\tau_i - (\sigma - u_w)_i \tan \phi'_{\min}] + c_s^{\max} \left[ \frac{(u_a - u_w)_u - (u_a - u_w)}{(u_a - u_w)_u - (u_a - u_w)_r} \right] \times \left[ 1 - \frac{(u_a - u_w)_r - (u_a - u_w)}{(u_a - u_w)_u - (u_a - u_w)_r} \right]$$

.....Equation 3.23

Valid for Zone 4 where suction  $(u_a - u_w)_r \geq (u_a - u_w) \leq (u_a - u_w)_u$  and net stress  $(\sigma - u_a) \geq (\sigma - u_w)_t$ .

Therefore a total of six equations (i.e. 3.12, 3.15, 3.20, 3.21, 3.22 and 3.23) are required to completely define the extended Mohr-Coulomb shear surface envelope shown in Figure 3.2. The equations form a smooth transition of shear strength between the zones.

Consider the state of shear strength is such that the stress condition is initially in zone 2, where the shear strength is represented by Equation 3.21. When the suction decreases below the residual suction, while the net stress remains constant, Equation 3.20 becomes the relevant equation since the current stress condition is within zone 1. However, when the suction is further reduced until it becomes zero and the soil becomes saturated, the suction term vanishes and the shear strength equation reduces to only the first term of Equation 3.20. This is actually Equation 3.13, which is the shear strength equation for saturated conditions. Similarly, if the stress state is initially in zone 4 and there is a similar suction reduction, the shear strength equation changes from Equation 3.23 to Equation 3.22 and finally when the conditions become saturated the equation reverts to Equation 3.14, which is the shear strength equation for saturated conditions at effective stress greater the transition effective stress.

### 3.2.5 Determination of the Seven Soil Shear Strength Parameters.

There are seven soil parameters involved in defining the proposed shear strength model. Three parameters define the saturated shear strength behaviour with respect to effective stress and four parameters define the shear strength behaviour with respect to suction.

The transition shear strength,  $\tau_t$ , transition effective stress,  $(\sigma - u_w)_t$ , and the effective minimum friction angle at failure,  $\phi'_{min}$ , are the three parameters that can be determined by conducting triaxial compression tests at different effective stresses on saturated specimens. The more tests at different effective stresses the easier it is to define the curvilinear line of the shear strength envelope at saturation. Along the

curvilinear line the effective stress that corresponds to the point that the curve changes to a straight line is taken as the transition effective stress,  $(\sigma - u_w)_t$  and the corresponding shear stress is taken as the transition shear strength,  $\tau_t$ . The inclination of the linear section of the envelope to the horizontal is the effective minimum friction angle at failure,  $\phi'_{\min}$ .

The maximum apparent cohesion,  $c_s^{\max}$ , residual suction,  $(u_a - u_w)_r$ , ultimate suction at zero effective stress,  $(u_a - u_w)_u^{\sigma'=0}$ , and the rate of change of ultimate suction with respect to net stress,  $\zeta$ , are the four parameters that can be determined by conducting triaxial compression tests at different suctions on unsaturated specimens, and for each value of suction tests are carried out at different net stresses. The tests at different net stress with identical suction give the shear strength envelope corresponding to the suction under consideration. The intersection of the curvilinear line envelope with the plane  $\tau : (u_a - u_w)$  determines the apparent shear strength,  $c_s$ , for the considered suction. By having a series of curvilinear line envelopes at different suctions, the curve for the variation of the apparent shear strength with respect to suction at different net stresses can be mapped onto the  $\tau : (u_a - u_w)$  plane. The maximum apparent shear strength,  $c_s^{\max}$  is taken at the apex of the curve formed on the  $\tau : (u_a - u_w)$  plane and the corresponding suction is taken as the residual suction. In other words residual suction is the value of suction that produces the maximum apparent shear strength.

The ultimate suction at zero net stress and the rate of change of ultimate suction with respect to net stress are determined by drawing the variation of the apparent shear strength (as the ordinate) with respect to suction (as the abscissa) at different net stresses. The contribution of the shear strength at the saturated condition is excluded in this procedure. The graphs should be overlapping for suctions less than residual suction, and at suctions higher than residual suction the graphs cut the suction axis at different values of ultimate suction. The value of the ultimate suction corresponding to each net stress is noted. Then the points are plotted on to the graph of ultimate suction as the ordinate and net stress as the abscissa and the best straight line is drawn

through the points. The gradient of the straight line is taken as the rate of change of ultimate suction with respect to net stress,  $\zeta$ , and the point at which the line intersects the ordinate is taken as the ultimate suction at zero effective stress,  $(u_a - u_w)_u^{\sigma'=0}$ . This procedure will be applied in Chapter 6 for the interpretation of the proposed warped-surface shear strength envelope.

Alternatively, residual suction can be obtained by conducting pressure plate tests. The procedure for determining the residual suction from the soil-moisture characteristic curve is described in Section 2.2.

### **3.2.6 Procedure for Drawing the Shear Strength Contours of the Shear Strength Surface Envelope in $\tau - s$ Space.**

One way to present the 3-D shear strength surface envelope in two dimensional space is to draw the shear strength contour lines at different net stress in  $\tau : (u_a - u_w)$  space. When the space between the contours is large it indicates a steep drop in shear strength with respect to net stress and vice versa. The primary requirement for this exercise is to obtain the seven soil shear strength parameters according to the proposed semi-empirical shear strength model as described in Section 3.2.5. The six shear strength equations required to plot the contours are Equations 3.4, 3.7, 3.12, 3.13, 3.14 and 3.15.

The following is the step by step procedure for drawing the contour lines.

1. Select the values of net stress that correspond to the contour lines to be drawn e.g. 0, 50, 100, 150, 200 kPa. These values of net stress will become the values of effective stress when the conditions becomes saturated.
2. Determine the shear strength at saturation that corresponds to the selected values of net stresses in step 1 by using Equations 3.13, 3.14 and 3.15.
3. Select the values of suction to be plotted on each contour line e.g. 0, 20, 40, 60 kPa. Use Equations 3.4, 3.7 and 3.12 to determine the apparent shear strength at the selected suction values. Use Equation 3.12 to determine the ultimate suction in Equation 3.7. Note that the value of ultimate suction varies with net stress.

4. Calculate the total shear strength at the respective suctions and net confining stresses by summing their corresponding values of shear strength at failure under saturated conditions,  $\tau_{sat_f}$ , and the apparent shear strength,  $c_s$ , determined in steps 2 and 3 respectively.
5. In the  $\tau : (u_a - u_w)$  space, for each respective net stress considered, plot the total shear strength that corresponds to the selected suction. Repeat this step for the rest of the selected net stresses. In this way the whole contour lines for the selected net stresses can be drawn.

This procedure will be applied in the drawing of the shear strength contours for the test material in Chapter 6.

### **3.3 Analytical Prediction by the Proposed Shear Strength Equations.**

The prediction by the equations that define the shear strength envelope must be checked against experimental data.

The performance of Equations 3.20, 3.21, 3.22 and 3.23 is carried out by checking the performance of their component equations, which are Equations 3.4, 3.7, 3.13 and 3.14. In other words, this involves the independent prediction of the shear strength behaviour with respect to suction and net stress. This is because normally when research has been carried out on unsaturated shear strength behaviour the saturated shear strength behaviour has been omitted, and vice versa. Therefore a complete performance test on the equations will only be achieved when both saturated and unsaturated shear strength tests are carried out on the same test material. Therefore the validation work in this section does not cover Equation 3.12, but this will be covered in the complete validation in Section 6.3 using the results of triaxial tests on saturated and unsaturated specimens.

#### **3.3.1 Analytical Prediction of Shear Strength Behaviour with Respect to Suction.**

This involved the analytical prediction by Equations 3.4 and 3.7, which are for suctions less than, and exceeding, residual suction respectively. The shear strength behaviours with respect to suction reported by Gan and Fredlund (1996), Toll *et al.* (2000) and Escario and Juca (1989) were chosen for this performance test since their

experimental data extended up to suction values which were high enough for the respective soils to achieve a reduction in shear strength. The data points and the corresponding analytical prediction curves using the proposed equations are presented in Figure 3.3 and 3.4. The shear strength parameters used in the equations to obtain the analytical curves are tabulated in Table 3.2.

The equations produced an excellent match with the experimental data.

### **3.3.2 Analytical Prediction of Shear Strength Behaviour with respect to Effective Stress at Saturation.**

This involved the analytical prediction by Equation 3.13, which is applied for net stress less than transition net stress, and Equation 3.14, which is applied for net stress exceeding the transition net stress. In other words Equation 3.13 is valid for net stress between zero and the transition net stress where the shear strength behaviour is non-linear with respect to net stress, while Equation 3.14 is valid from the transition net stress and higher where the shear strength behaviour is taken as linear with respect to net stress. The prediction by these equations is compared to the experimental data reported by Charles and Watts (1980) for coarse material of 38mm maximum particle size. The re-plotted experimental data points and the corresponding analytical prediction curves are presented in Figure 3.5 and the shear strength parameters used are tabulated in Table 3.3.

These equations again produced an excellent match with the experimental data.

### **3.4 Proposed Hypothetical Shear Strength-Volume Change Framework for Coarse-grained Soils.**

This section discusses the development of a hypothetical volume change framework intended to explain the volume change behaviour of coarse-grained unsaturated soils in the event of inundation and load increase. Section 2.5.2 of the literature review has revealed that the application of an elastic-plastic critical state framework to explain the different modes of volume change behaviour in fine grained unsaturated soils has limitations. This is as noted by Wheeler (2003), since the framework cannot model the irreversible volume change during cycles of wetting and drying as reported by

Alonso *et al.* (1995) and Sharma (1998). The limitation faced by the critical state framework is suspect due to the inadequacy of the definition of failure by suction changes. The cause of failure based on the combined effect by the principal stresses and suction must be taken into consideration when formulating a volume change framework for coarse-grained soils. If the way that failure is defined in the critical state framework is the cause of the problem then there is a great chance that it also will not work for coarse-grained soils. Therefore an alternative approach is required. In the alternative approach the hypothetical volume change framework is developed from the standpoint of the soil stress-strain and volume change behaviour. The magnitude of the deviator stress in the stress-strain curve determines the major principal net stress while the net confining pressure determines the minor principal net stress and the axial strain is taken as the yield parameter. The yielding or the soil compression is considered from the combined effects of the principal stresses and suction through the concept of the Mohr stress diagram in the extended Mohr-Coulomb space, as discussed in Section 3.1. The Mohr stress diagram represents graphically the state of stress at any point in a soil mass by accounting for the combined effect of the principal stresses and suction. The soil compression which governs the volume change behaviour can be modelled based on the interaction of the state of stress and the state of the mobilized shear strength. Mobilized shear strength increases with mobilized friction angle according to Equation 2.7 as discussed in Sections 2.3.1 and 2.3.2. Thence the curvilinear shape of the mobilized shear strength envelope rotates about the suction axis towards the soil shear strength envelope at failure as soil structure is compressed. The uniqueness of this hypothetical framework is that the mobilized shear strength envelope is also acting as the yield locus since the axial strain along the locus is considered constant irrespective of the net confining stress (i.e. effective stress or the net stress) or the soil suction. Soil compression is triggered when the state of stress exceeds the mobilized shear strength, or in other words the when the state of stress exceeds the yield surface. Thus in order to verify the applicability of the proposed hypothetical volume change framework the data from the triaxial compression tests on both saturated and unsaturated specimens must indicate that the yield surface is representing identical axial strains.

Since the mobilized shear strength envelope is a curvilinear surface, as shown in Figure 3.6, similar to the soil shear strength envelope the axial strain needs to be correlated to a parameter which is a constant to the yield envelope. This has to be the effective mobilized minimum friction angle,  $\phi'_{\min_{mob}}$ , which is the inclination of the linear section of the envelope to the horizontal (refer Figure 3.6). The changing of the effective mobilized minimum friction angle during soil compression is correlated to the axial strain and a unique relationship is sought. If this unique relationship exists at saturation and at different values of suction this would mean that the rotation of the yield surface envelope about the suction axis is like a rigid surface which retains its shape when identical soils at different suctions are compressed. Besides, the unique relationship that indicates the increase in the axial strain relative to the increase in the effective mobilized minimum friction angle would also imply greater rotation of the yield surface envelope is corresponding to a greater volume change. This is significant because the greater rotation of the yield envelope obtained during the simulation of wetting collapse when suction approaches zero (refer Section 3.4.5) would correspond to the massive volume change.

#### 3.4.1 Framework General Characteristics.

The literature review of volume change behaviour in fine and coarse-grained unsaturated soils, as presented in Section 2.5, has revealed the general characteristics of the volume change behaviour for coarse-grained soils. The proposed hypothetical shear strength-volume change framework needs to have all of these characteristics for it to be acceptable. The characteristics of the volume change behaviour of coarse-grained unsaturated soils are summarized as follow.

1. First and foremost, the soil compression is irrecoverable and therefore the simulation of the collapse compression by the hypothetical shear strength-volume change framework must be plastic in nature.
2. The changes in the applied stress are driving the stress state to the yield limit or the mobilized shear strength irrespective whether it is effective stress increase (loading collapse) or decrease (wetting collapse).
3. Collapse failure is not occurring at critical state since it occurs under stress changes. Besides, the collapse occurs due to the availability of the space for the particles to move into (Barden *et al.*, 1969) which causes the reduction in

the overall volume, and it is not straining under constant volume which is a characteristic of a critical state.

4. The framework involves a multiple yield surface since under a specific constant loading condition the soil compression ceases at one point, and changing the loading condition produces further compression which also ceases at another point (Rahardjo and Fredlund, 2003). It is suspected that the soil compression ceases when stress equilibrium is achieved between the state of stress in the soil and the mobilized shear strength.
5. Therefore the soil compression mechanism must be derived from the concept of stress equilibrium between the state of stress in the soil and the mobilized shear strength.
6. Soil compression due to inundation must exhibit massive volume decrease near saturation, and the compression stops when 100% saturation is achieved (Tadepalli *et al.* 1992).
7. Soil compression in a coarse-grained soil is immediate and the compression in fine grained soil is a slow process before stress equilibrium is reached due to the slow rate of dissipation of pore air and pore water pressure. In fine grained soils this process is termed as consolidation.
8. Collapse can occur under drying or suction increase conditions.

#### **3.4.2 Framework Principle Concept.**

Investigating the changes on the shear strength parameters when the soil structure is compressed has essentially revealed an increase in the mobilized friction angle,  $\phi'_{mob}$ , as discussed in Section 2.3.2. This is indicated through the rotation of the mobilized shear strength envelope in the extended Mohr-Coulomb space about the suction axis. Consider the compression of three triaxial test specimens subjected to three different effective stresses. They would exhibit three different magnitudes of peak stress at identical axial strain provided there is no particle breakage in the specimens. This is based on the reports that particle breakage delays the arrival of peak strength until higher axial strains (Bishop, 1966, 1972; Billam 1972). Reaching peak strengths at the same axial strain implies that the specimens have undergone the same volume change before achieving the peak strength irrespective of the applied effective stresses.

Therefore the shear strength surface envelope is representing identical axial strains experienced by the specimens even under different effective stresses provided there is no particle breakage. Similarly, it is anticipated that the mobilized shear strength envelope or the yield surface at a certain stage of the compression is representing the same axial strain. In other words the same rotation angle of the mobilized shear strength envelope is anticipated to cause the same axial strain irrespective of the magnitude of the effective stress. This holds as long as it is assumed that at low stress levels that particle breakage does not occur. Due to the rotation of the mobilized shear strength envelope, or the yield surface envelope, when the soil is compressed, the proposed hypothetical shear strength-volume change framework is called the “Rotational Multiple Yield Surface Framework”. High stress levels would cause particle breakage and would cause a variable axial strain along the mobilized shear strength envelope and therefore could not be regarded as the yield surface. This limits the application of the framework.

In the field with a horizontal ground surface, as horizontal stress increases with vertical stress the soil must still develop inclined planes of maximum shear stress. Thus it is anticipated that soil deformation is due to the combined action of shear and normal stress on the inclined planes. Initially, in a loose state the soil particles have room to adjust themselves in the direction of shear as they are being displaced vertically downwards. However, when they reach a tightly packed arrangement they have less freedom of movement and are said to be in the state of interlocking. At this stage increase in the vertical stress can only move the particles vertically downwards since lateral displacement has been restrained by the surrounding soil (Powrie, 1997). Therefore soil deformation is assumed to be vertically one-dimensional. This mode of deformation is approximately appropriate for soil subjected to vertical loads like pad, strip and raft foundations. This means that the action of shear and normal stress is the driving factor that governs the field soil compression and graphically it can be represented by the Mohr stress diagram. The mobilized shear strength,  $\tau_{mob}$ , is resisting the deformation and graphically it can be represented by the mobilized shear strength envelope. The deformation ceases when the mobilized shear strength equals or exceeds the stress state in the soil mass. Therefore soil deformation needs to be

assessed from the standpoint of shear stress, normal stress, suction and the mobilized shear strength in the soil.

Triaxial testing is the common laboratory method for evaluating the fundamental strength and deformation properties of soil based on the stress-strain behaviour. A close investigation of the stress-strain curve indicates that at one point on approaching the peak strength the soil starts to undergo a significant compression which corresponds to a small increase in the deviator stress. This is the point where the soil starts to undergo dilation and this point can be recognised as the point where the stress-strain curve starts to divert from a linear or an almost linear behaviour. However in contrast to this stress-strain curve, in the field, the soil is suppressed from dilating by the vertical net stress as well as being constrained laterally by the surrounding soil. The utmost volumetric state that the soil can achieve in the field is a full interlocking state which corresponds to the point on the stress-stress curve that the soil starts to dilate. Further compression beyond this point in the field (i.e. 1-D compression) is attributed to particle breakage. Nonetheless the peak strength is still attained in the field but not through dilation as in the triaxial specimen. It is achieved by particles squeezing between each other as they try to deform under the resultant net normal and shear stresses along the plane of maximum shear under the interlocking condition. Thence the stress-strain behaviour that range up to the peak strength only will be applied in the development of the shear strength-volume change framework. However, the corresponding maximum axial strain is taken as the abscissa of the intersection point between the extrapolated line from the linear section of the stress-strain curve and the horizontal line that passes through the peak deviator stress.

The maximum shear and normal stresses acting on an inclined shear plane are derived from the combination of major principal net stress,  $(\sigma_1 - u_a)$ , minor principal net stress,  $(\sigma_3 - u_a)$ , and suction,  $(u_a - u_w)$  as discussed in Section 3.1. The mobilized shear strength,  $\tau_{mob}$ , depends on the maximum attained net normal stress and the maximum achieved effective mobilized friction angle,  $\phi'_{mob}$ , or the maximum value of the effective mobilized minimum friction angle,  $\phi'_{min\,mob}$ , achieved as illustrated in Figure 3.6.

During inundation, the normal stress,  $\sigma_n$ , and the shear stress,  $\tau_D$ , along a shear plane remain constant even though there is a reduction in suction. This is because the principal net stresses (i.e.  $(\sigma_1 - u_a)$  and  $(\sigma_3 - u_a)$ ) which determine the circle diameter remain constant as the Mohr circle retreats towards the net stress axis. However the maximum mobilised shear strength,  $\tau_{mob}$ , defined by the mobilised shear strength envelope is still constant. Nonetheless the maximum mobilised shear strength at a specific suction decreases with suction according to the envelope. Thence at one point the soil state of stress as defined by the effective stress Mohr circle will touch the mobilised shear strength envelope. At this point the soil compression will be triggered. During compression the effective stress Mohr circle is growing in diameter and always at the point of touching the mobilised shear strength envelope which rotates with it. The point where the effective Mohr circle stop enlarging which is when the dissipation of the pore water pressure has ceased the circle is located slightly below the envelope. And at this point the settlement is completely stopped unless there is another change in the effective stress condition. Since soil compression is an irrecoverable volume change therefore it must be taking place after the yield point in the stress-strain curve. As the mobilized friction angle,  $\phi'_{mob}$ , increases with soil compression when the soil particles move to a denser arrangement then mobilized shear strength,  $\tau_{mob}$ , also increases with the collapse.

If the deviator stress is released at one stage of the shearing, like at point A in Figure 2.4(a), the mobilized friction angle stays constant even though the shear stress may decrease thereafter. Simultaneously, the mobilized shear strength decreases as the net normal stress on the inclined shear plane decreases. As the deviator stress is released the soil will recover part of the total strain that is elastic while the plastic strain is irrecoverable as discussed in Section 2.3.1. Upon the reapplication of the deviator stress the soil will undergo elastic compression until the mobilized shear strength is exceeded. From this point onwards the combination of plastic and elastic compression resumes until the peak strength is reached like at point P in Figure 2.4(a).

### 3.4.3 Framework Structure.

When a soil undergoes compression, its mobilized shear strength increases from zero up to the soil shear strength at failure, which corresponds to the peak deviator stress in the triaxial compression test on a dense specimen. The increase in the mobilized shear strength is marked by the increase in the effective mobilized friction angle,  $\phi'_{mob}$ , during the application of the deviator stress. Since the soil yield envelope is a curvilinear surface envelope as shown in Figure 3.6, soil yielding cannot be correlated to the mobilized friction angle,  $\phi'_{mob}$ , because it varies with effective stress unless the yield envelope is a plane surface. Referring to Figure 3.6, effective stress for Mohr stress circle 2 is higher than for Mohr stress circle 1. Therefore for consistency in the relationship the axial strain during soil compression needs to be correlated to the effective mobilized minimum friction angle,  $\phi'_{min\,mob}$ , associated to a yield surface envelope, which is shown in Figure 3.6, rather than the mobilized friction angle,  $\phi'_{mob}$ .

During a triaxial compression test on a saturated specimen the confining pressure,  $\sigma_3$ , which determines the minor principal effective stress,  $\sigma'_3 = \sigma_3 - u_w$  is maintained constant when the deviator stress is increased from  $q_{mob1}$  to  $q_{mob2}$  as shown in Figure 3.7. The Mohr stress circle grows from  $y1$  to  $y2$  and correspondingly the yield surface envelope is rotated from position 1 to position 2 as shown in Figure 3.8. The major principal effective stresses of the Mohr stress circles are given by Equations 3.24 and 3.25 respectively.

$$\sigma'_{1,y1} = \sigma_3 + q_{mob1} - u \quad \text{Equation 3.24}$$

$$\sigma'_{1,y2} = \sigma_3 + q_{mob2} - u \quad \text{Equation 3.25}$$

The change in the effective mobilized minimum friction angle,  $\Delta\phi'_{min\,mob}$ , is assumed to be equal to the change in the effective mobilized friction angle,  $\Delta\phi'_{mob}$ , as illustrated in Figure 3.8. Consider a line connecting the origin to any point on the surface envelope. By considering the envelope to rotate as a rigid body, then the change in the inclination of this line from the horizontal must equal to the change in the inclination of the linear section of the surface envelope from the horizontal. The referred point on

the surface envelope is taken as its intersection with the tangent line from origin to the Mohr circle. This intersection point is assumed to remain the same when the Mohr circle enlarged provided their  $\sigma_3'$  are the same.

$$\Delta\phi'_{mob} = \Delta\phi'_{min_{mob}} \quad \text{Equation 3.26}$$

The expression for the change in the effective mobilized minimum friction angle between the two yield surface envelopes is as Equation 3.27.

$$\phi'_{min_{mob,y_2}} = \phi'_{min_{mob,y_1}} + \Delta\phi'_{min_{mob}} \quad \text{Equation 3.27}$$

Substituting Equation 3.26 into Equation 3.27 gives;

$$\phi'_{min_{mob,y_2}} = \phi'_{min_{mob,y_1}} + \Delta\phi'_{mob} \quad \text{Equation 3.28}$$

Based on this concept, when the yield surface envelope is rotated to the soil shear strength surface envelope as shown in Figure 3.9, the corresponding deviator stresses are  $q_{mob1}$  and  $q_f$  respectively. The corresponding major principal effective stresses in Figure 3.9 are calculated as follows.

$$\sigma'_{1,y_1} = \sigma_3 + q_{mob1} - u \quad \text{Equation 3.29}$$

$$\sigma'_{1,f} = \sigma_3 + q_f - u \quad \text{Equation 3.30}$$

The effective mobilized minimum friction angle of the yield surface envelope,  $\phi'_{min_{mob}}$ , with reference to the effective mobilized minimum friction angle at failure,  $\phi'_{min_f}$ , (i.e. corresponding to the shear strength envelope) can be obtained as follows.

$$\phi'_{min_f} = \phi'_{min_{mob}} + \Delta\phi'_{min_{mob}} \quad \text{Equation 3.31}$$

$$\Delta\phi'_{min_{mob}} = (\phi'_{mob_f} - \phi'_{mob}) \quad \text{Equation 3.32}$$

$$\phi'_{min_f} = \phi'_{min_{mob}} + (\phi'_{mob_f} - \phi'_{mob}) \quad \text{Equation 3.33}$$

Rearranging,

$$\phi'_{min_{mob}} = \phi'_{min_f} - (\phi'_{mob_f} - \phi'_{mob}) \quad \text{Equation 3.34}$$

This increase in the effective mobilized minimum friction angle,  $\Delta\phi'_{min_{mob}}$ , with respect to axial strain as the soil structure is compressed is the basic principle used in the proposed shear strength-volume change framework. A unique relationship between the effective mobilized minimum friction angle,  $\phi'_{min_{mob}}$ , and axial strain is

expected for the hypothetical volume change framework to work. On the lower range of the effective mobilized friction angle,  $\phi'_{mob}$ , where the mobilized minimum friction angle,  $\phi'_{min_{mob}}$ , is small and at some point becomes negative the condition is omitted. This is because at this lower range the yield surface turns without taking the shape of the shear strength envelope at failure. It begins with a flat surface on the  $(\sigma - u_a) : (u_a - u_w)$  plane before the soil is compressed. As the surface turns from this point it starts to grow to the shape of the shear strength envelope at failure and only after a certain value of  $\phi'_{min_{mob}}$  the yield surface starts taking that shape. Therefore the small positive values and the negative values of the  $\phi'_{min_{mob}}$  obtained from Equation 3.34 are neglected. Regarding the latter the linear section of the yield envelope never has a negative inclination. The initial small positive values of  $\phi'_{min_{mob}}$  have to be neglected in order to achieve a smooth graph of  $\phi'_{min_{mob}} - \varepsilon_a$  that begins from the origin. Therefore the Equation 3.34 is only valid from a small positive value of  $\phi'_{min_{mob}}$  up to the  $\phi'_{min_f}$ .

The framework applies the concept of stress equilibrium between the imposed stress state represented by the Mohr stress circles and the mobilized shear strength represented by yield surface envelope. Soil compression or collapse failure is triggered when the Mohr circle touches or extends beyond the yield surface envelope indicating an imposed loading stress state that has exceeded the yield strength or the mobilized shear strength of the soil. Once this has happened, the yield surface envelope will rotate about the suction axis until it returns to a point that it is about to touch the Mohr circle. At this instance stress equilibrium is reinstated and the soil compression stops. As long as the change in stress state makes the Mohr circle move underneath the current yield envelope without touching or extending above it, no failure will be triggered. This is equivalent to the condition that the deviator stress changes below the point of maximum achieved deviator stress during unloading and reloading process discussed in Section 2.3.1 where there will be no plastic straining.

The collapse failure can be triggered by either the Mohr circle expanding (i.e. loading collapse), or moving laterally parallel to the suction axis towards a lower suction where there is a steep drop in the mobilized shear strength with respect to suction (i.e. wetting collapse), or moving towards a higher suction where the surface envelope is curving down gradually (i.e. drying collapse). The rate of rotation of the yield surface envelope or the rate of increase in the effective mobilized friction angle depends on the compression rate of the soil structure. This in turn depends on the rate of dissipation of pore water pressure in the case of a saturated soil and the dissipation of pore air and pore water pressure in the case of an unsaturated soil.

Consider the case of inundation in a coarse-grained soils where this is equivalent to the Mohr circle moving parallel to the suction axis towards a lower suction. The turning of the shear surface envelope about the suction axis is immediate whenever the Mohr circle touches or extends above the envelope. As the Mohr circle moves parallel to the suction axis towards the net stress axis in the case of wetting collapse the yield surface envelope rotates and when it is close to zero suction there is an abrupt greater turning of the yield envelope since the envelope bends steeply downward (further described in Section 3.4.7 and illustrated in Figure 3.11). If the turning angle of the yield envelope represents the volume change this would then correspond to the massive volume change near saturation. This is a sign of the potential to explain loading, wetting and drying collapse within the same framework. However this needs justification by the experimental data and if this is true then the framework is able to model all the three types of collapse failure including the massive volume reduction near saturation.

Generally the structure of the shear strength-volume change framework can be summarized as follows:

1. The framework is based on the stress-strain behaviour of the soils in the compression triaxial test.
2. The yield surface is taken as the mobilized shear strength envelope.
3. The yield surface represents the same axial strain irrespective of effective stress and suction.

4. Particle breakage is the limit for the application of the framework; therefore the framework is limited to relatively low stress levels.
5. The concept of a Mohr stress diagram in the extended Mohr-Coulomb space defining the soil state of stress at a point in the soil mass has already accounted for the combined effect of principal stresses and suction.
6. The state of soil current shear strength is taken as the mobilized shear strength envelope.
7. Soil compression or collapse failure is triggered whenever the state of stress in the soil is greater than the mobilized shear strength. Graphically this can be represented by the Mohr stress circle extending above the mobilized shear strength envelope.
8. When collapse failure is triggered the soil will be compressed and the mobilized friction angle increased and in turn the mobilized shear strength will increase. Graphically this is represented by the rotation of the yield surface envelope about suction axis until the envelope is at the point of engaging contact with the Mohr stress circle. At this point the soil is in a state of stress equilibrium and the compression of the soil has stopped.
9. Extension of the Mohr circle above the mobilized shear strength envelope can be brought about by either a Mohr stress circle enlargement which is referred to as loading collapse, or by the Mohr stress circle moving towards a lower suction, which is referred to as wetting collapse.
10. Loading collapse is driven by the increase in the vertical load which results in an increase in the major principal net stress, and wetting collapse is caused by inundation which decreases the suction in the soil.

#### **3.4.4 Qualitative Simulation of Loading Collapse.**

Consider the increase in vertical load which causes the soil to undergo one-dimensional compression. The changes in stress conditions are mapped in the extended Mohr-Coulomb space as shown in Figure 3.10 where the Mohr circles describe the soil stress conditions and the curved yield envelopes represent the mobilized shear strengths. The Mohr circle M1 and the yield envelope S1 are at the point of touching each other to represent the equilibrium between initial imposed stress state and the mobilized shear strength respectively. When the vertical imposed

load is increased the Mohr circle M1 enlarges to M2 and extends above the yield envelope S1 and therefore triggers the collapse failure categorised as loading collapse. As the soil structure is compressed the mobilized friction angle,  $\phi'_{mob}$ , increases and thereby increases the mobilized shear strength which is described by the turning of the yield envelope about suction axis to the position S2. This is the position that the surface envelope has rotated slightly beyond the Mohr circle M2 and thus an equilibrium condition is reached. This thereby stops the collapse. The enlargement of the Mohr circle from M1 to M2 is also showing a slight increase in the minor principal net stress,  $(\sigma_3 - u_a)$ , as well as the bigger increase in the major principal net stress,  $(\sigma_1 - u_a)$ . This due to the increase in the coefficient of earth pressure at rest,  $K_o$ , as void ratio decreases when the soil structure is compressed (Ting *et al.*, 1994) in the field.  $K_o$  is defined as the ratio of horizontal to vertical effective stress in an element of soil under zero lateral strain. This effect has shifted the Mohr circle slightly to the right. A further increase in the vertical load has enlarged the Mohr circle to position M3 and rotates the yield envelope to S3 where equilibrium is reinstated. Notice that the inclination of the linear sections of the envelopes from the horizontal is correspondingly increased to inclination angles of  $\phi'_{min 1}$ ,  $\phi'_{min 2}$  and  $\phi'_{min 3}$ .

#### 3.4.5 Qualitative Simulation of Wetting and Drying Collapse.

Consider the initial equilibrium stress state is such that the Mohr circle at M1 is about to touch the soil mobilized shear strength envelope represented by the envelope S1 as shown in Figure 3.11. When the suction is reduced due to inundation the Mohr circle is shifted from M1 to M2 moving in a direction parallel to the suction axis without affecting its diameter since the major and minor principal net stresses remain constant. The influence of suction is incorporated by the shifting of the Mohr circle from M1 to M2. During this retreat it extends beyond the shear surface envelope S1 and thereby triggers soil compression which is categorised as wetting collapse. This has caused it to rotate about the suction axis to mark the increase in mobilized friction angle,  $\phi'_{mob}$ , to the yield envelope S2 where a state of stress equilibrium is reinstated. At this instance the surface envelope S2 is at the point of engaging contact with the Mohr circle M2.

As suction is further reduced the Mohr circle advances to positions M3 and M4 and the corresponding rotated yield surface envelopes at equilibrium are at S3 and S4 respectively. Similarly those Mohr circles and their respective yield envelopes are at the point of making contact. Even though each reduction in suction is of the same magnitude, it should be noted that the rotation of the yield envelope from S3 to S4 is very much greater as shown in Figure 3.11(b). This occurs when the rotation of the surface envelope is drawn in accordance with the proportionate turning of the curvilinear tangent line to the Mohr circles, as shown in Figure 3.11(a). This is the result of the curving down of the yield envelope that gets steeper as it approaches the frontal plane ( $\tau$  versus  $(\sigma - u_a)$ ), which represents the steep reduction in mobilized shear strength as saturation is approached. This large turning of the yield envelope would represent the significant vertical compression which signified the massive volume reduction when suction approaches zero as reported by Alonso *et al.* (1990), Escario and Saez (1973), Matyas and Radhakrishna (1968) and Bishop and Blight (1963).

On the other hand, when the soil undergoes drying and suction is increased it causes the stress state to be shifted from Mohr circle M1 to M5. This is again causing soil compression since the Mohr circle M5 extends beyond the initial soil mobilized shear strength represented by the yield envelope S1. This is due to the shape of the yield envelope that gradually curves down beyond residual suction. This type of collapse is called drying collapse (Alonso *et al.* 1995, Sharma 1998). Along this drying path there will be no massive collapse encountered since the reduction in mobilized shear strength is always gradual up to the ultimate suction.

#### **3.4.6 Relationship between Mobilized Minimum Friction Angle and Axial Strain.**

The normal form of the constitutive equations for volume change relates deformation state variables to the stress state variables. This relationship requires the soil properties which are usually evaluated experimentally and appear as a volumetric deformation coefficient. However in the volume change framework there is a slight change in the approach where the influence of soil properties and the imposed stress are already incorporated into the shear strength-volume change framework. The

modelling of soil compression in the framework produces an increase in the mobilized minimum friction angle,  $\phi'_{\min_{mob}}$ . Therefore it is anticipated that there is a unique relationship between the increase in the mobilized minimum friction angle and the vertical or axial strain which is taken as the deformation state variable.

This unique relationship during the specimen compression will be inspected in triaxial tests on saturated and unsaturated specimens in the strain range up to the point of failure. This will only cover the case of loading collapse at different effective stress and suction. There were no triaxial tests involving inundation of unsaturated specimens in the test programme and therefore the soil compression due to suction decrease cannot be validated in this thesis. Likewise there were no tests that involved specimen drying.

#### **3.4.7 Yield Surface Envelope According to the Proposed Hypothetical Volume Change Framework.**

The proposed hypothetical volume change framework is based on a unique relationship between the mobilized minimum friction angle,  $\phi'_{\min_{mob}}$ , and the axial strain,  $\varepsilon_a$ , obtained from triaxial tests. This is because the existence of this unique relationship for different net confining pressures (i.e. net normal stress for unsaturated conditions and effective stress for saturated conditions) will allow the mobilized shear strength envelope to be considered as the yield surface. This yield surface is representing identical axial strains irrespective of the different values of net confining stress as long as they are in the range of low stress levels where the occurrence of particle breakage is disregarded. The absence of particle breakage during shearing at different net confining pressure is assumed to produce failure at identical axial strains. This is the primary requirement in order to obtain a unique relationship of  $\phi'_{\min_{mob}} - \varepsilon_a$ . Failure deviator stress attained at higher axial strain indicates the occurrence of particle breakage during shearing (Bishop 1966, 1972; Billam 1972), and particle breakage will invalidate the applicability of the framework. Also, the graph of  $\varepsilon_v$  versus  $\varepsilon_a$  must show the occurrence of dilation during shear since particle breakage

will suppress the specimen from dilating. Then the volume change behaviour is obtained from relationship between axial strain,  $\varepsilon_a$ , and volumetric strain,  $\varepsilon_v$ .

The following procedure describes how, according to the hypothetical volume change framework, the yield envelopes at various stages of the shearing stage in triaxial tests at different net confining pressures can be obtained. This will demonstrate that the yield envelope is rotating about the suction axis towards the soil shear strength envelope at failure as the specimens are being compressed by the increasing deviator stress. The position of the yield envelope can be recognized by the value of the mobilized minimum friction angle,  $\phi'_{\min_{mob}}$ . The corresponding axial strain,  $\varepsilon_a$  represented by the yield envelope can be obtained from the unique relationship of  $\phi'_{\min_{mob}} - \varepsilon_a$  and the state of the volumetric strain is obtained from the relationship of  $\varepsilon_v - \varepsilon_a$ .

1. Plot deviator stress versus axial strain for the tests at different net confining pressures and plot the corresponding volumetric strain,  $\varepsilon_v$ , versus percentage axial strain.
2. Calculate the effective mobilized friction angle,  $\phi'_{mob}$ , for every deviator stress according to Equation 2.11 for every test.
3. From the graph of deviator stress versus percentage axial strain determine the deviator stress at failure and the corresponding percentage axial strain.
4. Plot the graph of  $\phi'_{mob}$  against % axial strain.
5. Determine the effective mobilized friction angle,  $\phi'_{mob_f}$ , at peak deviator stress or at failure point.
6. From the triaxial tests at different net confining pressures draw the curvilinear shear strength envelope at failure and determine the  $\phi'_{\min_f}$ , which is the inclination of the linear section of the envelope from horizontal, for the soil.
7. Determine the value of the  $\phi'_{\min_{mob}}$  corresponding to each computed deviator stress according to Equation 3.34 for every test.

8. In order to draw the yield surface corresponding to a value of  $\phi'_{\min_{mob}}$  determine the corresponding major principal stress for every case of net confining pressure and draw the Mohr stress circles on the graph of shear stress versus net stress (i.e. unsaturated conditions) or the effective stress (i.e. saturated conditions). Then draw the corresponding curvilinear yield surface envelope using Equation 3.13 and 3.14 by estimating the values for the  $(\sigma - u_w)_i$  and  $\tau_i$ . Repeat this procedure for a higher value of  $\phi'_{\min_{mob}}$  and this will demonstrate that the yield surface is turning towards the shear strength surface envelope that has  $\phi'_{\min_{mob}} = \phi'_{\min_f}$ .
9. Plot  $\phi'_{\min_{mob}}$  versus axial strain,  $\epsilon_a$ , and neglect the section of the graph that has a negative value of  $\phi'_{\min_{mob}}$  (i.e. at that stage the value of  $\phi'_{\min_{mob}}$  is assumed to be always zero and the mobilized shear strength envelope is flattening as it approaches the plane  $(\sigma - u_a):(u_a - u_w)$  in the extended Mohr-Coulomb space.) The graphs of  $\phi'_{\min_{mob}}$  versus  $\epsilon_a$  for different net stress or effective stress will be overlapping due to their unique relationship. This will prove that the mobilized shear strength envelope is a yield surface since it represents identical axial strains. The increase of the value of  $\phi'_{\min_{mob}}$  relative to percentage axial strain in the graph is indicating the rotation of the curvilinear surface of the mobilized shear strength envelope or the yield envelope as the specimen is compressed and the corresponding yield, which is the axial strain,  $\epsilon_a$ , can be determined.
10. The corresponding volume change response can be determined from the graph of volumetric strain versus axial strain,  $\epsilon_a$ , as obtained in step 1.

However, the framework only considers all the plotted graphs up to the axial strain at failure. This is because in the field the soil can not dilate due to the suppression by the net vertical stress and being constrained from lateral movement.

In other words the framework is considering that if the soil shear strength is fully mobilized then its state of shear strength is represented by the shear strength envelope

at failure. In this state the framework assumes that the particles are fully interlocked and there is no room for vertical compression except when there is particle breakage. The advantage of this framework is that it can explain the soil compression or the volume change behaviour due to load increase or inundation within the same framework. Furthermore this hypothetical Rotational Multiple Yield Surface Framework can be used to predict the stress-strain curve from a triaxial compression test, which will be discussed in the following section.

### 3.4.8 Framework Prediction of the Stress-strain Curve for a Triaxial Compression Test.

This section describes the procedure to predict the soil stress-strain behaviour in a triaxial compression test at any net confining stress by the proposed volume change framework. The primary requirements are the unique relationship  $\phi'_{\min_{mob}} - \varepsilon_a$  and the shape of the shear strength envelope at failure of the soil. The latter is important because the shape of the mobilized shear strength envelope above a certain minimum angle of rotation (i.e.  $\phi'_{\min_{mob}} \geq 0$ ) is assumed to take its shape. Lower than the effective mobilized minimum friction angle,  $\phi'_{\min_{mob}}$ , of zero the mobilized shear strength envelope is assumed to flatten by maintaining  $\phi'_{\min_{mob}}$  equal to zero as it approaches the plane  $(\sigma - u_a) : (u_a - u_w)$ .

The procedure for obtaining the stress-strain curve is as follows.

1. Determine the shear strength envelope for the soil at failure.
2. Determine the unique relationship of  $\phi'_{\min_{mob}} - \varepsilon_a$  for the soil.
3. From the unique relationship of  $\phi'_{\min_{mob}} - \varepsilon_a$  select the effective mobilized minimum friction angles at certain increments and determine the corresponding axial strains e.g.  $\phi'_{\min_{mob}}$  equals  $10^\circ$ ,  $20^\circ$ ,  $30^\circ$  and  $34^\circ$  and the corresponding axial strains are  $\varepsilon_{a_{10^\circ}}$ ,  $\varepsilon_{a_{20^\circ}}$ ,  $\varepsilon_{a_{30^\circ}}$  and  $\varepsilon_{a_{34^\circ}}$ . This is illustrated in Figure 3.12(a).
4. In  $\tau : (\sigma - u_a)$  space for unsaturated conditions and  $\tau : (\sigma - u_w)$  for saturated conditions draw the shear strength envelope at failure and the yield surfaces at

the values of  $\phi'_{\min_{mob}}$  selected in step 1. Note that the yield surfaces and the shear strength envelope at failure for either saturated or unsaturated conditions are representing the axial strains  $\epsilon_{a_{10^\circ}}$ ,  $\epsilon_{a_{20^\circ}}$ ,  $\epsilon_{a_{30^\circ}}$  and  $\epsilon_{a_{34^\circ}}$  respectively as illustrated in Figures 3.12(b) and (c). For the saturated and the unsaturated conditions the axis of rotation of the yield envelope is perpendicular to the page and passes through the origin and at distance  $c_s$  above the origin respectively. Note that  $c_s$  is the apparent cohesion corresponding to the considered suction.

5. Identify the net confining pressure,  $(\sigma_3 - u_w)$  or  $(\sigma_3 - u_a)$ , for which the stress-strain behaviour is to be predicted and mark it on the effective stress or the net stress axes as shown in Figures 3.12(b) and (c) for saturated and unsaturated conditions respectively.
6. Draw the predicted Mohr circles corresponding to the yield surfaces and the shear strength envelope at failure. The Mohr stress circles should be touching their respective yield surfaces as illustrated in Figure 3.12(b) and (c).
7. Determine the magnitude of the net vertical stress corresponding to the Mohr circles drawn in step 4.
8. Deduce the corresponding deviator stress based on the equation  $q = \sigma'_1 - \sigma_3 - u_a$  for unsaturated conditions and  $q = \sigma'_1 - \sigma_3 - u_w$  for saturated conditions. Assume that the corresponding deviator stresses are  $q_{10^\circ}$ ,  $q_{20^\circ}$ ,  $q_{30^\circ}$  and  $q_{34^\circ}$ .
9. Draw the predicted stress-strain curve using the deviator stresses of  $q_{10^\circ}$ ,  $q_{20^\circ}$ ,  $q_{30^\circ}$  and  $q_{34^\circ}$  against the corresponding axial strains  $\epsilon_{a_{10^\circ}}$ ,  $\epsilon_{a_{20^\circ}}$ ,  $\epsilon_{a_{30^\circ}}$  and  $\epsilon_{a_{34^\circ}}$  as illustrated in Figure 3.12(d).

From the above procedure, the stress-strain curve up to the failure point at any net confining pressure can be predicted by changing the value applied in step 3. This procedure will be applied for the prediction of the stress-strain behaviour by the Rotational Multiple Yield Surface Framework carried out in Chapter 6.

### 3.5 Summary.

In this chapter a new semi-empirical extended Mohr-Coulomb shear strength model has been proposed and the shape of the shear strength envelope at failure has been applied in the proposed new hypothetical shear strength-volume change framework named the Rotational Multiple Yield Surface Framework. The performance of the shear strength model has been tested against the shear strength behaviour with respect to net stress and suction independently using the data reported in the literature. A fuller model prediction will be carried out against data from triaxial tests on saturated and unsaturated specimens of the test material described in Chapter 5. Qualitatively the proposed hypothetical shear strength-volume change framework is able to model loading, wetting and drying collapse, including the significant soil compression near saturation through changes in the effective mobilized minimum friction angle indicated by the framework when the soil structure is compressed. This is the consequence of considering soil compression or yielding based on the combined effect of principal stresses and suction through the concept of Mohr stress diagram. Soil is considered to yield when the state of stress equilibrium between the soil stress state and the mobilized shear strength is disrupted by the former exceeding the latter. However the existence of a unique relationship between the increase in effective mobilized minimum friction angle and the increase in the axial strain to represent the volume change behaviour is anticipated. This unique relationship is required in order to verify the applicability of the hypothetical framework. Therefore a laboratory test programme that can furnish the stress-strain and the volume change behaviour at different net confining pressures needs to be performed. Another advantage of the proposed hypothetical volume change framework is that it can be used to predict the stress-strain curve in a soil triaxial compression test through back calculation. The detailed test programme and test results will be described and discussed in the following chapters.

Table 3.1 Summary of the shear strength behaviour in the four distinct zones on the constitutive shear strength surface.

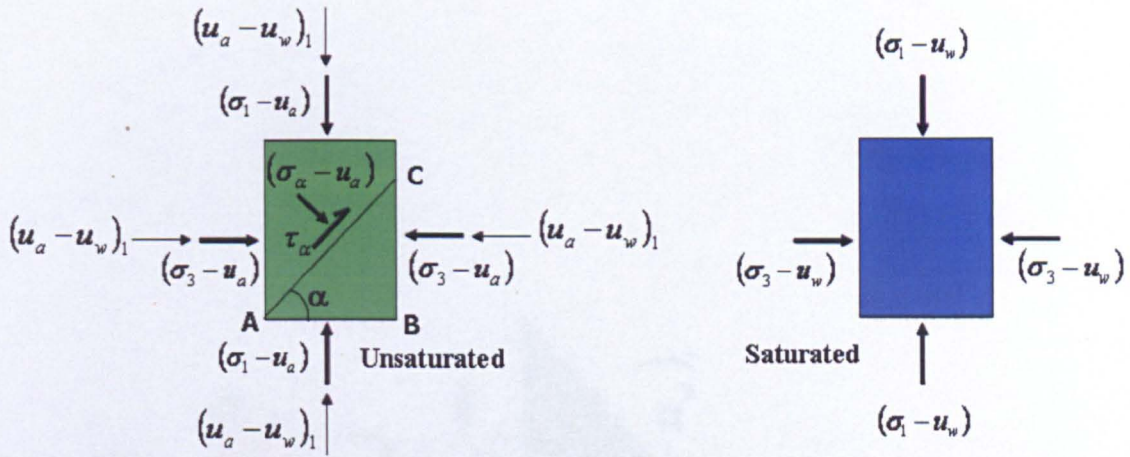
Zone of shear strength	Shear strength behaviour (with reference to Figure 3.2)	
	Relative to effective stress at saturation	Relative to suction
1	Non-linear increase of shear strength from zero effective stress up to transition effective stress, $\tau_t$ , bounded by curves OA and FE.	Non-linear increase of shear strength from zero suction up to residual suction, $(u_a - u_w)_r$ , bounded by curves OF and AE.
2	Non-linear increase of shear strength from zero effective stress up to transition effective stress, $\tau_t$ , bounded by curves FE and GH.	Shear strength decrease for suction greater than residual suction, $(u_a - u_w)_r$ , and the decrease becomes more gradual as effective stress increases bounded by curves FG and EH.
3	Linear behaviour of shear strength for effective stress higher than transition effective stress, $\tau_t$ , bounded by lines AB and EC.	Non-linear increase of shear strength from zero suction up to residual suction, $(u_a - u_w)_r$ , bounded by curves AE and BC
4	Linear behaviour of shear strength for effective stress higher than transition effective stress, $\tau_t$ , bounded by lines EC and HD.	Shear strength decrease for suction greater than residual suction, $(u_a - u_w)_r$ , and the decrease becomes more gradual as effective stress increases bounded by curves EH and CD.

Table 3.2 Shear strength parameters used in Equations 3.4 and 3.7 in the validation work.

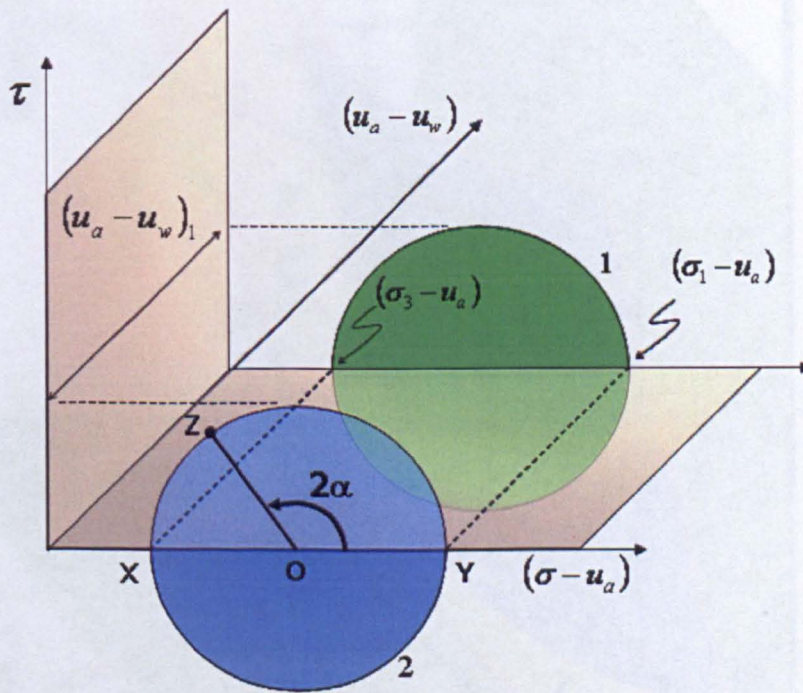
Author	Soil type	Net confining pressure (kPa)	Residual suction (kPa)	Ultimate suction (kPa)	Maximum apparent cohesion (kPa)
Escario and Juca 1989	Madrid clayey sand	600	800	15000	137
Escario and Juca 1989	Madrid clayey sand	120	800	6500	136
Gan and Fredlund 1996	Decomposed fine ash tuff, Hong Kong	20	120	430	31
Gan and Fredlund 1996	Decomposed fine ash tuff, Hong Kong	20	130	460	62
Gan and Fredlund 1996	Decomposed fine ash tuff, Hong Kong	100	83	750	35
Toll <i>et al.</i> 2000	Residual soil from Jurong formation, Singapore	50	150	450	45

Table 3.3 Constants used in Equation 3.13 and 3.14 in their validation against the experimental data by Charles and Watts (1980).

Soil type (maximum particle size of 38mm)	Transition effective stress (kPa)	Transition shear strength (kPa)	Minimum friction angle (degrees)
Basalt C	250	392	45
Sandstone A	200	240	34
Slate B2	300	240	26



(a) Stress state in an unsaturated triaxial specimen. (b) Stress state in a saturated triaxial specimen.



(c) Representation of unsaturated stress state by Mohr circle 1 and the saturated stress state by Mohr circle 2 in extended Mohr-Coulomb space.

Figure 3.1 Saturated and unsaturated triaxial stress states and the representing Mohr stress circles.

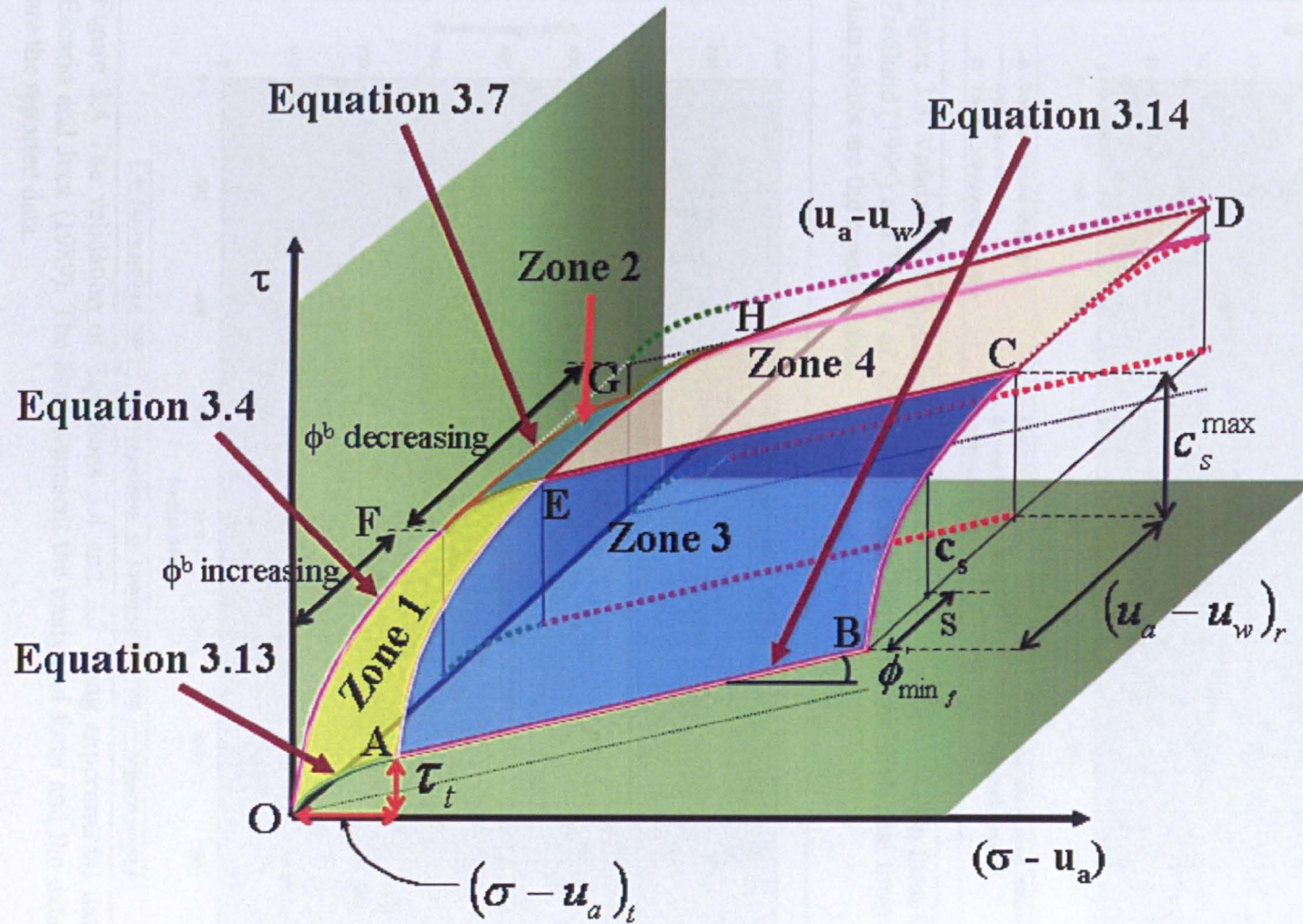


Figure 3.2 New proposed semi-empirical soil shear strength model.

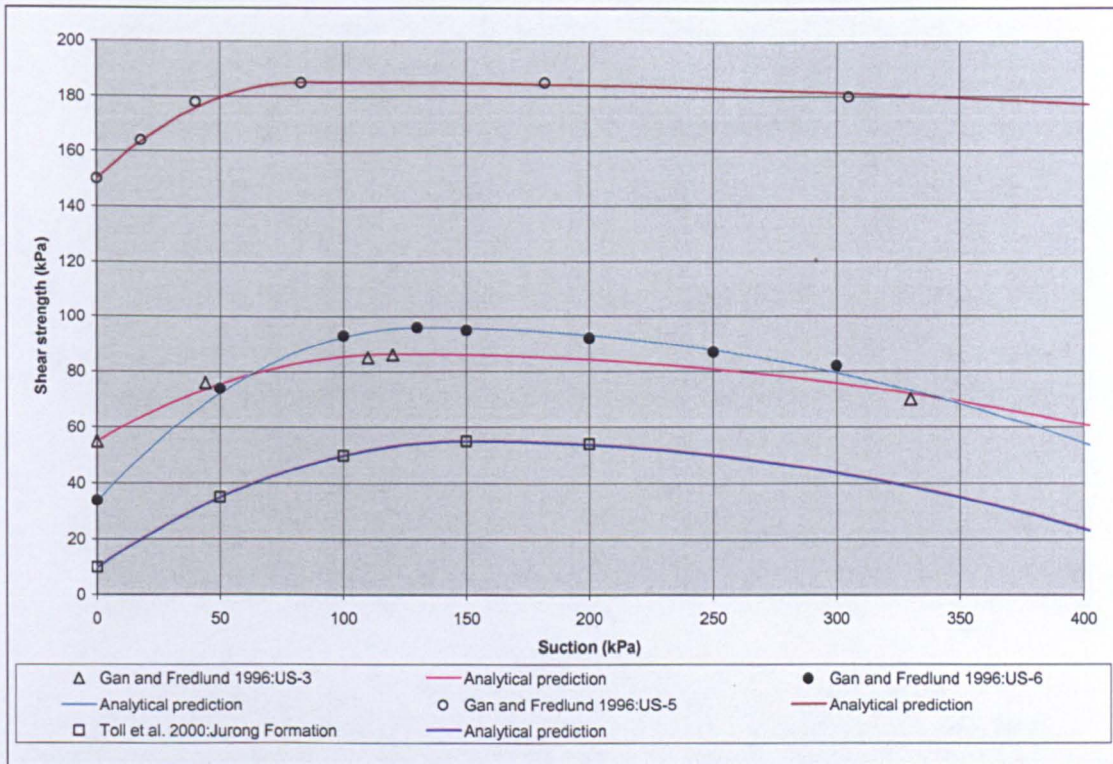


Figure 3.3. Validation of Equations 3.4 and 3.7 using experimental data from Gan and Fredlund (1996) and Toll *et al.* (2000). The lines represent the analytical form and the data points are the reported data.

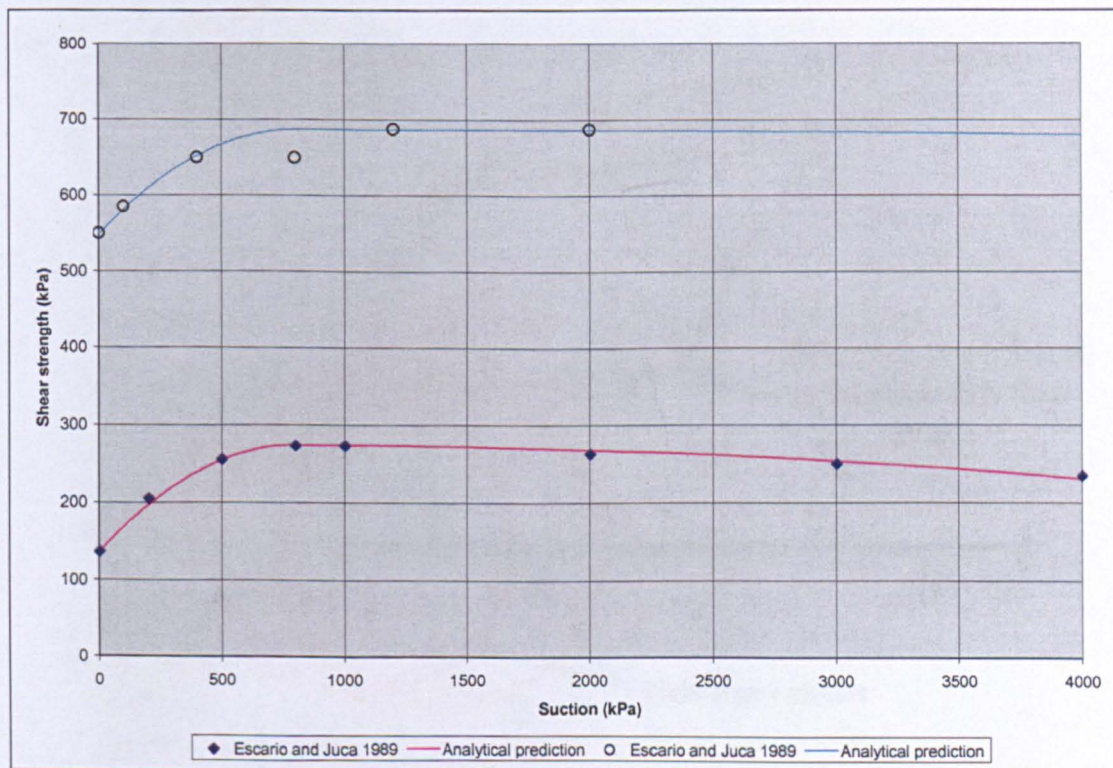


Figure 3.4 The validation of Equations 3.4 and 3.7 using experimental data from Escario and Juca (1989). The lines represent the analytical form and the data points are the reported data.

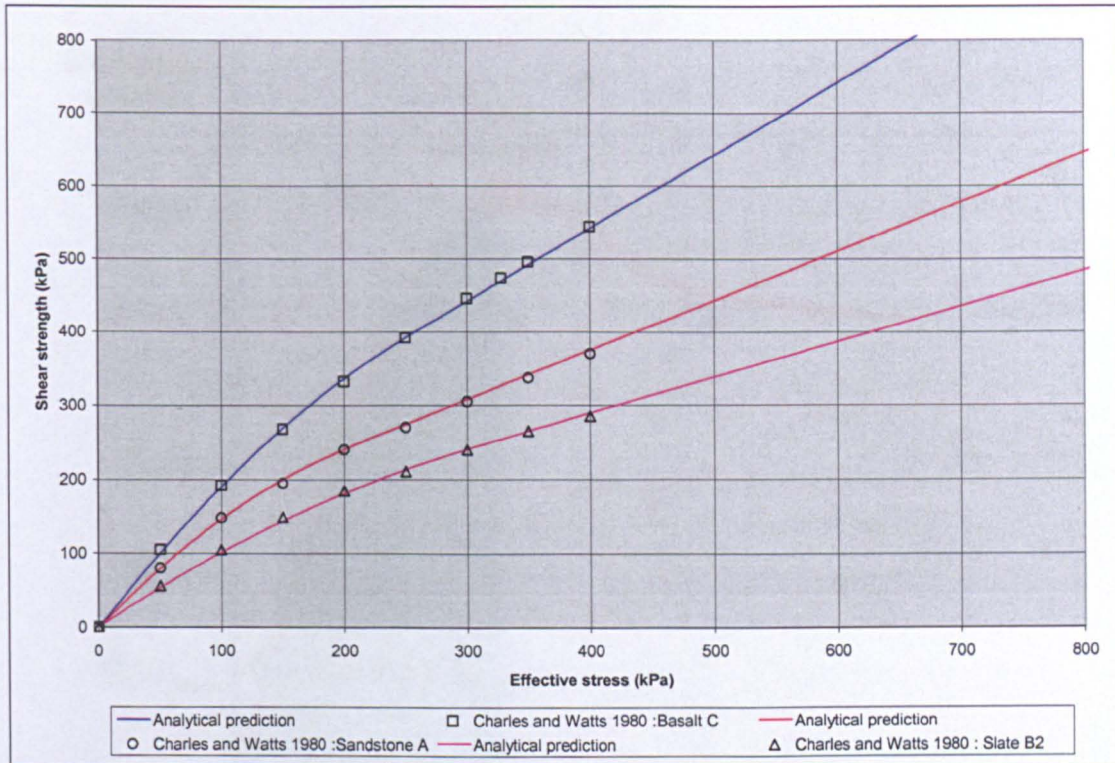


Figure 3.5 The validation of Equations 3.13 and 3.14 using experimental results from Charles and Watts (1980). The lines represent the analytical form and the data points are the reported data.

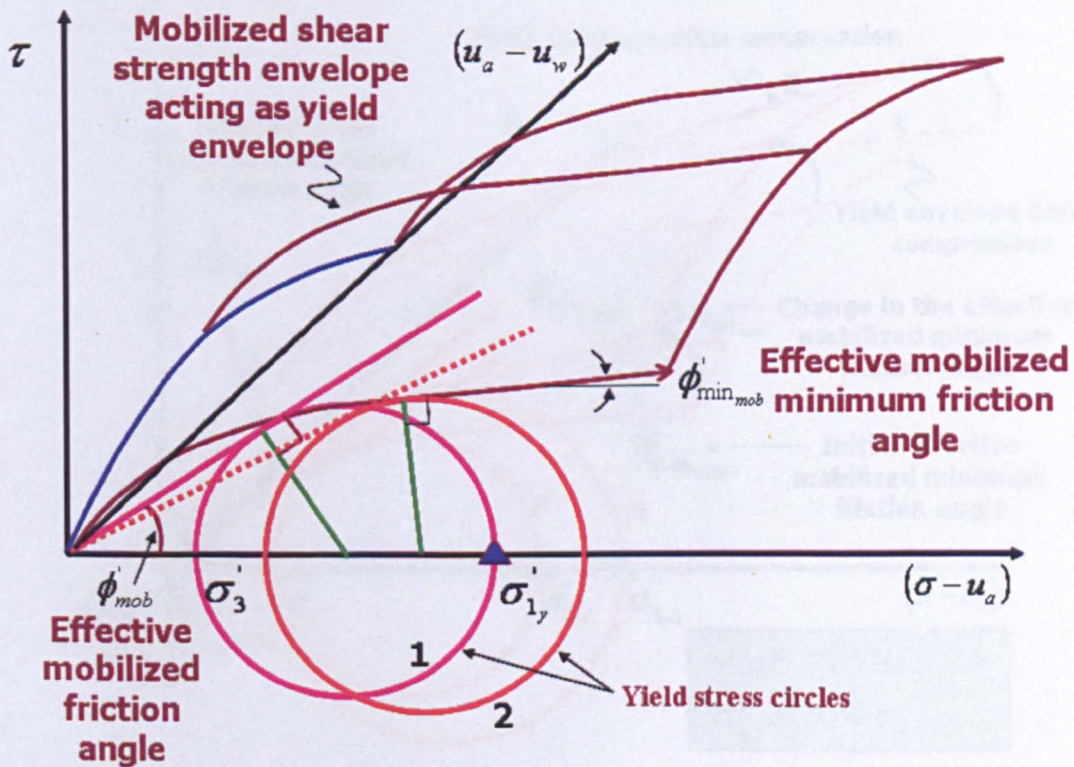


Figure 3.6 Mobilized minimum friction angle,  $\phi'_{min\_mob}$ , describes the position of the current yield envelope. All the points on the yield envelope represent the same axial strain irrespective of the net confining stress or suction.

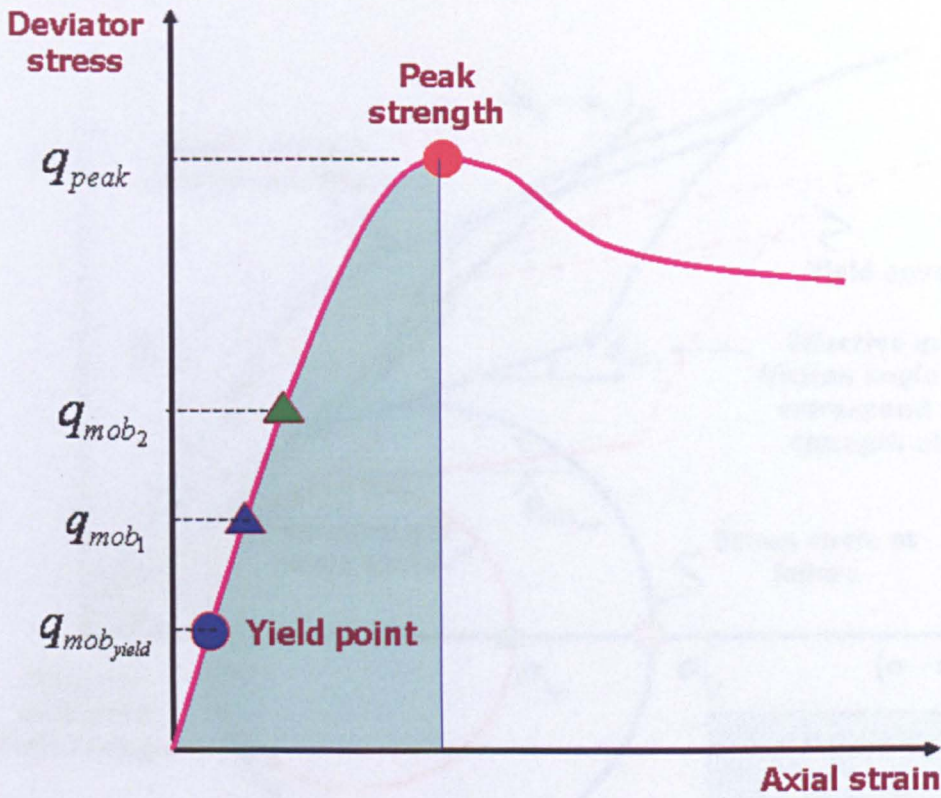


Figure 3.7 Typical stress-strain behaviour from triaxial compression test.

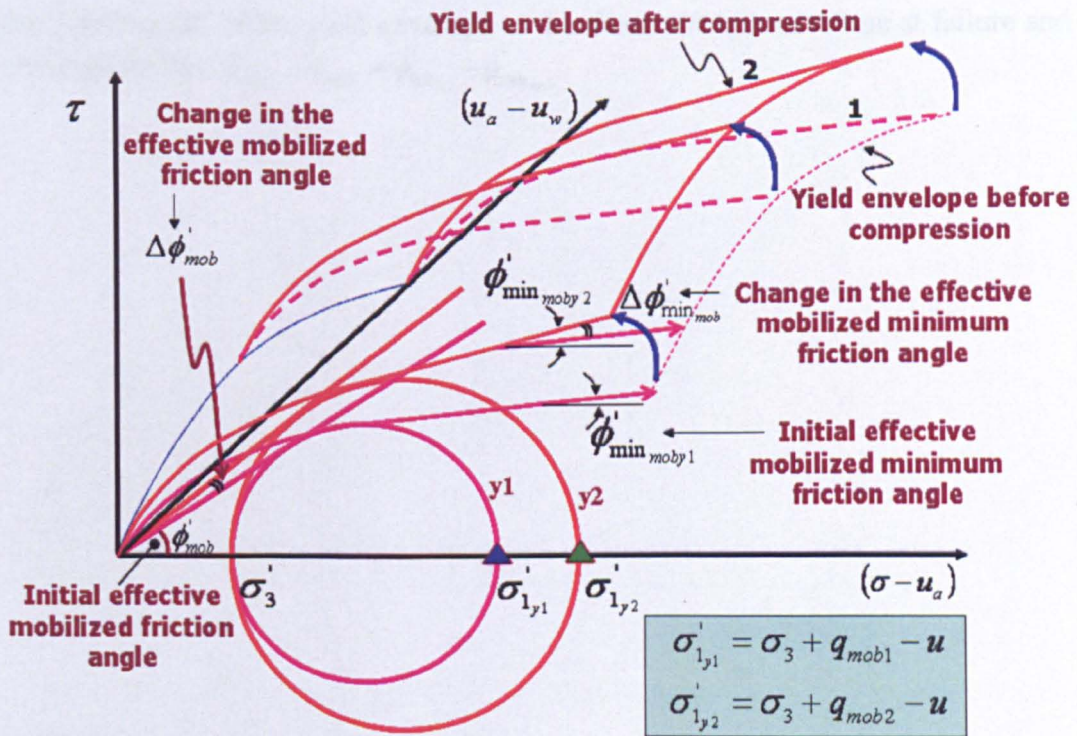


Figure 3.8 The rotation of the yield surface envelope as the deviator stress increases from  $q_{mob1}$  to  $q_{mob2}$  and the assumption that  $\Delta\phi'_{min\,mob} = \Delta\phi'_{mob}$ .

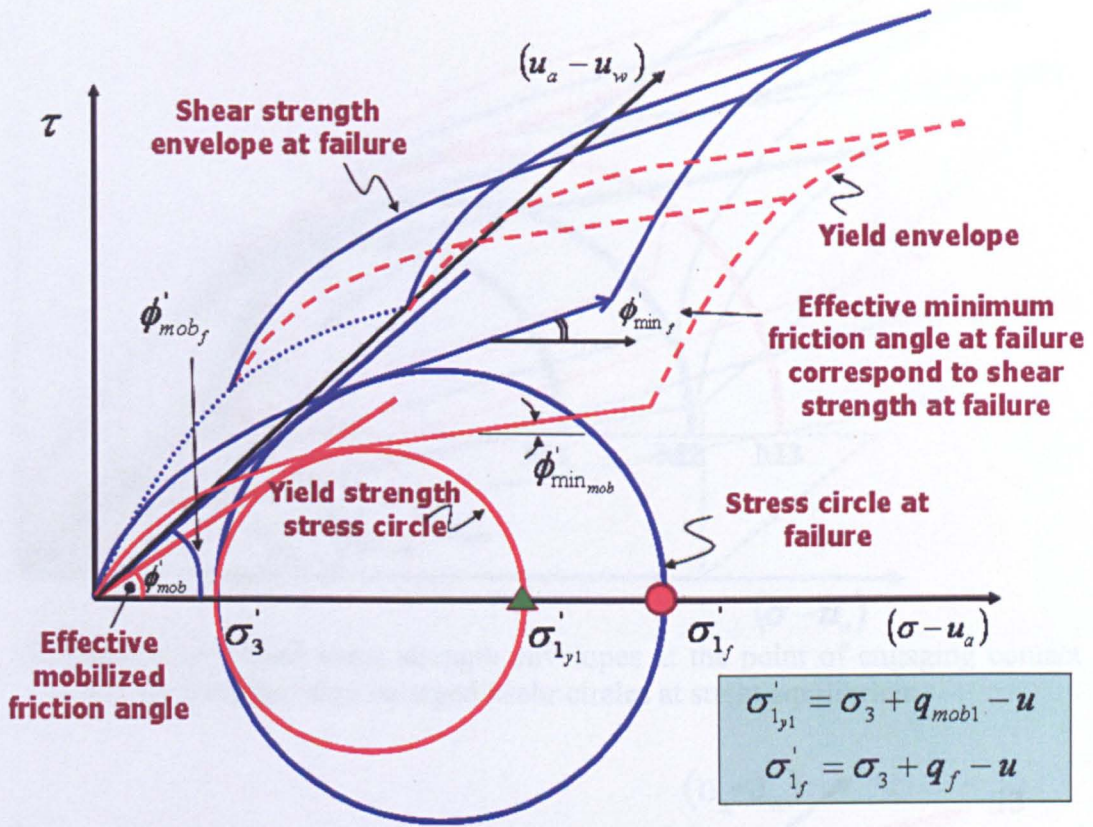
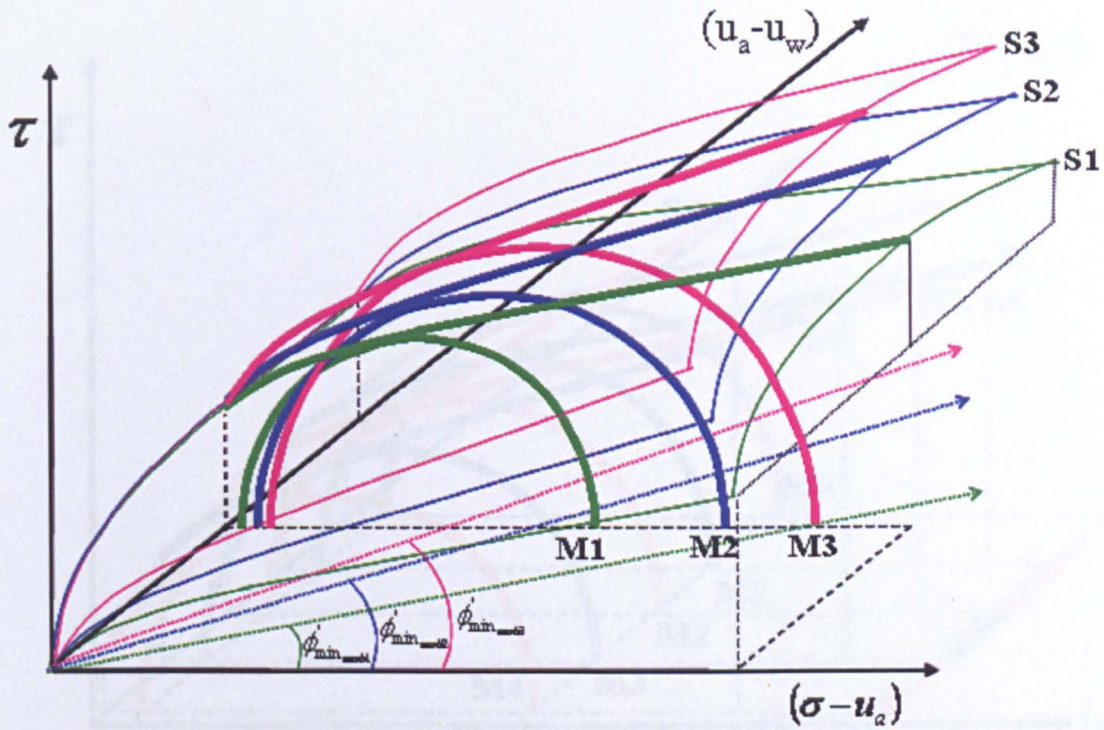
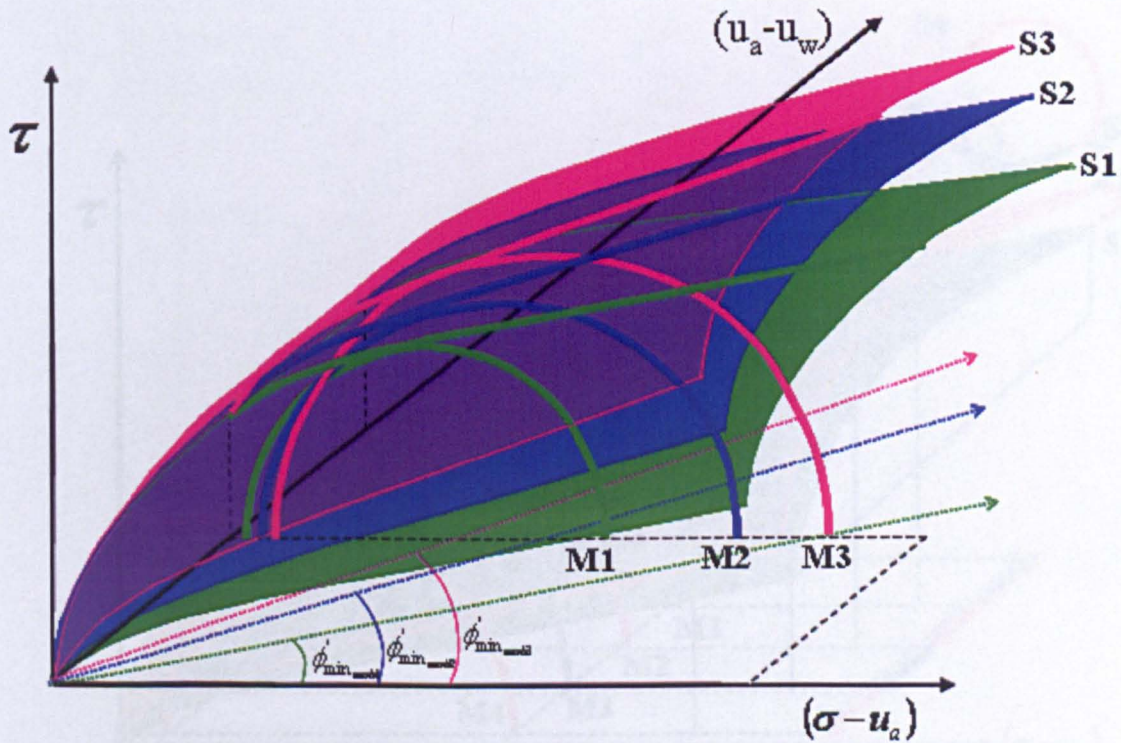


Figure 3.9 Rotation of the yield envelope to the shear strength envelope at failure and the assumption that  $\phi'_{mob_f} - \phi'_{mob} = \phi'_{min_f} - \phi'_{min_mob}$ .

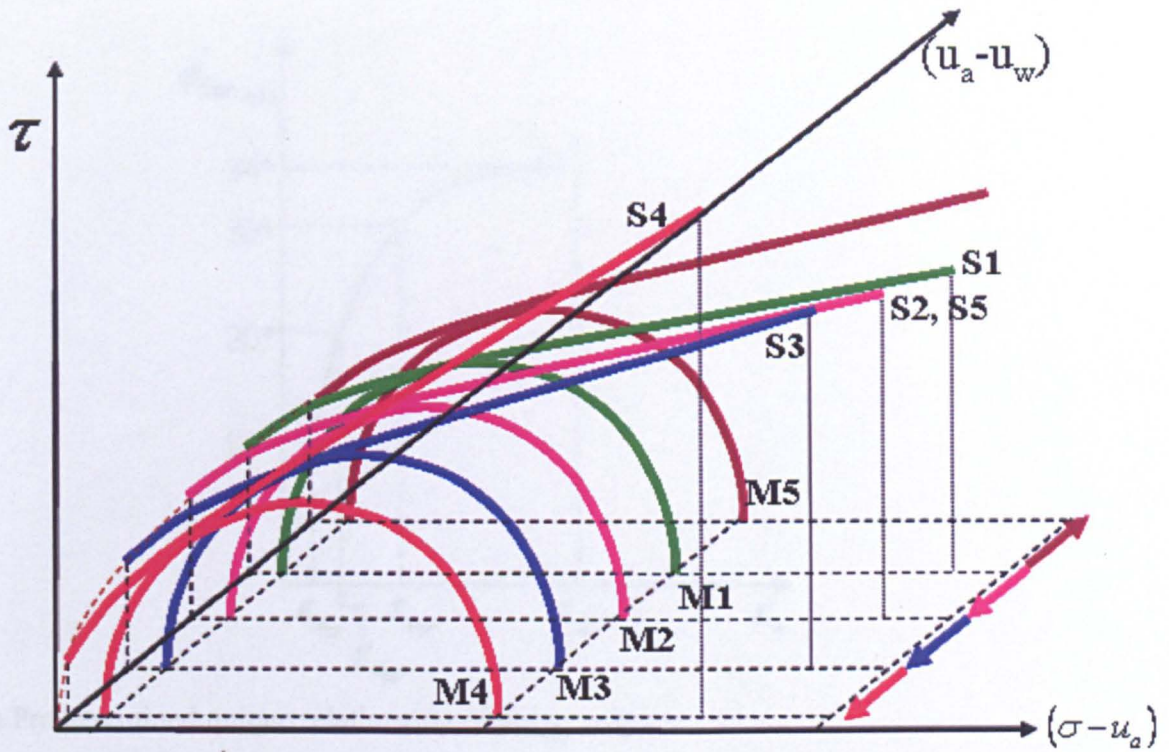


(b) Rotated mobilized shear strength envelopes at the point of engaging contact with the corresponding enlarged Mohr circles at stress equilibrium.

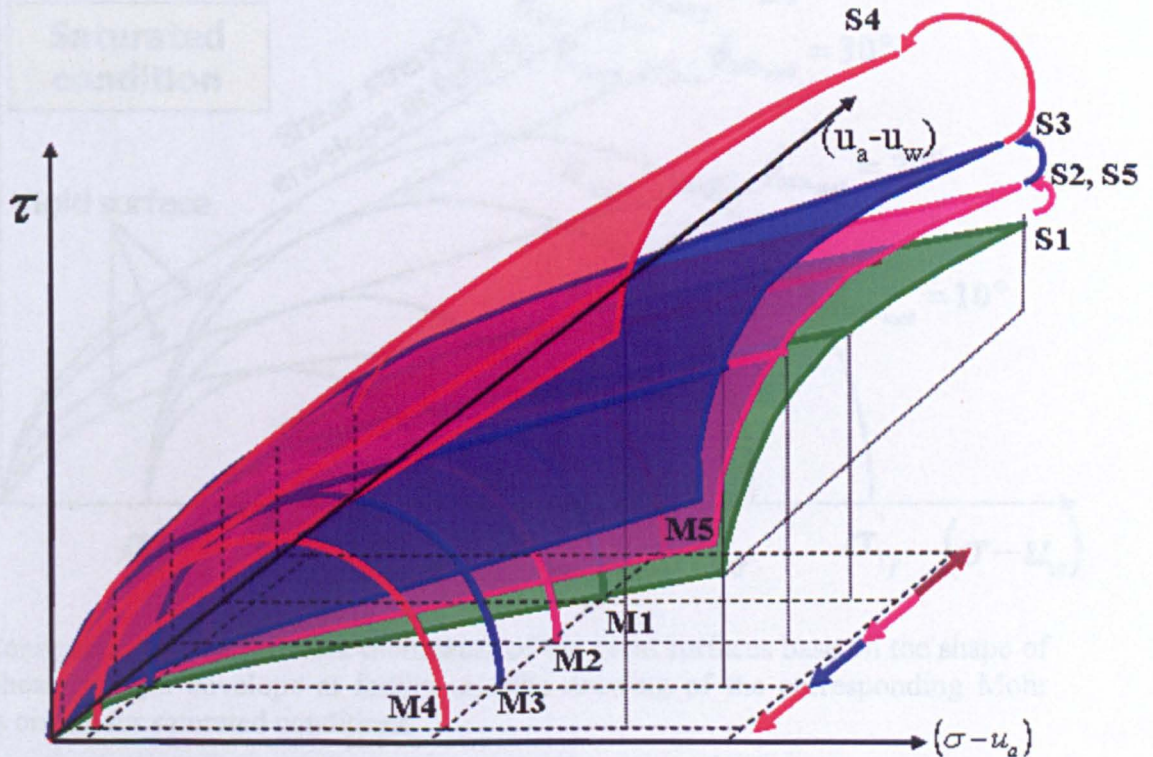


(b) The rotated mobilized shear strength envelopes about the suction axis that correspond to their curvilinear lines in (a).

Figure 3.10 Modelling loading collapse in the Rotational Multiple Yield Surface Framework.

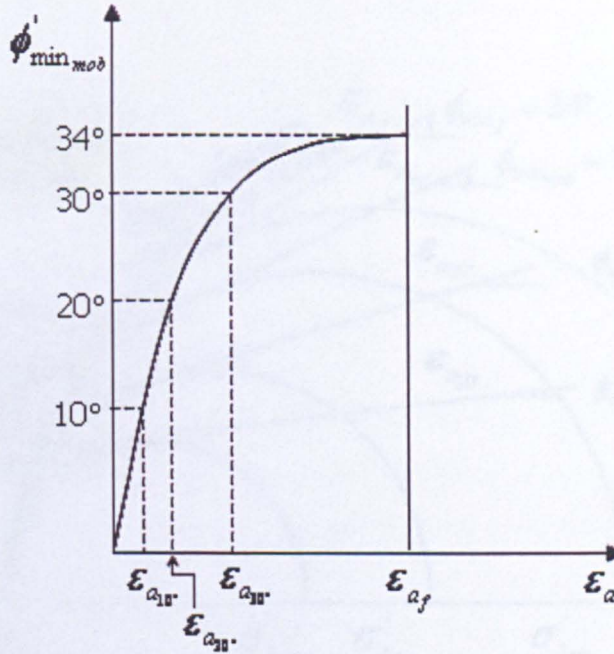


(a) Proportionate rotation of the curvilinear lines of the yield envelopes when Mohr circles retreat towards lower suction.

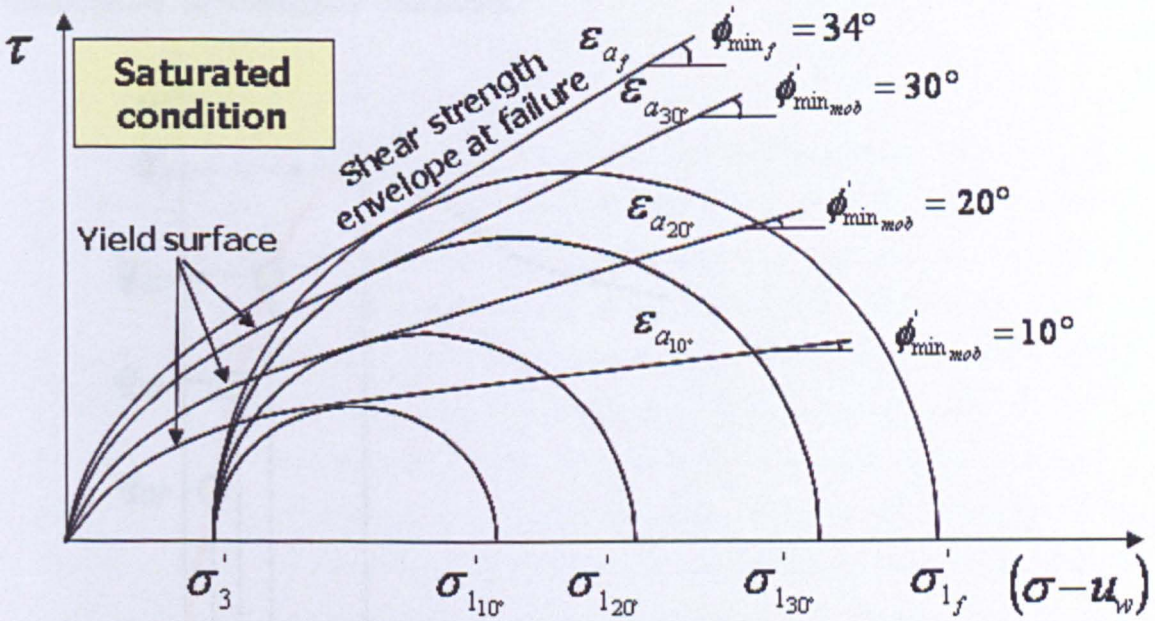


(b) The rotated yield envelopes about the suction axis that correspond to the curvilinear lines in (a).

Figure 3.11 Modelling wetting and drying collapse in the Rotational Multiple Yield Surface Framework.

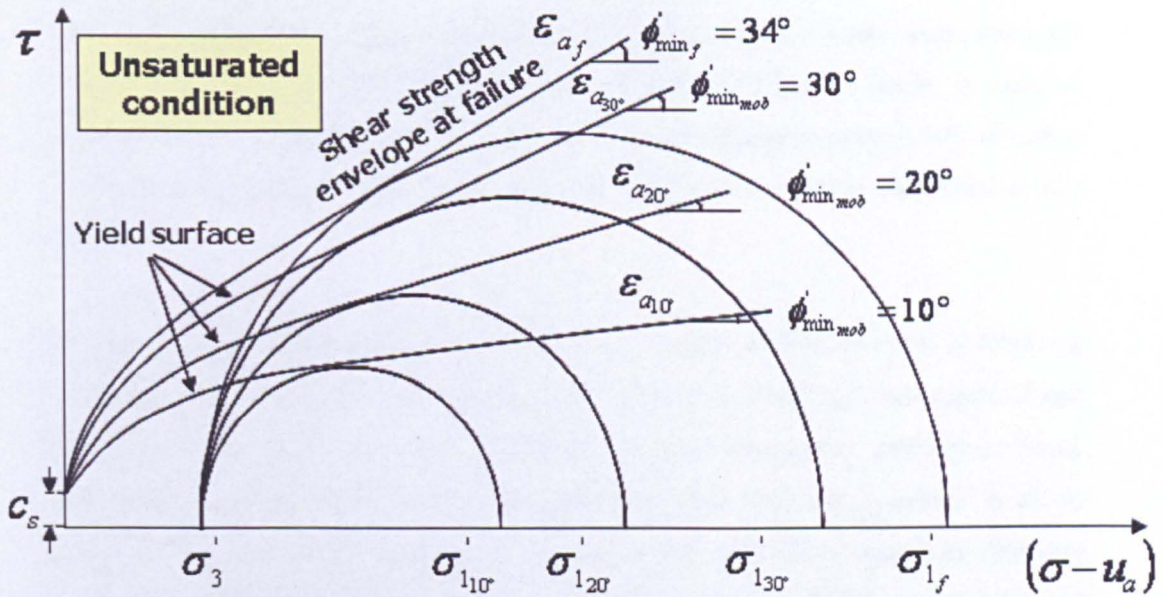


(a) Predetermined unique relationship of  $\phi'_{min\_mob} - \epsilon_a$ .

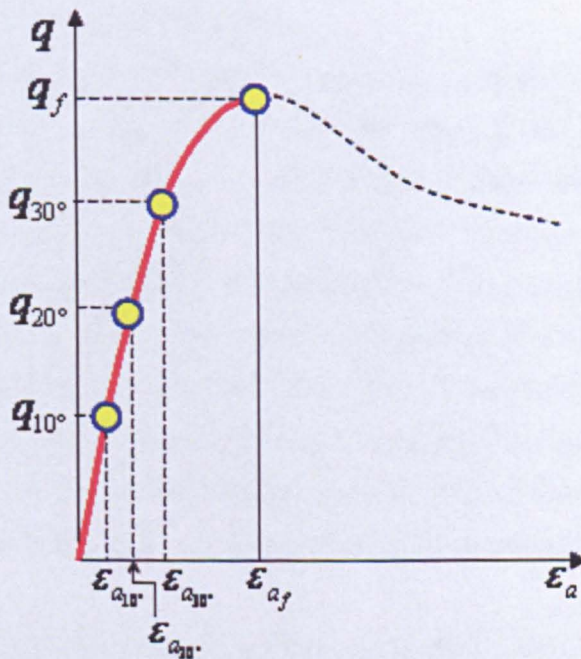


(b) Construction of the different inclination of the yield surfaces base on the shape of the shear strength envelope at failure and the drawing of the corresponding Mohr stress circles for saturated conditions.

Figure 3.12 Process of predicting the stress-strain curve by the Rotational Multiple Yield Surface Framework.



(c) Construction of the different inclination of the yield surfaces base on the shape of the shear strength envelope at failure and the drawing of the corresponding Mohr stress circles for unsaturated conditions.



(d) Predicted stress-strain curve of the soil at a net confining pressure.

Figure 3.12 (continued) Process of predicting the stress-strain curve by the Rotational Multiple Yield Surface Framework.

## Chapter 4

### Test Material and Equipment, Test Procedures and Test Programme.

#### 4.1 Introduction.

The previous chapter introduced a new shear strength model and a new shear strength-volume change framework by applying a new equation of effective stress. In order to validate the new model and the new framework this requires an appropriate selection of test material, equipment and test programme. All of these will be described in this chapter.

The chapter starts by describing the selection of the test material and this is followed by the description of the equipment required to test this material. Four types of test equipment were used and their experimental procedures are described. Some experimental methods have been improved from those used in previous work to ensure consistency in the setting up the specimens and these improvements are described. The description of the types of transducers, their calibration processes and data acquisition system used for the instrumentation follows. Finally the detailed test programmes and their objectives are explained.

#### 4.2 Choice of Test Material.

This research was focused on the shear strength and volume change behaviour of unsaturated coarse-grained soil. The coarse-grained soil used in this research was limestone aggregate of 5 mm nominal diameter supplied in bags of approximately 35kg weight by North Tyne Roadstone Limited, Northumberland from Mootlaw Quarry, near Matfan, Northumberland. The rock formation belongs to the Upper Limestone Series of the Upper Carboniferous Period, which is known locally as Blue Mountain Limestone (Goodwin, 1991). The soil contains about 8% of fines and the grading as delivered is shown as curve no.1 in Figure 4.1. However, the actual test material used in this research was the washed material where the fines content was washed out and the resultant grading is shown as curve no.2 in Figure 4.1.

The material was washed because the fines were suspected to cause an excessive period of pore water pressure equalization of about nine weeks during a preliminary triaxial test on an unsaturated specimen.

Chapter 3 revealed that when suction increases beyond residual suction, the apparent shear strength decreases gradually and vanishes when suction equals ultimate suction. For clay soils the value of residual suction has been shown to be about 800kPa and ultimate suction was more than 4000kPa, even at a net stress of 120kPa (i.e. Madrid clay by Escario and Juca, 1989). However for granular soils, like the granite residual soil from Hong Kong, the residual suction was about 100 to 150kPa and the ultimate suction was about 600kPa based on the data presented by Gan and Fredlund (1996) for a net stress of 20kPa. It was noticed that the value of residual suction and ultimate suction reduced drastically as the particle size increased. Therefore it was anticipated that for granular soil of 5mm particle size, the ultimate suction could be lower than 200kPa for a net stress of 100kPa. This is therefore an advantage of using coarse-grained soils as the trend of shear strength behaviour at the upper range of suction is within suction values that are much easier to attain in the laboratory.

Another advantage of using the coarse-grained soil was that it was similar to the soil used by Goodwin (1991) and Salman (1995); therefore most of the soil characterisation had already been carried out. The results of petrographic analysis on chemical composition using X-Ray Fluorescence is shown in Table 4.1 (Goodwin, 1991). The high degree of particle angularity was preferable due to its high compressibility (Kjaernsli and Sande, 1963; Pellegrino, 1965; Pigeon, 1969), which was required in the compression test. The specific gravity was taken as 2.71 i.e. similar to Goodwin (1991), since the material was from the same quarry.

#### **4.2.1 Sample Preparation and Grading Tests.**

The test material was supplied in bags of 30 to 35 kg. Each sample preparation used 5 of these bags to make up a total of approximately 150 to 170kg. They were first thoroughly mixed for 15 minutes in a 180kg capacity concrete mixing drum in an air dry condition. Then the material was tipped onto a clean dry concrete floor and quartered. The alternate quarters were mixed thoroughly and quartered again twice to end up with four portions. Each portion was riffled into two separate bags to end up with a total of 8 bags each weighing between 17 and 20kg. These bags were stored ready for the next preparation procedure before they were used for testing.

The samples were first washed to remove the fines by soaking with tap water in a tray and the resultant dark coloured liquid containing the fines was poured off. This process was repeated until a clear liquid was achieved. This was followed by 10 minutes mixing in a 30kg concrete mixing drum to break up the soft lumps of shale that were mixed with the limestone gravel. Plate 4.1(a) shows the dark coloured slurry formed due to the crushing of the shale grains when turned in the mixer for 10 minutes. The samples were then washed again and the clean samples were oven dried. Any remaining shale particles were picked out by hand before the samples were prepared for specimen compaction. Plate 4.1(b) shows a washed sample freshly removed from the oven.

#### **4.2.2 Compaction Test.**

Water was added to the oven-dried soil described in the previous section to get the required moisture content and it was uniformly mixed again in the 30kg motorised electric mixer (Plate 4.1(a)) for 10 minutes. Then 1.4kg of soil was compacted for 10 seconds in a cylindrical split-mould with internal diameter of 150 mm and height of 375 mm as shown in Figure 4.2 and Plate 4.2, using the vibrating Kango hammer shown in Plates 4.2 and 4.3. Further 1.4kg layers were treated in a similar way until the mould was full.

The same mould and same procedure were used for the compaction of saturated and unsaturated specimens used in the triaxial tests. The different compaction curves obtained for washed and unwashed samples are shown as curves no.1 and 2 respectively in Figure 4.3. The optimum moisture content for the washed sample (i.e. the test material) is 8%. Curve no. 3 shows the compaction curve for the unwashed sample when compacted at a lower energy level, which is 5 seconds compaction for every layer. The compaction curves no. 1 and 2 in Figure 4.3 shows a drastic change in the compaction behaviour when the fines were washed off. The washed sample shows a lower dry density compared to the unwashed sample and the density is almost uniform irrespective of the moisture content.

#### **4.3 Test Equipment.**

With the choice of test material discussed in Section 4.2 a proper selection of the test equipment was important so that adequate specimen sizes could be accommodated in

order to achieve representative behaviour. The first piece of equipment used was the pressure plate extractor fabricated by Soilmoisture Equipment Corporation, Santa Barbara, USA. The second and the third pieces of equipment were two existing triaxial cells which had been designed and fabricated in house for testing saturated and unsaturated soil specimens of maximum particle size of 20 mm (Anderson *et al.*, 1997) and were therefore appropriate for the current research. The former is called the Conventional Triaxial Cell and the latter is called the Double-wall Triaxial Cell. The fourth piece of equipment used was a large, suction control, Rowe hydraulic compression cell, which again had been designed and fabricated in house to accommodate specimens of 254 mm diameter and 130 mm high and was suitable for testing soils of maximum particle size of 20 mm (Goodwin 1991).

#### **4.3.1 Volumetric Pressure Plate Extractor Apparatus.**

Plate 4.4 and Figure 4.4 show the volumetric pressure plate extractor apparatus (Soilmoisture Equipment Corporation, 1985). It was used to obtain the soil-moisture characteristic curve. The specimens were contained in 25mm thick circular rings with an internal diameter of 100mm. They were placed directly on a 3 bar high air-entry ceramic disc as shown in Plate 4.4(a) and (b). The whole set up is contained in an air pressure chamber to drive the water in the flooded specimens out through the ceramic disc until the flow stops.

#### **4.3.2 Conventional Triaxial Cell.**

The overall set up of the conventional triaxial apparatus and the data acquisition system is shown in Plate 4.5. The cell was modified by inserting an aluminium cylinder at the base to extend the height in order to accommodate a specimen of diameter 150 mm and 375 mm height, which is suitable for obtaining the saturated shear strength of a coarse-grained soil up to a maximum particles size of 20 mm (Anderson *et al.*, 1997). The cell was used with a 50 kN loading machine. The plumbing arrangement is shown in Figure 4.5. The cell is connected to a water tap for filling and emptying. The cell pressure is measured by both a pressure transducer and a pressure gauge. The cell pressure gauge is connected to a large air-water interface tank and, via a pressure regulator to the air pressure supply line. The pore water pressure in the specimen is measured by a pressure transducer connected to the base pedestal of the triaxial cell. The back pressure line, which also comes out from the

base pedestal of the triaxial cell, is connected to a flow reversal unit that goes directly to a 100 cc specimen volume change unit. The flow reversal unit's function is to reverse the flow of water from the top cell of the volume change unit to the bottom cell and vice versa, so that the volume change measurement can be extended beyond the capacity of the unit (100 cc). In addition, the volume change unit is also used to measure the volume of the de-aired water flushed through the system during specimen saturation. The de-aired water comes from an air-water interface tank through which the pressure supply line is connected via a back pressure regulator to the tank air phase. The pressure gauge is connected to the tank water phase. An air drainage line is connected to the specimen's top cap for draining the air flushed from the specimen during the saturation stage. A burette is connected to the air drainage line during this saturation stage to observe the last air bubbles that come out from the line during flushing, and at the same time to measure the volume of the flushed water that comes out from the specimen. This volume is subtracted from the total volume of water that has been pushed into the specimen during saturation via the volume change unit to determine the volume of void spaces.

#### **4.3.3 Double-walled Triaxial Cell.**

Bishop and Donald (1961) were the first to introduce a double-walled triaxial cell to test unsaturated soil. Their soil specimen was surrounded by mercury. However, the upper part of their inner cell was filled with water and was directly connected to water in the outer cell. The specimen volume change was then measured by monitoring the level of the mercury. The disadvantages of this method are that the specimen is not visible and there is a hazard in handling the mercury. The mercury also caused a significant variation of lateral stress over the height of the specimen due to its high density.

The problem inherent in the Bishop and Donald (1961) cell was eliminated by a modified version of the cell introduced by Delage *et al.* (1987), in which the mercury in the inner cell was replaced with water, and the water in the outer cell and at the upper section of the inner cell was replaced with air. The suction was applied by osmosis. The specimen volume change was measured by the same principle as Bishop and Donald (1961).

Wheeler (1988) improved the double-walled set up of by introducing an automatic system of measuring specimen volume change. The system measured the volume of water entering or leaving the inner cell through a burette system with a paraffin-water interface.

Salman (1995) developed a double-walled triaxial cell specifically designed for testing coarse-grain soil with a maximum particle size of 20 mm. The specimen dimensions were 150 mm diameter and 375 mm height and the cell was used with a 100 kN loading machine. This set up was used to obtain the unsaturated shear strength properties of the test material in this research. The cell is shown in Plate 4.6 and the details of the equipment are shown in Figure 4.6. The diameter of the inner cell is 342 mm and the gap between the inner and the outer wall is 10 mm. It is able to withstand a working pressure of 1500 kPa. A high air entry ceramic disc is fixed to the base pedestal to separate air from water, which enables pore air and pore water pressure to be measured independently. The cell walls are made of Perspex cylinders with each of them split into lower and upper parts separated by a metal ring for housing three lateral strain LVDTs, spaced at 120° to each other. The vertical position of these lateral strain LVDTs is 15 mm below the centre of the specimen so that when the specimen shortens during shearing, the lateral strain measurements will always be close to the specimen mid-height. A 50 mm by 20 mm brass plate is glued to the membrane at mid-height of the specimen to act as the target for each lateral strain LVDT. Apart from the three lateral strain LVDTs there are another three axial strain LVDTs attached on the side of the specimen using a connecting system consisting of three Perspex curves assembled around the specimen as shown in Figure 4.7 with each holding an LVDT vertically. A similar system of the perspex curves is used at the lower end to hold the LVDTs target plate. All of the internal LVDTs are immersible free armature LVDTs.

The double-walled cell plumbing system is shown in Figure 4.8 and is briefly described below.

**1. Air Pressure Supply.** Air pressure is supplied by a compressor that is able to provide a maximum of 700 kPa air pressure with  $\pm 1$  kPa pressure variation. The air

pressure supply line is connected to the cell, pore air and pore water pressure line through a pressure regulator.

**2. Filling and Emptying System.** De-aired water used in the test is initially stored in two cylindrical storage tanks each of 30 litres capacity. The water is de-aired by two de-aerators each of 6 litres capacity and is transferred directly to the storage tanks through a tube driven by vacuuming the storage tanks. The storage tanks are connected to the triaxial cell, volume change units, air-water interface tanks and burette for the de-aired water supply. The triaxial cell is connected directly to a drainage line that goes to a sink through which other parts of the system are emptied.

**3. Cell Pressure System.** The double-walled cell consists of inner and outer cells which are connected to the same air pressure supply so that the inner and outer are always subjected to the same pressure. The air pressure supply is connected to two pressure regulators and two pressure gauges arranged in parallel where one line is for low pressure range (0-1 bar) and the other is for high pressure range (0-8 bar). From here the air pressure supply is split into two lines where one line goes through an air-water interface connected to the outer cell while the other line goes through a large volume change unit and connected to the inner cell and a pressure transducer. In this way the specimen volume change can be monitored by the large volume change unit without any chance for the inner cell wall to expand since it is subjected to the same cell pressure on both sides of the wall.

**4. Pore Water and Back Pressure System.** A pore water pressure line comes out from the bottom centre of the base pedestal and is connected to a pressure transducer and a 100cc specimen water volume change unit which is then connected to two pressure regulators and two pressure gauges arranged in parallel.

**5. Flushing System.** During long duration tests, air may dissolve in the specimen pore water and travel through the high air entry ceramic stone and come out from solution underneath the ceramic stone as bubbles. These bubbles must be removed through the flushing system and they are measured in a 10 cc burette so that the recorded specimen water volume change can be corrected. This is also to avoid errors in the measurement of pore water pressure. During flushing the pressure in the flushing line is set equal to the pore water pressure to prevent water from entering or leaving the specimen. In this way the flushing is driven by the difference in pressure head between flushing storage and collector tanks. The flow reversal unit in the flushing system is to reverse the water flow in the spiral grooves underneath the high

air entry ceramic disc where the trapped air bubbles may not be mobilised by flushing in one direction only.

**6. Specimen volume change unit.** The specimen volume change is taken as the volume change of the water in the inner cell. This volume change is measured using an automatic system developed by Fair (2004), which combines the air-water interface tank and the volume change unit into one cylinder as shown in Figure 4.9. The unit has a 70 mm internal diameter and 600 mm internal height giving a measurable volume change of 1770 ml. A magnetic resonance transducer made up of a 10 mm diameter and 500 mm long rod is fitted in the centre of the cylinder from the top cap. The volume of water in the cylinder is measured through the height of a circular magnet fastened on top of a circular float moving concentrically with the transducer rod as water level changes in the unit. The advantage of this large volume change unit is that there is no need to reverse the flow as in the 100cc Imperial College type volume change unit when the volume change is greater than 100 cc. The float is made up of three white coloured low-density engineering plastic discs screwed together.

Due to a lengthy equalisation stage the tests on unsaturated specimens took many weeks. This slow process provided an opportunity for algae growth and this caused the volume change unit float to tilt as shown in Plate 4.7(a). This affected the readings of the specimen volume change as the float carries the responsive circular magnetic ring. Algae are a diverse group of plants that require inorganic nutrients, temperature and radiant energy of sunlight to carry on the processes of photosynthesis for growth (Vandiver, 2002). As dark coloured surfaces absorb light energy then a lesser amount of light will be available for algae growth than with a white coloured surface. Therefore a dark coloured hollow float of smaller diameter of 61.0mm, thickness 15.0mm and mass of 31.0g, as shown in Plate 4.7(b), was designed to replace the earlier float diameter of 66.0mm, thickness 26.0mm and mass of 79.0g. Since the cell inner diameter is 70.0mm there is an adequate clearance of 4.5mm from the wall to avoid the new float getting stuck. Using this float there was no further problems with algae growth.

#### **4.3.4 Rowe Consolidation Cell.**

Based on having a specimen height to particle size ratio of at least 4, Goodwin (1991) developed a Rowe consolidation cell for testing a maximum particle size of 20 mm. The cell and its plumbing system, shown in Figure 4.10, were used to conduct saturated and unsaturated 1-D compression tests. The cell has a 254 mm internal diameter and is made of two conventional Rowe cell bodies, each of height 127 mm, concentrically bolted together with eight bolts. The set up can accommodate a maximum specimen height of 130 mm. The cell was fitted with high air-entry discs at the base of specimen to separate the measurement of the pore air and pore water pressure in the specimen. The measuring system consisted of five 3-bar high air entry ceramics in an aluminium locking ring as shown in Figure 4.11 with an anodised aluminium spiral grooved plate attached on the drainage side underneath. The detailed assembly of the base platen of the consolidation cell is shown in Figure 4.12.

The vertical stress is applied through a water pressure chamber above the top platen and the specimen pore air pressure line went through the central piston attached to the top platen (Figure 4.10). On top of the specimen there was a porous plastic disc of 2mm thickness with 3mm clearance from the cell wall. Goodwin's (1991) original set up for the top platen had three load cells between the parts of the platen which measured directly the load transmitted to the specimen. They have been replaced by steel cylinders since the old load cells were not functioning and much higher stresses than Goodwin's were being used in the current tests.

#### **4.4 Instrumentation and Calibration.**

All four types of laboratory test were conducted in an air-conditioned, temperature-controlled laboratory where the temperature was maintained within  $\pm 2^{\circ}\text{C}$  of  $20^{\circ}\text{C}$ . The calibrations of all measuring devices were conducted in the same laboratory. They were carried out at the beginning and at the end of the testing programme. All calibrations were conducted by the three-cycle method, which involved taking readings at certain increments in three cycles where a cycle is considered from zero to the maximum value and back to zero. All calibrations were made with a voltage

supply of  $\pm 10\text{mV}$  except for the 1770cc volume change unit, used with the double-wall triaxial cell, which used  $\pm 10\text{V}$  supply.

#### **4.4.1 Measuring Devices.**

The pressure plate extractor equipment used one pressure gauge, which was used to set the required air pressure applied to the specimen, and the volume of water expelled from the specimen was measured in a burette. No electronic devices were used with this equipment.

The measuring devices used with the Conventional Triaxial Cell are listed in Table 4.2 and the purposes of the readings are summarized in Table 4.3.

The Double-Wall Triaxial Cell used a total of thirteen transducers. The list of the different transducers, their serial numbers, measuring range and type of measurement are shown in Table 4.4. There were two types of volume change unit used with this cell. The Imperial College type 100cc volume change unit was used to measure specimen water volume change and the 1770cc volume change unit (Fair 2004) was used to measure the inner cell volume change representing the specimen volume change. The purposes of the transducer readings are summarised in Table 4.5.

Tests using the Rowe cell were carried out after the tests with the Conventional Triaxial Cell had finished and used the same pore water pressure, cell pressure and axial displacement transducers as for the Conventional Triaxial Cell. However it had an additional pressure transducer for measuring air pressure applied to the specimen. The devices used with this equipment are listed in Table 4.6 and the purposes of the readings are summarized in Table 4.7. The Imperial College type 100cc volume change unit was only used to measure specimen water volume change during the compression of the specimen. The stress on the specimen was measured through the applied water pressure in the chamber above the top platen by subtracting the effect of wall friction. The wall friction was determined by noting the pressure needed to move the top platen.

#### **4.4.2 Calibration.**

The data from the three cycle calibrations was analysed using a linear regression technique to calculate the calibration factors. The accuracy of each transducer was calculated by dividing the maximum deviation of the logged data from the best fit linear regression line by the full measuring range of the transducer. Calibrations of the transducers were carried out at the beginning and at the end of the testing programme related to the equipment. The time gaps between the initial and the final calibration for the conventional triaxial cell and the double-wall triaxial cell were 17 and 30 months respectively and for the pore air pressure transducer used with the Rowe compression cell was 5 months. The drift, which is the variation in the calibration factor with time, for each transducer was determined after the final calibrations and those that showed a significant drift were corrected by assuming a linear variation of the calibration factors with time.

A Labview computer program from National Instruments was purchased to be used as the new data acquisition software for the Double-wall Triaxial Cell. A graphic type computer program, which could accommodate one channel at a time, was developed for the calibration process. The program consisted of a front control panel and its corresponding circuit diagram. The front panel was designed to define the channel number corresponding to the transducer to be calibrated, the frequency of logging and the filename to store the data. The frequency of logging data could be changed while the program was running. The calibration factor was set as unity with zero intercept during the calibration process. The program for the calibration is detailed in Appendix 1.

Quick Log software was used in the calibration of the transducers used with the Conventional Triaxial Cell and the Rowe cell. The following subsections describe the method used in the calibration of each type of the measuring device.

##### **4.4.2.1 Displacement Transducers.**

There were three types of LVDTs used in the current research. Two were the free armature immersible LVDTs of range 10 and 25 mm used to measure the internal radial and axial strains in the double-wall triaxial cell and the third type was the 50

mm range LVDT, which was used to measure the external axial strain in the double-wall triaxial cell, conventional triaxial cell and the Rowe cell.

The LVDTs were left connected to the logging system for at least one day to warm up before calibration was carried out. They were calibrated using Mitutoyo digital vernier of accuracy 0.0001mm with 1 mm, 2mm and 5 mm displacement increments for the first, second and third types respectively. The typical initial and final calibration curves for the external axial strain, internal radial strain immersible type and the internal axial strain immersible type LVDTs are shown in Figure 4.13, 4.14 and 4.15 respectively.

Table 4.8 shows the calibration factors, accuracies and the drift of each LVDT. The maximum accuracies for type 1, 2 and 3 were 0.34%, 0.4% and 0.2% respectively. The error due to drift of these LVDTs was negligible with a maximum of 0.03mm per month over full range.

#### **4.4.2.2 Volume Change Units.**

There were two Imperial College 100cc type volume change units and one large (1770 cc) fabricated in house volume change unit used in this research. Their uses have been summarised in Tables 4.3, 4.5 and 4.7.

Before calibration, the volume change units were flushed and filled with de-aired and de-ionised water and left under 300kPa pressure connected to the logging system for at least one day to warm up the electrical system and to force any trapped air bubbles into solution. The 100 cc and the 1770 cc volume change units were calibrated against a GDS unit by applying 10 cc and 100 cc volume increments respectively. They were calibrated by doing three filling-emptying cycles under 300 kPa pressure. The typical initial and final calibration curves for all the volume change units are shown in Figure 4.16, and 4.17 respectively.

Table 4.9(a) shows the calibration factors and the maximum accuracy of the Imperial College 100cc type and the large volume change unit were 3.62% and 0.44% and their maximum drifts per month over full range were 0.83cc and negligible respectively.

The significant drift in the 100cc Imperial College type volume change unit used with the conventional triaxial cell was corrected in order to obtain the real volume read out. First the voltage read by the volume change transducer was determined by back calculation from the volume read out and the initial calibration factors applied. Then the actual volume due to the drift was calculated by applying the voltage read to the corrected calibration factors. The latter were deduced base on the date the test was conducted between the dates of the initial and the final calibrations by assuming linear variation. The corrected calibration factors applied for the respective test are shown in Table 4.9(b).

#### **4.4.2.3 Load Cell.**

Two load cells of maximum capacity of 25kN were used. Before starting the calibration the load cells were connected to the logging system for twenty-four hours to warm up and were twice loaded to the maximum load and unloaded.

They were calibrated against a Budenburg Oil Dead Weight tester Model 380 using load frame Model 500 with accuracy 0.4% of the applied load. The load increments applied were 200N up to 2000N, followed by increments of 2000N up to 24,000N and the final increment of 1000N to make up the maximum load of 25,000N. The same magnitudes of load reductions were applied during the unloading cycles. Typical initial and final calibration lines for a load cell are shown in Figure 4.18.

Table 4.10 shows the calibration factors, accuracy and the drift for the load cells used. The accuracies were 1.28% and 0.28% and their drifts in 24 months were 0.78% and 2.27% respectively. Their maximum drift per month over full range was only 37.0N.

#### **4.4.2.4 Pressure Transducers.**

The pressure transducers whose uses are detailed in Tables 4.3, 4.5 and 4.7 were calibrated using a Budenburg Oil Dead Weight tester Model 380. They were initially connected to the logging system for 24 hours and then were quickly loaded twice to the maximum pressure and unloaded before the calibrations were carried out. The calibration was conducted by doing three loading and unloading cycles with 100 kPa increments. Typical initial and final calibration lines for a pressure transducer are shown in Figure 4.19.

Table 4.11 shows the calibration factor, maximum accuracy and the drift of the pressure transducers. The maximum accuracy of the pressure transducers was 1.89% and the maximum drift per month over full range was only 0.34kPa.

#### **4.4.2.5 Pressure Gauges.**

All pressure gauges were calibrated using a Budenburg oil dead weight tester and their accuracy was 1 kPa. The pressure gauges were only used as a pressure reading guide during the pressure application, except for the pressure plate extractor test where pressure gauge readings were taken since no pressure transducer was used to monitor the applied pore air pressure.

#### **4.4.3 Corrections.**

In the triaxial test for the unsaturated specimens the volume change of the specimens was deduced by measuring the inner cell water volume change. However, corrections have to be made for the membrane penetration into the specimen when cell pressure changes and piston penetration into the inner cell during shearing. Corrections for membrane penetration were carried out when there was a cell pressure change, e.g. at the beginning of the consolidation stage where the cell pressure was raised by the magnitude of net stress required. The total volume change due to both the membrane penetration and the compression of the specimen was determined from the volume change indicated by the 1770cc volume change unit. The volume change due to the compression of the soil was calculated based on the soil radial compression indicated by the radial displacement transducers assuming a uniform compression throughout the specimen's height. In this way the volume of membrane penetration can be differentiated from the total volume change. The technique involved the plotting the curve for the variation of the total volume change and the curve for the average radial displacement relative to time during the consolidation on the same graph. This is further discussed in Chapter 5.

Corrections for the piston penetration during the shearing stage have to be carried out in the calculation for the deviator stress since the advancement of the piston also changes in the inner cell water volume.

Another problem, especially when testing using large cells, is water leakage. A leak test was conducted on the double-wall cell in the preliminary stages of the project with the cell being left under a pressure of 250kPa for 2 weeks. The top face of the base pedestal containing the spiral groove was plugged using a rubber membrane of thickness 2.0mm sandwiched between the base pedestal at the bottom and a circular metal plate of the same diameter at the top. The circular metal plate was fastened to the base pedestal using 12 screws. The leak rate was found to be 0.0157cc/hour. However the leak was found to be inconsistent between tests. This may be because as the cell was dismantled and re-assembled, the channel shape, size and length through the O-rings changed between one test and another. Therefore a different correction for water leakage was applied for every test. The correction was only made for the consolidation stage due to the length of time that this stage took. The values of the leakage corrections are presented in Section 5.3.3. No correction was necessary for the shearing stage due to the short test duration. A volume change correction for Perspex absorption was not necessary since the Perspex cylinders were kept submerged in water when not in use, even before starting the first test.

In the Conventional Triaxial Cell tests the membrane penetration during cell pressure increase at the beginning of the consolidation stage has to be corrected. However, in this cell the specimen radial displacements were not monitored and the membrane penetration was judged based on the consolidation curve (i.e. volume change versus time) itself. The initial linear section of the curve was assumed to be due to membrane penetration. The point where the curve diverged from the linear section was taken as the volume of membrane penetration. This is further discussed in Chapter 5.

No correction was made to the specimen axial stress due to membrane restraint since the membrane buckled during shearing. This indicated that the axial stress due to membrane restraint was negligible as well as confirming that there was no slippage between the inner and the outer membranes fitted to the specimen. This indicates that measurement of the internal axial strains by the local axial transducers were reliable.

#### **4.4.4 Data Acquisition System.**

Transducers used with each piece of equipment were connected to a data logging system. The conventional triaxial cell and the 1-D compression Rowe cell used the

same Quick Log logging system, and the double-wall cell used the National Instrument logging system.

Plate 4.8 shows the Logitech data logging system used with Conventional Triaxial Cell. The transducers were connected to a junction box, which was directly linked to a Logitech card slotted in the computer's motherboard. Its software was called Quicklog, which requires calibration factors to convert the signal to the real values to be seen on the screen and automatically saved to the hard disk with a specified filename. The same system was used with the 1-D compression Rowe cell.

Plate 4.9 shows the National Instrument data logging system used for the Double-wall Triaxial Cell. The whole system consists of a signal-conditioning amplifier, to which the thirteen transducers were directly connected. The amplified signals were then passed through a junction box to the National Instrument DAQ cards slotted in the computer's mother board. The Labview software received the signals from the DAQ card and converted them based on the calibration factors. These were displayed as the real values on the screen and saved on the hard disk when required. A similar Labview computer program from National Instruments, as described in Section 4.4.2, was developed for the data acquisition with the Double-wall Triaxial Cell. This data acquisition software accommodated all the thirteen channels at once as opposed to that used during instrument calibration where only one channel could be accommodated. The front panel was designed to define the channel number associated with each transducer and all the initial conditions which included the specimen initial dimensions, the initial transducer readings and filenames used to store the data. The frequency of logging data could be change at the front panel while the program was running. The flow of the program is structured in the block diagram which is interactive with the front panel. The Labview program was linked to Measurement and Automation Explorer which is a Windows-based application and part of the National Instrument software where the calibration factor associated with each channel is defined. The front panel and the block diagram of the program are presented in Appendix 2.

#### **4.5 Test Procedures.**

This section describes the compaction procedure for the preparation of the specimens used for the tests, followed by the detailed test procedures used for setting up and testing the saturated and unsaturated specimens in the pressure plate test, triaxial test and the Rowe cell test.

##### **4.5.1 Determination of the Soil-moisture Characteristic Curve Using the Pressure Plate Extractor Apparatus.**

The pressure plate extractor apparatus and the prepared specimens are shown in Plate 4.4. This experiment was to obtain the soil-moisture characteristic curve of the test material, which relates the moisture content and suction. Each soil specimen was contained in a ring and placed directly onto a 3 bar high air-entry ceramic disc as shown in Plate 4.4(a) and (b). The 3 bar high ceramic disc was saturated before the test and left saturated throughout the test. As long as the air pressure was less than 300kPa the air would not pass through it.

To achieve a constant dry density an identical oven dry mass (341.0g) of the sample was used in each test. It was placed carefully in a 100mm diameter and 25mm high ring, and tapped with the hammer shown in Plate 4.4(b), until the surface was level with the ring's top face. The specimen's density was then 1.74Mg/m<sup>3</sup>. The experiment started with the specimen and the disc flooded with de-aired and deionised water.

With the top cap fastened a constant air pressure was applied to push water through the specimen and the high air-entry disc. Excess water was collected in the burette as shown in Plate 4.4(c) and Figure 4.4, and when an equilibrium condition was reached the outflow ceased and the water level in the burette remained constant. This was because the suction developed between the soil grains due to the formation of a water meniscus and equalled the applied air pressure. By keeping the water level in the burette at mid specimen height the pore water pressure was maintained at atmospheric pressure. Since the difference between the pore-air and the pore-water pressures was the suction then the air pressure applied to the chamber was representing the imposed suction. This process is called equalization and took a minimum of 24 hours depending on the suction induced. The higher the suction the longer was the

equalization period. The specimen was considered equalised when the water level in the collecting burette remained constant for at least 10 hours. The evaporation of water in the burette was prevented by placing a thin layer of kerosene on the water surface. Any expulsion of diffused air through the ceramic disc was readily removed by bubbling out through the burette and thus did not affect the equalised water level in the burette.

This equipment was suitable for a low range of suction application; with a 3-bar ceramic plate extractor the maximum suction that could be applied was about 290 kPa. At the end of equalization the corresponding gravimetric moisture content was determined by immediately weighing the wet specimen and reweighing it after it being dried in the oven for a minimum of 24 hours under temperature of 110 °C.

#### **4.5.2 Conventional Triaxial Cell.**

The conventional triaxial cell was used to obtain the shear strength of saturated specimens using consolidated drained triaxial tests. Initially multistage tests were conducted and then single stage tests were carried out to check the reliability and the repeatability of the results. Each single stage test took approximately a week and the multistage test took 2 days longer with data equivalent to three single stage tests.

##### **4.5.2.1 Preparatory Stage.**

The preliminary stage for the conventional triaxial test was the preparation of the soil sample (Section 4.2.1) and the triaxial apparatus itself. The air-water interface and the 100cc Imperial College type volume change unit have to be replenished with fresh de-aired and de-ionised water since air might have found its way into the units during the period since the last test. The cell base pedestal, the plumbing lines for the back pressure and the pore water pressure were flushed with fresh de-aired and de-ionised water to remove trapped air bubbles.

##### **4.5.2.2 Specimen Compaction Procedure.**

The compaction of the specimens for the triaxial tests used the same mould and the same procedure as described for the compaction test in Section 4.2.2. Initially a membrane, of thickness about 0.5 mm, was folded from inside over the bottom and

the top ends of the mould and secured at both ends using O-rings. Then, a vacuum was applied between the membrane and the mould inner wall to flatten the membrane against the wall. During the compaction process a collar (shown in Figure 4.2) was put in place to protect the membrane from being damaged by the hammer at the top edge.

Layers were added, as described in Section 4.2.2, until the top level of the mould was exceeded and the collar was then removed. The specimen was trimmed slightly lower than mould height by about 2mm to make space for a porous disc to be held firmly in place before the whole mould was turned upside down. Different densities of the soil specimens were achieved by varying the moisture content rather than the compactive effort.

#### **4.5.2.3 Specimen Placement.**

In the preliminary tests, after the specimen had been compacted the mould was placed with its base level with the top of the metal porous disc sitting on the triaxial cell base pedestal as shown in Plate 4.10(a). The mould's tie-bars were then removed and the mould was slid across its base to the pedestal as shown in Plate 4.10 (b). This sliding technique had been used by Salman (1995) but it was found that there was a tendency to lose some of the base particles during sliding if the mould was accidentally tilted.

In order to overcome this problem a new procedure was developed. The specimen was prepared as described in Section 4.5.2.2 with the base porous stone placed on top of the specimen to cap it before the whole set up, weighing about 23 kg, was turned upside down by holding on to the porous stone and placing it directly on to the cell bottom pedestal as shown sequentially in Plates 4.11(a) and (b). This was followed by removing the tie bars and dismantling the mould base plate. Subsequently the top cap was placed onto the specimen. The membrane was then folded around the top cap and the base pedestal and sealed with an O-ring at each end. With the top cap on, the mould needed to be vertically aligned so that the load cell tip would sit directly in the recess on the top cap when the cell body was lowered into position. This was achieved by having a guide beam that spanned between the two loading machine uprights with a centre-indicating needle as shown in Plates 4.12(a) and (b). At this stage the

verticality of the specimen can still be adjusted, but not after the application of a vacuum to the specimen.

Two more O-rings and a second membrane were stretched around two separate split rings of diameter 170 mm and width 30 mm. The split rings and their specially designed connectors are shown in Plate 4.13(a). The pore air pressure line was then put through the split rings and connected to the top cap as shown in Plate 4.13(b). Following this, a vacuum of about 70kPa was applied through the pore air pressure line to hold the specimen and this allowed the mould to be removed. The specimen dimensions were taken as described in Section 4.5.3.3 and a layer of silicon grease was smeared over the membrane to resist the penetration of air through membrane microstructure. This was followed by the installation of the second membrane and finally the specimen was gripped by two O-rings at both ends. With this completed, the next step of the set up was the cell assembly.

#### **4.5.2.4 Cell Assembly.**

The procedure of cell assembly was started by silicon greasing the groove and the O-ring located between the bottom plate and the cell body flange to try to avoid water leakage through the joint. The top cell body containing the load cell was then lowered around the specimen and bolted to the bottom plate. It was very important at this stage to make sure that the load cell tip was correctly positioned in its recess shoe located at the centre of the top platen.

The cell was filled with water until there was overflow from the top bleed valve to avoid trapping air. Then a low cell pressure of 20 kPa was applied and the vacuum was released from the specimen. Subsequently the air pressure line coming out from the specimen top cap was connected to a burette and the specimen was ready for the saturation procedure.

#### **4.5.2.5 Saturation Stage.**

The saturation stage was started by flushing de-aired and de-ionised water from the air-water interface cell (Figure 4.5) through the specimen to fill the void spaces. The volume of flushing water was measured through the Imperial College 100cc volume change unit in the back pressure line. The water was pushed in under a back pressure

of 15 kPa with the cell pressure maintained at 20 kPa by alternate reversing of the Water Flow Reversal Unit. This process continued until air bubbles stopped coming out from the outlet line connected to the top cap and monitored through a burette. This was to make sure that almost all the air voids in the specimen and the top and bottom porous discs were full of water. When this condition was achieved the outlet line was closed and kept closed throughout the test. The next stage was the real saturation stage when a back pressure was applied until a Skempton pore pressure parameter,  $B$ , of close to unity was reached.

This saturation stage was performed using cell pressure increments of 50 kPa followed by similar back pressure increments, always keeping the back pressure 10 kPa less than the cell pressure. A minimum back pressure of 200 kPa was required (Head, 1981) to fully dissolve any air trapped within the specimen. A considerable amount of time was allowed during the water push-in process until the volume change unit indicated no water flow. The Skempton  $B$  value (i.e.  $\Delta u/\Delta\sigma_3$ ) was checked by imposing an increase in cell pressure of 50 kPa and noting the increase in the pore water pressure. A minimum Skempton  $B$  value of 0.92 was obtained for a minimum back pressure of 340 kPa. The saturation stage took approximately 10 hours.

#### **4.5.2.6 Consolidation and Shearing Stages.**

For the consolidation process the cell pressure was elevated higher than the back pressure by the magnitude of the effective stress required for the shearing stage. The back pressure used at the end of the saturation stage was maintained for all tests, except for one multistage test on a specimen compacted at 4% moisture content where the back pressure was reduced. The back pressure should not be reduced by more than 150 kPa and it must be more than 200 kPa to avoid air coming out of the solution and forming air bubbles in the specimen (Head, 1981). The consolidation was carried out by opening the back pressure line under a constant effective stress and monitoring the volume of water expelled. The consolidation of the coarse-grained soil took about one hour until a constant pore water pressure, equal to the back pressure, or the constant specimen volume was achieved.

Once consolidation was complete, the deviator stress could be applied for the shearing stage.

#### **4.5.2.7 Multistage and Single Stage Triaxial Tests.**

In a preliminary test on an unsaturated specimen various strain rates of 0.004, 0.008, 0.0016, 0.0032, 0.0064, 0.0128 and 0.0256mm/min were tried and the pore water pressure was found to be constant throughout the test even with the fastest strain rate. When the fastest strain rate of 0.0256mm/min was tried on a saturated specimen a similar consistent pore water pressure equal to the back pressure was achieved. Therefore this strain rate was chosen for both triaxial tests on saturated and unsaturated specimens. With this strain rate the failure was estimated at 2.5 hours for a strain of 0.8 to 1%, and this fulfilled the requirement for actual time to failure not being less than 2 hours (Head, 1986).

Both single and multistage consolidated drained triaxial tests were performed. This was to check whether the multistage test had any effect on the derived shear strength.

The main advantages of using the multistage technique were that the effect of soil variability in repeat tests can be eliminated and it also allowed for maximum information from a limited number of tests. The multi stage “cyclic loading” procedure (Ho and Fredlund 1982) was adopted where the deviator stress was released whenever the peak value was apparently reached or the specimen started to dilate. This apparent peak deviator stress value was judged based on a maximum rate of increase of deviator stress of 1.0kN/m<sup>2</sup> over 0.01% axial strain. This was followed by another consolidation stage under a new set of stresses. At the end of this consolidation stage, the loading process was repeated. This procedure was again repeated for the third stage.

The single stage triaxial tests were used to determine the volume change behaviour with respect to the net vertical stress before the specimen dilates. Within this strain range the compression was assumed to be one dimensionally vertical. A unique relationship between the rate of increase in internal friction angle and the change in the volumetric state variables is required. The location of the point at which dilation started was very important as it was taken as the upper limit of one-dimensional

vertical compression. It was anticipated that this could be easily determined from the saturated single stage triaxial tests. The unique relationship was required to prove that the angle of rotation of the surface envelope is representing the change in the volumetric state variable and this would thereby validate the proposed shear strength-volume change framework. The dilation point was difficult to ascertain in the multistage test since the first and the second shearing stages had to be stopped whenever it was anticipated that the dilation has started, based on the volume change behaviour and the rate of increase of deviator stress relative to the increase in axial strain. This was not be very accurate since the real behaviour after the stoppage point was uncertain. Moreover, in the third shearing stage particle breakage could have been occurring in the earlier stages and therefore the interpretation of the volume change behaviour would not be convincing.

#### **4.5.3 Double-wall Triaxial Cell.**

The double-wall triaxial cell was described in Section 4.3.3 and the overall set up is shown in Plate 4.14. The step by step cell setting up procedure, starting from the fixing of the high air-entry ceramic disc on to the base pedestal until the specimen was ready for equalisation, is listed in Appendix 3. Equalisation is the process of achieving an equilibrium condition between water content in the specimen and the applied suction. During this process water may be expelled or drawn in through the ceramic disc. Equalisation was carried out under a net cell pressure,  $(\sigma_3 - u_a)$ , of 10kPa and suction,  $(u_a - u_w)$ , equal to the suction under which the specimen was to be sheared.

Improvements to the experimental setting up procedures used by Salman (1995) with this cell include the specimen placement technique and the internal transducer holding system and the installation of this system.

##### **4.5.3.1 Preparatory Stage.**

Initially the double cylindrical storage tanks shown in Plate 4.14 were filled with fresh de-aired and de-ionised water for each test. Before the cell setting up was carried out all the plumbing systems involving the pore water and the cell water were flushed with de-aired and de-ionised water in order to get rid of air bubbles. The triaxial cell bottom plate, base pedestal and inner top plate, assembled with the piston and load

cell at its end, were fixed to the loading machine platen for the duration of the testing. During setting up the piston was raised and clamped from the top face of the inner top plate to prevent it interfering with the space needed for the specimen placement.

Saturation of the high air-entry ceramic disc for the cell base platen began at least four days before the cell setting up. The saturation was carried out by fixing the disc onto the base plate of a Rowe cell, as shown in Figure 4.20, and filling the chamber with de-aired and de-ionised water subjected to a constant pressure. The 1-bar and the 3-bar ceramic discs used with the double-wall cell were saturated at pressures of 240 and 500kPa respectively. This pushed the water through the high air-entry ceramic disc. Every day, water was allowed to flow through the disc for 5 minutes and the de-aired and de-ionised water was topped up whenever required. This 5 minute flow was performed for three consecutive days before the disc could be used.

The compaction of the specimen was carried out in a similar manner to that described in Sections 4.2.2 and 4.5.2.2. Layers were added until the top level of the mould was exceeded and the collar was then removed. In this case the specimens were trimmed to the exact height of the mould so that the soil was flush with a metal plate placed on top of it. This avoided soil disturbance when the whole mould was turned upside down using the new specimen placement technique. All specimens were compacted at 4% moisture content except for one specimen which was compacted at 1% moisture content.

The installation of the ceramic disc onto the pedestal was carried out once the compacted specimen was ready to be put in the cell. Before the ceramic disc was placed onto the base pedestal, the spiral groove on the top face of the base pedestal was cleaned and smeared with silicon grease to prevent water leakage. Once in place the disc bottom must be at all times connected to a continuous supply of de-aired and de-ionised water stored in the Flushing Storage Tank (Plate 4.14) and linked through the Flow Reversal Unit. When the atmospheric pressure outlet valve of the flushing storage tank was closed negative pressure was developed in the system. It was very important that this negative pressure did not become less than -100 kPa (i.e. for the 1 bar high air-entry ceramic disc) when the vacuum was applied to the specimen during its installation process. This was to avoid any air coming out of solution and

infiltrating the ceramic disc from the bottom face. As long as this condition was met the atmospheric outlet valve of the flushing storage tank could be closed to avoid water filling up the specimen during the cell assembly process.

#### **4.5.3.2 Specimen Placement and Measurement of Specimen Dimensions.**

When using this equipment Salman (1995) had transferred the compacted specimen to the base pedestal by a similar sliding technique to that described for the Conventional Triaxial Cell in Section 4.2.5.3. Loss of material during the sliding jeopardized the quality of the specimen. The same improved technique as used in the conventional cell could not be applied here since the high air-entry ceramic disc needed to be fitted onto the cell base pedestal prior to the specimen placement.

After compaction the specimen was trimmed level with the mould top edge. Then a rigid metal plate of thickness approximately 1.0 mm with a grip hole in it was placed over the mould and, while continuously pressing it against the mould, the whole set up was turned upside down and placed on a wooden block as shown in Plate 4.15(a). At this point the base of the rigid metal plate was level with the top of the ceramic disc. Then the mould base plate, which was now at the top, was removed as shown in Plate 4.15(b). As the height of the wooden block was level with the top of the ceramic disc the whole set up was able to be slid to sit directly on top of the ceramic disc by pushing the rigid metal plate as shown in Plate 4.15(c). In this way there was no chance of tilting the mould and losing material. Three clamps on the three inner cell columns held the mould centrally in place as shown in Plate 4.15(d). Then the nut and bolt system was fitted on each clamp and the three jacking nuts (Plate 4.15(d) and Plate 4.16) were turned carefully to prop the mould without inducing any lifting. The rigid metal plate separating the specimen and the ceramic disc could then be gently pulled out since the mould was clamped firmly in place. This technique succeeded in placing the specimen without losing any material.

Once the mould and the specimen were positioned exactly on the ceramic disc then the lower end of the membrane and the O-ring were rolled off the bottom of the mould and onto the base pedestal. Then a metal porous disc and the top cap were placed on the specimen and the top end of the membrane was folded over and gripped by an O-ring. The load cell was lowered to sit directly in the recess at the centre of the

top cap thus properly aligning the specimen. This was followed by stretching two O-rings and a membrane around split rings (Plate 4.12(a)) in similar manner for setting up the conventional triaxial cell (Section 4.5.2.2) and putting them round the air pressure line as shown in Plate 4.17. The pore-air pressure line was then fitted to the top cap and subsequently a vacuum was applied to the specimen to allow the removal of the split-mould. Once the cylindrical specimen enclosed by the first membrane was exposed, the diameter and height were measured. Three diameter measurements were taken, two of which were close to the ends and one at the centre height using the special calliper shown in Plate 4.18.

Silicon grease was then uniformly applied to the membrane before a second membrane was placed around it, as shown in Plate 4.19. Then both O-rings were shifted carefully one after another to grip onto the second membrane at both ends avoiding loss of the vacuum.

#### **4.5.3.3 Installation of the Local Displacement Transducers.**

According to the installation technique developed by Salman (1995) the level for the local axial strain LVDT Perspex holder curves and LVDT Perspex target holder curves were marked on the membrane. Then the top and bottom Perspex curves holder systems were placed around the specimen as shown in Figure 4.7, level with the marks and glued to the membrane using superglue.

Problems of alignment were encountered using the Salman (1995) holders shown in Figure 4.21. The problems were overcome by redesigning the joint system for the top and bottom Perspex curves system to have a double, and symmetrical, guide rod system as shown in Figure 4.22. With this type of jointed system the internal axial transducers could be easily aligned and also it ensured a uniform expansion of the system, which was essential to maintain the verticality of the transducers whenever the specimen changed shape during the test.

To ensure the verticality of the internal axial transducers, the top and bottom systems of three Perspex curves have to be aligned in the same horizontal plane. To make sure that the elevation of the internal axial transducers and the gauge height were consistent in every set up, a standard procedure was employed. Three stands with

equal fixed height were used to hold the Perspex curves during their installation. This produced a consistent position of the gauge height in every test. It also eased the installation of the Perspex curves by holding them at this exact height and thus ensured they were level in the same horizontal plane. Since there were two sets of Perspex curve systems (i.e. transducers holder and the transducers target holder) at different levels, two sets of stands were required with each set consisting of three stands of equal height. The heights of the three-stand system were designed to produce a centre gauge height of 200 mm. The taller and shorter sets of the three-stand system are shown in Plate 4.20(a) and (b) respectively. The installation began with the fixing of the top transducers' holder system. Once this had been assembled by having the two sets of rubber bands at each joint in place as shown in Figure 4.22, the glue was applied at the three points on the membrane to stick the centre of each Perspex curve onto it. After applying the glue the Perspex curves were adjusted to sit firmly on to the stands while waiting for the glue to set. Then the taller set of the three-stand system was removed and the same procedure was applied to the lower transducers' target holder system. In this way the verticality of the transducers and gauge height of 200mm could be set up consistently in every test without having to make any marks on the membrane.

Once the two Perspex curves holding systems were installed and the transducers and their armatures and extenders were fitted, the lower inner and outer cell and the radial LVDT housing ring (see Figure 4.6) could be lowered into position ready for the installation of the radial transducers and their targets. The targets were rectangular 1mm thick aluminium plates of dimensions 20 mm by 15 mm stuck to the membrane using superglue.

Once the radial LVDT housing ring was put in place and the radial transducers and their target plates had been installed, the rest of the cell components could be assembled. The bleed ring at the top of the cell was the last to be fastened. The bleed ring was put in place when the cell water was filled up to the level that would produce a slight overflow when it was fastened. This was to avoid trapping air bubbles at the bottom of the inner top plate.

When the cell assembly had been completed the transducer leads were plugged into the signal amplifier and the instrumentation was allowed to warm up for 20 minutes. In the meantime a cell pressure of 30 kPa was applied and the vacuum on the specimen could be released. The air line was connected to the pore air pressure line and an air pressure of 20 kPa and pore water pressure of 10 kPa were applied. At this point, the specimen was ready for the equalisation stage.

Before commencing the equalisation stage the Labview program was run and initial data were stored under an appropriate filename. The equalisation stage was carried out under cell and pore air pressures of 100 and 90 kPa respectively for the tests with suctions of 25, 50 and 60 kPa using a 1 bar air-entry ceramic disc. However for tests with a suction of 90 kPa cell and pore air pressures of 110 and 100 kPa respectively were applied, but using a 3 bar air-entry ceramic disc. The required suction, ( $u_a - u_w$ ) was achieved by adjusting the pore water pressure. However, due to the application of a vacuum to the specimen during the setting up process some water had been drawn in, and in the equalisation stage the excess water was drained out of the specimen until the drain rate decreased to 0.05 cc in 12 hours. Once this rate of water drainage was achieved the equalisation stage was considered complete and the specimen was ready for the next stages which were the consolidation and multi-stage shearing.

#### **4.5.3.4 Multistage Consolidation and Shearing.**

Apart from the advantages described in Section 4.5.2.7, there are other advantages of using multistage shearing for shear strength tests on unsaturated specimens of compacted coarse-grained soil. This method can considerably reduce the testing time since the equalisation stage required for the large specimen size (i.e. 150mm diameter and 375mm height) was approximately six to eight weeks. Therefore with the multistage method the whole test for three different effective stress levels will take a maximum of nine weeks. Using the single stage technique to obtain the same amount of data would have taken almost three times as long. The same method of multistage testing described in Section 4.5.2.7 for the triaxial tests on saturated specimens was applied in the Double-wall Triaxial Cell.

At end of equalisation the pore air pressures were either 90 or 100kPa depending on the air-entry value of the disc used (refer to Section 4.5.3.4). In the first, second and

third consolidation stages the cell pressures were raised to achieve net pressures of 100, 200 and 300kPa respectively while the inner and the outer cell pressure valves were closed. The consolidation was started by opening both valves simultaneously. Before these valves were opened the volume change unit was already subjected to the elevated cell pressure since it was directly connected to the cell pressure supply (refer Figure 4.8). Therefore the change in the water level in the inner cell water volume change unit when the consolidation began was purely due to the specimen volume change and not the compression of the water. The specimen was allowed to consolidate for about 10 hours.

Once the consolidation was complete the deviator stress was applied to begin the first shearing stage. The strain rate for all shearing stages was maintained at 0.0256mm/min. Failure was indicated by the flattening of the curve of deviator stress versus external axial strain monitored on the computer screen which also indicated that a maximum rate of increase in the deviator stress of  $1.0\text{kN/m}^2$  with respect to the increase in the axial strain of 0.01% was achieved. Once this was achieved the axial load was rapidly released until the reading of the load cell was zero and approximately 1 hour was allowed for the specimen's dimensions to stabilise before commencing the second consolidation stage. A similar procedure was applied for the second consolidation and shearing stages up to the third consolidation stage. In the third shearing stage the shearing was extended beyond the point of peak deviator stress. During the consolidation and shearing all the readings of the thirteen transducers were logged.

The graphs of deviator stress versus axial strain are similar to the single stage test graphs except that the curves for the second and the third shearing stages start from the strain corresponding to the unloaded condition of the previous stage. The graphs for the first two stages were extrapolated on similar lines to the behaviour of the third stage in order to determine their failure conditions.

#### **4.5.4 Suction Controlled Compression Test Using a Modified Rowe Cell.**

The set up of the modified Rowe cell and the plumbing system are shown in Figure 4.10. Before starting the test the ceramic disc was fastened to the base plate and saturated by pressurising de-aired and de-ionised water at 500kPa in the cell for three

consecutive days and allowing a three hour flow each day. In the unsaturated compression test the suction was again applied using the axis-translation technique, where the pore-water pressure was set to atmospheric by connecting the chamber below the 3-bar high air-entry ceramic disc to an open burette while the required pore air pressure was applied to the main chamber containing the specimen.

The bottom high air entry ceramic plate was used to separate air from water, which enabled the independent measurement of the pore air and pore water pressure. During the equalisation stage, water always drained out from the specimen and the rate was measured by timing the volume collected in a burette connected to the outlet. Equalisation was considered complete when the outflow rate reached 0.05cc in 12 hours.

#### **4.5.4.1 Specimen Placement and Cell Assembly.**

The samples were prepared in a similar manner to the triaxial test samples as described in Section 4.2.1. Water was added to the washed sample to get the required moisture content and it was mixed for 10 minutes in the 30kg mixer and subsequently poured loose into the Rowe cell from the level of the cell top up to a marked level. The marked level corresponded to a specimen height of 125.0mm. This was followed by the insertion of the top platen using the jack system shown in Plate 4.21. The jack was bolted to the top platen at three anchorage points and to the Rowe cell body on its upper flange at four points, with spacers between the cross bar supporting the jack and cell flange to allow the top platen to be manually wound clear of the cell. The same set up was used to extrude the top platen from the cell at the end of the test. Once the top platen was wound into place the jack system was dismantled and the top cap was bolted down. The chamber between the top plate and the top platen was filled up with water. The details of this procedure can be found in Goodwin (1991).

#### **4.5.4.2 Equalisation Stage.**

The equalization was carried out by applying the appropriate pore air pressure to the specimen. In this case, since the pore water pressure below the high air-entry ceramic disc was set at atmospheric, the magnitude of the applied pore air pressure represented the applied suction. However to avoid the top platen from being pushed upwards during the application of the pore air pressure, this pressure was balanced with the

same water pressure in the chamber between the top plate and the top platen. At this stage excess pore water will be forced through the high air-entry ceramic disc fastened onto the base plate and the volume monitored in an open burette. However the volume of water discharged had to be corrected for the volume of diffused air trapped underneath the ceramic disc. The volume of diffused air was determined by flushing the compartment below the ceramic disc with a pressure of 50 to 100kPa and the diffused air was collected in an inverted test tube initially filled with de-aired water as shown in Figure 4.10. The maximum period of each equalization flow was 15 hours and the minimum was several minutes, especially during the early stages of equalization. The equalization was achieved when the net outflow rate reached 0.05cc in 12 hours.

#### **4.5.4.3 Compression Stage.**

Once equalisation had been achieved the specimen was ready for the compression stage where it was subjected to increments of constant net vertical pressure until the settlement ceased under each increment. The magnitude of the friction between the top platen and the inner cell wall had to be determined to apply an appropriate correction to the applied pressure. The friction prior to each test was determined by applying an effective cell pressure with increments of 10kPa until an apparent movement of the piston was noticed. At this point the magnitude of the effective cell pressure was taken as the friction.

In the compression stage the pore-water pressure line was connected to a burette where the specimen water volume changes were measured. The specimen height was measured using an external LVDT fixed on to the central piston rod protruding above the top plate. The total specimen volume change was obtained by multiplying the cross sectional area of the cell with the changes in the specimen height measured with an LVDT mounted on the central piston rod connected to the top platen. The specimen was compressed with effective stress increments of 50kPa up to 500kPa. Under each effective stress the pressure was maintained until the specimen height remained constant which took between 15 to 40 minutes.

#### **4.6 Test Programmes and Objectives.**

The laboratory test programme was to achieve objective numbers 4 to 8 (refer to Chapter 1) and was divided into series A, B, C, D and E. Test series A, B and C were to achieve objective numbers 4, 5 and 6 respectively. The combination of test series A, B and C was targeted to obtain the shear strength envelope for the test material and at the same time to validate the proposed shear strength model which was objective number 2. Test series B and C were also used to find out whether particle breakage had imposed any limitations on the framework; this was objective number 7. Test series D was to determine how overall interparticle contact area determined by the soil grading affected the shape of the shear strength envelope. This was to be linked with the effect of particle breakage on shear strength which is part of objective number 7. Test series E was to determine the volume change behaviour of the test material with respect to suction, net stress and effective stress and to prove that the test material does exhibit collapse behaviour when inundated. The combination of test series B, C and E was to completely fulfil objective numbers 8 and 9, which were the validation of the shear strength-volume change framework and the formulation of the constitutive volume change equation for saturated and unsaturated soils. The details of the laboratory test programmes and their respective objectives are described in the following sub sections.

##### **4.6.1 Test Series A: Determination of the Soil-Moisture Characteristic Curve.**

The main purpose of this series of tests carried out using pressure plate apparatus was to obtain the soil-moisture characteristic curve for the test material. The significance of this curve is that it will determine the residual suction, which corresponds to the maximum apparent shear strength of the test material. The tests used a 3-bar high air-entry ceramic disc so that a maximum suction of 290kPa could be achieved. The tests were conducted for suctions of 5, 6, 10, 15, 20, 50, 75, 100, 125, 150, 175, 200, 225, 250, 275, 290kPa.

##### **4.6.2 Test Series B: Determination of the Saturated Shear Strength Behaviour with respect to Effective Stress.**

The objective of this series was to obtain the variation of saturated shear strength with respect to effective stress. Consolidated drained triaxial tests were carried out at

effective stresses of 100, 200 and 300kPa. One test was carried out at an effective stress of 250kPa due to a problem encountered with the pressure supply. The tests were carried out on specimens compacted at moisture contents of 4%, 6%, 8% and 12%.

Both, multistage and single stage tests were conducted. The single stage tests were to confirm the reliability of the multistage test since in the triaxial tests on unsaturated specimens only multistage tests were conducted for maximum information due to the very long period of equalization required in every test. The tests carried out for this series are as tabulated in Table 4.12.

The tests were coded as S4%SSSES100 where the first alphabet S denotes the saturated triaxial test, the second numeric percentage denotes the moisture content when the specimen was compacted, and the following coding is either SS, which stands for single-stage triaxial test or MS, which stands for multi-stage triaxial test. The end coding ES stands for effective stress followed by a three-digit number which indicates the magnitude of the effective stress in kPa.

#### **4.6.3 Test Series C: Determination of the Unsaturated Shear Strength Behaviour with respect to Suction.**

The objective of this series was to determine the variation of apparent shear strength with respect to suction and effective stress. Initially all specimens were planned to be compacted at 4% moisture content. However, when it was realised that the moisture content did not have a significant influence on the achieved compacted dry density, the specimen for suction 90kPa was compacted at moisture content of 1% so as to accelerate the process of equalization. All tests were conducted by the multistage technique.

The test conditions for this series are summarized in Table 4.13. The tests were coded as USSuc50NS100 where the first two letters indicated a test on unsaturated specimen and the following five codes denoted the magnitude of suction applied in the test indicated by the two numeric letters, and the last five codes denoted the magnitude of the applied net stress in kPa indicated by the last three numbers.

#### **4.6.4 Test Series D: Determination of the Effect of Particle Size Distribution on the Shear Strength Surface Envelope.**

The objective of this series was to determine how particle size distribution affected the shape of the failure envelope at the point before any breakage occurred. This was achieved by conducting consolidated drained triaxial tests on saturated specimens of uniform grading made up of particles of minimum size of 5mm. The samples for these tests were obtained by sieving the washed material through a 5mm sieve and using the material retained on the sieve to form the specimens. There were two single stage triaxial tests carried out in this series and the specimens were sheared under effective stresses of 100 and 200kPa only since a higher effective stress could have induced breakage. The wider grading of the original test material was to represent the strength of the greater overall interparticle contact area which contained particles smaller than 5mm. The shearing rate was similar to the other triaxial tests, i.e. 0.0256mm/min.

The tests were coded similar to test series B but the addition of “Min5” of the test code was to indicate the minimum particle size of 5mm. The test conditions and the corresponding test codes for this series are summarised in Table 4.14.

#### **4.6.5 Test Series E: Determination of the 1-D Volume Change Characteristics of the Test Material under Different Suctions.**

The objective of this series was to determine the volume change behaviour with respect to net vertical stress under different suctions and to find out whether the test material exhibited collapse behaviour when the conditions approached saturation. The large Rowe compression cell apparatus was used for this test series. There were three tests in this series as listed in Table 4.15. The first two were unsaturated compression tests carried out under suctions of 25 and 50kPa and the third one was compression under saturated conditions. In the first two tests the soil samples were mixed uniformly with moisture contents of 2.1% and 1.9% respectively. These moisture contents were anticipated to correspond to the targeted suctions so as to speed up the process of equalization. For the saturated test a dry soil sample was poured into the cell in the same manner as the unsaturated specimens and de-aired and deionised water was added later. The water was added gently from the specimen’s top face until the specimen was flooded and no collapse was noticed at this stage. This was followed by the installation of the top platen and the cell top cap. For the unsaturated

tests the equalization stage began by applying the appropriate pore air pressure to the specimen with the pore water pressure being zero by opening the pore water line from the bottom of the ceramic disc to the atmosphere. The specimen condition was considered equalized when the outflow rate reached 0.05cc in 12 hours. In the case of the saturated test the compression stage could begin immediately once the top cap was placed. The tests in this series are coded as “CompSuc50” where the word “Comp” denotes a 1-D compression test and this is followed by the code that signified the magnitude of suction applied in the case of unsaturated tests. The saturated compression test was denoted by “CompSat”.

Table 4.1 Chemical composition of test material (Goodwin, 1991).

Chemical compound	Percentage of total by mass
CaCO <sub>3</sub>	79.97
MgCO <sub>3</sub>	11.50
SiCO <sub>2</sub>	2.80
CaSO <sub>4</sub>	2.28
Fe <sub>2</sub> O <sub>3</sub>	2.03
Al <sub>2</sub> O <sub>3</sub>	1.00
K <sub>2</sub> O	0.12
MnO	0.06
P <sub>2</sub> O <sub>5</sub>	0.05
TiO <sub>2</sub>	0.03
Na <sub>2</sub> O	< 0.10
Total	99.84 excluding Na <sub>2</sub> O

Table 4.2 Transducers used in the Conventional Triaxial Cell Tests.

No. of Transducers	Type of Transducer	Serial No.	Measuring Range	Type of Measurement
1	LVDT	HS50/4017	0 – 50mm	Specimen external axial strain
1	Imperial College 100cc volume change unit	VOL/G 025	0 – 100cc	Specimen volume change
2	Pressure transducer	334740 and 334923	0 – 700kPa	Cell and pore water pressures
1	Load cell	8903979	0 – 25kN	Piston load

Table 4.3 Purposes of the transducers used with the Conventional Triaxial Cell.

No.	Transducer type	Dimension measured	Transducers' readings application in the calculation of stress and strain.
1.	External axial displacement transducer.	To measure the penetration of the load cell piston into the cell during shearing.	To calculate the % axial strain. To determine the specimen's shortened height during the application of deviator stress so as to calculate the current cross sectional area. This is required for the calculation of the deviator stress.
2.	100 cc Specimen water volume change unit.	To measure and monitor the specimen volume change during shearing.	To determine specimen current volume during shearing in order to calculate the specimen's current cross sectional area for the calculation of deviator stress.
3.	Load cell	To measure the applied load during shearing.	To calculate the deviator stress during shearing.
4.	PWP transducer	To measure the pore water pressure during consolidation and ensure it is constant during shearing in the drained triaxial test.	To calculate the actual effective stress applied to the specimen during shearing.
5.	Cell pressure transducer	To measure the cell pressure applied during the test.	To calculate the major and minor principal stresses.

Table 4.4 Transducers used in Double-wall Triaxial Cell Tests.

No. of Transducers	Type of Transducer	Serial No.	Measuring Range	Type of Measurement
3	Free Armature, Immersible LVDT	DS200W-50953 DS200W-50954 DS200W-50955	0 – 10mm	Internal radial displacement
3	Free Armature, Immersible LVDT	DS500W-50956 DS500W-50957 DS500W-50958	0 – 25mm	Internal axial displacement
1	LVDT	HS50/7070	0 – 50mm	Specimen external axial strain
3	Pressure transducer	TJE229184 TJE243512 TJE233165	0 – 700kPa	Cell, pore air and pore water pressures
1	Imperial College type volume change unit	LVDT6015	0 – 100cc	Specimen water volume change
1	Large volume change unit fabricated in-house	Nil	0 – 1770cc	Specimen volume change
1	Load cell	22848	0 – 25kN	Piston load

Table 4.5 Purposes of the transducers used with the Double-wall Triaxial Cell.

No.	Transducer type	Dimension measured	Transducers' readings application in the calculation of stress and strain.
1.	Internal radial displacement transducers (3 nos.)	To measure the radial expansion of the specimen at mid height.	During shearing the diameter changes were based on the readings of these transducers and the cell volume change unit. These radial strains were used with the internal axial strain to calculate the volumetric strain, $\epsilon_v$ .
2.	Internal axial displacement transducers (3 nos.)	To measure the height changes within the gauge height of 200mm of the specimen during consolidation and shear.	To calculate the changes in the specimen gauge height during consolidation and shearing and used in the calculation to obtain the resultant specimen's cross sectional area.
3.	External axial displacement transducer	To measure the penetration of the piston into the inner cell during shearing.	To calculate the volume change the load cell piston penetration into the inner cell during shearing process. A correction can then be made for the calculation of the current cross sectional area of the specimen.
4.	1770 cc inner cell water Volume Change Unit	To measure the volume change due to the dilation or shrinkage of the specimen during shearing.	Primarily used to calculate the change in the cross sectional area of the specimen during shearing. To measure the specimen volume change during consolidation and shearing. The effect of the membrane penetration that occurs at the beginning of the consolidation process when the cell pressure is elevated has to be taken into account.
5.	100 cc Specimen water volume change unit.	To measure and monitor the changes in the specimen water during equalisation and shear	To calculate the rate of water dissipated or drawn into the specimen during equalisation and which determines the end of equalisation stage.
6.	Load cell	To measure the applied load during shearing.	To calculate the deviator stress during shearing.
7.	PWP transducer	To measure the applied constant PWP during equalisation and to monitor PWP variation if any during consolidation and shearing.	To calculate the suction.
8.	PAP transducer	To measure the applied constant PAP during equalisation, consolidation and shearing	To calculate the suction, net cell pressure and net vertical pressure.
9.	Cell pressure transducer	To measure the cell pressure applied during the test.	To calculate the major and minor principal stress.

Table 4.6 Transducers used in the Rowe Consolidation Cell.

No. of Transducers	Type of Transducer	Serial No.	Measuring Range	Type of Measurement
1	LVDT	HS50/4017	0 – 50mm	Specimen external axial strain
1	Imperial College 100cc type volume change unit	VOL/G 025	0 – 100cc	Specimen water volume change
3	Pressure transducer	334740, 334923 and L117287	0 – 700kPa	Cell, pore water and air pressures

Table 4.7 Purposes of the transducers used with the Rowe Consolidation Cell.

No.	Transducer type	Dimension measured	Transducers' readings application in the calculation of stress and strain.
1.	External axial displacement transducer	To measure the axial movement of the top platen.	To calculate the volume change of the specimen during the compression.
2.	PAP transducer	To make sure that a constant pore air pressure is maintained throughout the equalization and compression stages.	To calculate the suction, net vertical stress and effective stress applied to the specimen.
3.	Cell pressure transducer	To measure the cell pressure applied during the test.	To calculate the net vertical stress applied during compression stage.

Table 4.8 Calibration factors and drift for displacement transducers (LVDTs).

LVDT's serial number	Type of equipment	Type of measurement	Calibration factor before and after test programme	R <sup>2</sup> Before and after tests	Accuracy %	Drift per month over full range
HS50/4017	Conventional Triaxial Cell and Rowe cell	Specimen external axial displacement	-3698.2 and -3662.2 mm/V	1.0000 and 1.0000	0.17	0.03mm
DS200W-50953	Double-wall Triaxial Cell	Internal radial displacement	-0.5071 and -0.5052 mm/mV	1.0000 and 1.0000	0.25	negligible
DS200W-50954	Double-wall Triaxial Cell	Internal radial displacement	-0.7551 and -0.7500 mm/mV	1.0000 and 1.0000	0.34	negligible
DS200W-50955	Double-wall Triaxial Cell	Internal radial displacement	-0.7465 and -0.7414 mm/mV	1.0000 and 1.0000	0.30	negligible
DS500W-50956	Double-wall Triaxial Cell	Internal axial displacement	-1.2665 and -1.2549 mm/mV	1.0000 and 1.0000	0.40	negligible
DS500W-50957	Double-wall Triaxial Cell	Internal axial displacement	-1.2711 and -1.2567 mm/mV	1.0000 and 1.0000	0.32	negligible
DS500W-50958	Double-wall Triaxial Cell	Internal axial displacement	-1.2630 and -1.2544 mm/mV	1.0000 and 0.9999	0.24	negligible
HS50/7070	Double-wall Triaxial Cell	Specimen external axial displacement	2.5821 and 2.5851 mm/mV	1.0000 and 1.0000	0.20	negligible

Table 4.9 Calibration factors, drift and corrected calibration factors for volume change units.

## (a) Calibration factors and drift for volume change units.

Type of volume change unit and serial number	Type of equipment	Type of measurement	Calibration factor before and after test programme	R <sup>2</sup> Before and after test	Accuracy %	Drift per month over full range
Imperial College 100cc type VOL/G 025	Conventional Triaxial Cell	Specimen volume change	-4227.2 and -4469.2 cc/V	0.9996 and 0.9982	1.37	0.83cc
Imperial College 100cc type LVDT 6015	Double-wall Triaxial Cell	Specimen water volume change	-4.8534 and -4.8713 cc/mV	0.9991 and 0.9978	3.62	negligible
Large volume change unit 1900cc	Double-wall Triaxial Cell	Specimen volume change	-102.35 and -102.46 mm/mV	1.0000 and 1.0000	0.44	negligible

## (b) Corrected calibration factors for 100 cc Imperial College volume change unit used with the conventional triaxial cell due to significant drift.

Test code	Test date	Period from initial calibration (days)	Calibration factors	
			m	c
Initial calibration	28.07.2003	0	-4227.2	+140.1
Final calibration	15.12.2004	504	-4469.2	+128.3
S4%SSES100	23.11.2003	119	-4284.3	+137.3
S4%SSES200	11.2.2004	199	-4322.8	+135.4
S4%SSES300	18.2.2004	206	-4326.1	+135.3
S6%SSES100	10.12.2003	146	-4297.3	+136.7
S6%SSES200	2.3.2004	218	-4331.9	+135.0
S6%SSES250	6.3.2004	222	-4333.8	+134.9
S8%SSES100	5.12.2003	131	-4290.1	+137.0
S8%SSES200	31.5.2004	309	-4375.6	+132.9
S8%SSES300	6.6.2004	315	-4378.5	+132.7
S0%SSES100	19.4.2004	267	-4355.4	+133.8
S0%SSES200	22.4.2004	270	-4356.8	+133.8
S0%SSES300	29.4.2004	277	-4360.2	+133.6
S4%MST1	25.9.2003	60	-4256.0	+138.7
S4%MST2	3.11.2003	109	-4279.5	+137.5
S12%MST1	13.11.2003	119	-4284.3	+137.3

Table 4.10 Calibration factors and drift for load cells.

Type of load cell and serial number	Type of equipment	Type of measurement	Calibration factor before and after test programme	R <sup>2</sup> Before and after test	Accuracy %	Drift per month over full range
Wykeham Farrance Int.Ltd. 8903979	Conventional Triaxial Cell	Axial load	3197541.5 and 3222370.0 N/V	1.0000 and 1.0000	1.28	37.0N
Wykeham Farrance Int.Ltd. 22848	Double-wall Triaxial Cell	Axial load	-1286.12 and -1315.30 N/mV	1.0000 and 0.9995	0.28	1.2N

Table 4.11 Calibration factors and drift for pressure transducers.

Transducer's type and serial number	Type of equipment	Type of measurement	Calibration factor before and after test programme	R <sup>2</sup> Before and after test	Accuracy %	Drift per month over full scale
10Volts Druck Ltd. 334923	Conventional Triaxial Cell and Rowe cell	Pore water pressure	17991.9 and 18078.1 kPa/V	1.0000 and 1.0000	0.22	0.34kPa
10Volts Druck Ltd. 334740	Conventional Triaxial Cell and Rowe cell	Cell pressure	18246.3 and 18054.8 kPa/V	1.0000 and 1.0000	0.28	0.04kPa
R.D.P. Electronic Ltd. TJE233165	Double-wall Triaxial Cell	Pore water pressure	35.811 and 35.638 kPa/mV	1.0000 and 0.9999	0.08	negilgible
R.D.P. Electronic Ltd. TJE243512	Double-wall Triaxial Cell	Pore air pressure	35.427 and 35.414 kPa/mV	1.0000 and 1.0000	0.15	negilgible
R.D.P. Electronic Ltd. TJE229184	Double-wall Triaxial Cell	Cell pressure	36.530 and 37.333 kPa/mV	1.0000 and 0.9998	1.14	0.03kPa
10Volts Druck Ltd. L117287	Rowe Cell	Pore air pressure	39506.3 and 40085.6 kPa/V	0.999 and 1.0000	1.89	0.20kPa

Table 4.12 List of consolidated drained triaxial tests on saturated specimens for test series B.

Test no.	Type of test	% moisture content during specimen compaction	Effective stress (kPa)	Test code
1	Single stage	4%	100	S4%SSES100
2	Single stage	4%	200	S4%SSES200
3	Single stage	4%	300	S4%SSES300
4	Single stage	6 %	100	S6%SSES100
5	Single stage	6 %	200	S6%SSES200
6	Single stage	6 %	250	S6%SSES250
7	Single stage	8%	100	S8%SSES100
8	Single stage	8%	200	S8%SSES200
9	Single stage	8%	300	S8%SSES300
10	Single stage	Loose pour	100	S0%SSES100
11	Single stage	Loose pour	200	S0%SSES200
12	Single stage	Loose pour	300	S0%SSES300
13(a)	Multistage	4 %	100	S4%MST1ES100
13(b)			200	S4%MST1ES200
13(c)			300	S4%MST1ES300
14(a)	Multistage	4 %	100	S4%MST2ES150
14(b)			200	S4%MST2ES200
14(c)			300	S4%MST2ES300
15(a)	Multistage	12%	100	S12%MST1ES100
15(b)			200	S12%MST1ES200
15(c)			300	S12%MST1ES300

Table 4.13 List of consolidated drained triaxial tests on unsaturated specimens for test series C.

Test no.	Type of test	% mc during compaction	Effective stress (kPa)	Suction (kPa)	Test code
1(a)	Multistage	4%	100	25	USSuc25NS100
1(b)		4%	200	25	USSuc25NS200
1(c)		4%	300	25	USSuc25NS300
2(a)	Multistage	4%	100	50	USSuc50NS100
2(b)		4%	200	50	USSuc50NS200
2(c)		4%	300	50	USSuc50NS300
3(a)	Multistage	4%	100	60	USSuc60NS100
3(b)		4%	200	60	USSuc60NS200
3(c)		4%	300	60	USSuc60NS300
4(a)	Multistage	1%	100	90	USSuc90NS100
4(b)		1%	200	90	USSuc90NS200
4(c)		1%	300	90	USSuc90NS300

Table 4.14 List of consolidated drained triaxial tests on saturated specimens for test series D.

Test no.	Type of test	% mc during compaction	Effective stress (kPa)	Test code
1	Single stage	0%	100	Min5SSES100
2	Single stage	0%	200	Min5SSES200

Table 4.15 List of Rowe cell compression tests for test series E.

Test no.	Type of test	Suction (kPa)	Applied pore air pressure (kPa)	Applied pore water pressure (kPa)	Test code
1	Rowe cell compression under constant suction	25	20	0	CompSuc25
2	Rowe cell compression under constant suction	50	50	0	CompSuc50
2	Rowe cell compression under saturated conditions	0	0	0	CompSat



(a) The soil sample after being ground for 10 minutes to crush down the soft particles of shale.



(b) Washed sample freshly removed from the oven to be cooled down before carrying out the specimen compaction.

Plate 4.1 Initial preparation of soil samples.



Plate 4.2 Hammer held vertically and vibrated under its own weight as a standard compaction procedure for the triaxial test specimens.

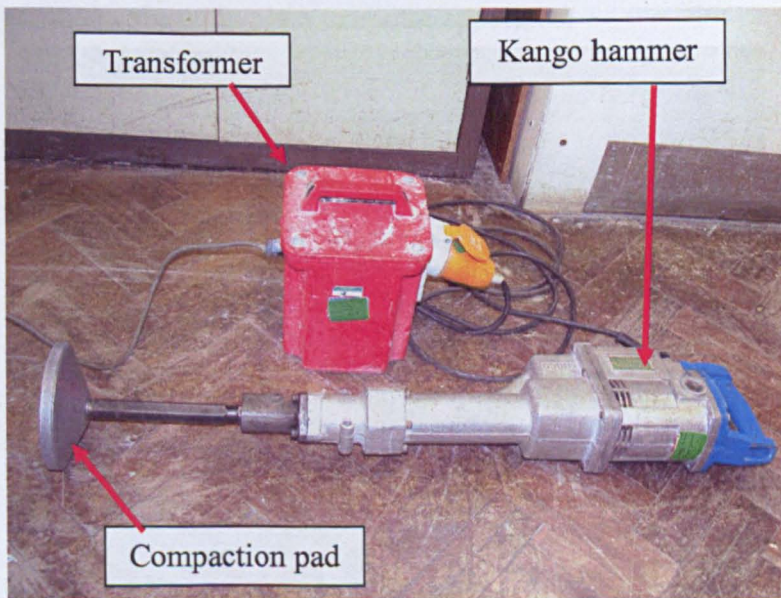
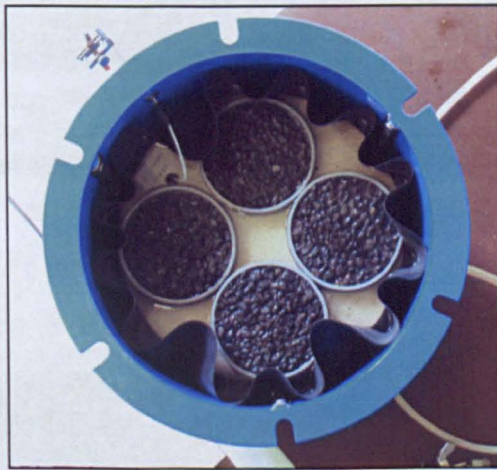


Plate 4.3 Kango hammer and transformer used to compact saturated and unsaturated specimens for triaxial tests.



(a) Test material contained in circular rings and compacted by tapping lightly with a hammer placed directly on the 3-bar ceramic disc.



(b) Specimens placed in plate extractor apparatus.



(c) Pressure plate extractor connected to a burette to collect excess water during equalization.

Plate 4.4 Pressure plate extractor apparatus and the prepared specimens.

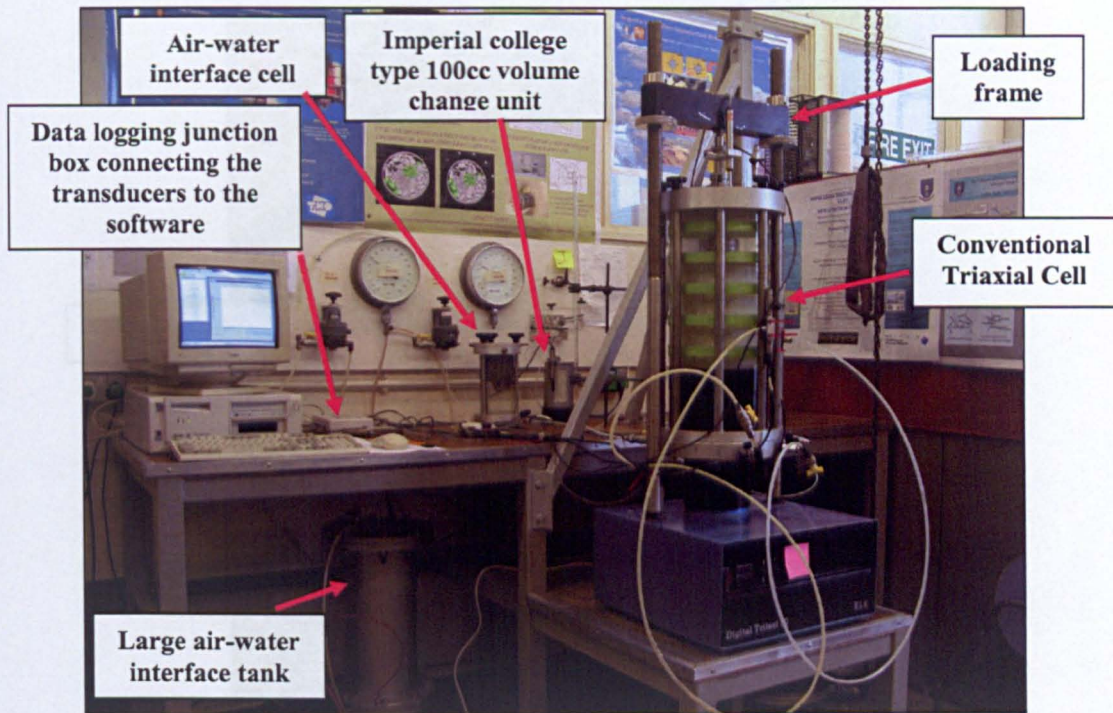
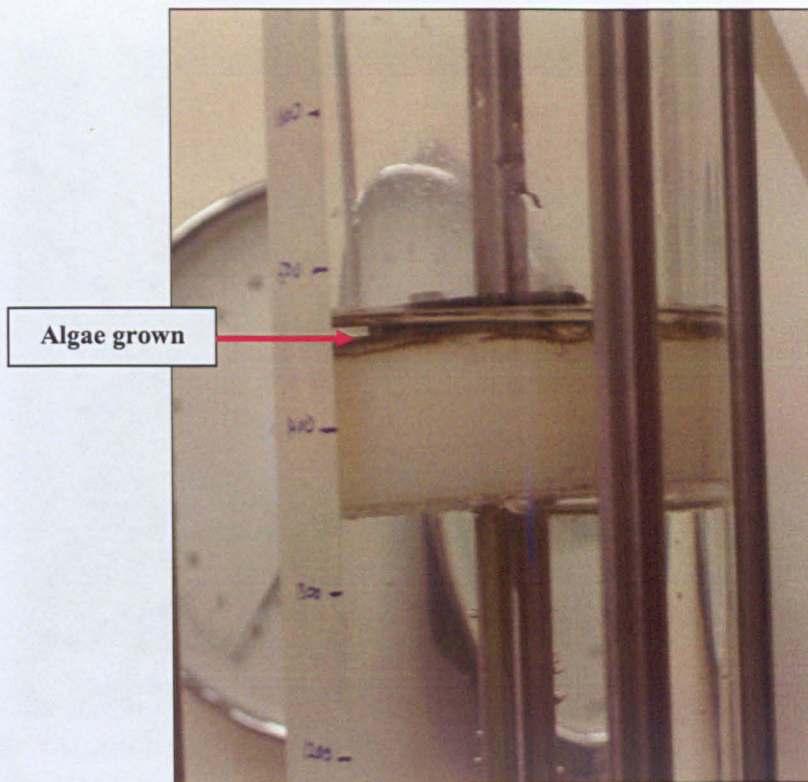


Plate 4.5 The overall set up for the conventional triaxial cell for testing a specimen of diameter 150 mm and height 375 mm.



Plate 4.6 Double-walled triaxial cell for testing unsaturated coarse grain soil (Salman, 1995) and the large volume change unit (Fair, 2004) connected to the inner cell to measure specimen volume change during testing.



(a) Algae grow on the white coloured float causing it to tilt and stick to the wall of the volume change unit.



(b) New improved dark coloured hollow float of smaller diameter.

Plate 4.7 Float improvement for the 1770cc volume change unit.

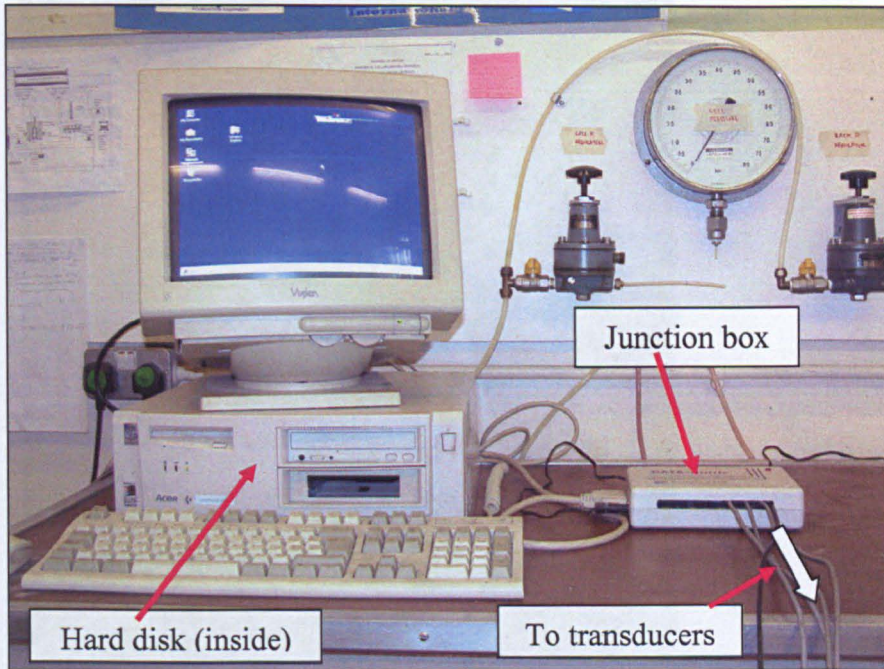


Plate 4.8 Quick Log data logging system for the conventional triaxial cell and the Rowe consolidation cell.

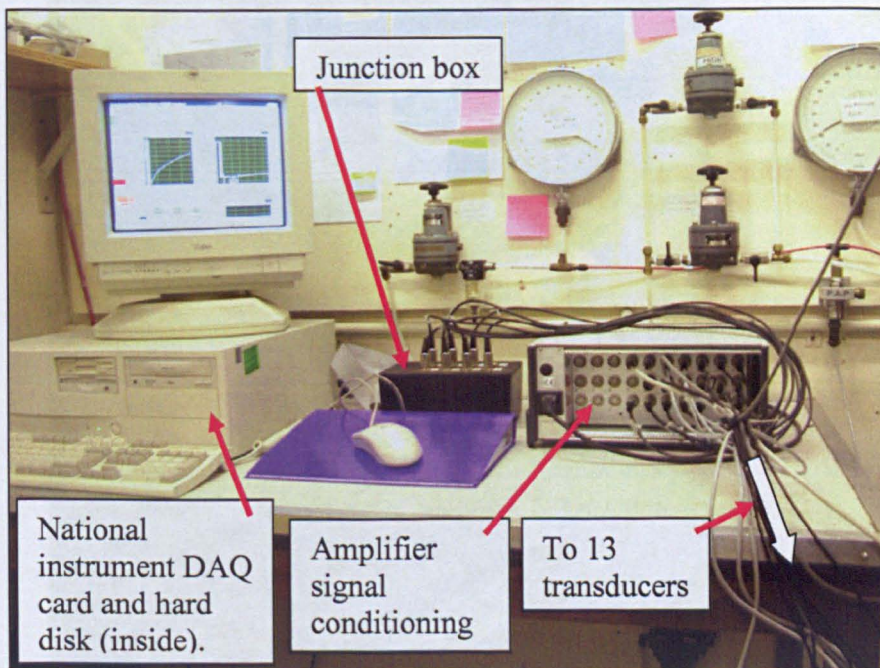
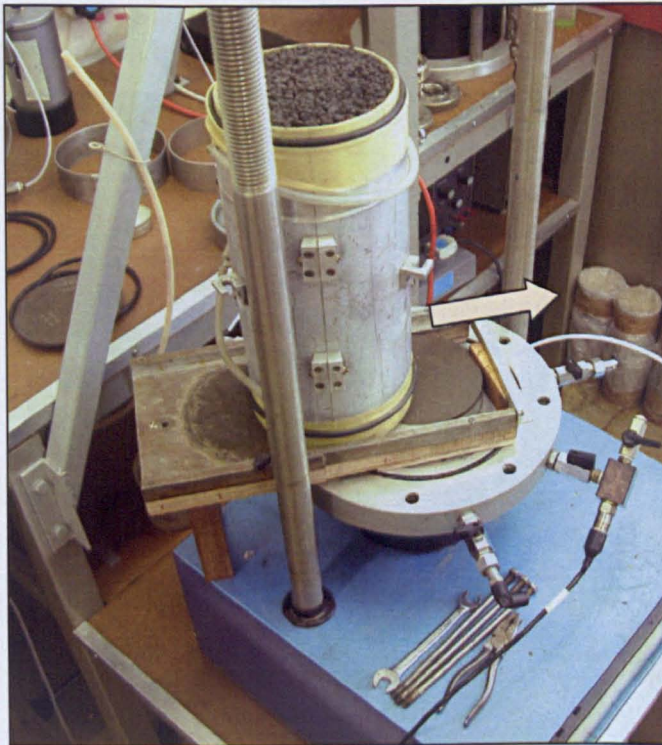


Plate 4.9 Data logging system for the double-wall triaxial cell.



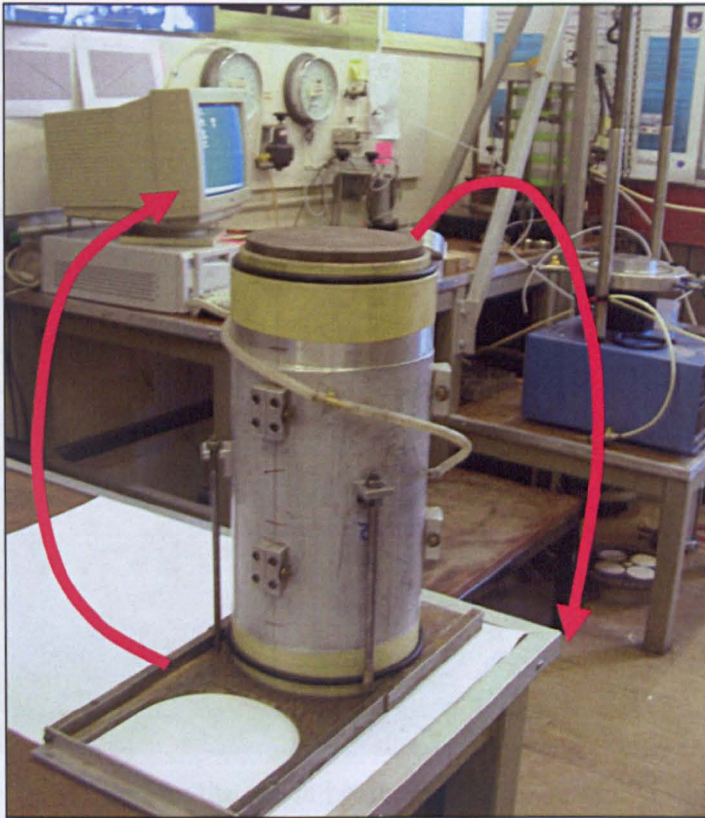
(a) Mould containing the compacted specimen placed with its base level with the porous disc sitting directly on top of the triaxial cell pedestal.



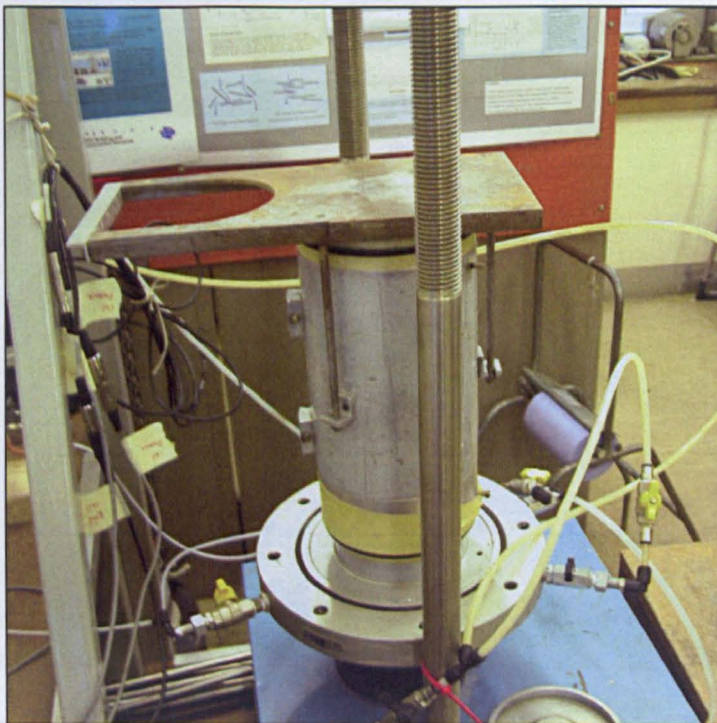
(b) Three tie rods outside the mould are removed and the mould is slid horizontally to sit over the pedestal.

(c) The specimen is placed directly onto the pedestal.

Plate 4.10 Sliding technique for specimen placement onto the cell base pedestal (Salman, 1995).

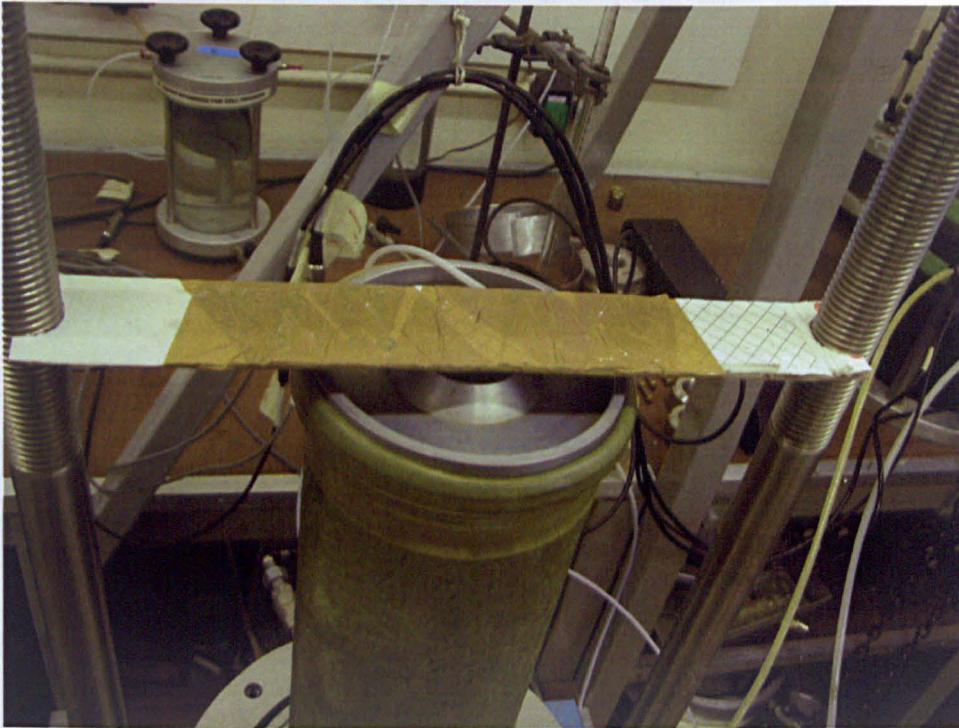


(a) The base disc is placed on top of the specimen before the whole unit is turned upside down by holding to the porous disc.

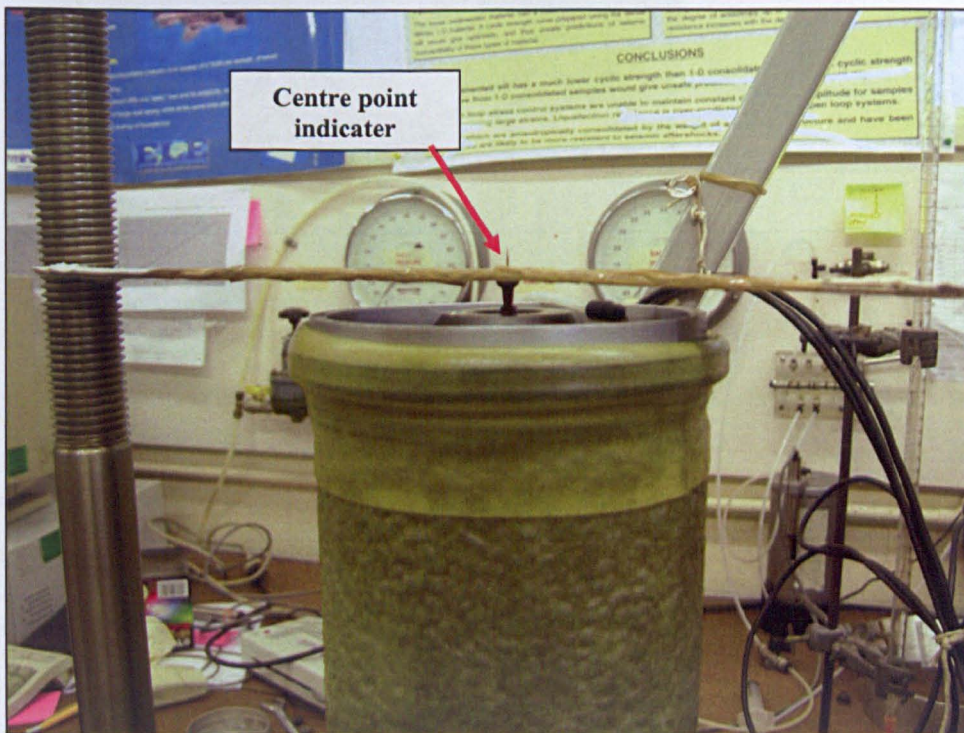


(b) The upside down unit is placed directly on to the pedestal.

Plate 4.11 Improved specimen placement technique for the saturated shear strength test in the conventional triaxial cell.

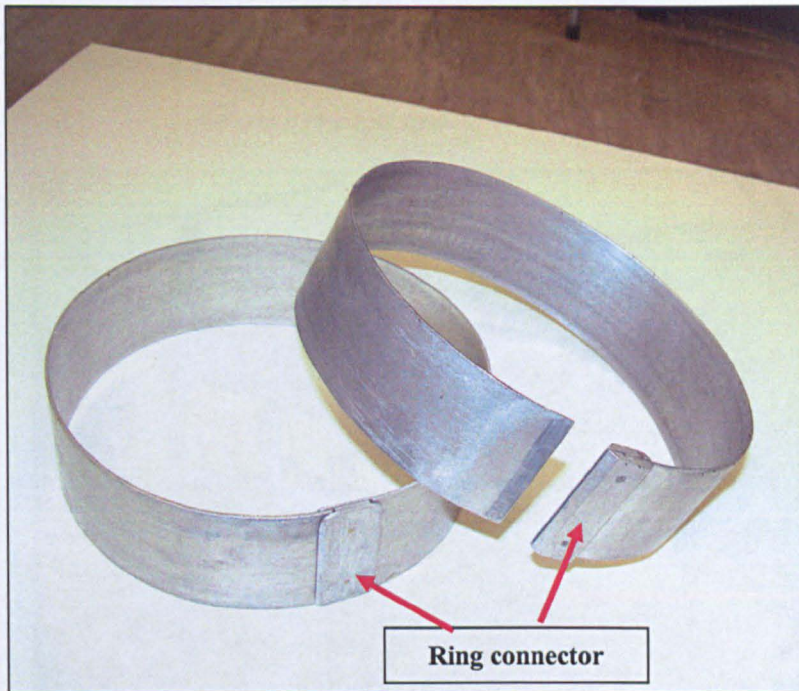


(a) Top view showing the guide beam and the specimen aligned.

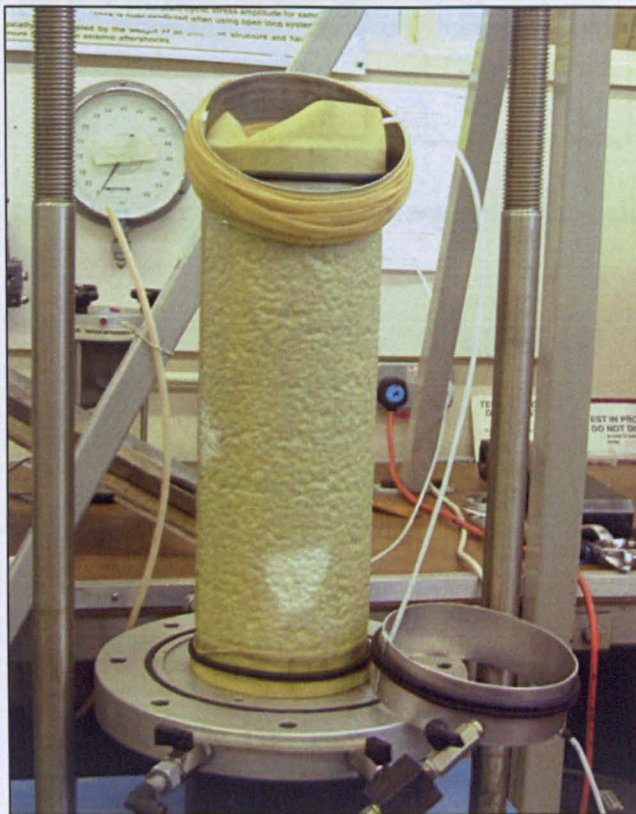


(b) Side view showing the centre pointing needle aligned at the centre of the top cap.

Plate 4.12 Guide beam spanning between the two loading machine uprights with the centre pointing needle helping to align the specimen vertically.



(a) New improved split ring system with special connectors used to stretch O-rings and the second membrane during the setting up of saturated and unsaturated triaxial test specimens.



(b) Vacuum applied, mould removed, and the two O-rings and the second membrane stretched around the split rings ready to be installed.

Plate 4.13 Split rings of diameter 170 mm and width 30 mm used to stretch the O-rings and the second membrane.

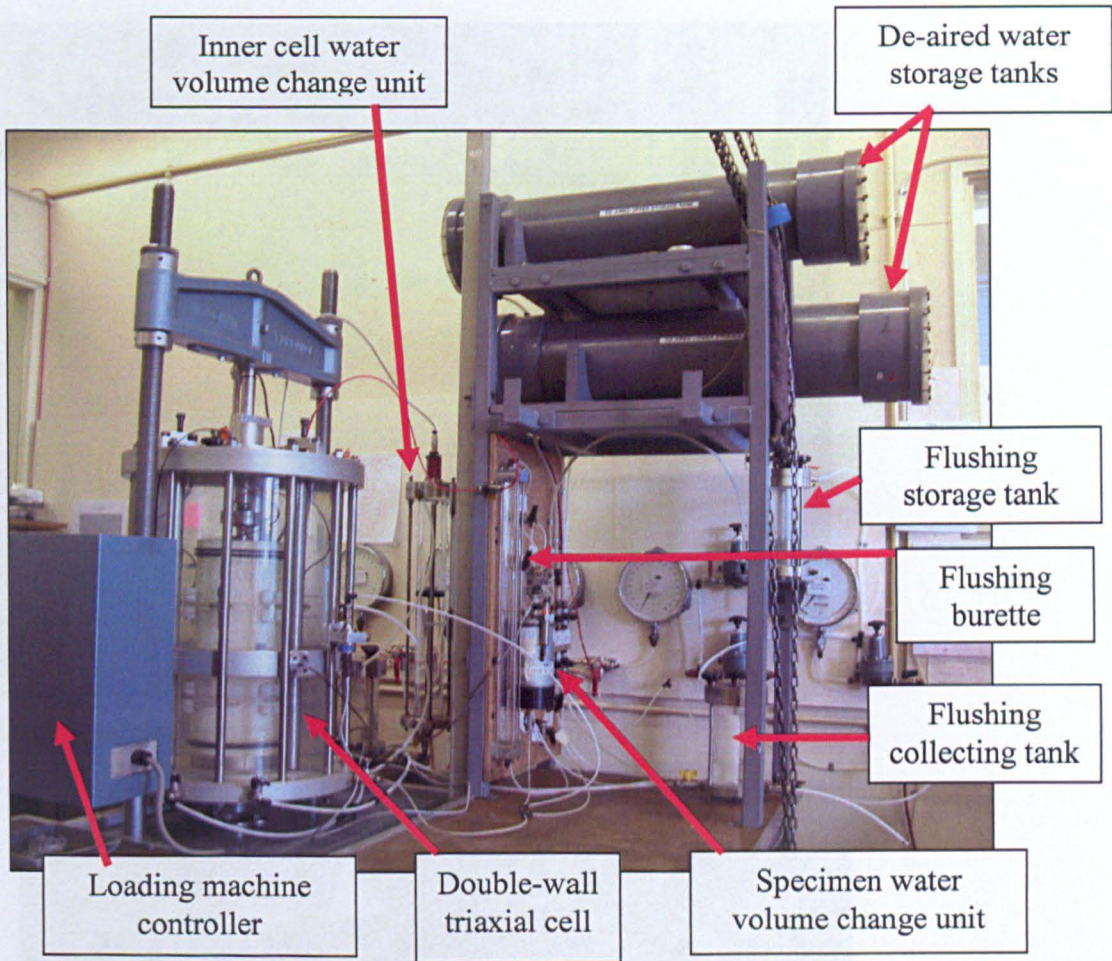
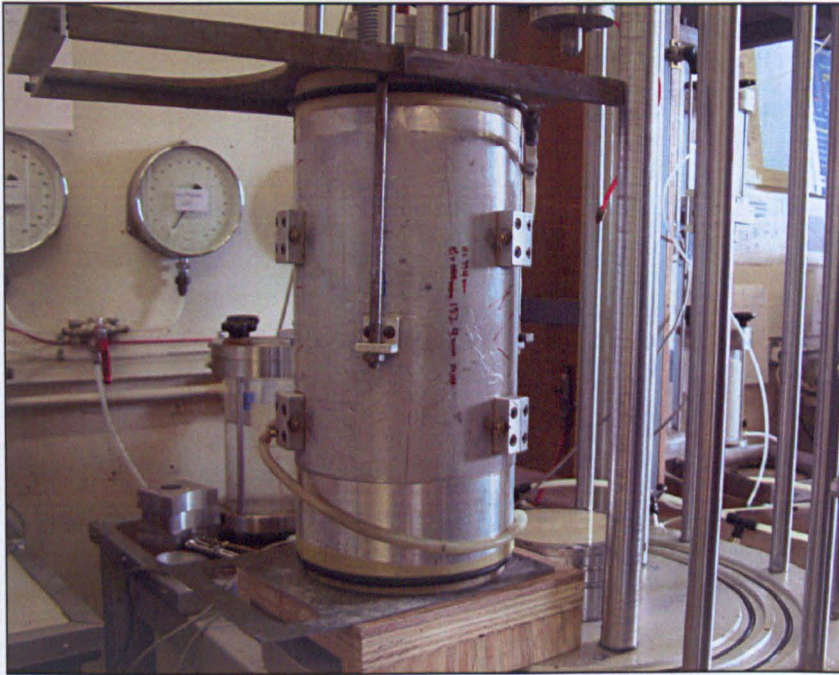


Plate 4.14 Overall view of the double-wall triaxial cell.

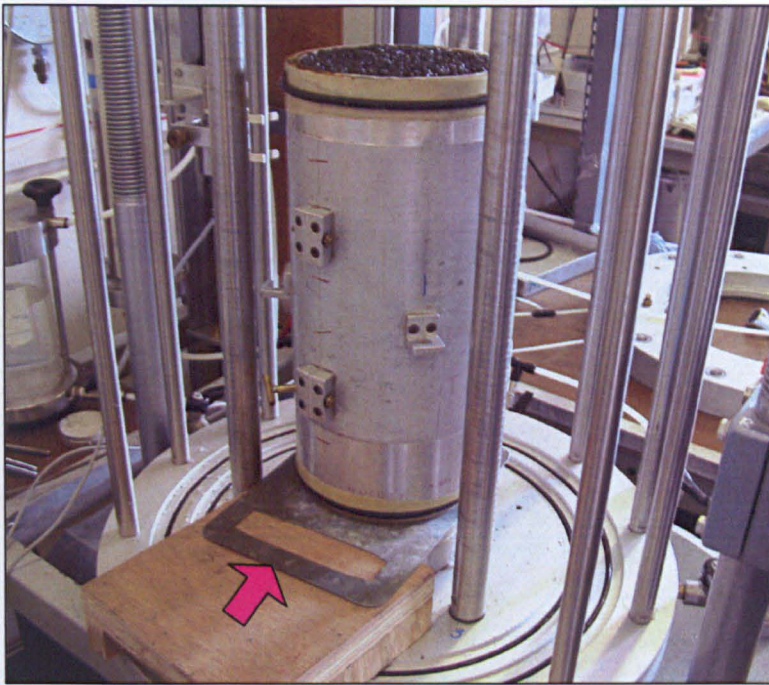


(a) Mould is turned upside down to sit on a rigid plate.



(b) Base plate is removed.

Plate 4.15 The sequence of specimen placement onto the base pedestal of the double-wall triaxial cell.



(c) The mould is slid onto the pedestal by pushing the rigid plate.



(d) The clamp system is assembled to hold the mould rigidly in place before the plate is pulled out.

Plate 4.15 (continued) The sequence of specimen placement onto the base pedestal of the double-wall triaxial cell.

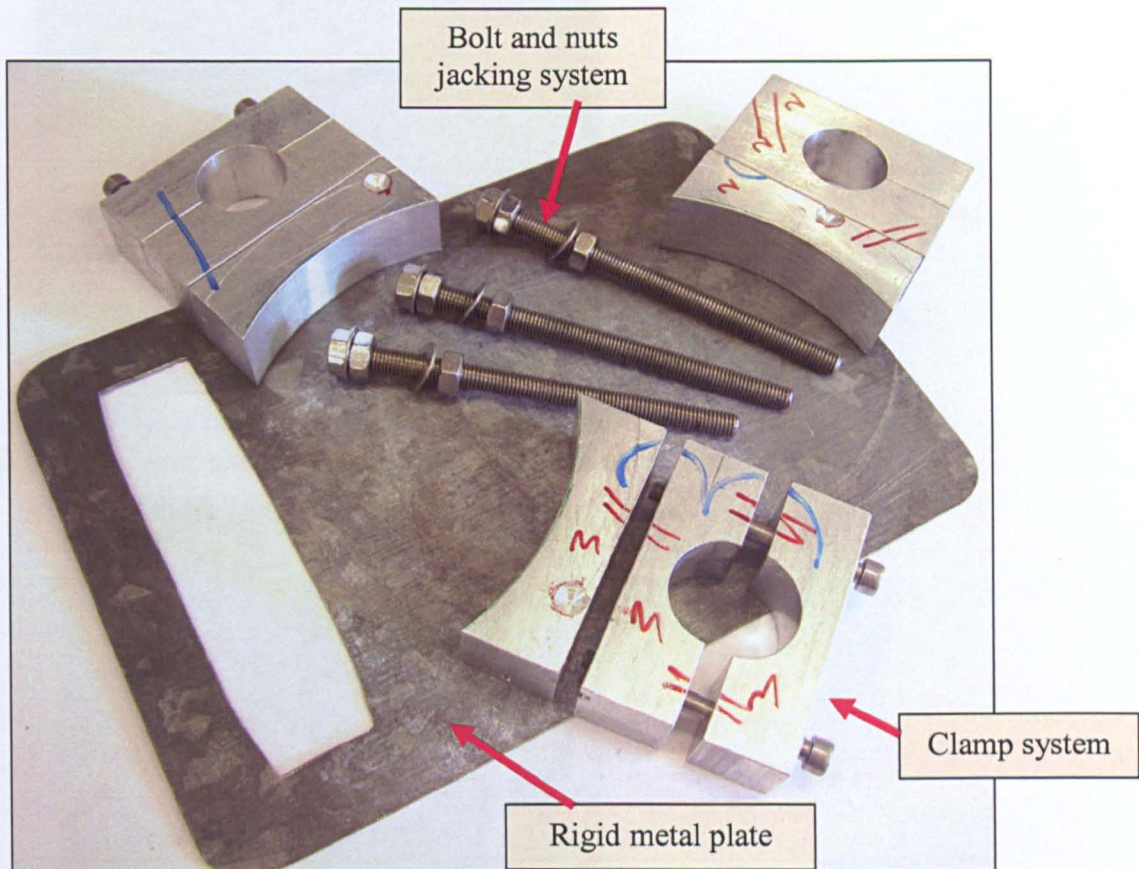


Plate 4.16 Clamp components and a rigid sliding plate for the specimen placement.



Plate 4.17 Two O-rings and the second membrane stretched around the split rings ready to be installed after the application of a vacuum and subsequent mould removal.



(a) Gauge calliper used to measure specimen diameter.



(b) Measuring the mid height specimen diameter using the fabricated gauge calliper with the aid of the electronic vernier scale ruler.

Plate 4.18 Calliper for measuring specimen diameter in the conventional and double-wall triaxial cell tests.

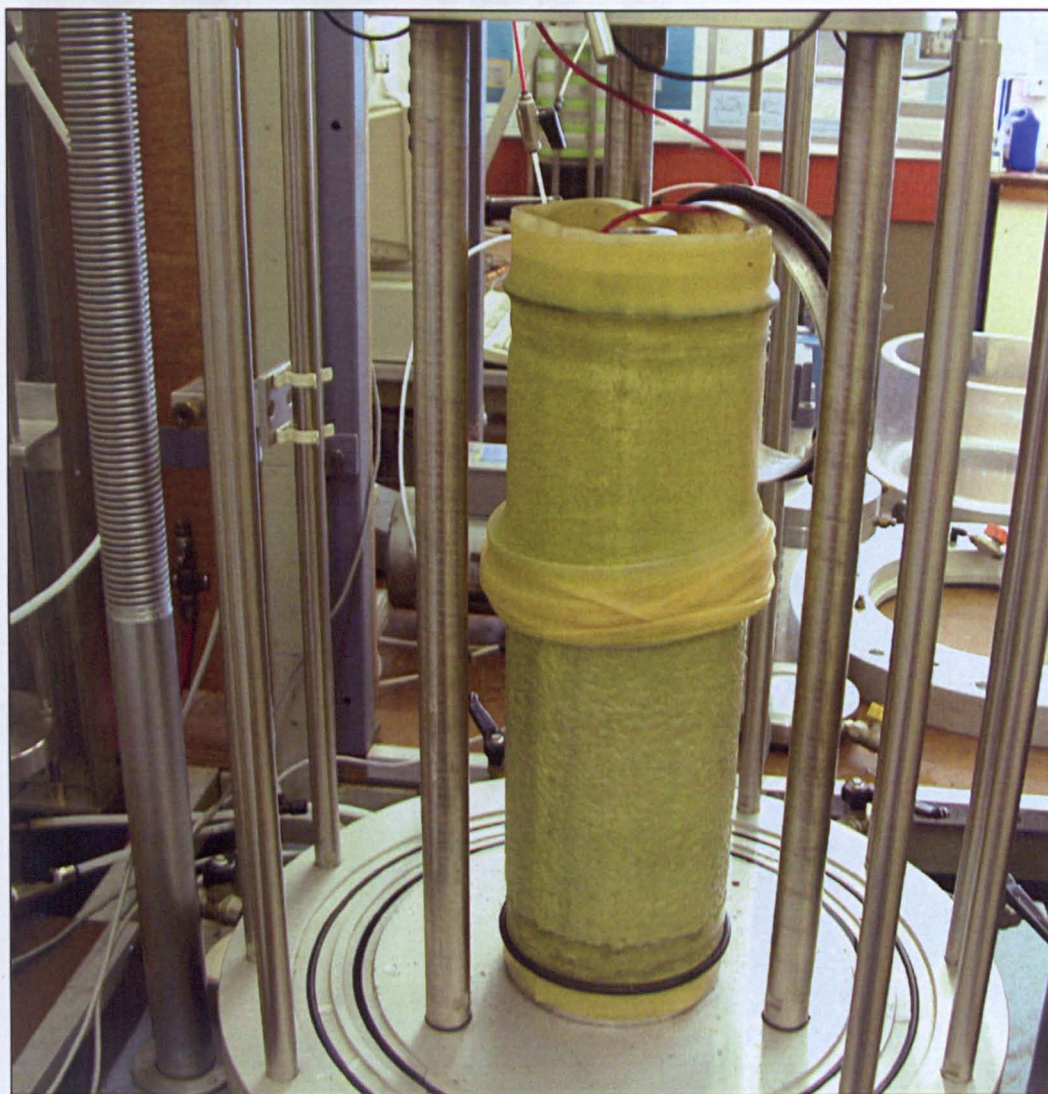
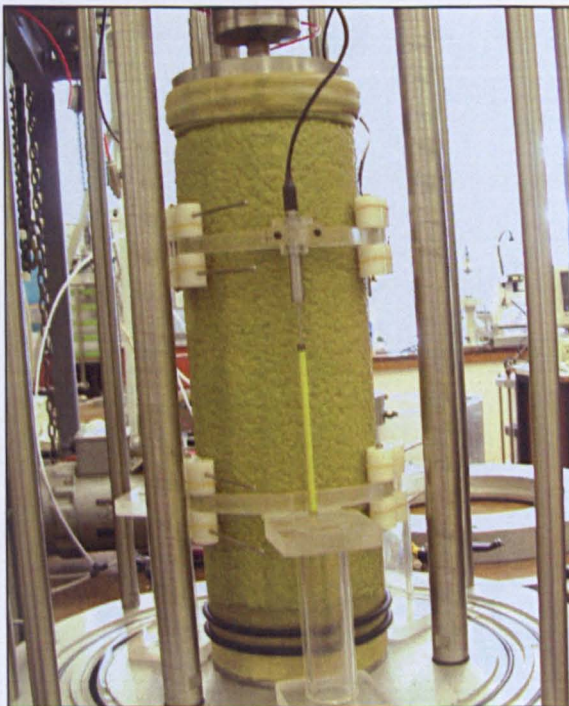


Plate 4.19 Lowering the second membrane after silicon grease is uniformly applied onto the first membrane.



(a) Taller stand system for installing top Perspex curve system.



(b) Shorter stand system for installing bottom Perspex curve system.

Plate 4.20 Three stand system to ease installation of the top and bottom Perspex curves transducer holders.

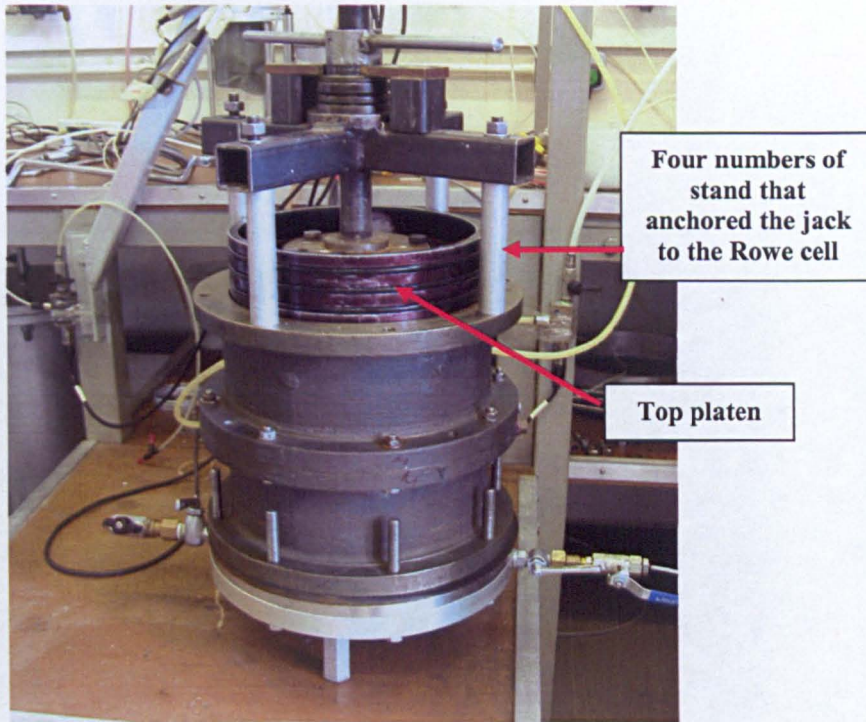


Plate 4.21 Screw type jack system used to install and remove the Rowe cell top platen.

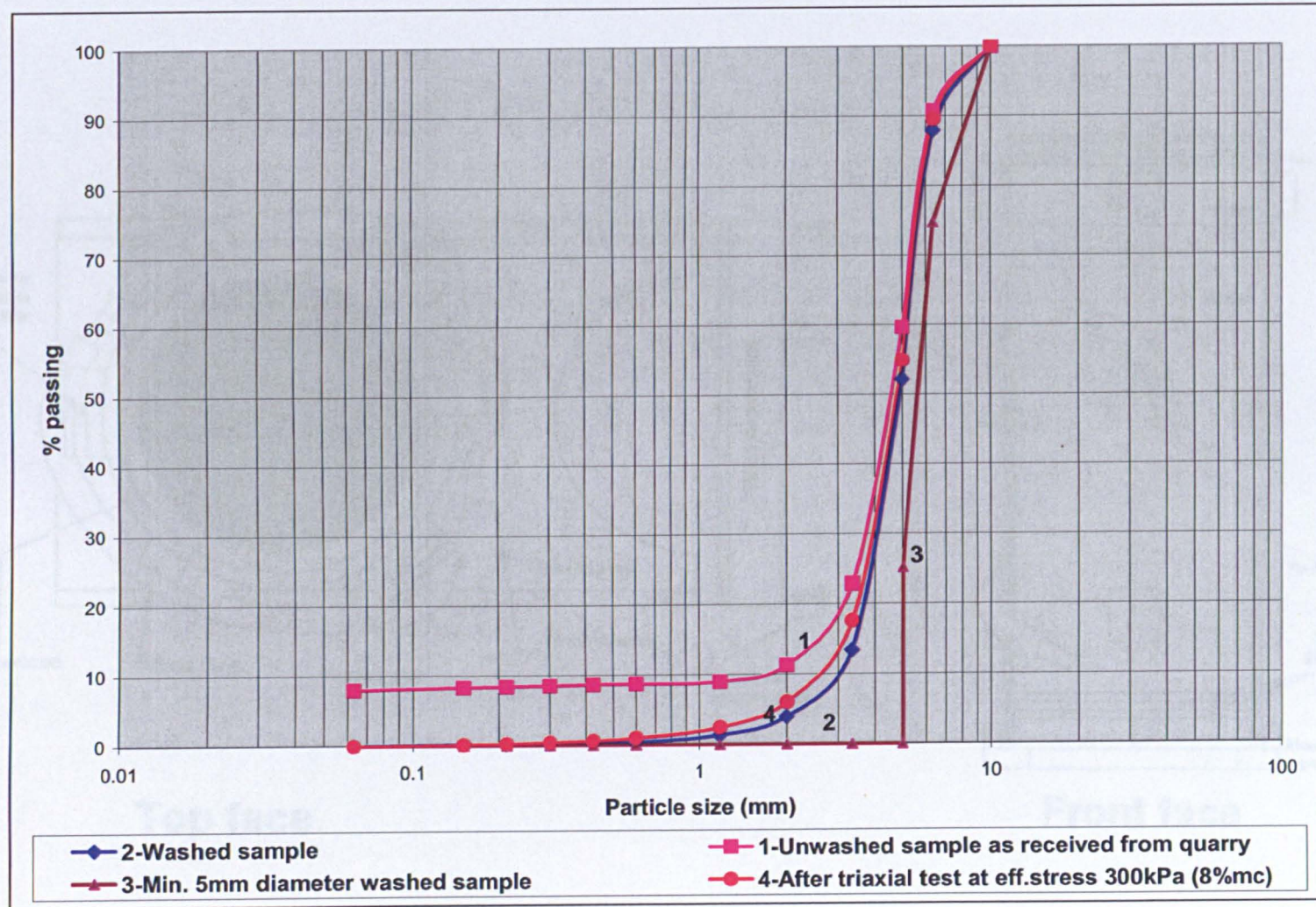


Figure 4.1 Grading curves for the test material.

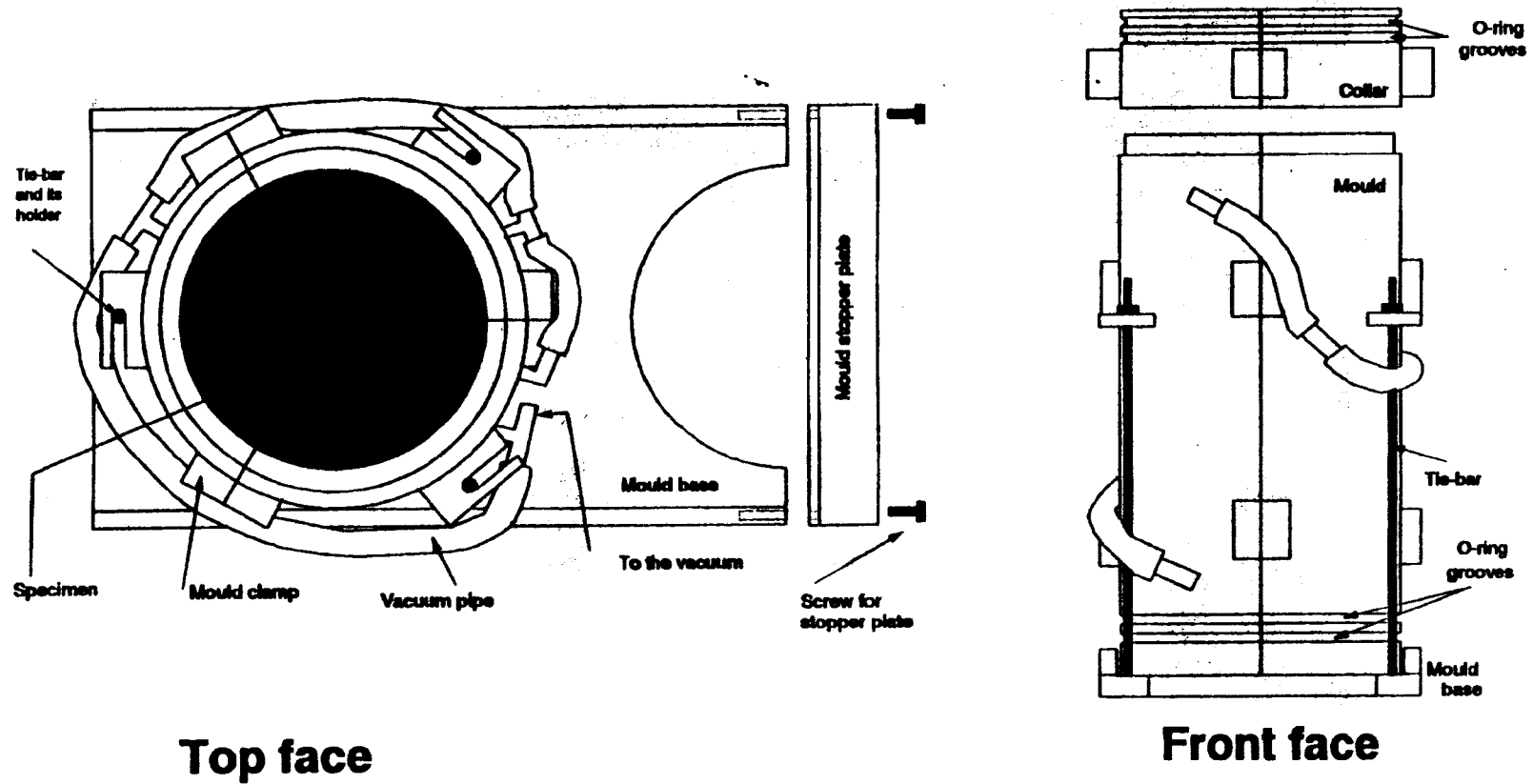


Figure 4.2 Specimen compaction mould.

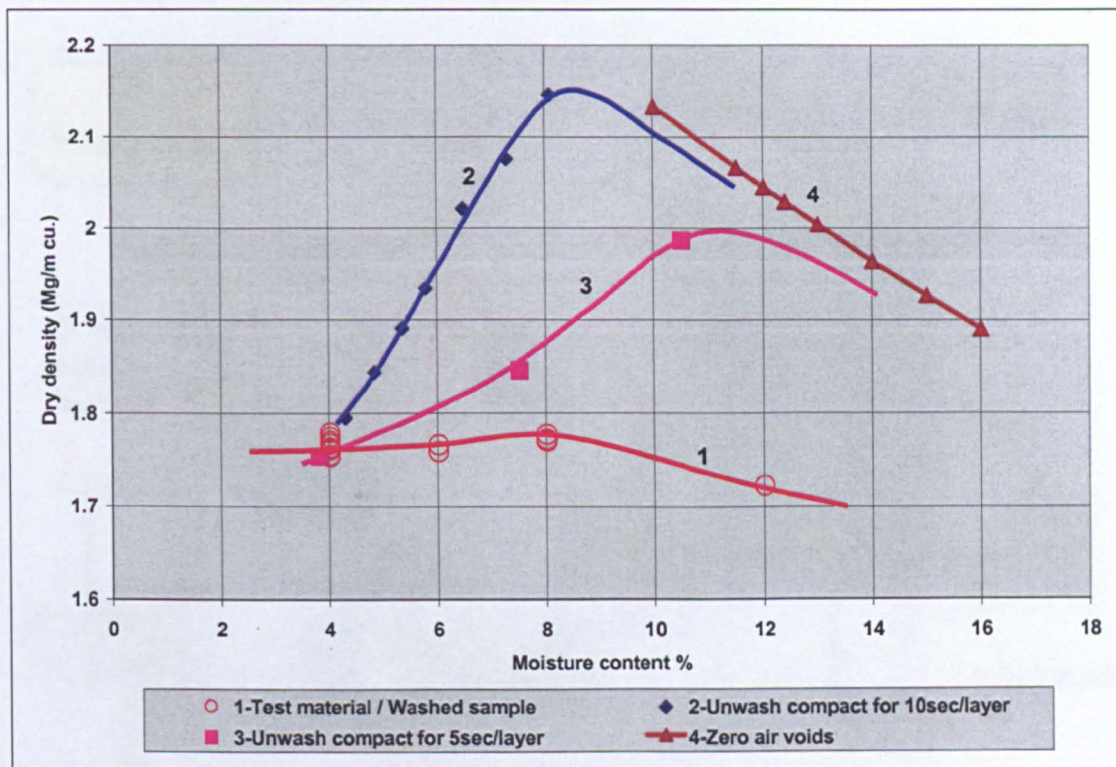


Figure 4.3 Compaction curves for washed and unwashed samples.

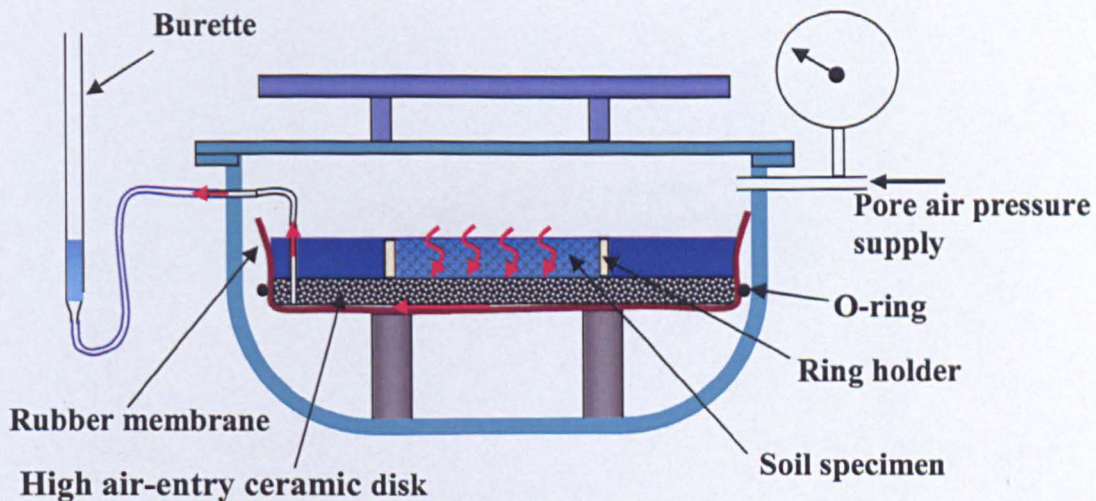


Figure 4.4 Pressure plate extractor apparatus illustrating the flow of excess water during the equalisation process with the specimen initially flooded with de-ionised and de-aired water.

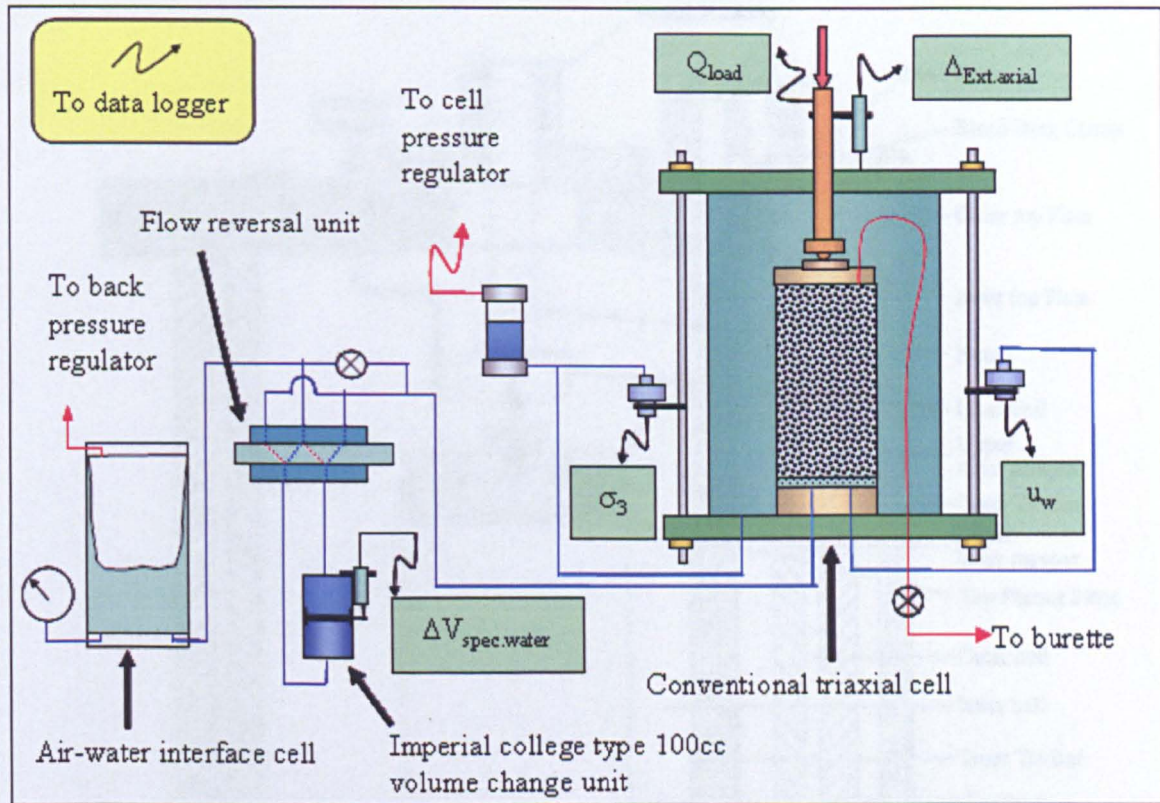


Figure 4.5 Plumbing system for the conventional triaxial cell (Salman 1995).

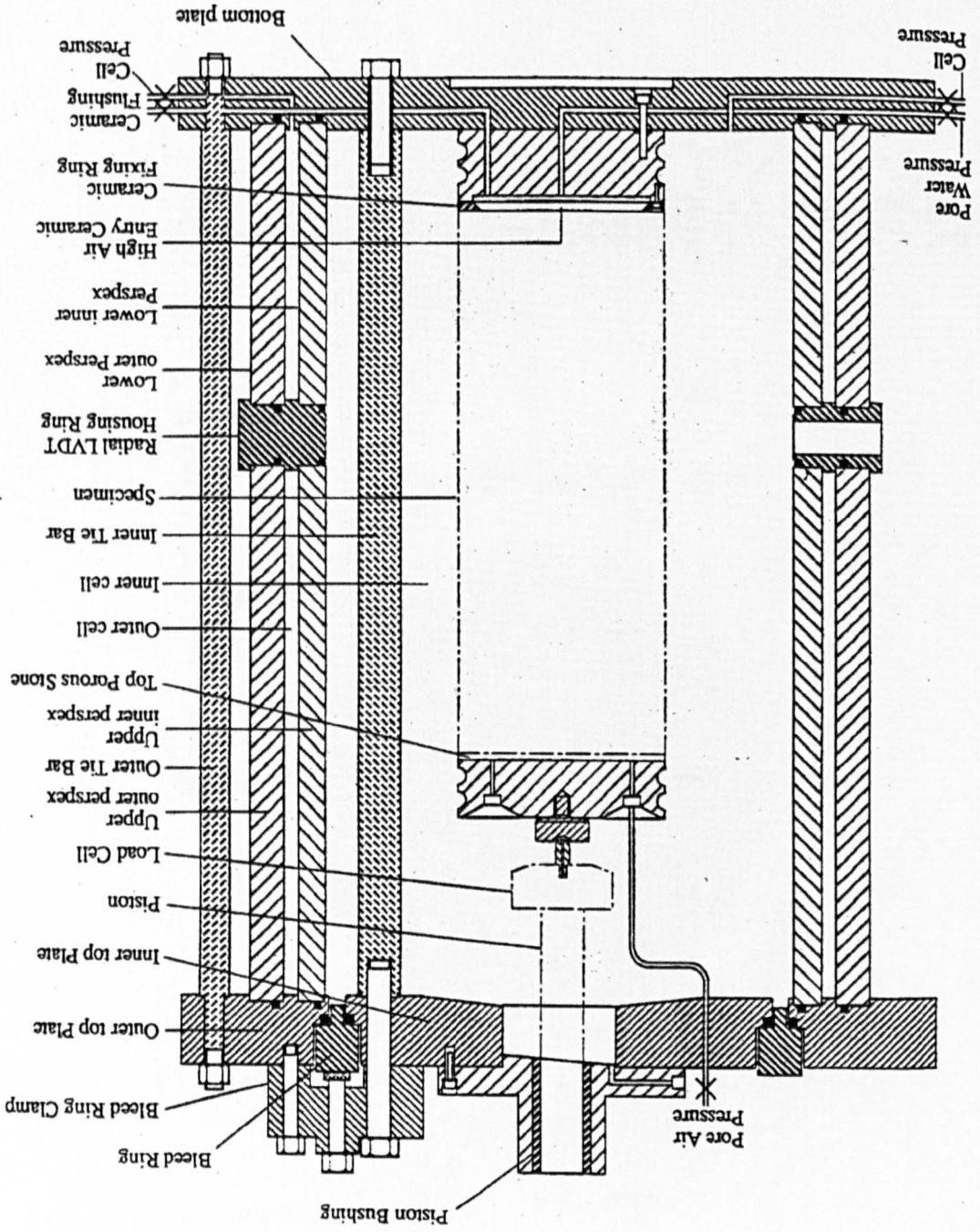


Figure 4.6 Double-wall triaxial cell for testing unsaturated soils after Salmaan (1995).

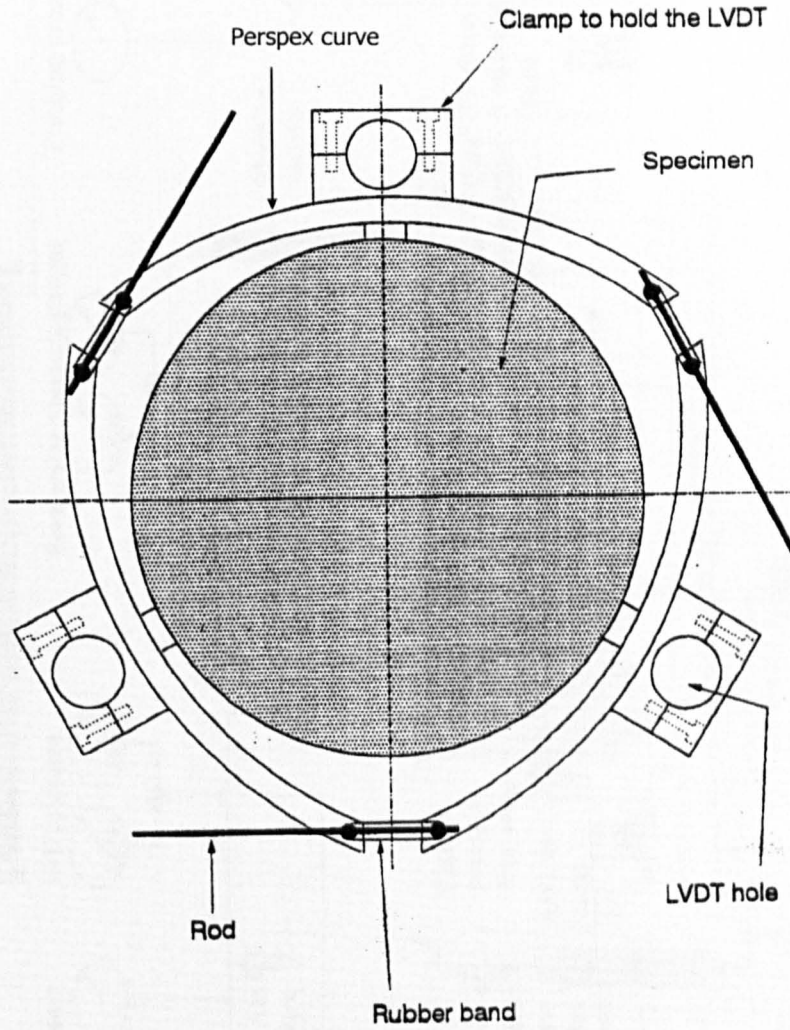


Figure 4.7 Plan view of the Perspex curves mounting system for the axial LVDTs used for the specimen internal axial strain measurements (Salman, 1995).

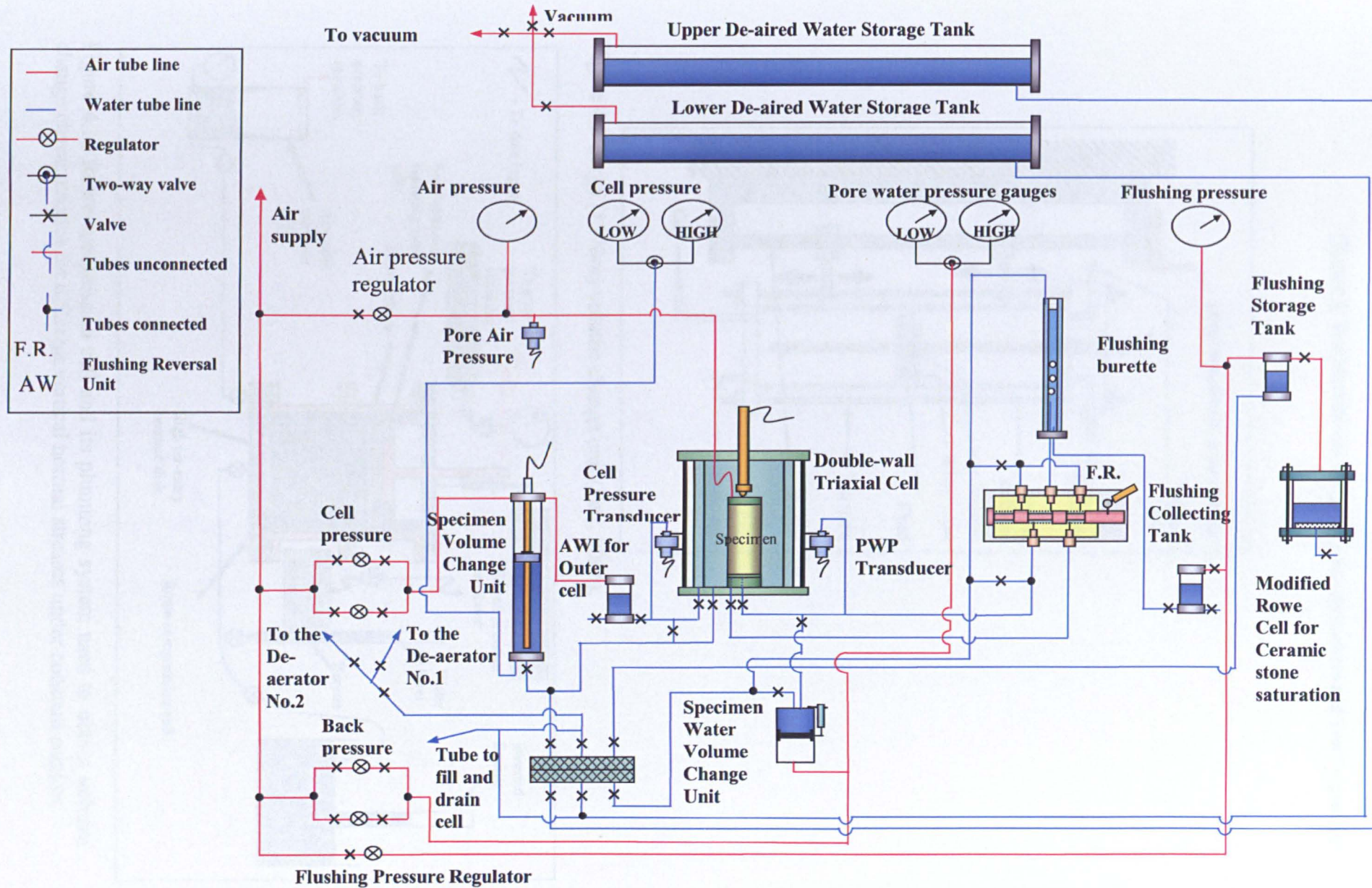


Figure 4.8 Plumbing system for the Double-walled Triaxial Cell (Salman 1995).

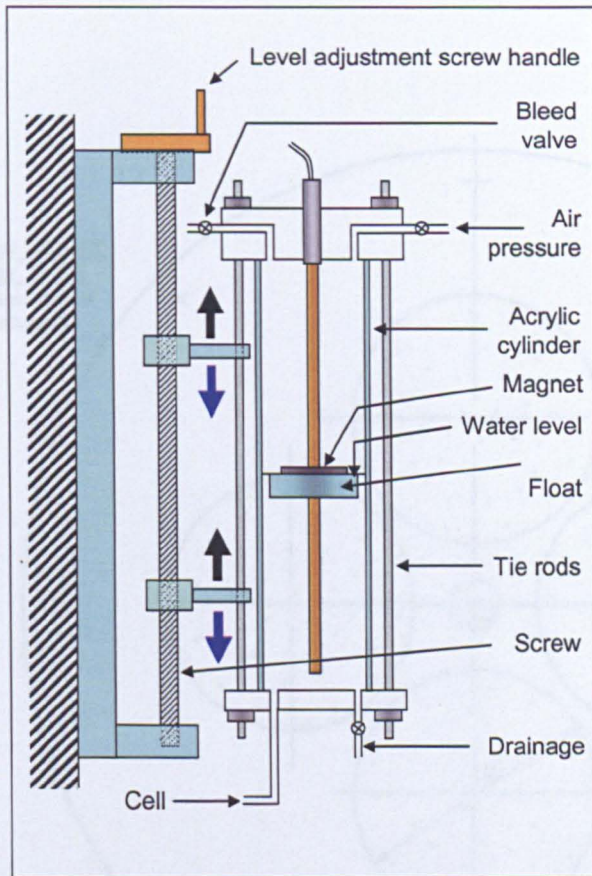


Figure 4.9 Large (1770cc) volume change unit (Fair, 2004).

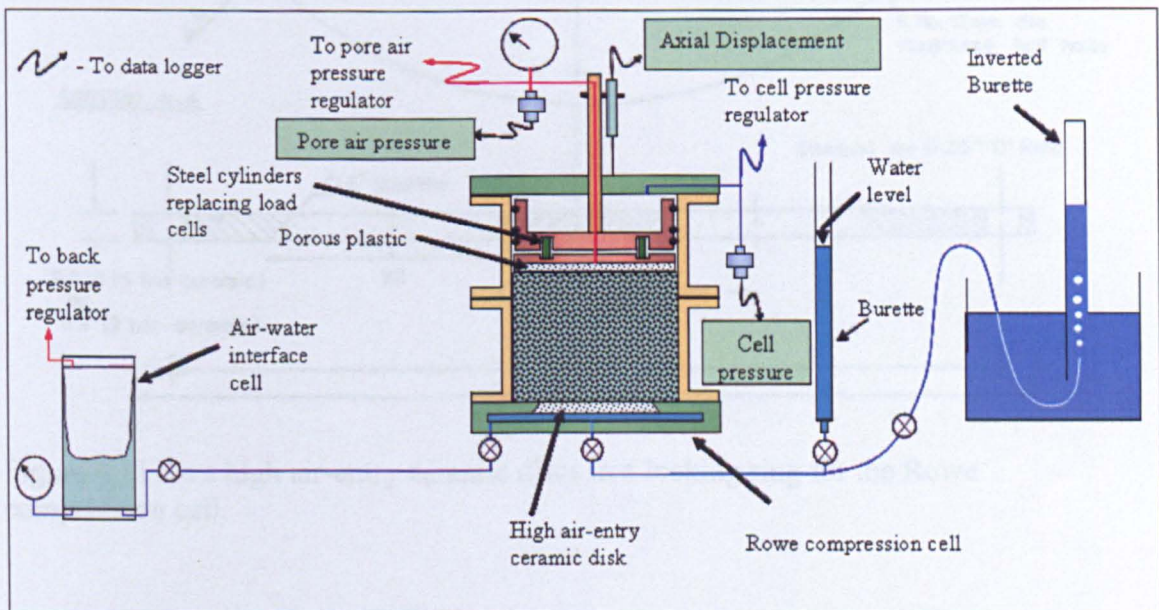


Figure 4.10 Rowe compression cell and its plumbing system used to obtain volume change characteristics for different vertical normal stresses under constant suction.

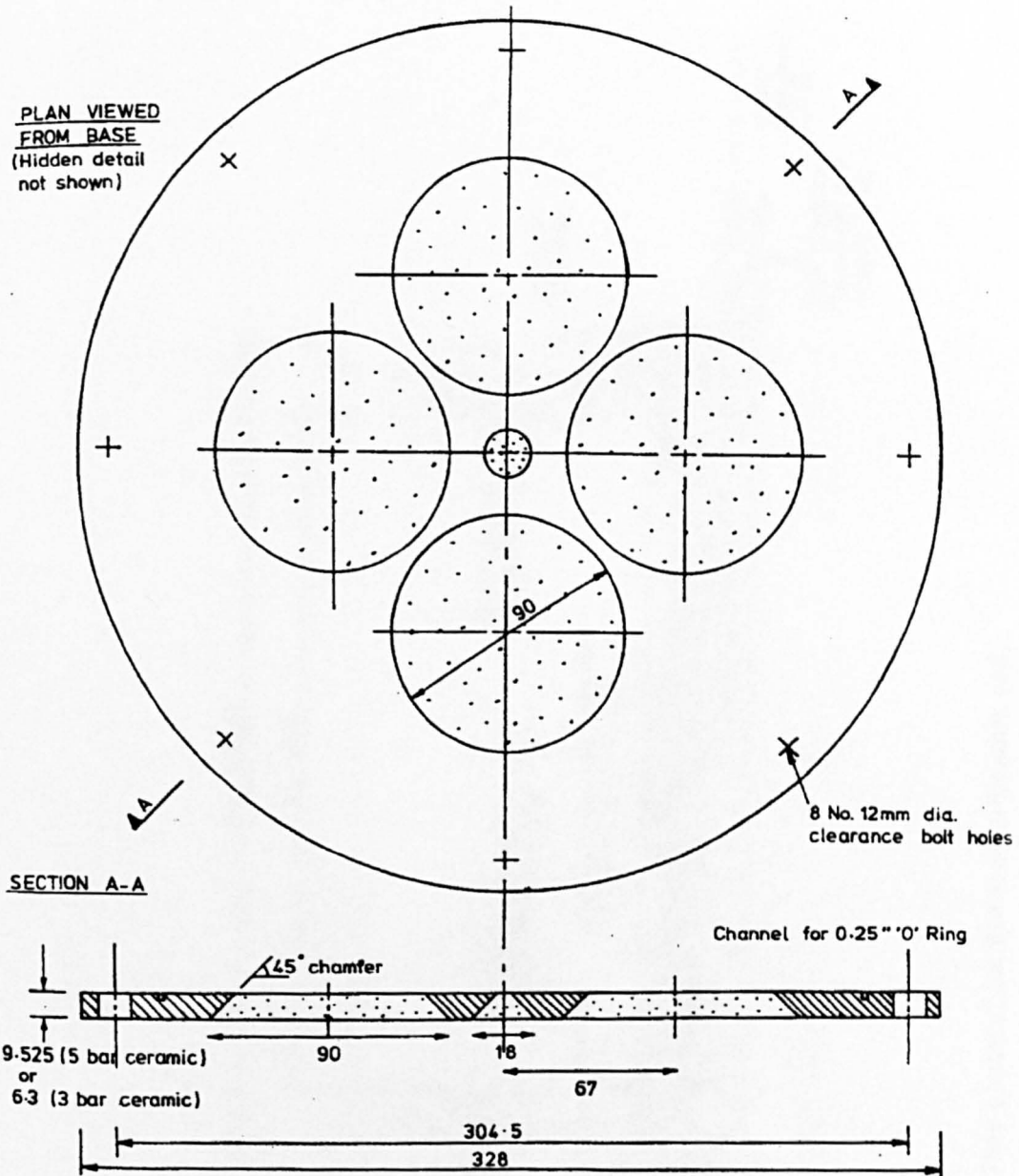


Figure 4.11 Five high air-entry ceramic discs in a locking ring for the Rowe compression cell.

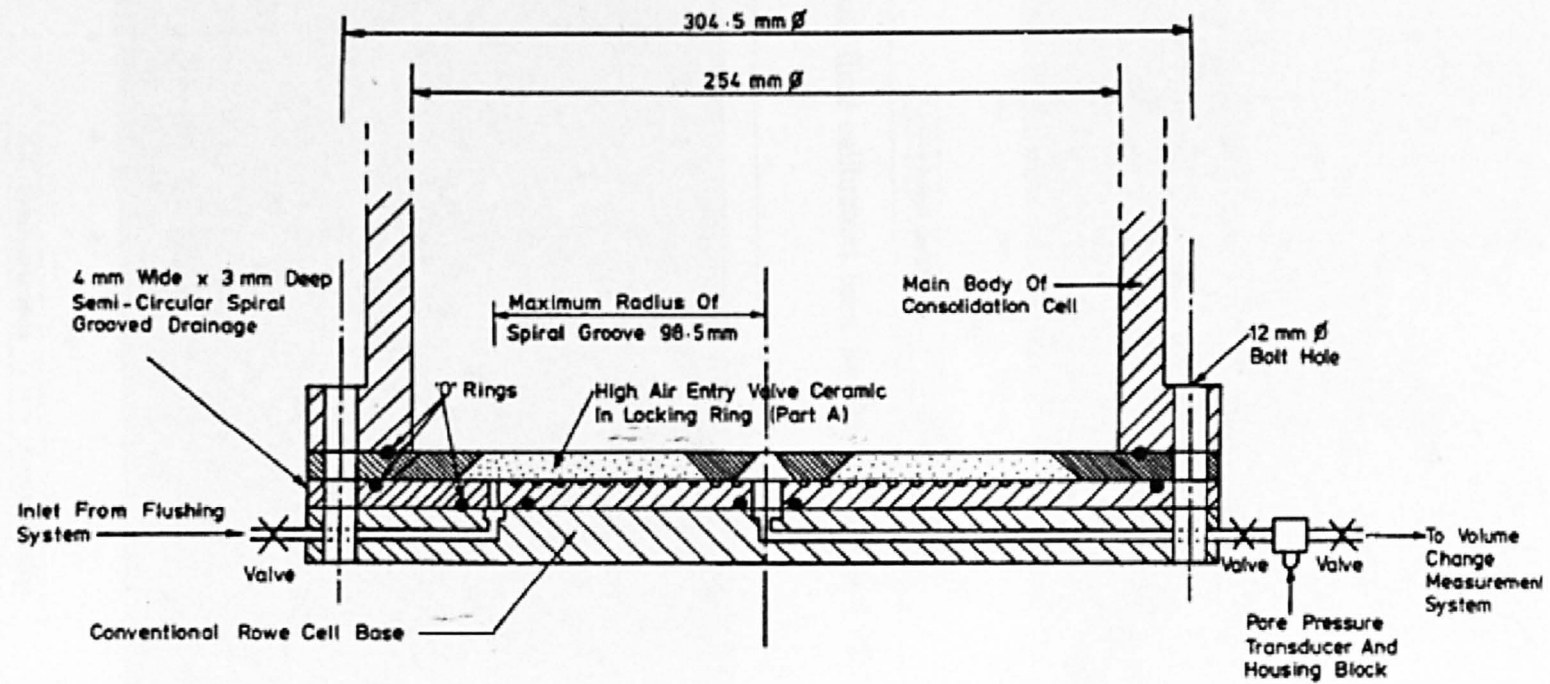


Figure 4.12 General assembly of the base platen of the Rowe consolidation cell.

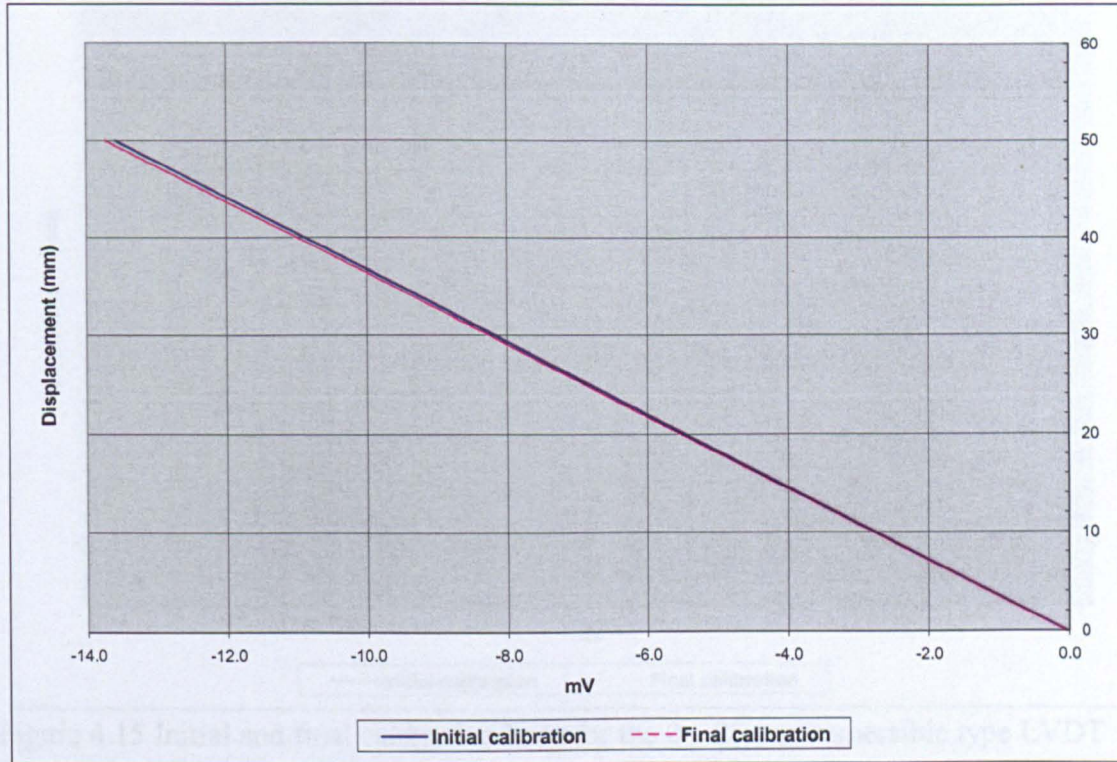


Figure 4.13 Initial and final calibration lines for the 0 – 50mm LVDT (Serial No. HS50/4017).

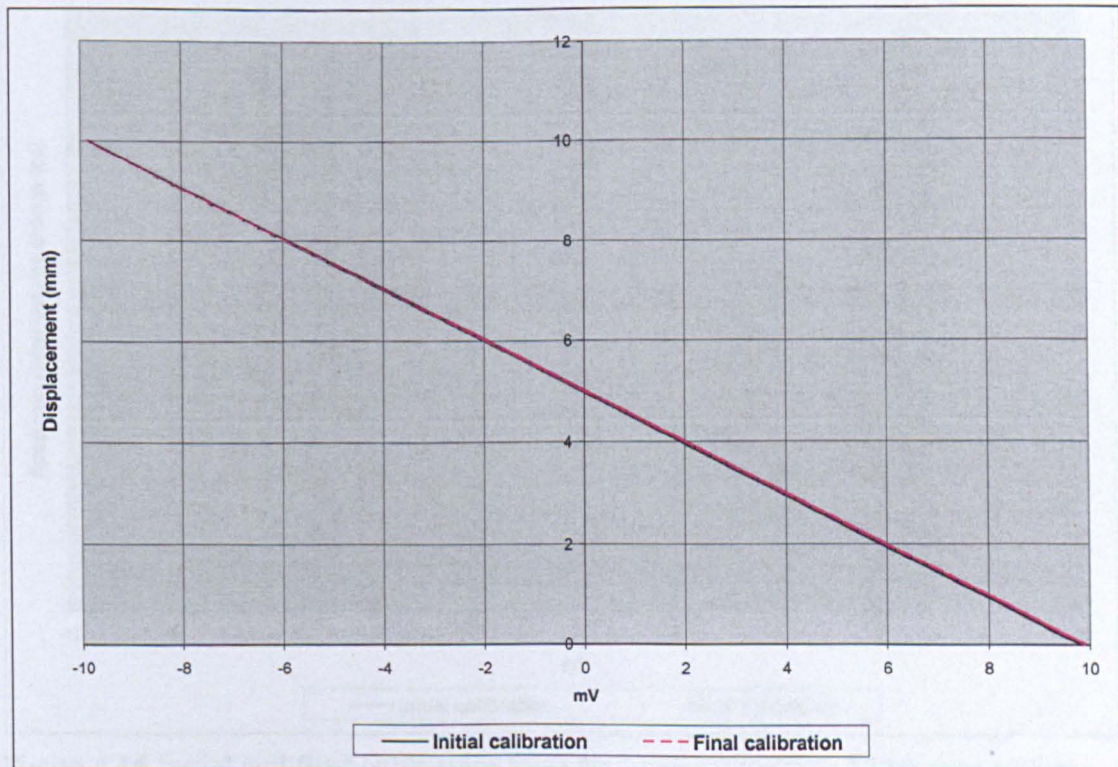


Figure 4.14 Initial and final calibration lines for the 0 – 10mm immersible type LVDT (Serial No. DS200W – 50953).

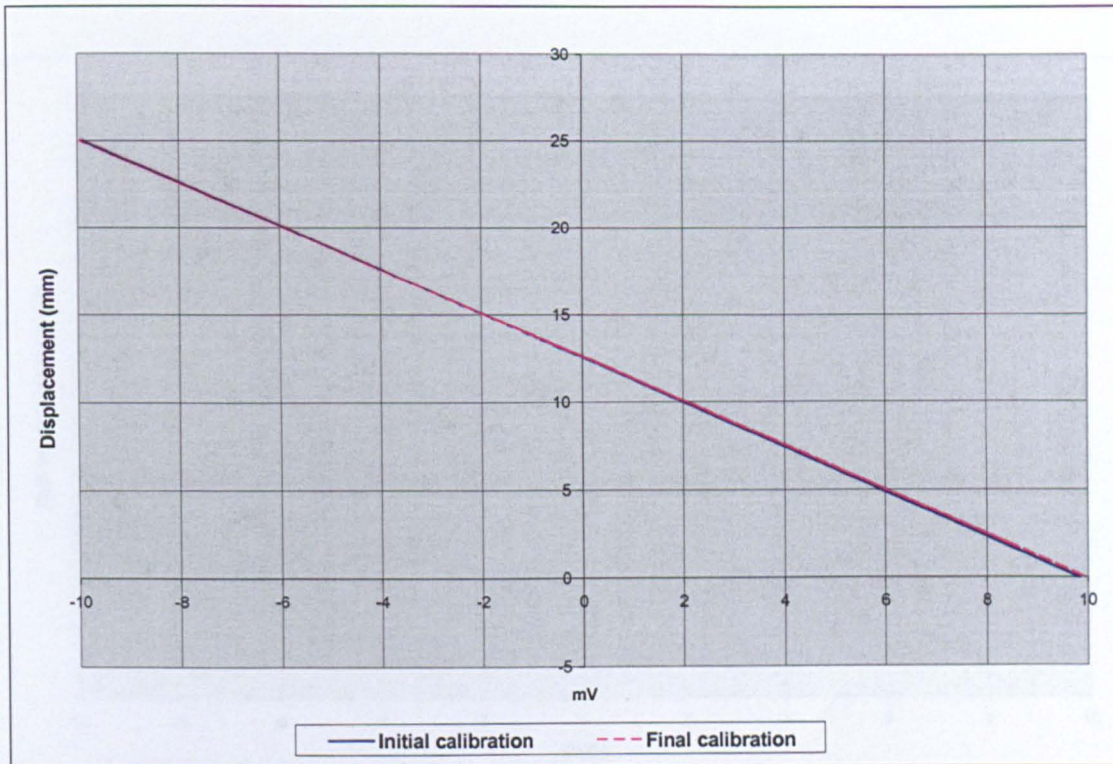


Figure 4.15 Initial and final calibration lines for the 0 – 25mm immersible type LVDT (Serial No. DS500W – 50956).

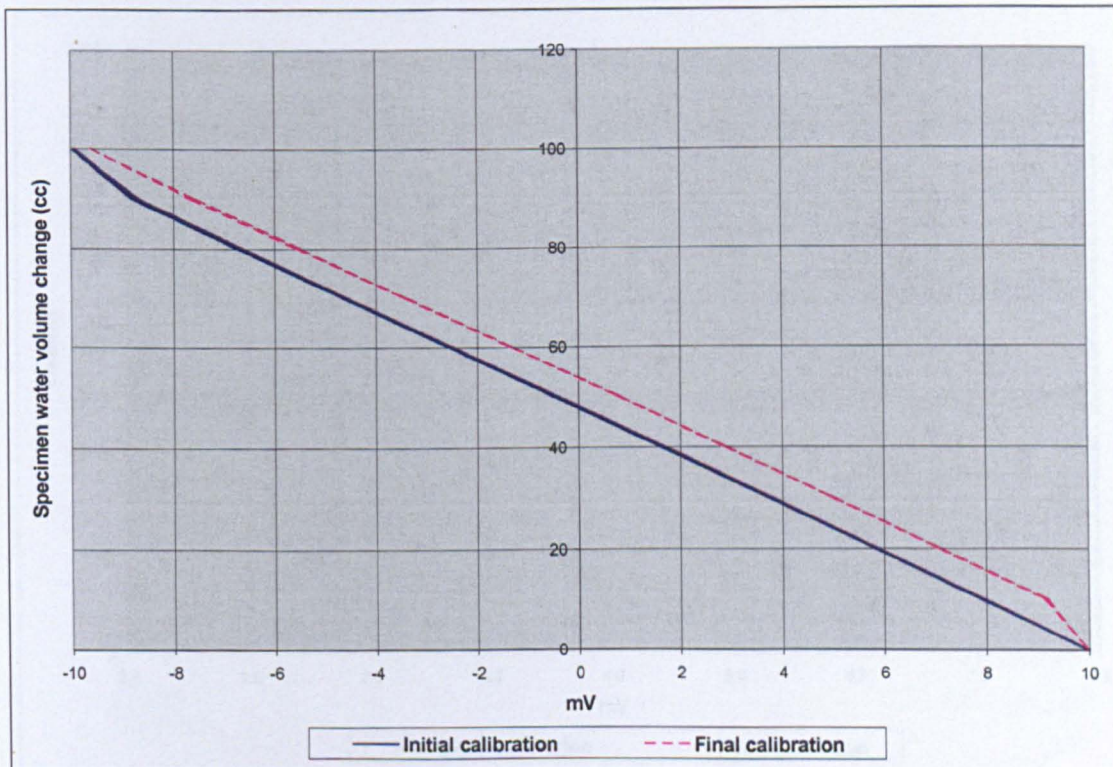


Figure 4.16 Initial and final calibration lines for Imperial College 100cc type volume change unit (Serial No. LVDT 6015).

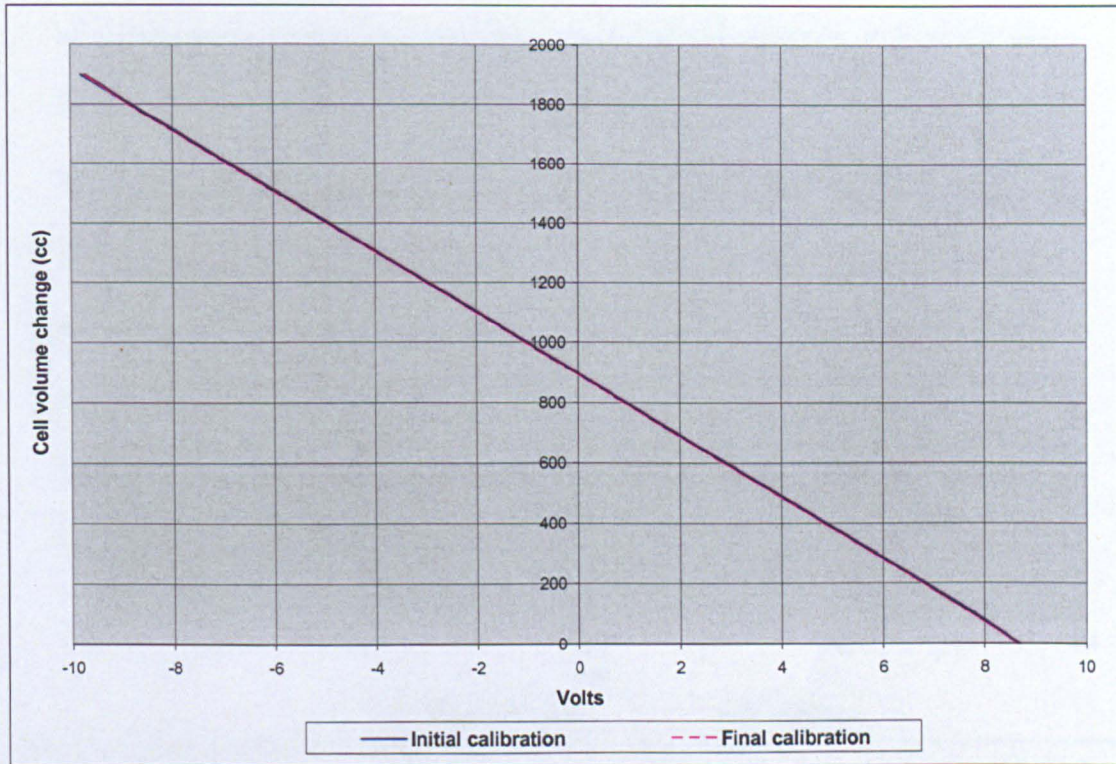


Figure 4.17 Calibration lines for 1770cc volume change unit fabricated in house.

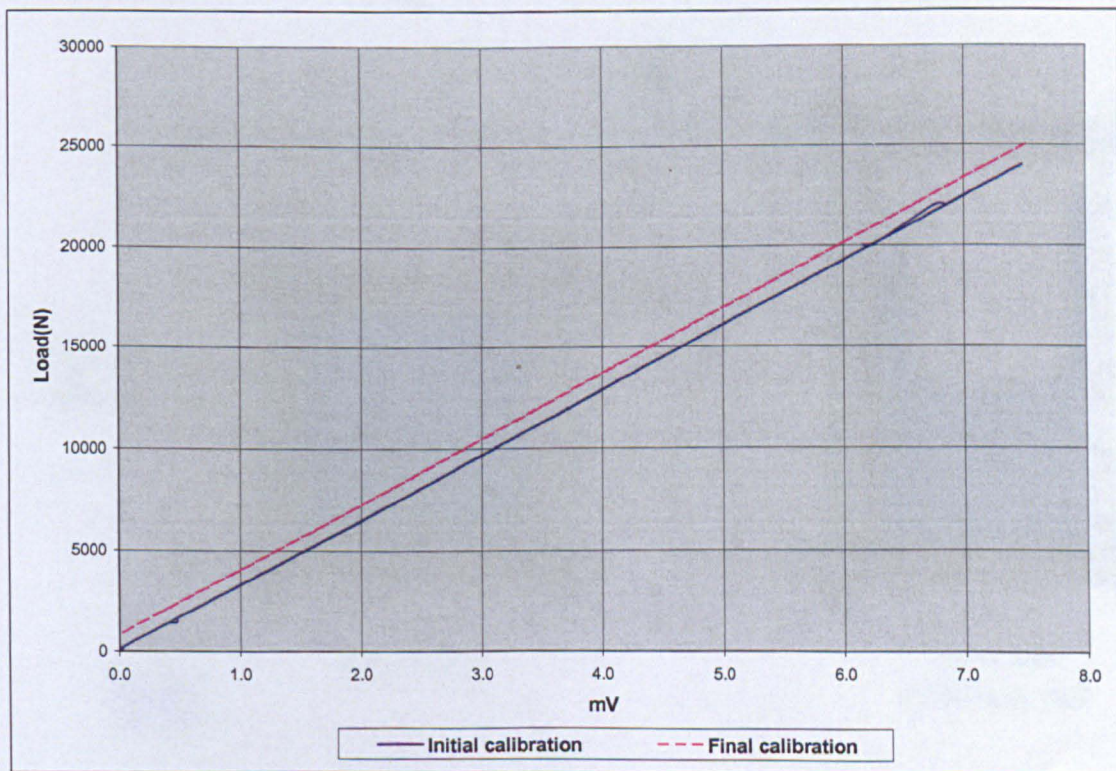


Figure 4.18 Initial and final calibration lines for the load cell (Serial No. 8903979).

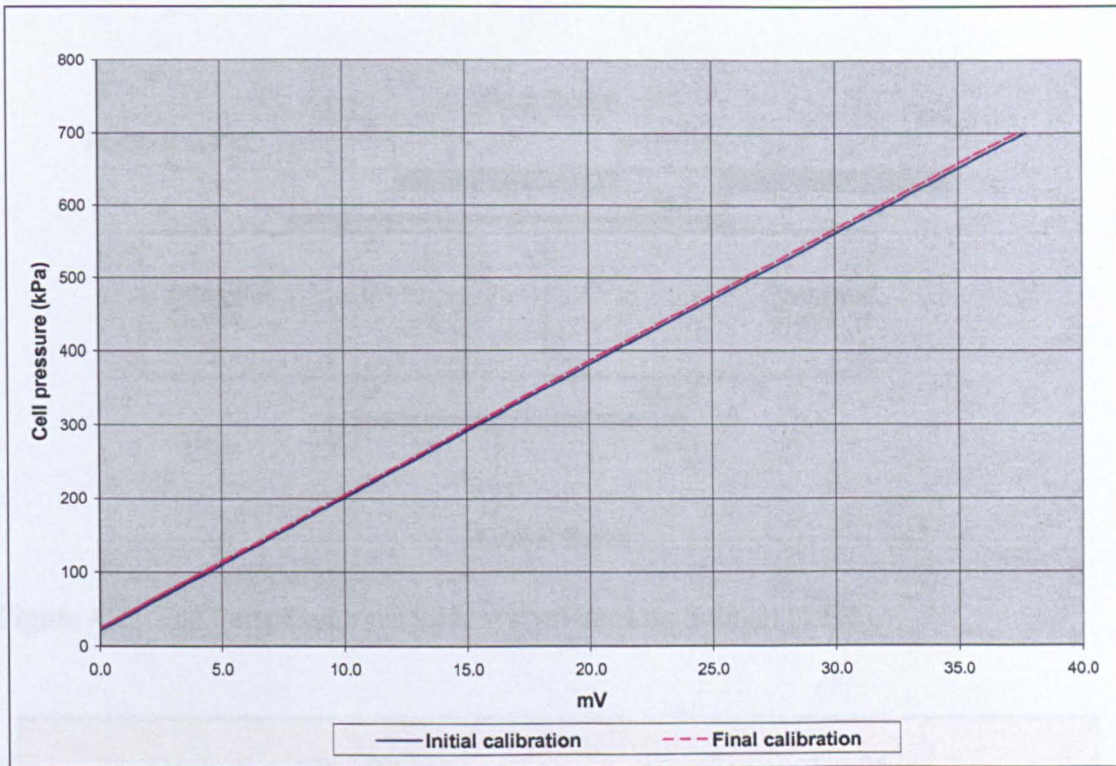


Figure 4.19 Typical initial and final calibration lines for a pressure transducer (Serial No. 334923).

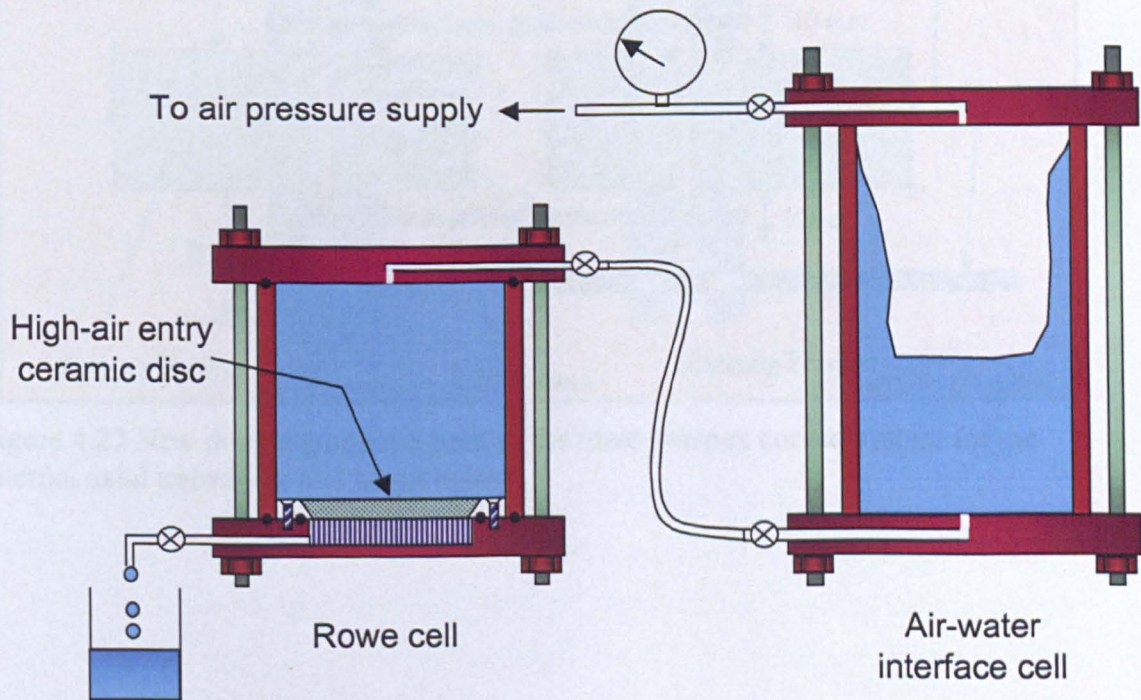


Figure 4.20 Saturation set up for the high air-entry ceramic disc to be used in the Double-wall Triaxial Cell.

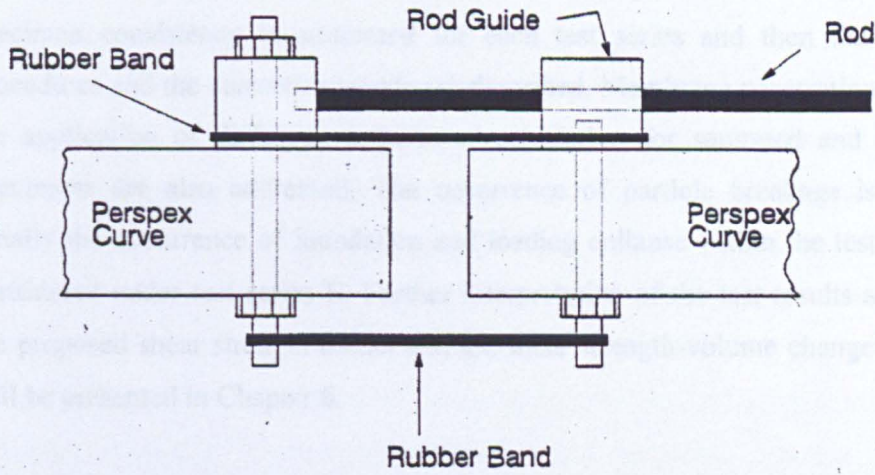


Figure 4.21 The Perspex curves joint system used by Salman (1995).

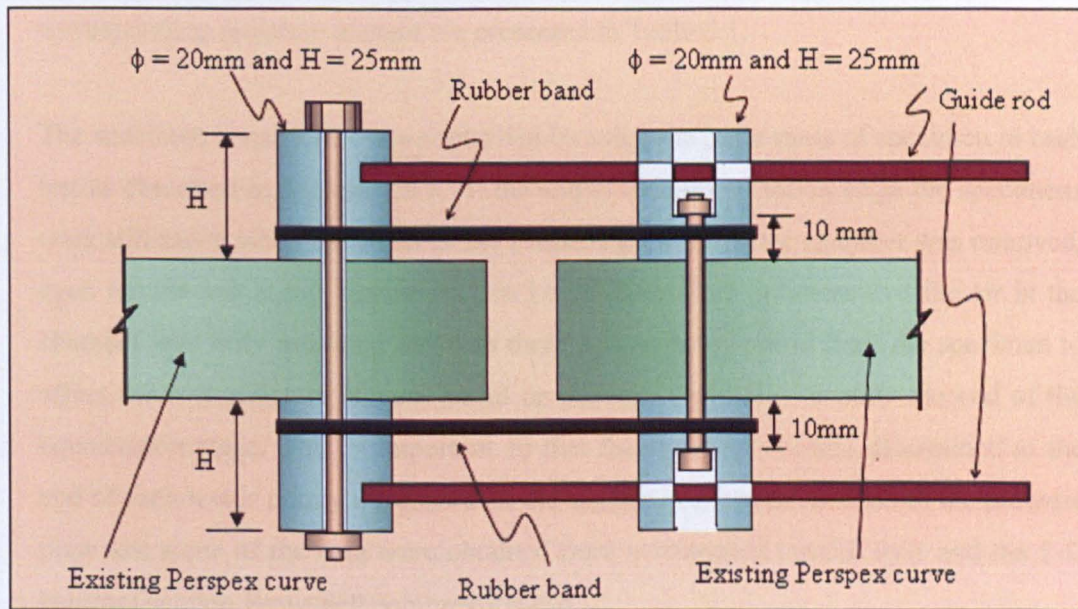


Figure 4.22 New double guide rod joint in the three Perspex curved system for the internal axial transducer and target holder.

## Chapter 5

### Test Results

This chapter presents all of the test results and their initial interpretation. The specimen consistency is addressed for each test series and then the calculation procedures and the corrections made are described. Membrane penetration effects and the application of different methods of calculation for saturated and unsaturated specimens are also addressed. The occurrence of particle breakage is examined. Finally the occurrence of inundation and loading collapse within the test material is considered under test series E. Further interpretation of the test results according to the proposed shear strength model and the shear strength-volume change framework will be presented in Chapter 6.

#### 5.1 Results of Test Series A.

This test series using the pressure plate equipment was to determine the soil moisture characteristic curve of the test material. The magnitude of applied suction and the corresponding moisture content are presented in Table 5.1.

The specimen consistency was controlled by using the same mass of specimen in each test as described in Section 4.5.1. At the end of each equalisation stage the specimens were still moist when the cover of the pressure plate extractor chamber was removed, even for the test at the highest suction i.e. 290kPa. This indicates that the air in the chamber was fully saturated and thus there was no evaporation from the specimen to affect the soil moisture content based on suction, especially towards the end of the equalisation stage. This is important so that the moisture content determined at the end of each test is purely dependent on the applied suction. In addition to the pressure plate test some of the data were obtained from unsaturated triaxial tests and the 1-D constant suction Rowe cell compression test.

The soil moisture characteristic curve of the test material is shown in Figure 5.1. The curve indicates that the residual suction of the test material is about 15 kPa according to the definition by Fredlund and Xing (1994) as illustrated in Figure 2.4. Curve no.8 in Figure 5.2 shows the soil-moisture characteristic curve of the test material relative to finer materials. The low value of residual suction obtained for the test material is in

accordance with the report that residual suction decreases as the soil gets coarser (Fredlund and Xing, 1994).

## 5.2 Results of Test Series B.

Test series B was carried out to determine the shear strength behaviour with respect to effective stress for saturated conditions by conducting consolidated drained triaxial tests on saturated specimens. Single stage and multistage tests were carried out to check the reliability of the multistage test. This is important because all of the triaxial tests on unsaturated specimens were carried out by the multistage method in order to optimise the test programme in the available time period. The reliability of these tests was verified by the repeatability between multistage and single stage tests on saturated specimens. If the results are considered repeatable then any difference in results between the multistage triaxial test on saturated and unsaturated specimens should only be due to their different states of internal stress.

### 5.2.1 Specimen Consistency.

The specimen preparation procedure and placement techniques described in Section 4.5.1 and Section 4.5.2.2 were able to produce consistent specimens. The almost uniform initial specimen dimensions in this test series and their dry densities are listed in Table 5.2.

### 5.2.2 Saturation Stage.

All of the specimens in this test series were saturated to a minimum Skempton's B value of 0.92 as shown in Table 5.3. The volume of water that entered the specimen air voids was measured during the saturation process with the intention of determining the volume of the voids. However, due to the errors caused by membrane compression, compression of air trapped between the membranes, the gap between the specimen and the top cap and the voids in the porous disk this was not possible so the volume of the voids,  $V_v$  was calculated using the formulae;

$$V_v = V_T - V_s \quad \text{Equation 5.1}$$

$$V_s = \frac{M_s}{G_s \times \gamma_w} \quad \text{Equation 5.2}$$

where  $V_T$  is the total volume of the specimen,

$V_s$  is the volume of soil solid,

$M_s$  is the weight of dry specimen in kg, determined at the end of each test.

$G_s$  is the specific gravity of the soil solid taken as 2.71 and

$\gamma_w$  is the unit weight of water taken as  $9.81\text{kN/m}^3$ .

The specimen initial volume was assumed to be unchanged by the saturation stage and thence the volume before consolidation was assumed as the measured initial volume.

### 5.2.3 Consolidation Stage.

The specimen consolidation caused the specimen to shrink, and the reduction in volume had to be determined in order to calculate the specimen's cross sectional area before the shearing stage. The specimens were consolidated by elevating the cell pressure higher than the existing back pressure achieved at the end of the saturation stage by either 100 or 200 or 300kPa depending on the effective stress required in the shearing stage. The consolidation curves for all tests in this series are shown in Figures 5.3 - 5.6. The plots that indicate that the specimens are swelling slightly at the later stages of the consolidation are not actually due to swelling. The volume change was due to a very slight leak at the bleed valve on top of the 100cc Imperial College type volume change unit. These graphs are the S8%SSES100 in Figure 5.3(a) and S4%SSES200, S4%SSES300 and S6%SSES100 in Figure 5.3(b).

Upon elevating the cell pressure, membrane penetration occurred and the consolidated specimen volume change indicated by the volume change unit was higher than the actual value and had to be corrected for the volume change caused by membrane penetration. The ambiguity here was that the soil might be consolidating at the same time as the membrane penetration. If this is the case it is impossible to differentiate between these two volume changes unless the radial contraction of the specimens was monitored as in the Double-wall Triaxial cell. Nonetheless, this ambiguity can be sorted by making reasonable assumptions.

The consolidation was started by opening both the drain and the cell pressure valves simultaneously. The moment the cell pressure valve was opened to apply the increased cell pressure the membrane penetration dominated the initial volume change

and the soil consolidation was assumed to be negligible. The consolidation involved the mobilisation of the soil particles against the frictional force between them until a state of interlocking was achieved. Logically the cell pressure would cause deformation at the weakest point before it started to overcome the higher deformation resistance. This weakest point is presumably the stretching of the membrane at the empty void spaces behind it and the friction between the soil particles was assumed to be much higher. This is based on the assumption that the frictional resistance between the soil particles was greater than stretching the membrane. The weakness of the membrane against withstanding the elevated cell pressure can be seen when the membrane was pushed right to the face of the inner particles once the elevated cell pressure was applied. This was a clear sign that stretching the membrane required less effort than consolidating the specimen. This was supported by the consolidation curve, which indicated that specimen consolidation took a much longer period than membrane penetration. Therefore the initial volume change during consolidation must be due to the membrane penetration. This presumption was supported by the initial linear portion of the consolidation curve (note this not a  $\sqrt{t}$  scale) as shown in Figure 5.4 which must be due to deflection of an elastic material. When the deflection of the membrane was at its limit where it could not be stretched further, then the cell pressure started to act uniformly on the specimen. This is where the soil consolidation starts. When the soil particles were starting to move the presence of friction between the particles reduced the rate of volume change and there was a divergence from linearity in the behaviour of volume change with respect to time. The changes in the rate of volume change should be asymptotic as the soil approached an interlocking arrangement. The point where the curve of volume change versus time diverges from linearity is taken as the volume of membrane penetration. The consolidated volume of the specimen was taken as the volume change that occurred after this point. In order to determine the volume due to membrane penetration the consolidation curves have been redrawn with a bigger scale for the first 100 seconds as shown in the typical graphs in Figure 5.7 - 5.12. The actual consolidation volume and the volume of membrane penetration in each test are listed in Table 5.4.

The single stage triaxial tests for the compacted specimens are giving an almost consistent volume of membrane penetration for the same effective stress within a

variation of 10 cc. A slightly higher membrane penetration was encountered for the loosely prepared specimen (i.e. S0%SSES100, S0%SSES200 and S0%SSES300). This is likely to be due to the higher void ratio indicated by the lower dry density in Table 5.2.

The membrane penetration for the multistage tests as indicated in Table 5.4 is showing a decrease in the volume of membrane penetration as each test stage is carried out at a higher pressure. This is expected since most of the membrane penetration took place during the first consolidation stage. However if the cumulative volume of membrane penetration is considered then it can be seen that the value of membrane penetration increases with effective stress.

#### 5.2.4 Shearing Stage.

At the end of the consolidation stage, the shearing stage was begun by applying the deviator stress. The deviator stress was taken as the applied vertical force divided by the specimen's cross sectional area,  $A'$ . The concept for the calculation of  $A'$  was that the initial specimen volume before shearing began,  $V_i$ , minus volume decrease due to shearing,  $\Delta V$ , must equal to the final specimen's volume,  $V_f$ ;

$$V_i - \Delta V = V_f \quad \text{Equation 5.3}$$

$$\Rightarrow \frac{\pi D_i^2}{4} \times H_i - \Delta V = A' \times (H_i - d) \quad \text{Equation 5.4}$$

where  $D_i$ ,  $H_i$  and  $d$  are the initial specimen diameter, initial specimen height and the specimen's vertical displacement respectively. The specimen volume change,  $\Delta V$ , was determined from the volume change indicated by the volume change unit. From here the effective cross sectional area,  $A'$ , at any stage can be determined; thus the deviator stress can be calculated by dividing the applied vertical load by  $A'$ . The graphs of deviator stress versus axial strain for the tests are plotted in Figure 5.13 - 5.18. The deviator stresses at failure were deduced from these graphs and are listed in Table 5.3. For the compacted specimens, failure was taken as the maximum deviator stress for those graphs that showed a well defined peak. For those tests that showed that the deviator stress was continuously increasing after the first kink, the failure point was taken at an additional 0.2% axial strain from the first kink. This is because this type of curve is anticipated to show the peak value at this point if there is no

particle breakage, since particle breakage seems to cause a continuous increase in deviator stress. This judgement is based on the graphs that showed a well defined peak. In other words defining failure in this manner is considering particle breakage as a criterion of failure. This is considered reasonable since particle breakage is an indication that the soil has failed to withstand that limit of deviator stress.

For the loosely prepared specimens the graphs of deviator stress versus axial strain do not show a well defined peak but gradually increase and tend to level out at higher strains. The failure point was taken at 5% axial strain.

The graphs of specimen volume change versus axial strain during shearing are plotted in Figures 5.19 - 5.24.

All of the tests on compacted specimens at an effective stress 300kPa showed a continuous increase in deviator stress with respect to axial strain including the multistage test third shearing stage. On the other hand, all the single stage tests at lower effective stresses i.e. 100, 200 and 250kPa showed a well defined peak stress. The continuous increase in the deviator stress may be related to particle breakage for the higher effective stress. If this is so then particle breakage is producing an increase in the strength and will have influence on the proposed shear strength-volume change framework which only considers the increase in strength due purely to closer arrangement of the particles and not particle breakage.

This effect due to particle breakage is supported by grading curve number 4 in Figure 4.1 determined at the end of the shearing stage under effective stress of 300kPa for the specimen compacted at 8% moisture content (i.e. S8%SSSES300). There was a slight increase in the proportion of particle sizes less than 5mm diameter compared to curve number 1, which represents the general initial particle size distribution before shearing. This therefore provides the evidence that particle breakage is occurring and may be responsible for the increase in strength.

During the initial stage of the application of deviator stress, the particles move to a denser packing by moving into empty void spaces until an interlocking condition is achieved. At this stage the volume change unit is indicating a continuous specimen

volume decrease. However there are two possible scenarios after the full particle interlocking position has been achieved where the specimen volume can either be increasing or decreasing. In both cases the specimen height is shortened due to the advancement of the load cell piston. In the first case the height shortened while the specimen dilates which resulted in an overall volume increase and in turn the deviator stress decreased. In the second case, as the specimen's height became shorter the overall volume decreased without any specimen radial expansion. In this case there had to be particle breakage otherwise dilation would have occurred since the particles were already interlocking. The deviator stress would have still increased in this case even though the specimen's cross sectional area remained constant since the frictional resistance between the particles increased as their overall contact area increased. This is because the breakage caused smaller chippings to fill up the void spaces. Therefore when there is a volume decrease after the particles have fully interlocked, particle breakage must have occurred.

The problem now is to determine the point where the particles are fully interlocked. If this can be identified then it should be easy to locate the point at which the particles start breaking by cross reference with the graph of specimen volume change versus axial strain.

Table 5.3 summarises the deviator stress and effective stress at failure for all the single stage and multistage tests on saturated specimens. Referring to all of the tests on specimens compacted at 4% moisture content, for effective stress of 100kPa the deviator stresses at failure were 563 and 549kPa, while for effective stress 200kPa the deviator stresses were 813 and 833kPa and for effective stress of 300kPa the deviator stresses at failure were 915, 891 and 980kPa. The maximum difference between these results for effective stress of 100, 200 and 300kPa are 2.5%, 2.4% and 9.1% respectively. Therefore, these results show reasonable comparability between single stage and multistage tests, especially for lower effective stress i.e. 100 and 200kPa.

### **5.3 Results of Test Series C.**

Test series C was carried out to determine the shear strength behaviour with respect to net stress when the soil was unsaturated at a certain constant value of suction. This was done by conducting consolidated drained triaxial tests on unsaturated specimens. All specimens were compacted at 4% moisture content except for the test at a suction of 90kPa where it was compacted at a moisture content of 1%. Only multistage tests were carried out in this series. The tests were carried out for net stresses of 100, 200 and 300kPa at suctions of 25, 50, 60 and 90kPa. The shear surface envelope obtained from the Mohr circles drawn for this respective combination of net stress and suction represents the overall shear strength which is the sum of shear strength at saturation and the apparent shear strength. Therefore the apparent shear strength at different levels of net stress and suction was determined by deducting the shear strength for the saturated condition from the overall shear strength.

#### **5.3.1 Specimen Consistency.**

The specimen preparation procedure and the placement technique were described in Section 4.5.1 and Section 4.5.3.3 and were able to produce consistent specimens. This is indicated by the similar initial specimen dimensions and dry densities listed in Table 5.5. Test no.4 in test series C was compacted at 1% moisture content for the test at suction of 90kPa. It will be noted that this produced a dry density similar to the 4% moisture content specimens for the washed material.

#### **5.3.2 Equalisation Stage.**

The equalisation process was conducted under a net cell pressure (i.e. cell pressure minus pore air pressure) of 10kPa. The suction was applied by the axis translation technique where pore air pressure was elevated higher than the pore water pressure. The specimen water drained out of the specimen for all tests. The changes in the specimen water content were recorded during equalisation and a correction was made for the intrusion of diffused air from the specimen through the high air-entry ceramic disk to the water compartment below the disk. Since this compartment is directly linked to the specimen water volume change unit, then the bubbling of the diffused air out of the cell would affect the reading indicated by the water volume change unit. The equalisation was stopped when the flow of the specimen water was less than 0.05

cc in 12 hours. The equalisation curves for the four suction values in this test series are plotted in Figure 5.25.

The duration of an equalisation process depends on several factors like the level of suction to be attained and the air-entry value of the ceramic disk used. The higher the imposed suction value the longer will be the equalisation period due to a greater volume of water needing to be expelled. Despite the very low permeability, the use of the higher air-entry value ceramic disk (i.e. 3 bar) will be of advantage. This is because it can reduce the amount of water entering the specimen when the vacuum is applied to the specimen during the process of setting up. The setting up took approximately 4 hours before the vacuum could be released. Thus the low permeability could considerably reduce the amount of water entering the specimen. At this stage a continuous flow of water from the specimen water volume change unit to the compartment below the ceramic disc was preferable to avoid air bubbles forming along this line when the pore water pressure became negative. This would have occurred if the flow was stopped by closing the valve at the specimen volume change unit and the result was the development of negative pore water pressure below the ceramic disc. The development of the negative pressure underneath the ceramic disc could have desaturated the disc and therefore stopping the flow was a very risky step in the effort to reduce the amount of water entering the specimen. This technique has been applied to the specimen tested for suction of 90kPa and the period of equalisation was considerably reduced to less than 100 hours as shown by the equalisation curve in Figure 5.25. In this way the whole multistage test would only have required a maximum of 11 days compared with the former technique which took between 6 to 8 weeks.

### **5.3.3 Consolidation Stage.**

The specimens were consolidated at net cell pressures of 100, 200 and 300kPa and the consolidation curves for these triaxial tests at different suctions of 25, 50, 60 and 90kPa are shown in Figures 5.26 - 5.29 respectively. The specimen volume change was monitored through the large volume change unit and this also needed correction for the membrane penetration. The advantage here is that there were three local radial transducers fixed at the specimen's centre height to monitor the lateral movement of the soil particles. However, to judge the specimen volume change throughout the test

from the spot readings of these transducers would not be as accurate as using the volume change unit.

In the Conventional Triaxial Cell, membrane penetration was assumed to stop when the graph of volume change versus time diverged from linearity. However in the Double-wall Triaxial Cell the membrane penetration was occurring faster due to the expulsion of air compared to water in the Conventional Triaxial Cell. This faster rate of consolidation was not anticipated and the data logging rate was not frequent enough at the beginning of the consolidation in order to determine the point where it diverged from linearity. Therefore membrane penetration was assumed to have already stopped when the graph of volume change versus time was almost horizontal as indicated in the typical enlarged consolidation curves plotted in Figures 5.30 - 5.32. In the first few seconds (i.e. 4 to 8 seconds) of the consolidation where membrane penetration was thought to have ceased, the uniform lateral contraction of the specimen was obtained by averaging the soil lateral movements indicated by the radial transducers. These are plotted in the same figures. The volume of specimen contraction,  $V_{Rad}$ , at this instant was calculated by assuming a uniform contraction over the entire height,  $H$ , of the specimen. If the average radial contraction indicated by the radial transducers is  $d_{Rad}$  and the diameter of the specimen is  $D$  then,

$$V_{Rad} = \pi D \times H \times d_{Rad} \quad \text{Equation 5.5}$$

The volume change indicated by the large volume change unit,  $V_{VCU}$ , for the same time period is the volume change from both specimen contraction and the membrane penetration. Then the volume change due to membrane penetration,  $V_{MP}$ , can be determined by subtracting  $V_{Rad}$  from  $V_{VCU}$ :

$$V_{MP} = V_{VCU} - V_{Rad} \quad \text{Equation 5.6}$$

This procedure for the determination of the volume of membrane penetration was performed using the typical enlarged curves of volume change and specimen radial contraction versus time shown in Figures 5.30 - 5.32. The volume of membrane penetration and the correction for water leakage for all consolidation stages in this test series are summarised in Table 5.6. Similar to the membrane penetration for the multistage triaxial test on saturated specimens as discussed in Section 5.2.3, the actual volume of membrane penetration at any stage is the cumulative volume change from

the lower cell pressure stages. There is an almost equal volume of membrane penetration for both the saturated and unsaturated specimens.

During the consolidation process in this test series, where the specimens were left to consolidate for at least 10 hours, specimen volume change indicated a continuous contraction of the specimen which is not logical and the reason for this is unknown. It could be some form of creep or a water leak. In every test a correction for this was performed.

#### 5.3.4 Shearing Stage.

The specimen volume change monitored through the large volume change unit was assumed to be that within the central gauge height of 200mm only. The zones above and below the gauge height were assumed as dead zones where the particles did not move due to end friction (Kirkpatrick and Beshaw, 1968 and Kirkpatrick and Younger, 1970). However the monitored volume change had to be corrected for the penetration of the load cell piston into the inner cell. In the calculation of the deviator stress, the effective specimen cross sectional area,  $A'$  was assumed uniform over the gauge height and was calculated according to Equation 5.5.

$$A' = \frac{V_i - \left( \Delta V_{VCU} + \frac{\pi D_p^2}{4} \times d_{axial} \right)}{(H_i - d_{axial})} \quad \text{Equation 5.5}$$

$V_i$  is the initial gauge volume,  $\Delta V_{VCU}$  is the volume change indicated by the large volume change unit,  $D_p$  is the load cell piston diameter,  $d_{axial}$  is the vertical travel of the piston and  $H_i$  is the initial specimen gauge height. The deviator stress at any stage was obtained by dividing the vertical load by  $A'$ .

The graphs of deviator stress versus average internal axial strain for tests at suctions of 25, 50, 60 and 90kPa are shown in Figures 5.33 - 5.36 respectively. The graphs of specimen volume change and specimen water volume change versus average internal axial strain are shown in Figures 5.37 - 5.40 respectively. Apparently there is only a small insignificant decrease in the specimen water content during shearing despite the suction reading being constant throughout the test.

Referring to the graphs of deviator stress versus internal axial strain at the third shearing stage, there are two types of shear strength behaviour. The normal type of behaviour for dense granular soils or overconsolidated clay is that the maximum deviator stress can be detected as shown by the graph of deviator stress versus internal axial strain in Figure 5.33 and 5.34, which are the tests at suctions of 25 and 60kPa. However the second type of graph of deviator stress versus internal axial strain is that shown in Figure 5.35 and 5.36, which are the tests at suctions of 50 and 90kPa. In these graphs the deviator stress continuously increases as the specimen's volume decreases asymptotically without indicating any dilation.

Failure is taken either at the maximum deviator stress or at an additional 0.2% axial strain from the first kink as discussed in Section 5.2.4. The values of cell pressure, pore water pressure, pore air pressure, net stress and deviator stress at failure are summarised in Table 5.7.

The specimen volume change graphs associated with a peak deviator stress (i.e. Figure 5.37 and 5.38) indicate that the specimen volume first decreased and then increased due to dilation before the peak deviator stress was achieved. The dilation is due to the effect of particles interlocking and sliding over each other without any breakage. This can be seen clearly in the first shearing stage of all of the tests in this series and in the third shearing stage for the test at suction 25 and 50kPa. However in the third shearing stage for suctions of 60 and 90kPa, as indicated in Figures 5.35 and 5.36, the volume kept on decreasing and stabilised at a higher deviator stress. An explanation for this is that as the specimen shortened, its diameter expanded to compensate for the volume decrease, and this is confirmed by the increasing diameter indicated by the increasing average radial displacement in the third shear stage as shown in Figures 5.43 and 5.44. However, if the particles are sliding over each other and causing the specimen to dilate the deviator stress would be decreasing as well as the specimen volume increasing. Instead, the deviator stress keeps on increasing and the specimen volume remains constant. The possible explanation is that the particles are being crushed resulting in an increase in strength.

The variations of the average radial displacement during shearing up to the point where the specimens start to dilate are plotted in Figures 5.41 - 5.44. The graphs

indicate only a small dilation of less than 0.5mm (i.e. 0.67%) laterally took place at this stage. Table 5.8 lists the specimen's central height lateral displacement at the point of specimen dilation. The occurrence of large radial displacement during the third stage of shearing for suctions of 60 and 90kPa has to be ignored since there is no well defined dilation point and the particles were suspected of undergoing breakage as discussed earlier. Therefore it can be assumed that the specimen underwent a one-dimensional compression before it started to dilate.

#### **5.4 Results of Test Series D.**

This test series was carried out to determine the effect of soil grading on the shape of the failure envelope. The soil samples that represent uniform grading were test materials retained on the 5mm sieve. The soil sample that represents a wider grading material is the test material itself. The 5mm minimum particle size specimens were prepared by light compaction under dry conditions to avoid particle breakage during compaction which would have changed the grading. The initial specimen dimensions and the dry density are presented in Table 5.9. The shear strength at saturation was obtained by conducting triaxial tests on saturated specimens at effective stresses of 100 and 200kPa. When both specimens were saturated an identical Skempton B value of 0.96 was obtained. Figure 5.45 shows their consolidation curves. The variations of the deviator stress and specimen volume change against axial strain are plotted in Figure 5.46 and Figure 5.47 respectively. Table 5.10 shows the cell pressure, pore water pressure and the deviator stress at 5% axial strain which is considered as failure. The Mohr Coulomb envelope of the sieved material compared to the test material will be plotted and discussed in Chapter 6.

#### **5.5 Results of Test Series E.**

The objective of this test series was to determine the volume change behaviour with respect to net stress for unsaturated specimens and with respect to effective stress for saturated specimens. It also gave an opportunity to find out whether the soil exhibited massive collapse behaviour near saturation.

##### **5.5.1 Specimen Consistency.**

Throughout the tests the axial displacement transducer was locked at a fixed position attached to the cell top cap and its reading was calibrated with a known dummy

specimen height. Since all the specimens were prepared to the marked height then the position when the top platen touches the specimen can be detected through the axial displacement transducer's reading. Almost consistent specimen heights and dry densities were obtained for the tests as listed in Table 5.11.

### **5.5.2 Equalization Stage.**

For the unsaturated specimens the equalisation process was started by applying the appropriate pore air pressure to the specimen and zero pore water pressure was applied to the bottom of the 3-bar air-entry ceramic disk fixed at the base of the specimen by exposing the outlet to the atmosphere through a burette. The rate of volume of water discharged to the burette was measured. Correction to this volume has to be made for the infiltration of diffused air from the specimen through the ceramic disk to the water compartment underneath it. The volume of diffused air was obtained by flushing the water compartment under a back pressure of 50 kPa to an inverted test tube filled up with water. The specimen water volume change during the equalisation of the tests CompSuc25 and CompSuc50 is shown in Figure 5.48. The equalisation was stopped when the discharge rate reduced to 0.05cc in 12 hours.

### **5.5.3 Determination of Friction between Cell Wall and Top Platen.**

This was a very important part of the test since the three internal load cells previously used by Goodwin (1991) to eliminate the effect of cell wall friction were not functioning and had been replaced by three identical length steel cylinders. Therefore the friction between the top platen and the cell wall had to be predetermined before the soil was compressed. For both tests on unsaturated specimens, while the top platen was still clear from the specimen, a cell pressure increment was applied to the top of the platen until it started to move. This can be seen from the graph of the axial displacement transducer's reading against the net stress (Figure 5.49 -5.51). The net stress is the difference between the cell pressure and the pore air pressure. The net pressure that began to move the top platen and stopped at the level of the specimen surface was taken as the wall friction. Since at this point the total vertical force is almost zero then the platen will automatically stop once it touches the specimen. Figure 5.49 and 5.50 indicate that the wall friction for the test CompSuc25 and CompSuc50 were equivalent to applied pressures of 145 and 80 kPa respectively.

However the wall friction for the test on the saturated specimen, i.e. CompSat, was determined to be only 30kPa and the data for the friction test was recorded manually and not electronically logged. The net pressure was increased from 10kPa by increments of 5 kPa until a net pressure of 30kPa which drove the axial displacement transducer reading from 2.81mm to stop at 7.40mm which corresponded to the specimen height as indicated in Figure 5.51. Since the specimen's pore water pressure was set to atmospheric during the friction test on the saturated specimen then the net pressure is the applied pressure itself. When the net pressure has been balanced up by the wall friction then there will be no stress imposed on to the specimen during the friction test.

The great variation of the wall friction from one test to another is very unexpected since the wall and the O-rings on the top platen were well greased before the top platen was jacked into place. The room temperature was maintained constant throughout the tests. However the real friction value indicated during the test has to be used for the analysis and the reason for the variation cannot be detected.

#### **5.5.4 Compression Stage.**

The compression stage was performed by applying net stress increments of 50kPa and at every pressure increment the soil was allowed to be compressed until the movement of the top platen ceased. This indicated that a state of stress equilibrium between the mobilized shear strength and the shear stress between the soil particles had been achieved. On the next increment of net stress, a further soil compression took place and in turn increased the mobilized friction angle and produced an increase in the mobilized shear strength which at some point equalised with the applied stress state. Once the stress equilibrium is reinstated the settlement ceased. This is the phenomenon of loading collapse discussed in Chapter 3.

The magnitude and the duration of the applied net stress for test code CompSuc25, CompSuc50 and CompSat are shown in Figures 5.52 - 5.54 and the graphs of net stress against axial displacement are shown in Figures 5.55 - 5.57. The arrival at another stress equilibrium condition was judged from the graph of axial displacement versus time when the graph became horizontal indicating that the settlement has stopped while the net stress remained constant. The graphs also indicate that the

arrival of the stress equilibrium condition is not immediate upon the application of vertical stress increment. This is due to the time taken to overcome the friction between the cell wall and the top platen. The edges of the step-like graph in Figures 5.55 - 5.57 represent the axial displacement at which the mobilized shear strength is in equilibrium with the corresponding applied stress. The linear variation of these axial displacements against applied net stresses represented by the straight line that cuts through the origin is apparent, and this is in accordance with the findings of Cox (1978), Fedá (1988), Brandon *et al.* (1990), Basma and Tuncer (1992) and Vilar (1995).

The graph of effective stress versus axial displacement for the saturated condition, shown in Figure 5.57, also indicates a significant axial displacement of approximately 4.3mm upon the application of a net stress of 50kPa. This is equivalent to the inundation collapse when the soil was inundated under this effective stress. However, if instead of applying the first effective stress of 50kPa, an effective stress of 150kPa was applied, then the collapse would be 5.0mm as indicated in Figure 5.57. Therefore the magnitude of the collapse settlement due to an effective stress increase is equivalent to the corresponding settlement along the red line in Figure 5.57. Thence this graph is actually representing the magnitude of inundation collapse for the corresponding effective stress.

Table 5.1 Results of pressure plate test on the test material (i.e. no fine content).

No.	Suction (kPa)	Moisture content (%)
1	5	13.80
2(a)	6	13.58
2(b)	6	12.92
3(a)	10	1.12
3(b)	10	1.10
3(c)	10	1.05
4(a)	15	0.92
4(b)	15	1.00
4(c)	15	1.00
5(a)	20	0.99
5(b)	20	0.91
5(c)	20	0.94
6	100	0.71
7	125	0.77
8	150	0.71
9	175	0.60
10	200	0.68
11	225	0.74
12	250	0.68
13	275	0.71
14	290	0.68

Table 5.2 Initial specimen dimensions and dry density for the test series B.

Test no.	Test Code	Dry wt. of specimen (kg)	Initial specimen diameter measured on a layer of membrane (mm)			Initial specimen height (mm)			Spec. initial dry density (Mg/m <sup>3</sup> )
			1	2	3	1	2	3	
1	S4%SSES100	11.752	151.8	151.8	151.8	374	374	374	1.74
2	S4%SSES200	11.749	151.5	151.8	151.1	375	375	375	1.74
3	S4%SSES300	11.640	151.4	151.8	150.7	374	374	374	1.73
4	S6%SSES100	11.800	151.8	151.8	151.7	375	374	374	1.74
5	S6%SSES200	11.742	151.4	151.4	151.1	375	375	375	1.74
6	S6%SSES250	11.776	152.0	152.0	151.5	375	375	375	1.73
7	S8%SSES100	11.815	151.7	151.9	151.9	374	374	374	1.75
8	S8%SSES200	11.827	151.2	151.5	150.8	377	377	377	1.75
9	S8%SSES300	11.806	150.6	150.8	151.6	376	376	376	1.75
10	S0%SSES100	11.125	150.1	150.7	151.0	372	372	371	1.68
11	S0%SSES200	11.125	151.3	151.3	151.4	370	370	370	1.67
12	S0%SSES300	11.125	150.9	151.0	150.8	373	373	373	1.67
13	S4%MST1	11.752	151.4	151.3	151.0	376	375	375	1.74
14	S4%MST2	11.750	151.4	151.3	151.1	378	378	378	1.73
15	S12%MST1	11.752	151.8	151.8	151.3	378	378	378	1.72

Table 5.3 Skempton's B value, effective stress, deviator stress, cell pressure, pore water pressure and back pressure for all consolidated drained triaxial tests on saturated specimens in test series B.

Test no.	Test code	Skempton's B value	Effective stress at failure (kPa)	Deviator stress at failure (kPa)	Cell pressure (kPa)	Pore water pressure at failure (kPa)	Back Pressure (kPa)
1	S4%SSES100	0.97	100	563	640	540	540
2	S4%SSES200	0.92	200	813	540	340	340
3	S4%SSES300	0.96	300	915	640	340	340
4	S6%SSES100	0.98	105	614	591	486	490
5	S6%SSES200	0.97	199	867	690	491	490
6	S6%SSES250	0.98	245	1008	632	387	390
7	S8%SSES100	0.97	105	600	590	485	490
8	S8%SSES200	0.99	199	871	589	390	390
9	S8%SSES300	1.0	304	1074	690	386	390
10	S0%SSES100	1.0	105	453	490	385	390
11	S0%SSES200	0.97	205	708	592	387	390
12	S0%SSES300	1.0	301	853	691	390	390
13(a)	S4%MST1ES100	0.96	100	549	190	90	90
13(b)	S4%MST1ES190		190	757	291	101	100
13(c)	S4%MST1ES300		299	891	390	91	90
14(a)	S4%MST2ES150	0.95	150	712	490	337	340
14(b)	S4%MST2ES200		200	833	541	338	340
14(c)	S4%MST2ES300		300	980	641	337	340
15(a)	S12%MST1S100	0.97	105	580	491	386	390
15(b)	S12%MST1S200		202	822	590	388	390
15(c)	S12%MST1S300		305	974	691	386	390

\*Note : For test no. 13(a), (b) and (c) the specimen was saturated up to back pressure of 340 kPa and was reduced at the various stages as stated.

Table 5.4. Volume of membrane penetration at the start of the consolidation stage in test series B.

Test no.	Test code	Total specimen volume change indicated by V.C.U. (cc)	Cumulative volume of membrane penetration (cc)	Actual volume of specimen consolidation (cc)
1	S4%SSES100	53.7	30.7	23.0
2	S4%SSES200	69.0	40.3	28.7
3	S4%SSES300	89.7	55.8	33.9
4	S6%SSES100	43.8	26.0	17.8
5	S6%SSES200	71.1	44.5	26.6
6	S6%SSES250	69.0	48.3	20.7
7	S8%SSES100	52.1	35.6	16.5
8	S8%SSES200	65.6	38.7	26.9
9	S8%SSES300	78.5	55.2	23.3
10	S0%SSES100	47.6	27.4	20.2
11	S0%SSES200	72.6	45.8	26.8
12	S0%SSES300	126.4	72.9	53.5
13(a)	S4%MST1ES100	26.4	17.0	9.4
13(b)	S4%MST1ES200	2.9	17.3	2.6
13(c)	S4%MST1ES300	17.6	24.9	10.0
14(a)	S4%MST2ES100	47.1	25.8	21.3
14(b)	S4%MST2ES200	9.5	31.3	4.0
14(c)	S4%MST2ES300	12.4	39.3	4.4
15(a)	S12%MST1ES100	48.6	16.5	32.1
15(b)	S12%MST1ES200	16.4	23.9	9.0
15(c)	S12%MST1ES300	13.2	31.2	5.9

Table 5.5 Initial specimen dimensions and dry densities for triaxial tests on unsaturated specimens for test series C.

Test no.	Test code	Dry wt. of spec. (kg)	Specimen diameter measured on a layer of membrane (mm)			Specimen height (mm)			Initial dry density (Mg/m <sup>3</sup> )
			1	2	3	1	2	3	
1	USSuc25	11.950	151.7	151.9	151.9	379	379	380	1.74
2	USSuc50	11.720	150.4	150.3	150.2	378	378	379	1.75
3	USSuc60	11.620	150.1	150.8	150.5	378	378	379	1.73
4	USSuc90	11.790	150.7	150.8	150.5	378	378	380	1.75

Table 5.6. Volume of membrane penetration at the start of the consolidation stage and the leak correction made to the consolidation and shearing in test series C.

Test no.	Test code	Leak rate corrected during consolidation and shear (cc/min)	Total specimen volume change indicated by V.C.U. (cc)	Volume of membrane penetration (cc)	Actual volume of specimen consolidation (cc)	Corrected leak rate during consolidation and shearing (cc/min)
1(a)	USSuc25NS100	0.00750	48.5	34.2	14.3	0.00750
1(b)	USSuc25NS200	0.00812	26.0	14.5	11.5	0.00812
1(c)	USSuc25NS300	0.00823	18.6	9.9	8.7	0.00823
2(a)	USSuc50NS100	0.00069	42.9	27.6	15.3	0.00069
2(b)	USSuc50NS200	0.00458	26.3	16.0	10.3	0.00458
2(c)	USSuc50NS300	0.00216	18.0	9.8	8.2	0.00216
3(a)	USSuc60NS100	0.00413	51.2	39.6	11.6	0.00413
3(b)	USSuc60NS200	0.00340	30.5	13.5	17.0	0.00340
3(c)	USSuc60NS300	0.00427	19.7	10.1	9.6	0.00427
4(a)	USSuc90NS100	0.00479	50.3	29.2	21.1	0.00479
4(b)	USSuc90NS200	0.00244	27.1	14.7	12.4	0.00244
4(c)	USSuc90NS300	0.00475	16.8	9.5	7.3	0.00475

Table 5.7 Net stress, deviator stress, cell pressure, pore water pressure and pore air pressure at failure for all consolidated drained triaxial tests on unsaturated specimens in test series C.

Test no.	Test code	Net stress at failure (kPa)	Deviator stress (kPa)	Cell pressure (kPa)	Pore water pressure (kPa)	Pore air pressure (kPa)
1	USSuc25NS100	100	672	190	65	90
	USSuc25NS200	200	955	290	65	90
	USSuc25NS300	300	1209	390	65	90
2	USSuc50NS100	100	670	190	40	90
	USSuc50NS200	200	924	290	40	90
	USSuc50NS300	300	1142	390	40	90
3	USSuc60NS100	100	566	190	30	90
	USSuc60NS200	200	822	290	30	90
	USSuc60NS300	300	1132	390	30	90
4	USSuc90NS100	99	561	200	11	101
	USSuc90NS200	199	837	300	11	101
	USSuc90NS300	299	1075	400	11	101

Table 5.8 Central height radial displacements at the point of specimen dilation during the shearing stage in unsaturated consolidated drained triaxial tests in test series C.

Test no.	Test code	Suction (kPa)	Targeted Effective stress (kPa)	At the point of specimen dilation		
				Corresponding % internal axial strain	Radial displacement (mm)	% radial strain ( $R \approx 75\text{mm}$ )
1	USSuc25NS100	25	100	0.2	0.32	0.43
	USSuc25NS200	25	200	0.65	0.4	0.53
	USSuc25NS300	25	300	1.13	0.48	0.64
2	USSuc50NS100	50	100	0.2	0.33	0.44
	USSuc50NS200	50	200	0.69	0.51	0.68
	USSuc50NS300	50	300	1.4	1.04	1.4
3	USSuc60NS100	60	100	0.22	0.25	0.33
	USSuc60NS200	60	200	1.05	0.77	1.02
	USSuc60NS300	60	300	1.7	1.0	0.67
4	USSuc90NS100	90	100	0.19	0.08	0.11
	USSuc90NS200	90	200	0.53	0.15	0.20
	USSuc90NS300	90	300	3.0	1.17	1.56

Table 5.9 Initial specimen dimensions and dry densities for the test series D.

Test no.	Test Code	Dry weight of specimen (kg)	Initial specimen diameter measured on a layer of membrane (mm)			Initial specimen height (mm)			Spec. dry density ( $\text{Mg/m}^3$ )
			1	2	3	1	2	3	
1	Min5SSES100	10.804	150.7	151.1	150.8	368	368	367	1.64
2	Min5SSES200	10.798	150.8	151.0	150.9	369	369	369	1.64

Table 5.10 Skempton's B values, effective stress, deviator stress, cell pressure and pore water pressure at failure during shearing for triaxial tests on saturated specimen in test series D.

Test no.	Test code	Skempton's B value	Effective stress at failure (kPa)	Deviator stress at failure (kPa)	Cell pressure (kPa)	Pore water pressure at failure (kPa)	Back Pressure at failure (kPa)
1	Min5SSES100	0.96	106	500	490	384	390
2	Min5SSES200	0.96	204	753	590	386	390

Table 5.11 Specimen and cell properties in Rowe cell compression tests under constant suction in test series E.

Test no.	Test code	(equals pore air pressure) Suction (kPa)	%m.c. during specimen preparation	Friction between piston and cell wall (kPa)	Specimen initial height (mm)	Weight of soil solid (g)	Initial dry density (Mg/m <sup>3</sup> )
1	CompSuc25	25	2.1	145	123.7	9210	1.47
2	CompSuc50	50	1.9	80	125.5	9224	1.45
3	CompSat	0	0	30	124.6	9216	1.46

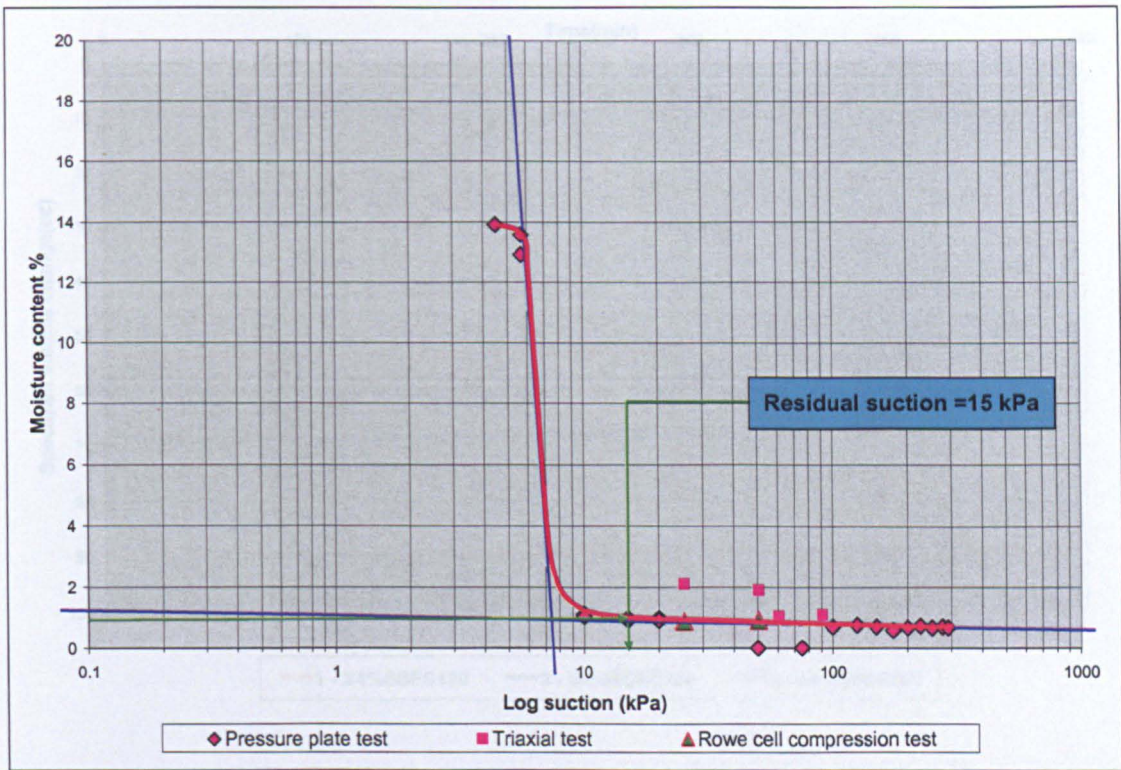


Figure 5.1 Soil-moisture characteristic curve and residual suction of 15 kPa of the test material.

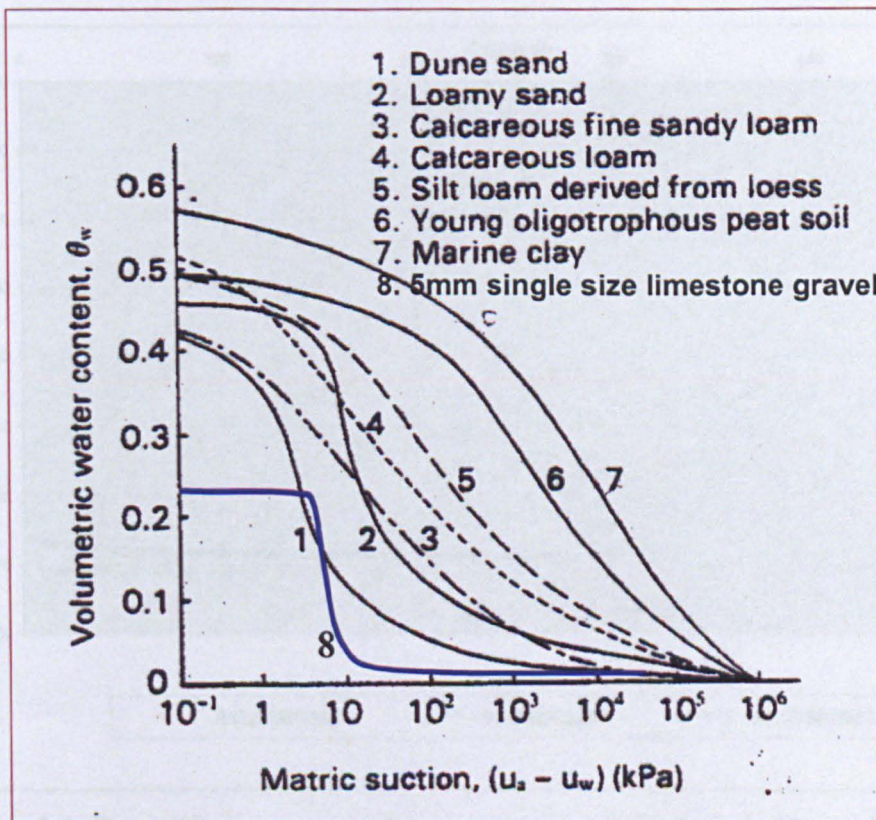


Figure 5.2 Soil moisture characteristic curve of the test material relative to finer materials.

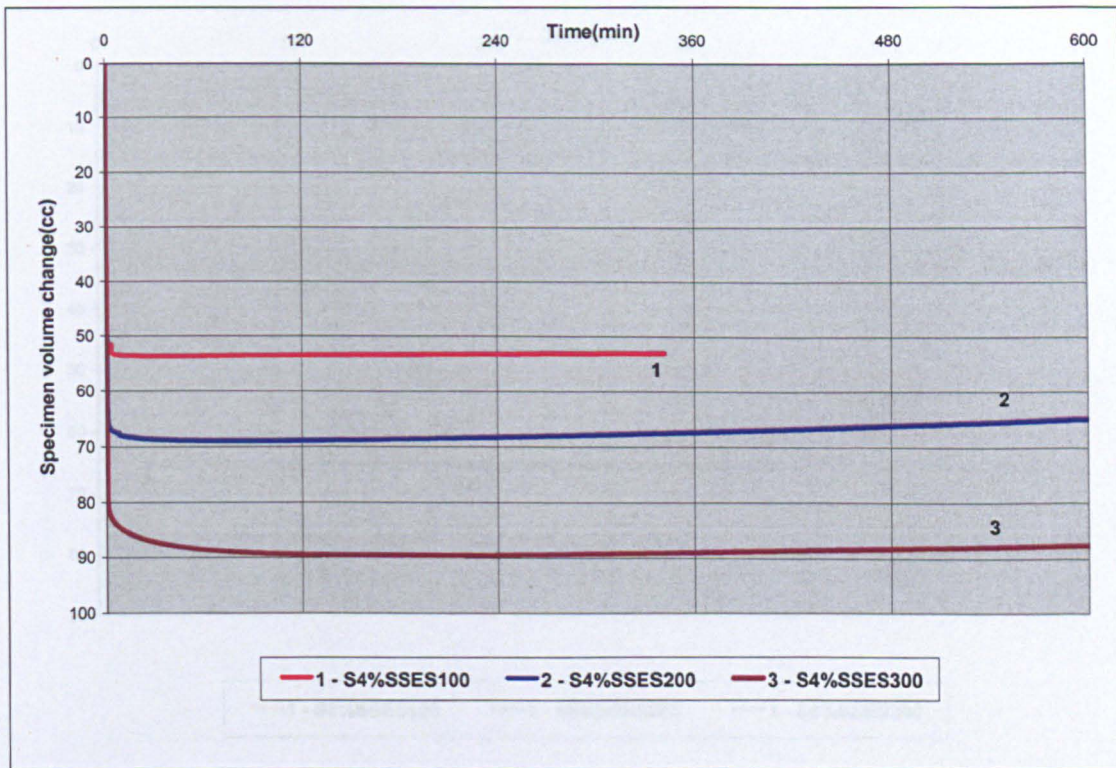


Figure 5.3 Consolidation curves for specimens compacted at 4% moisture content (Test series B).

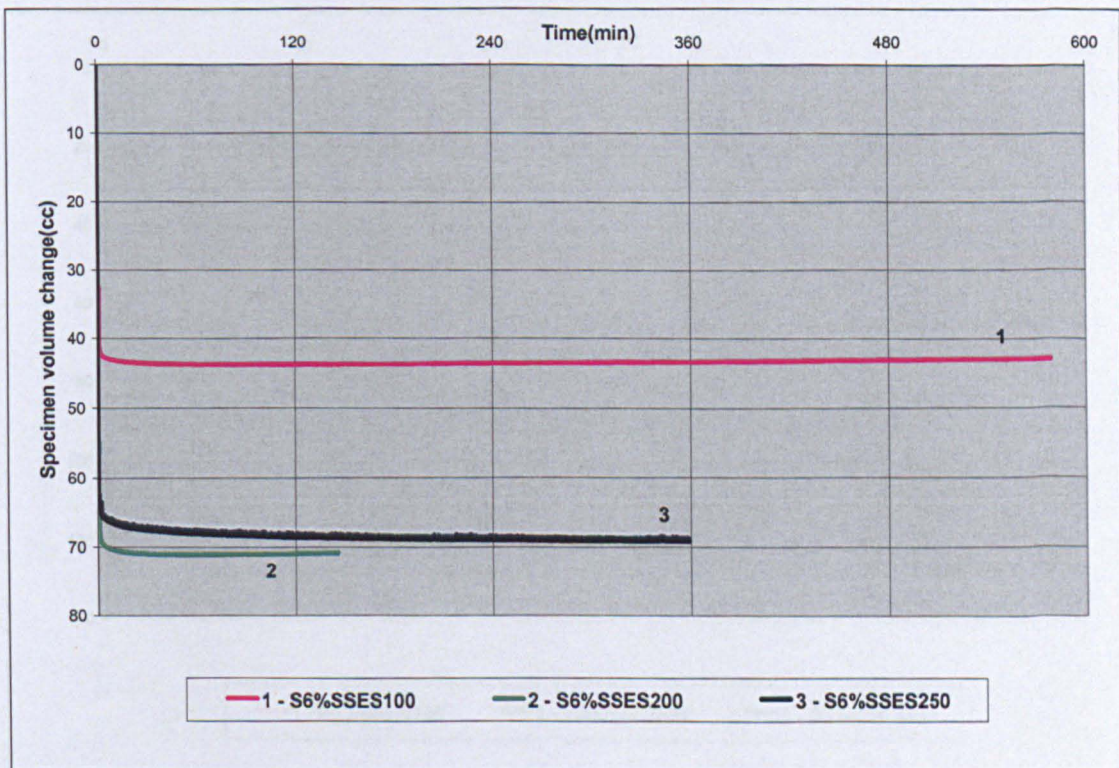


Figure 5.4 Consolidation curves for specimens compacted at 6% moisture content (Test series B).

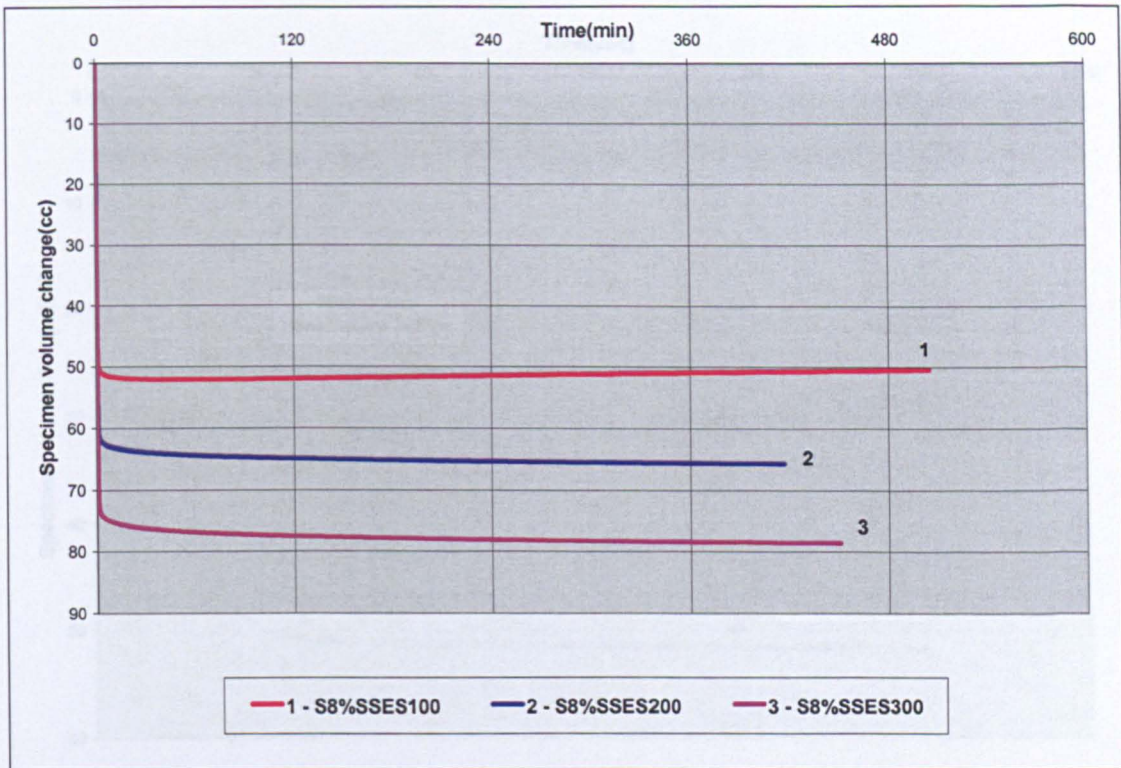


Figure 5.5 Consolidation curves for specimens compacted at 8% moisture content (Test series B).



Figure 5.6 Consolidation curves for specimens prepared with loose poured dry soil (Test series B).

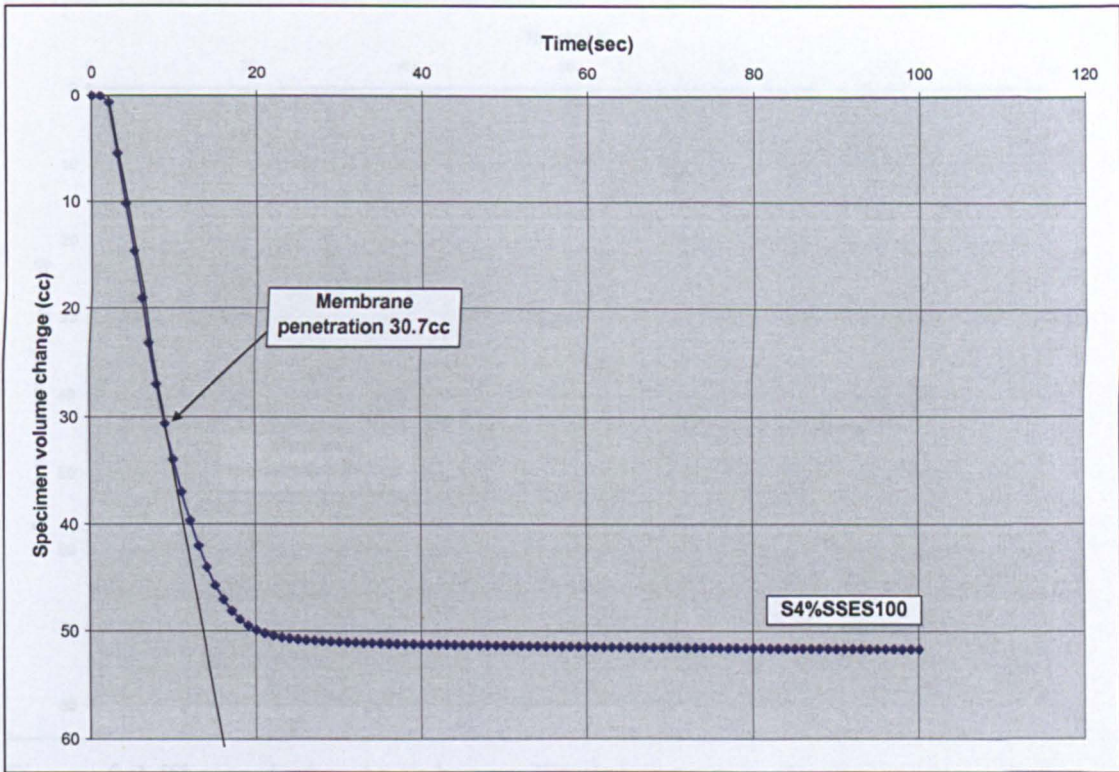


Figure 5.7 The typical enlarged consolidation curve to determine the volume of membrane penetration for effective stress 100kPa (Test no.1 in Test series B).

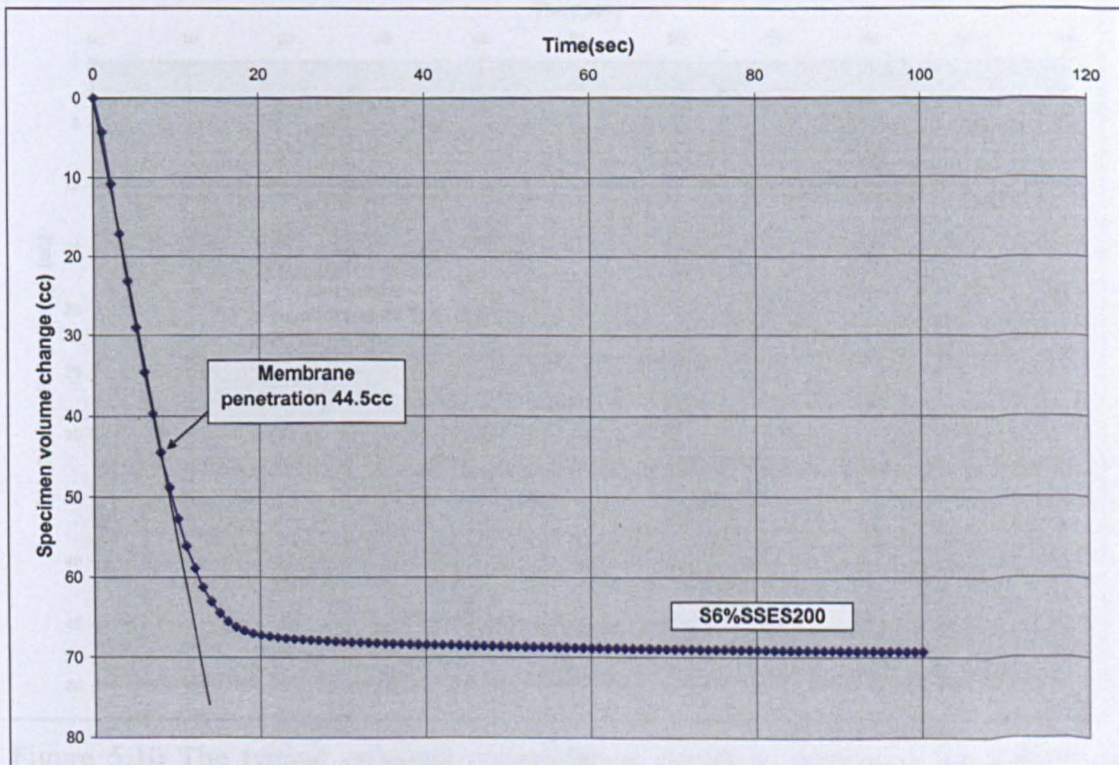


Figure 5.8 The typical enlarged consolidation curve to determine the volume of membrane penetration for effective stress 200kPa (Test no.5 in Test series B).

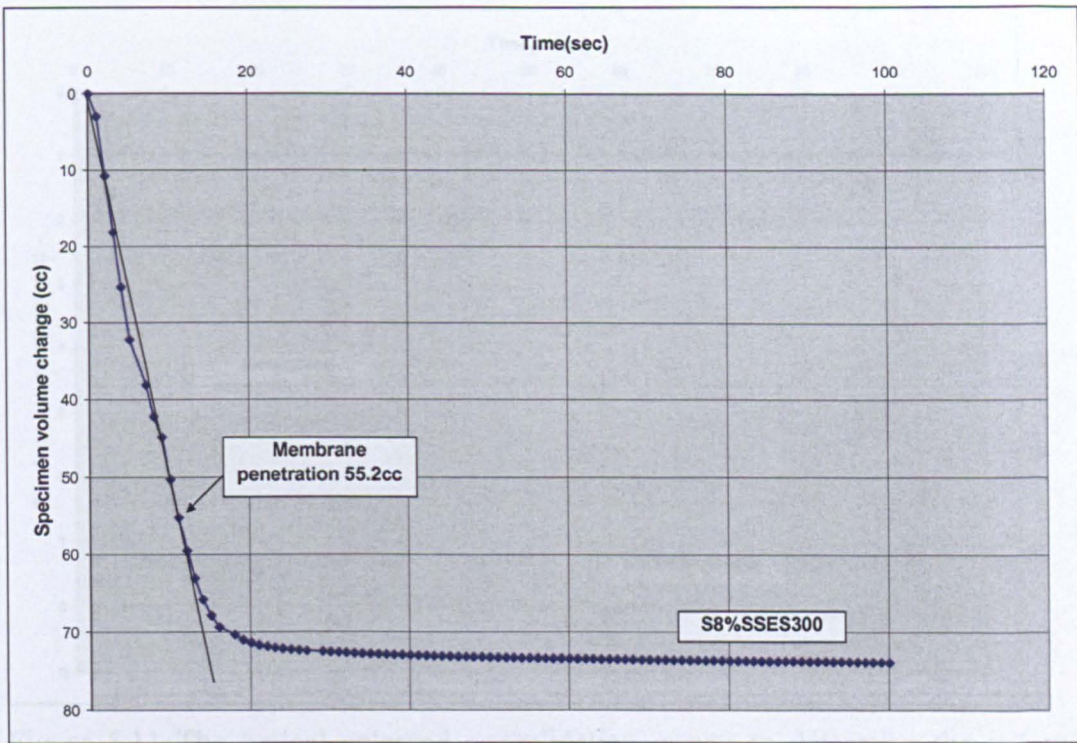


Figure 5.9 The typical enlarged consolidation curve to determine the volume of membrane penetration for effective stress 300kPa (Test no.9 in Test series B).

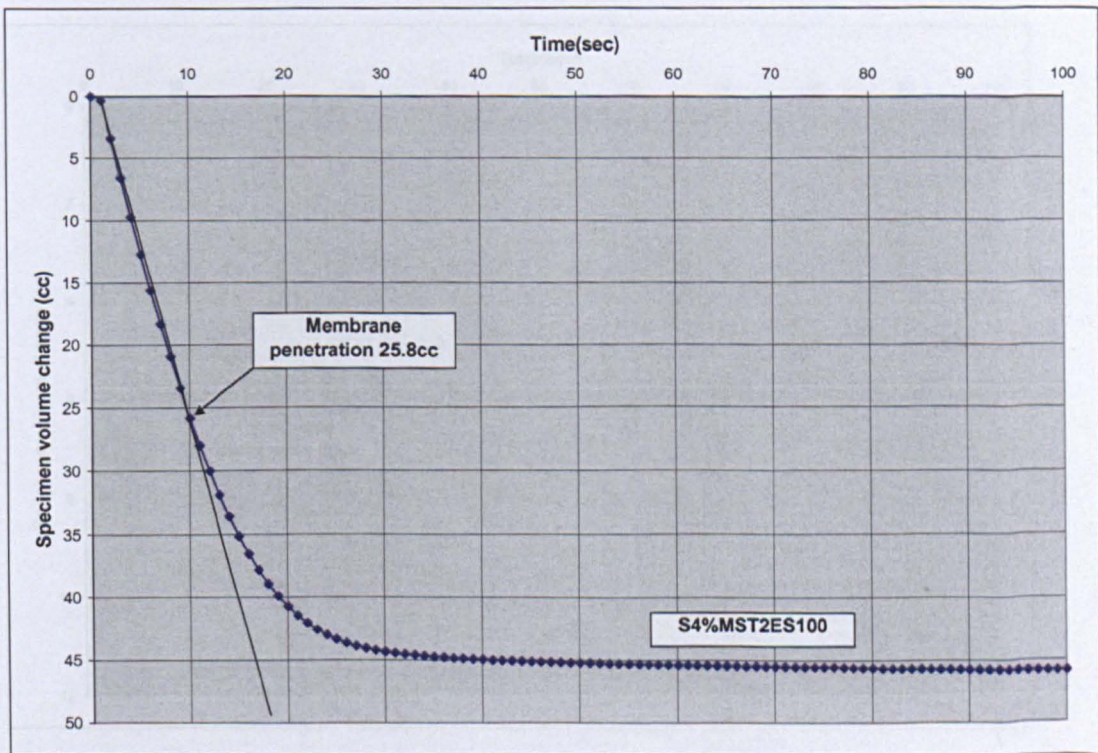


Figure 5.10 The typical enlarged consolidation curves to determine the volume of membrane penetration for multistage triaxial tests at effective stress of 100kPa (Test no.14(a) in test series B).

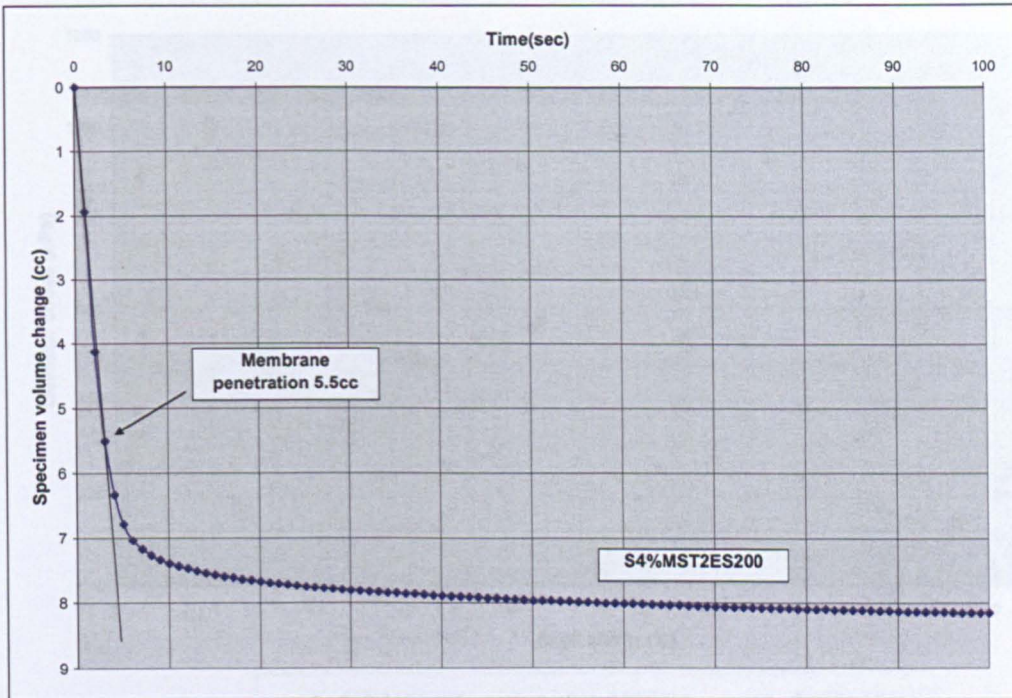


Figure 5.11 The typical enlarged consolidation curves to determine the volume of membrane penetration for multistage triaxial tests at effective stress of 200kPa (Test no.14(b) in test series B).

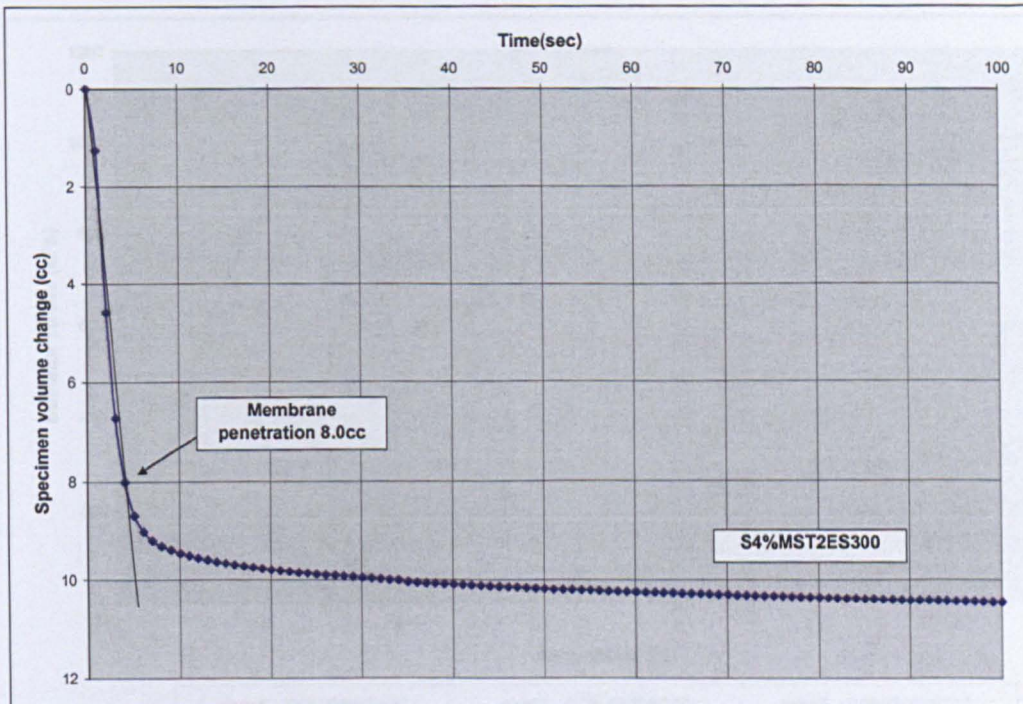


Figure 5.12 The typical enlarged consolidation curves to determine the volume of membrane penetration for multistage triaxial tests at effective stress of 300kPa (Test no.14(c) in test series B).

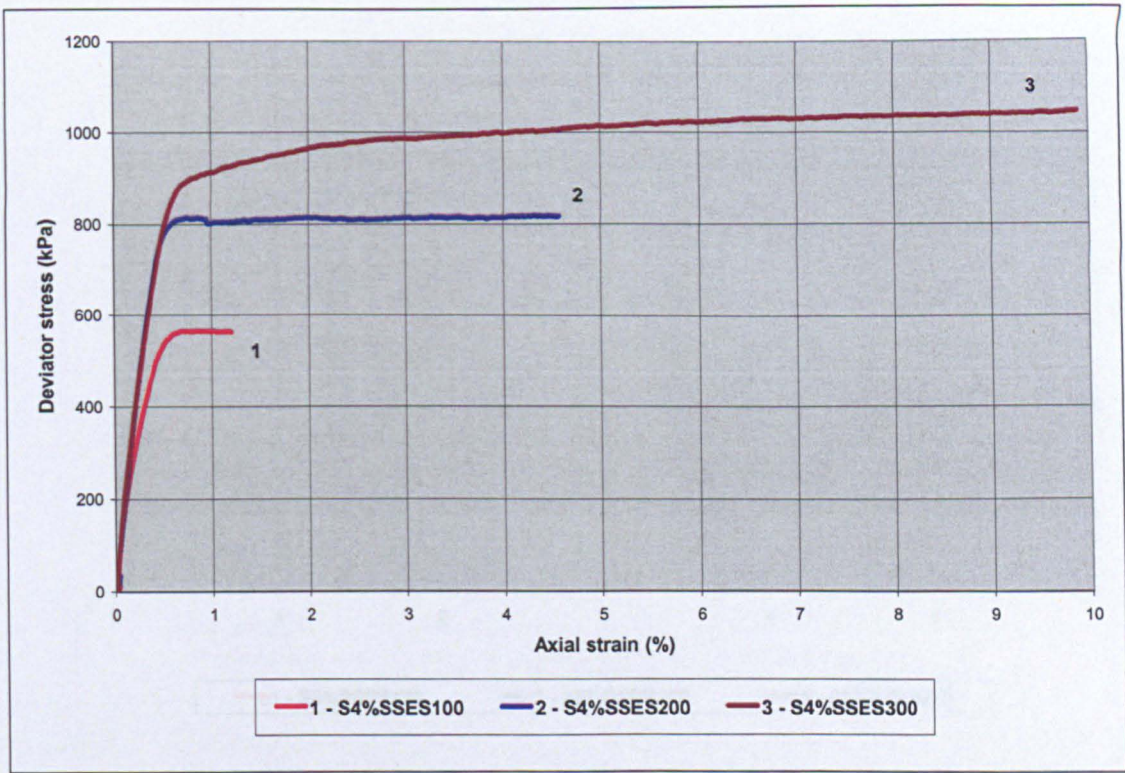


Figure 5.13 Curves of deviator stress versus axial strain for specimens compacted at 4% moisture content (Test series B).

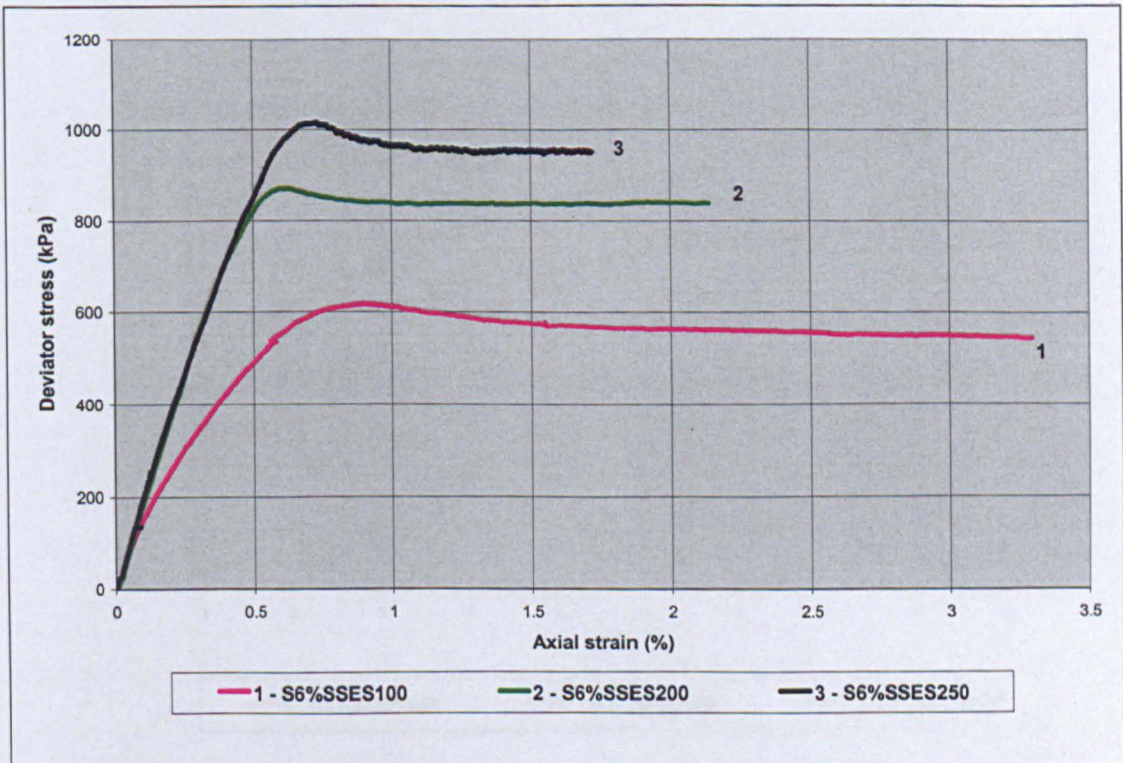


Figure 5.14 Curves of deviator stress versus axial strain for specimens compacted at 6% moisture content (Test series B).

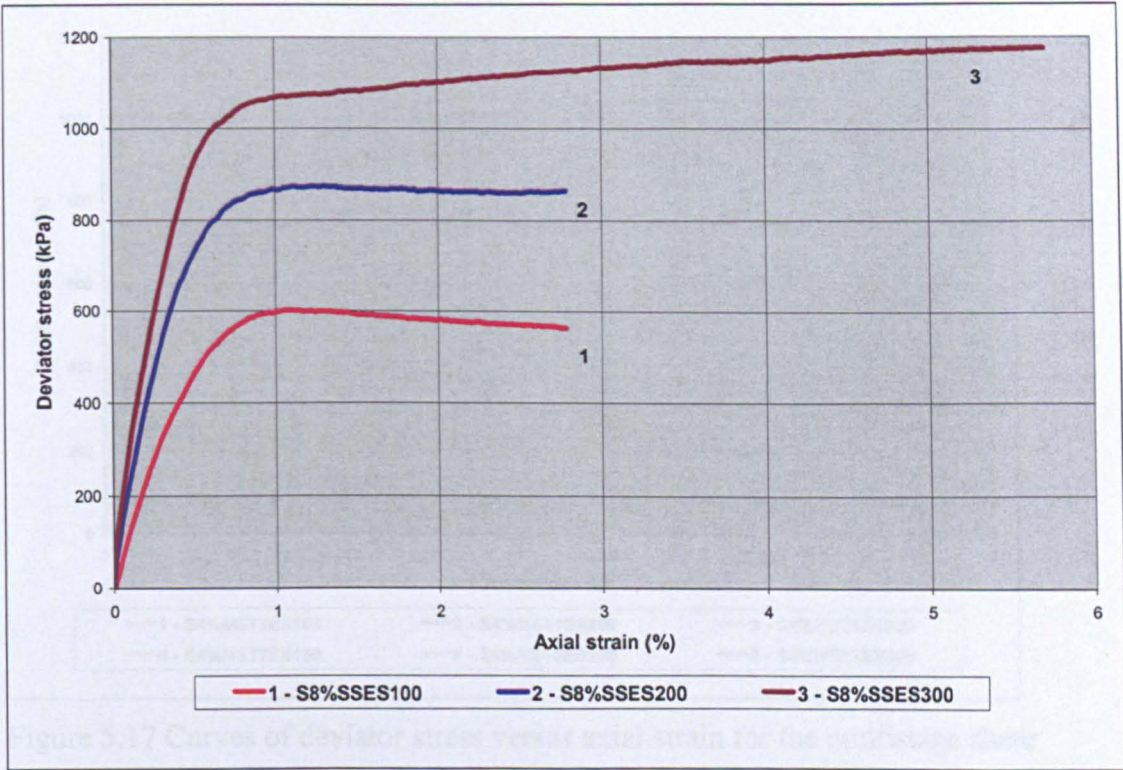


Figure 5.15 Curves of deviator stress versus axial strain for specimens compacted at 8% moisture content (Test series B).

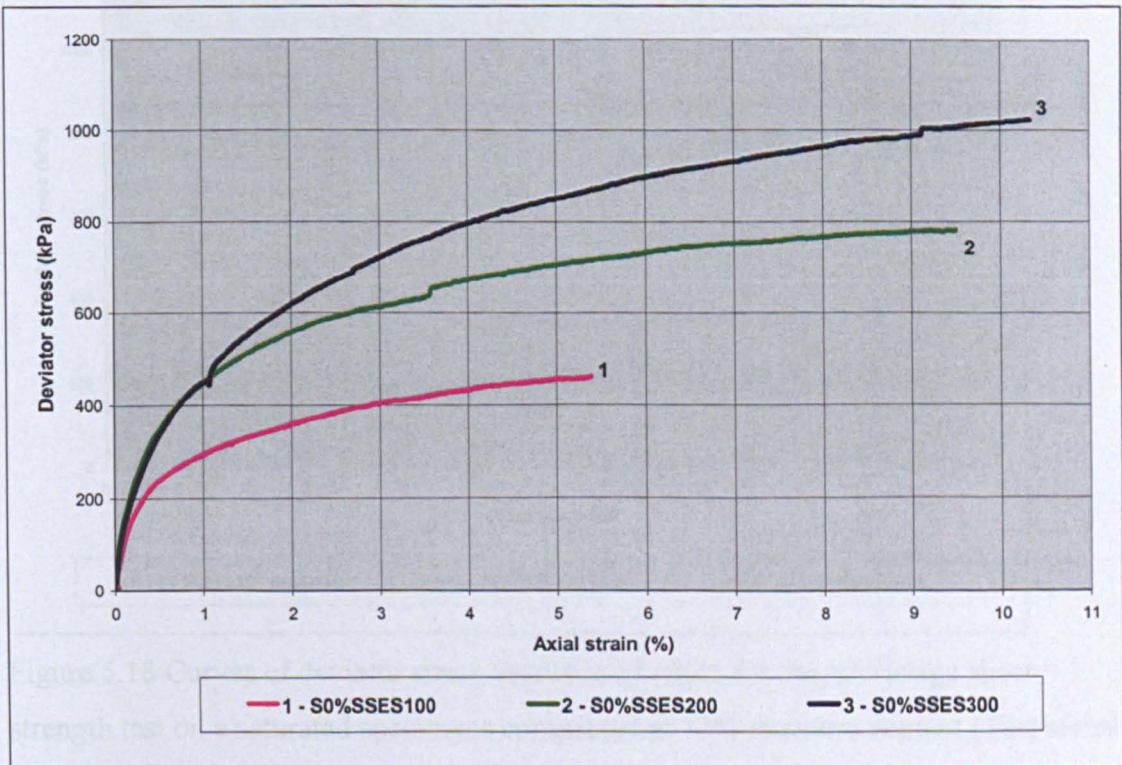


Figure 5.16 Curves of deviator stress versus axial strain for specimens prepared with loose poured dry soil (Test series B).

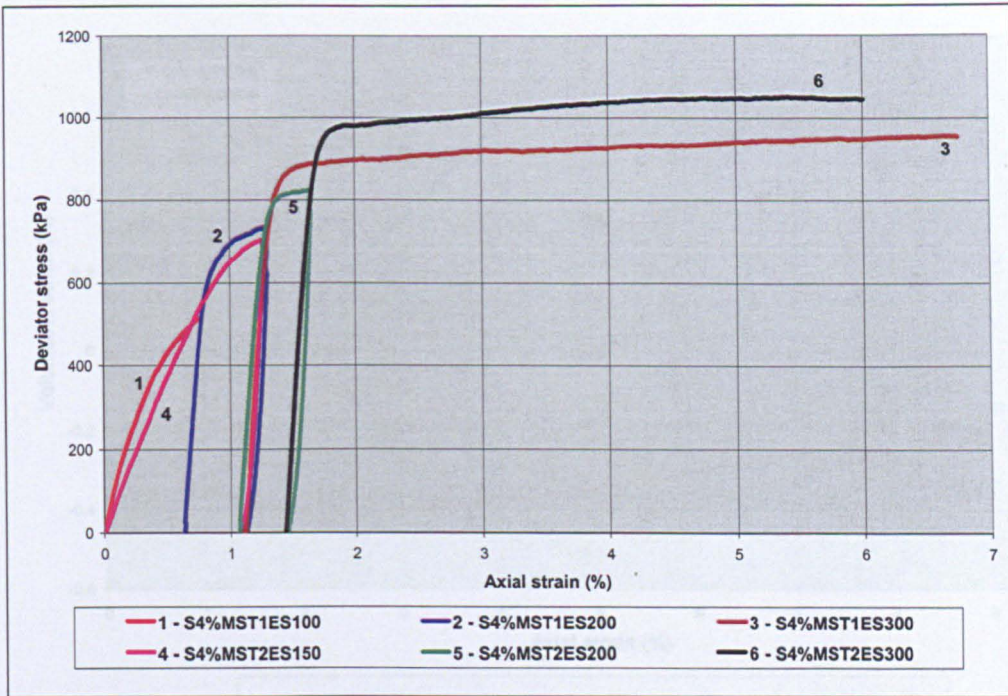


Figure 5.17 Curves of deviator stress versus axial strain for the multistage shear strength test on saturated specimens compacted at 4% moisture content (Test series B).

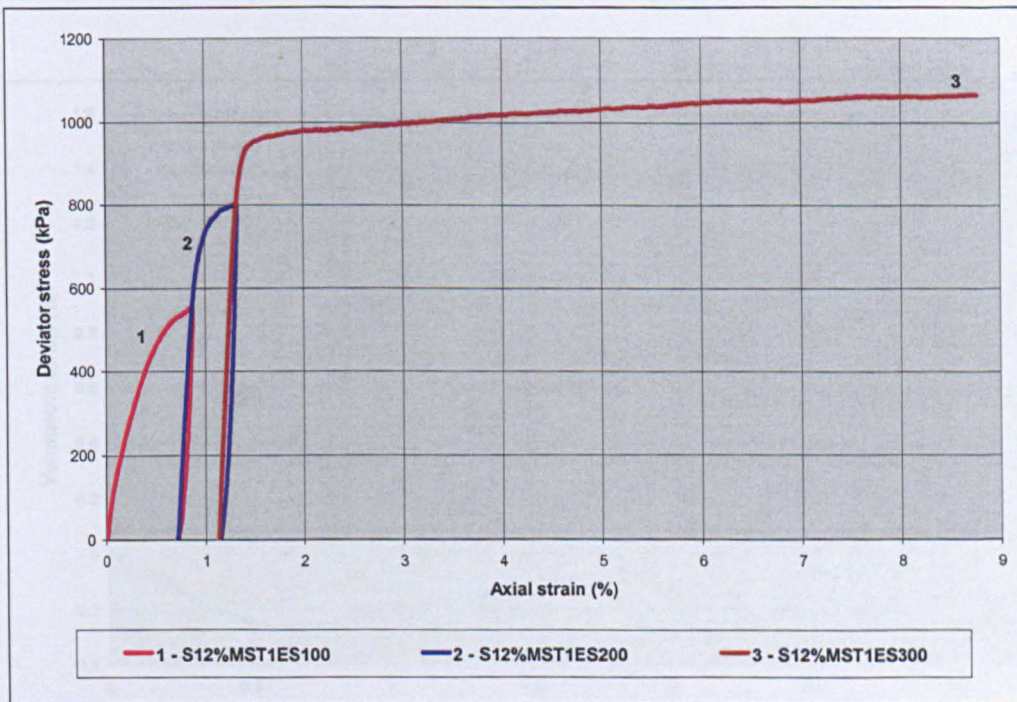


Figure 5.18 Curves of deviator stress versus axial strain for the multistage shear strength test on a saturated specimens compacted at 12% moisture content (Test series B).

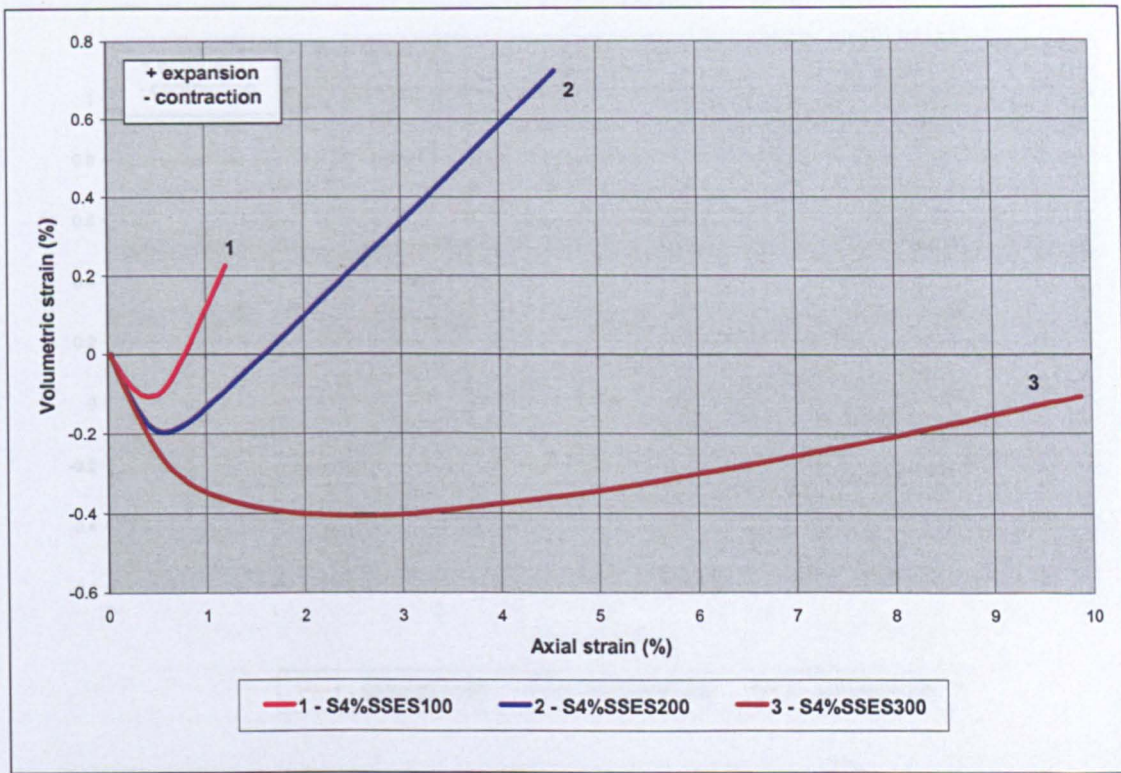


Figure 5.19 Curves of volumetric strain versus axial strain during the shearing stage for specimens compacted at 4% moisture content (Test series B).

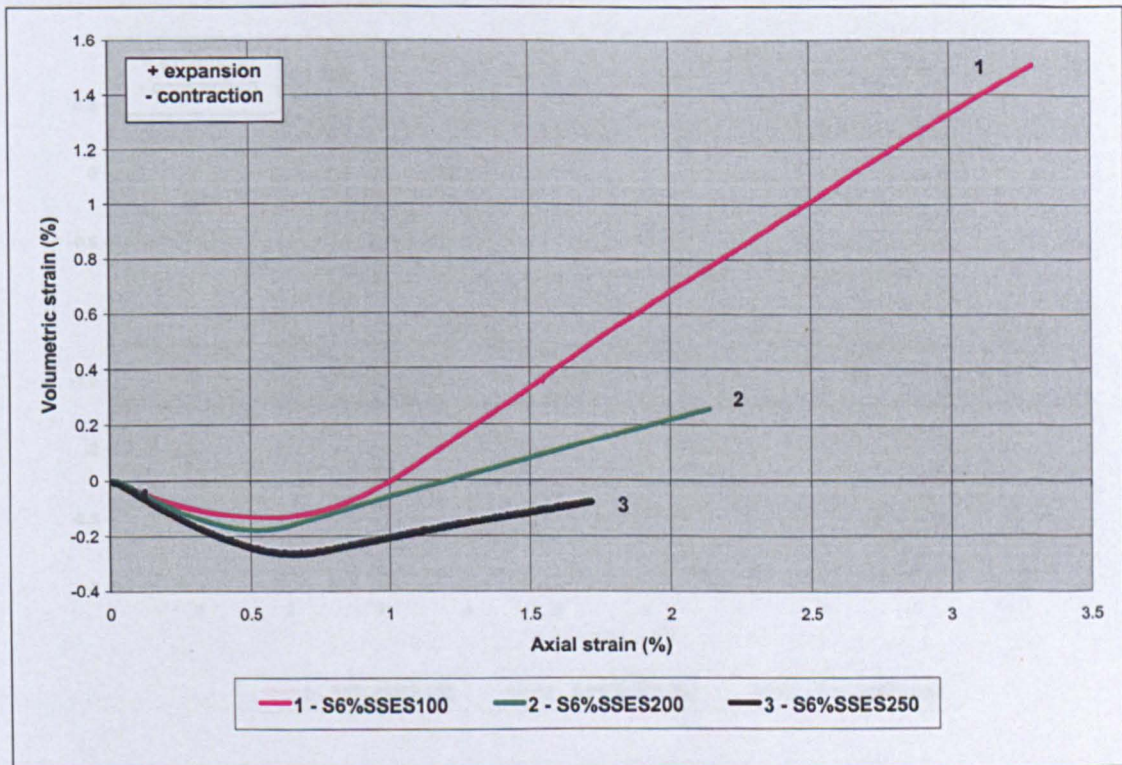


Figure 5.20 Curves of volumetric strain versus axial strain during the shearing stage for specimens compacted at 6% moisture content (Test series B).

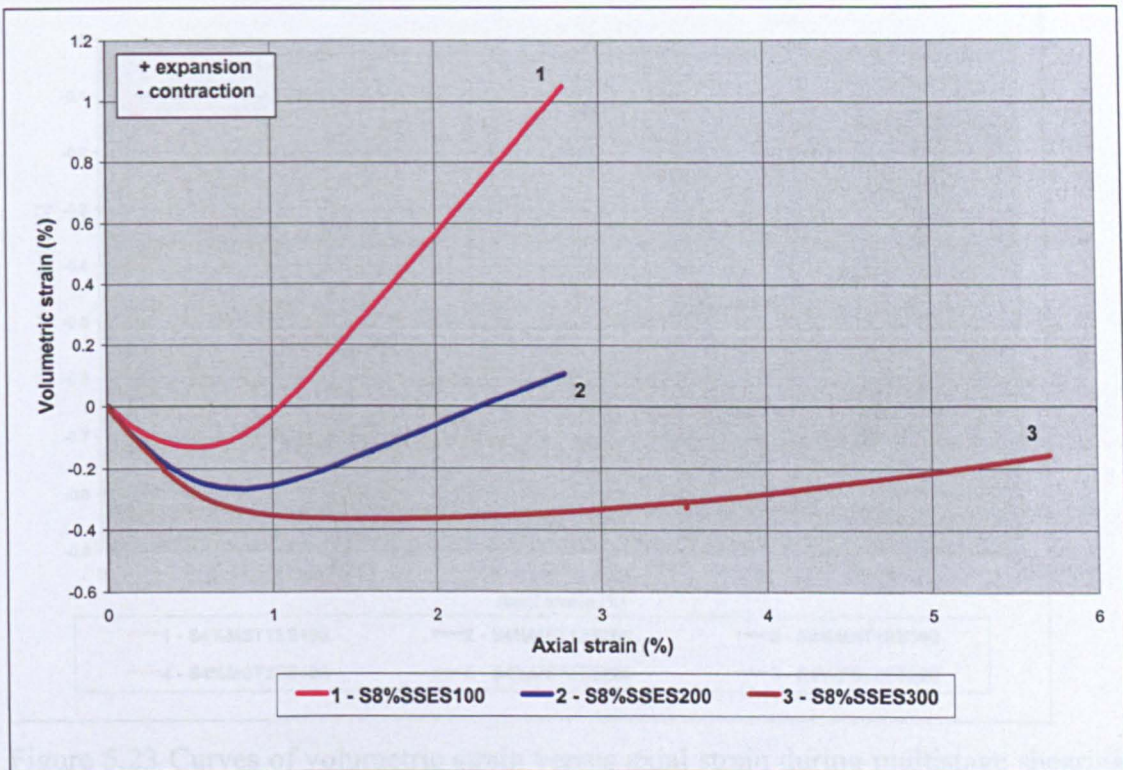


Figure 5.21 Curves of volumetric strain versus axial strain during the shearing stage for specimens compacted at 8% moisture content (Test series B).

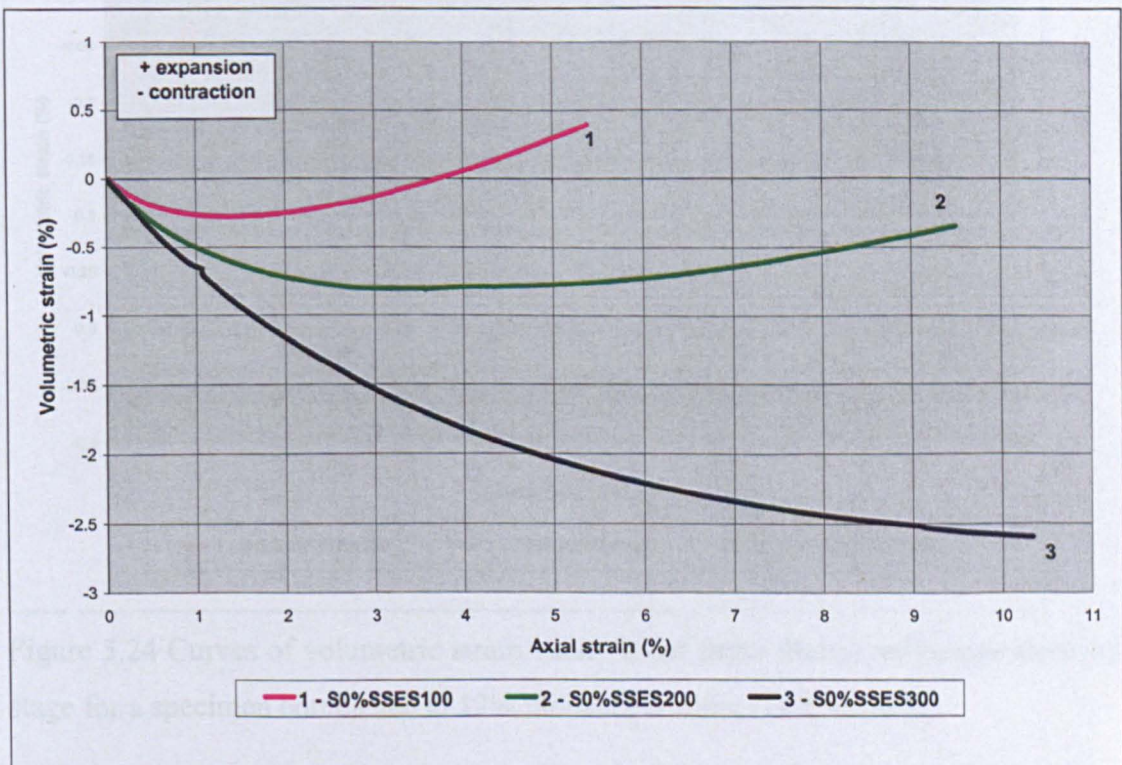


Figure 5.22 Curves of volumetric strain versus axial strain during the shearing stage for specimens prepared by loose poured dry soil (Test series B).

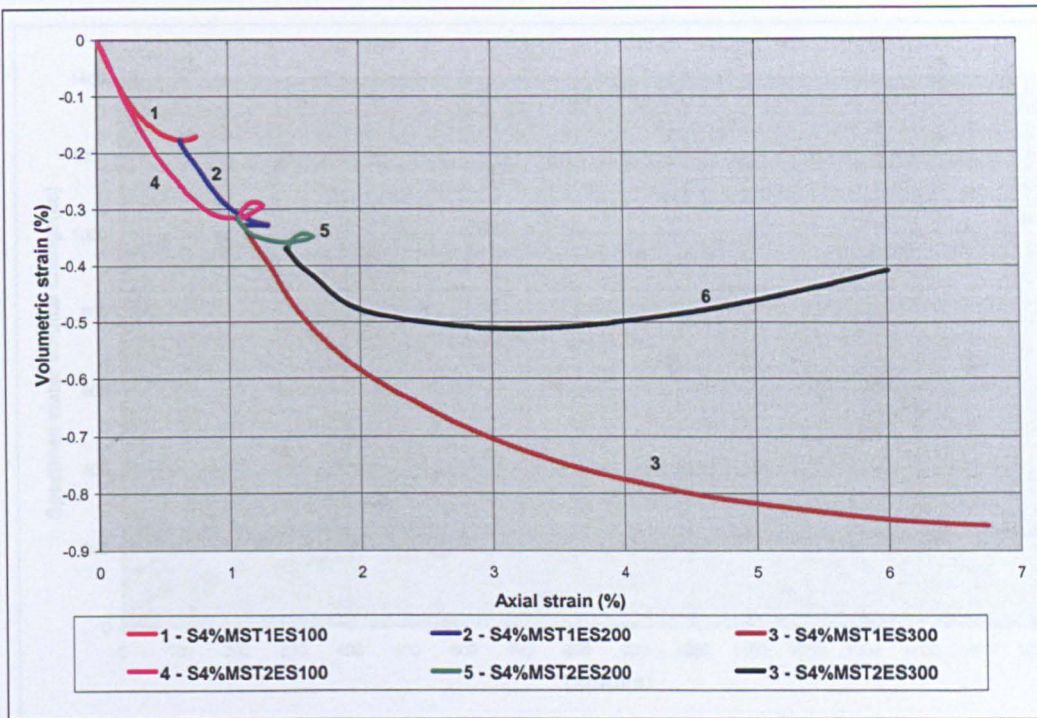


Figure 5.23 Curves of volumetric strain versus axial strain during multistage shearing stage for specimens compacted at 4% moisture content (Test series B).

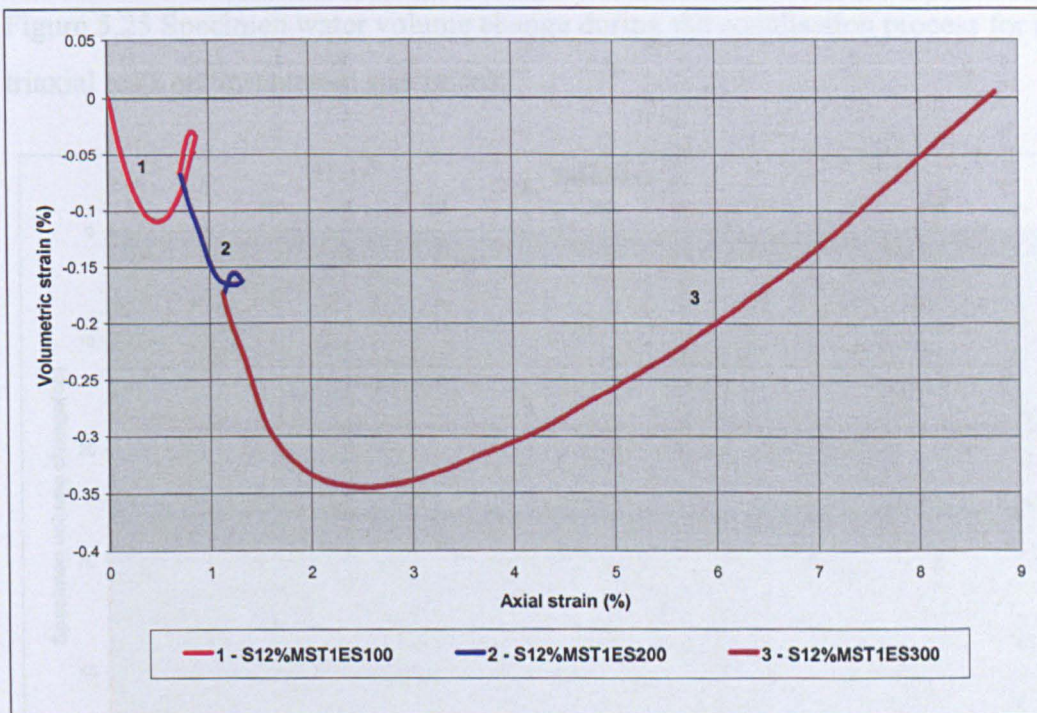


Figure 5.24 Curves of volumetric strain versus axial strain during multistage shearing stage for a specimen compacted at 12% moisture content (Test series B).

Figure 5.26 Consolidation curves for soil specimens of 25, 50 and 75 kPa at suction of 25 kPa (Test series C).

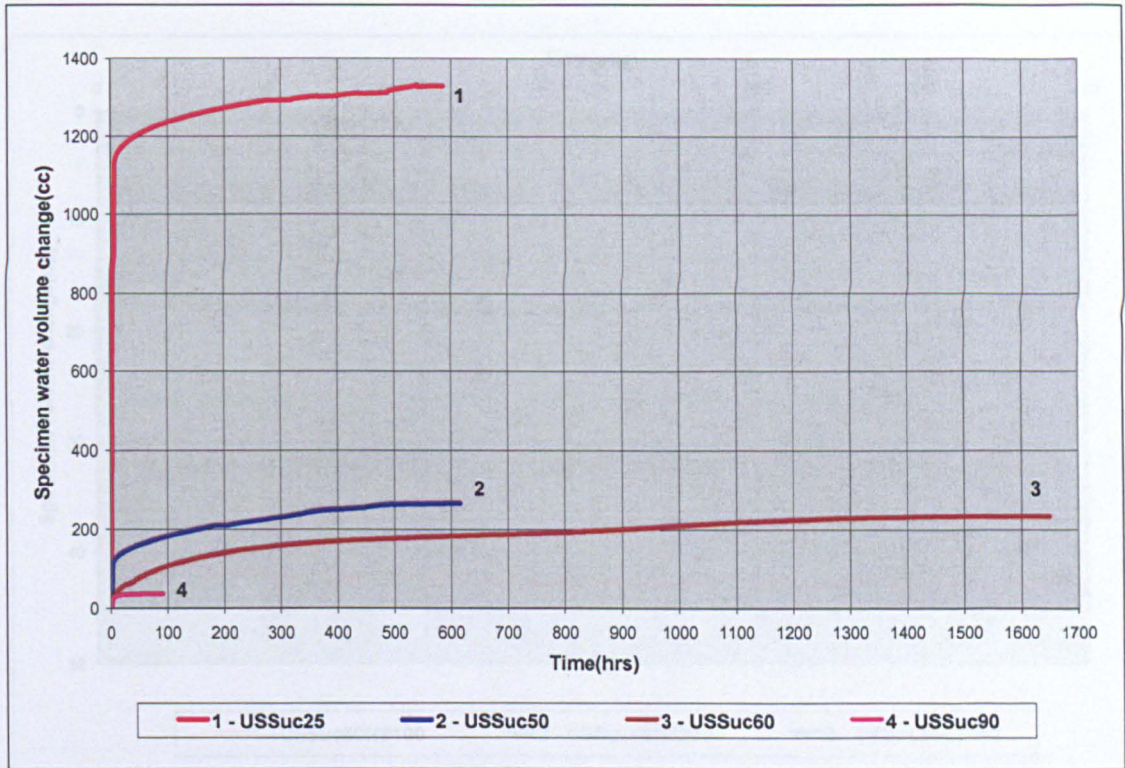


Figure 5.25 Specimen water volume change during the equalisation process for the triaxial tests on unsaturated specimens.

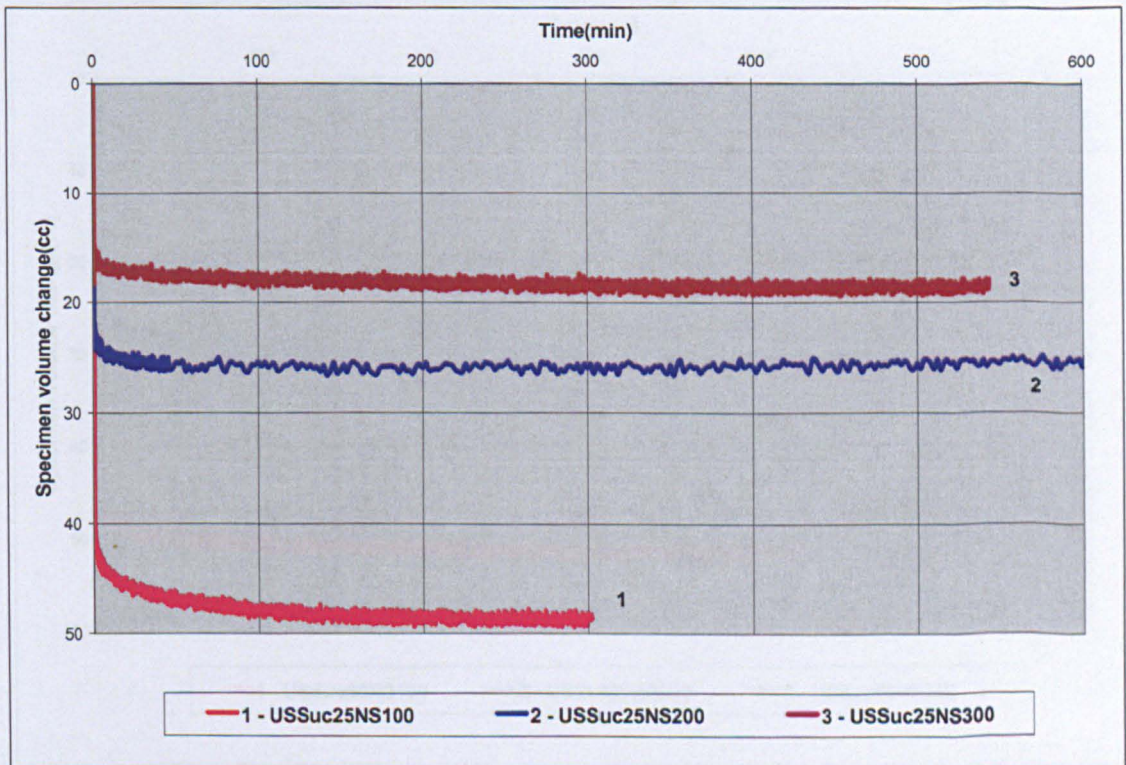


Figure 5.26 Consolidation curves for net stresses of 100, 200 and 300kPa at suction of 25 kPa (Test series C).

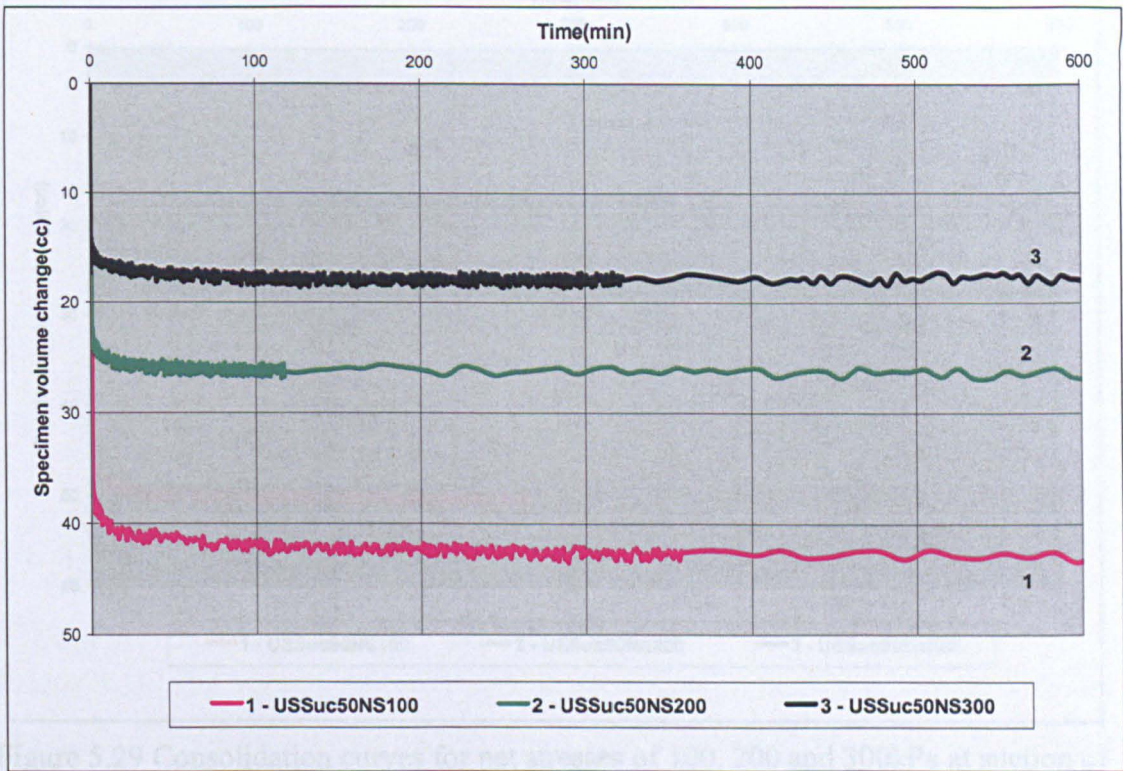


Figure 5.27 Consolidation curves for net stresses of 100, 200 and 300kPa at suction of 50 kPa (Test series C).

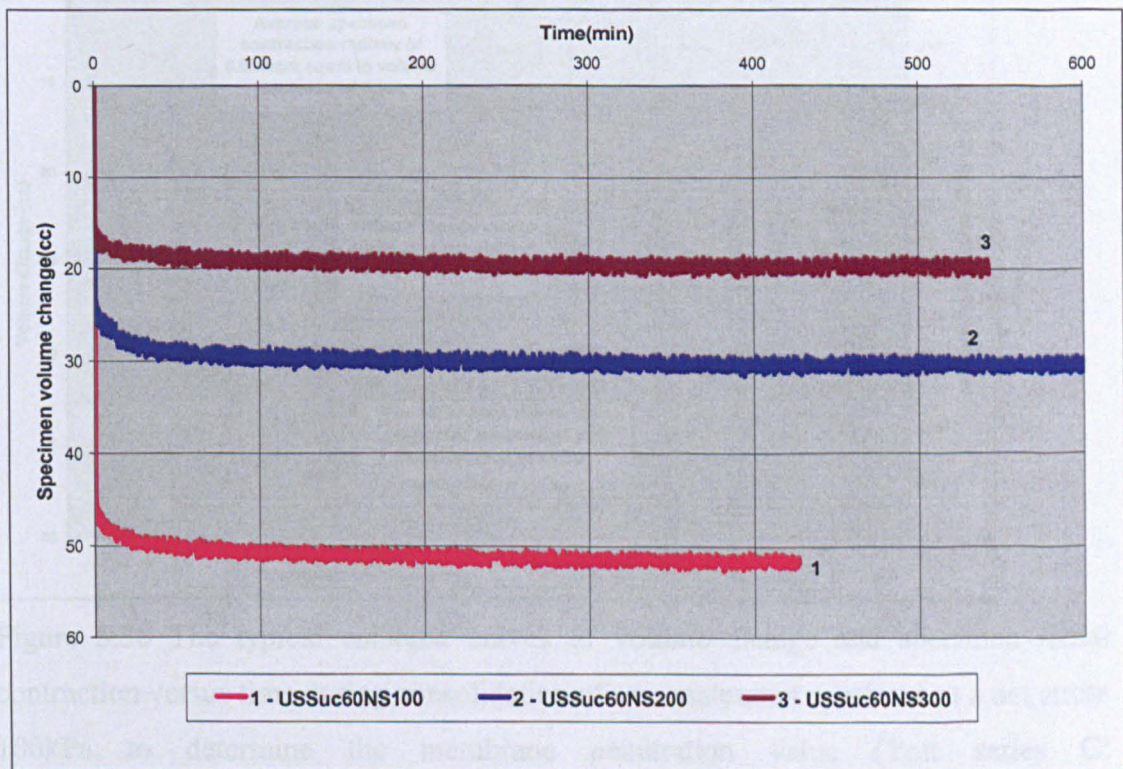


Figure 5.28 Consolidation curves for net stresses of 100, 200 and 300kPa at suction of 60 kPa (Test series C).

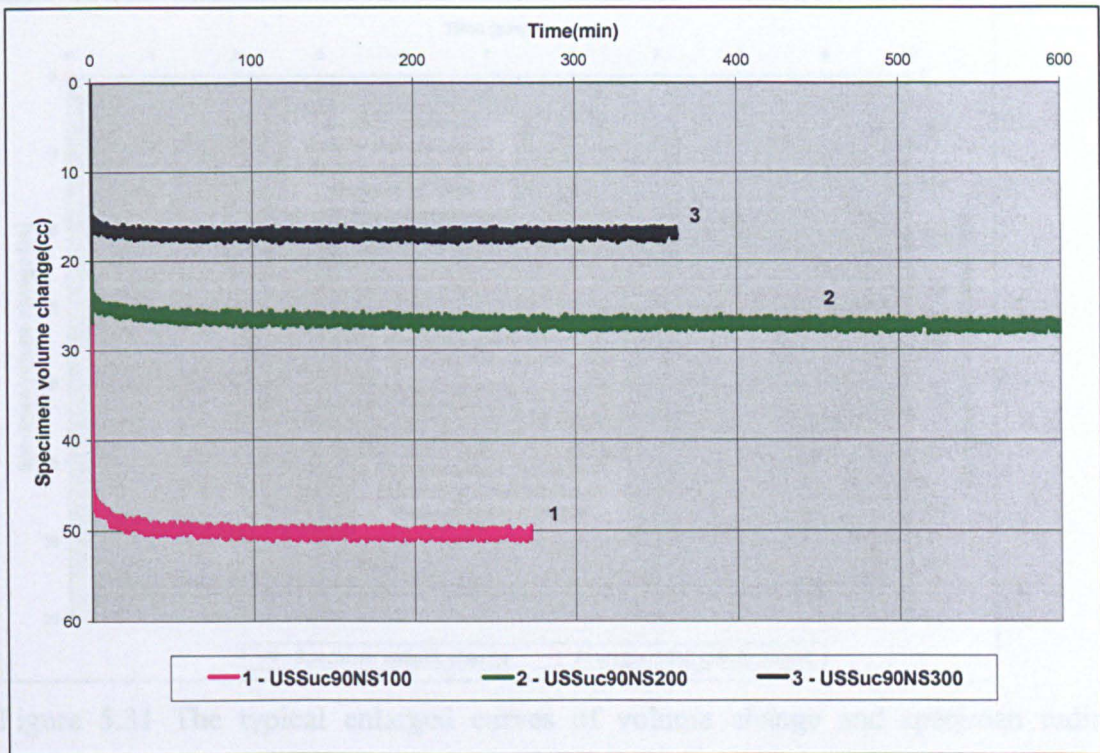


Figure 5.29 Consolidation curves for net stresses of 100, 200 and 300kPa at suction of 90 kPa (Test series C).

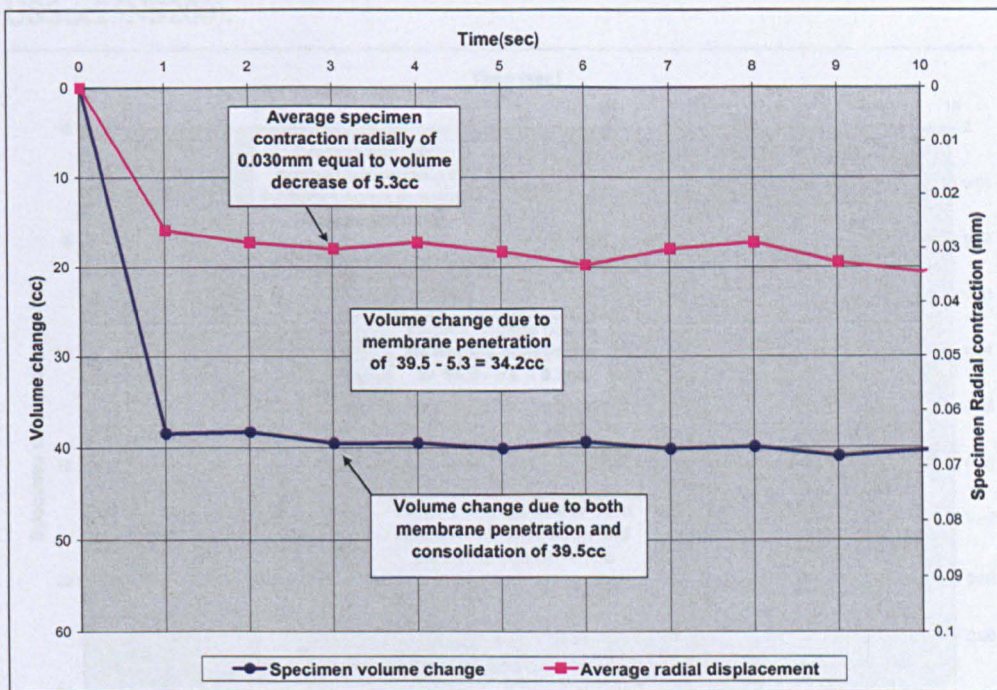


Figure 5.30 The typical enlarged curves of volume change and specimen radial contraction versus time during consolidation of an unsaturated specimen at a net stress 100kPa to determine the membrane penetration value (Test series C: USSuc25NS100).

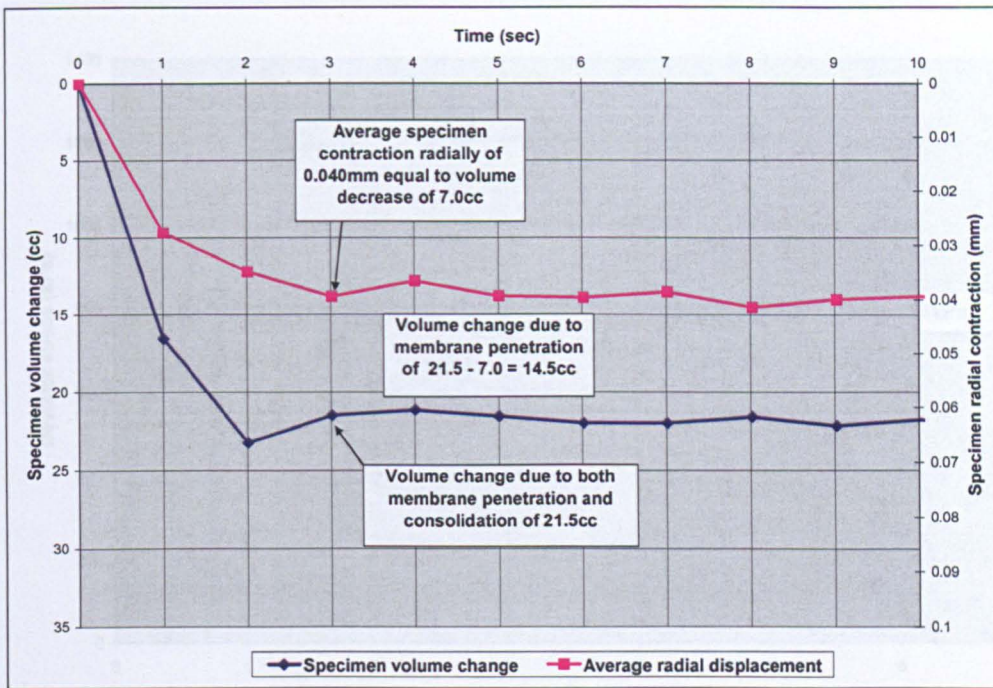


Figure 5.31 The typical enlarged curves of volume change and specimen radial contraction versus time during consolidation of an unsaturated specimen at a net stress 200kPa to determine the membrane penetration value (Test series C: USSuc25NS200).

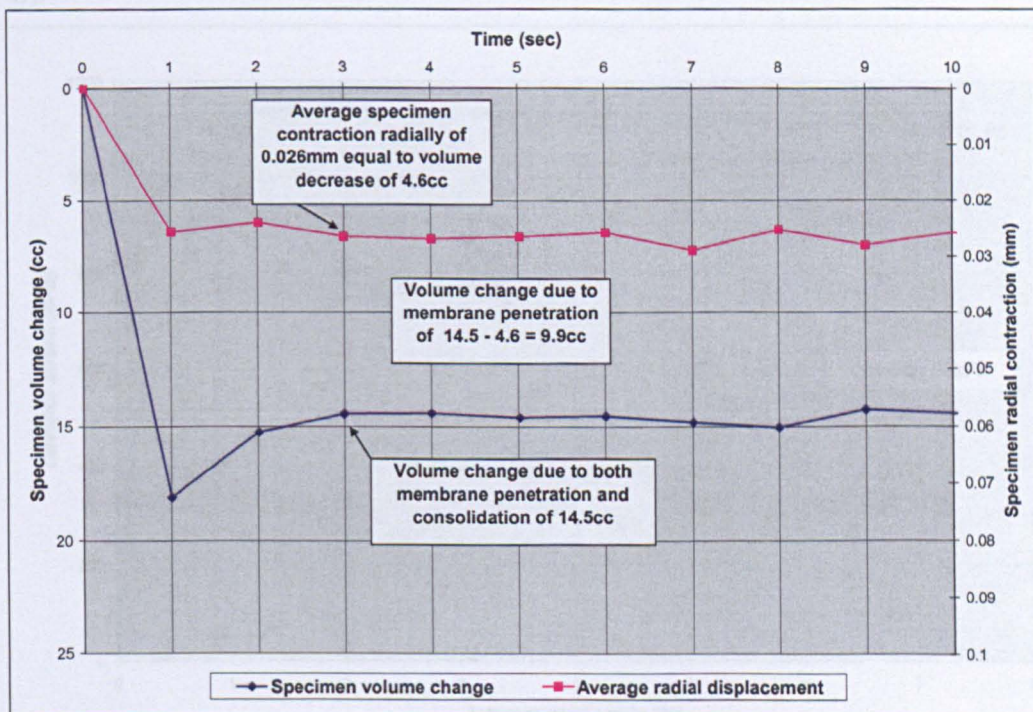


Figure 5.32 The typical enlarged curves of volume change and specimen radial contraction versus time during consolidation of an unsaturated specimen at a net stress 300kPa to determine the membrane penetration value (Test series C: USSuc25NS300).

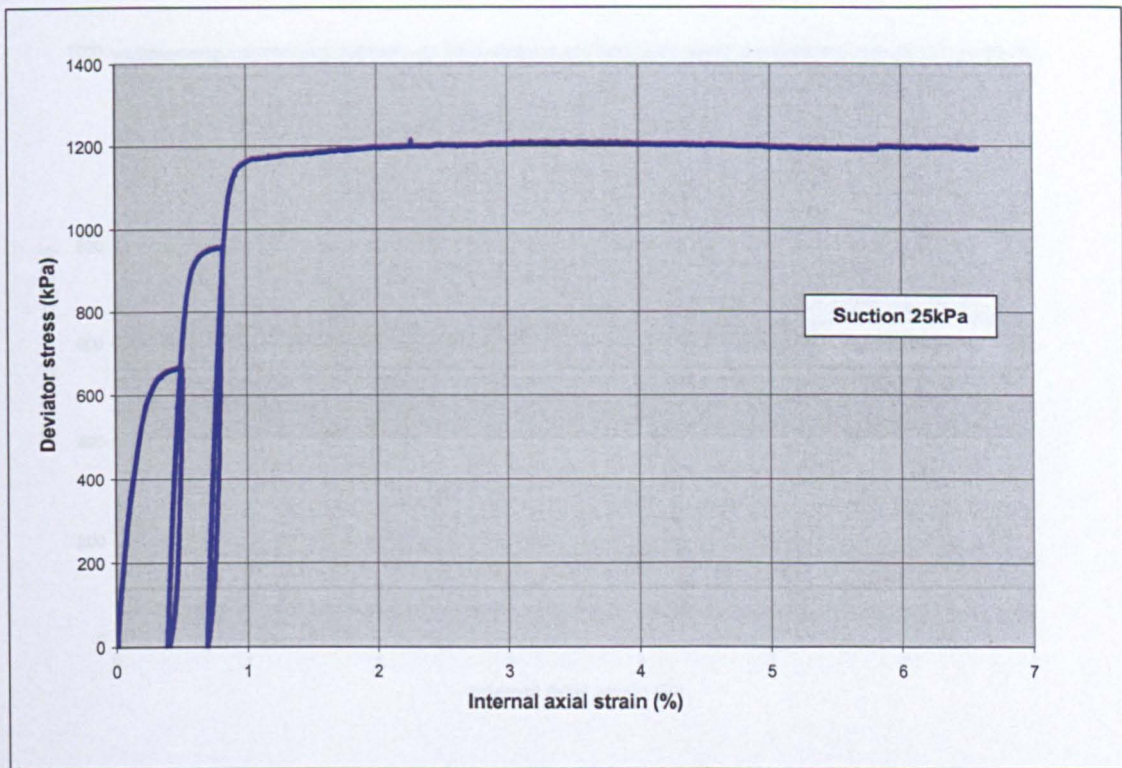


Figure 5.33 Graph of deviator stress versus internal axial strain during shearing for the multistage triaxial test on an unsaturated specimen at a suction of 25kPa (Test series C).

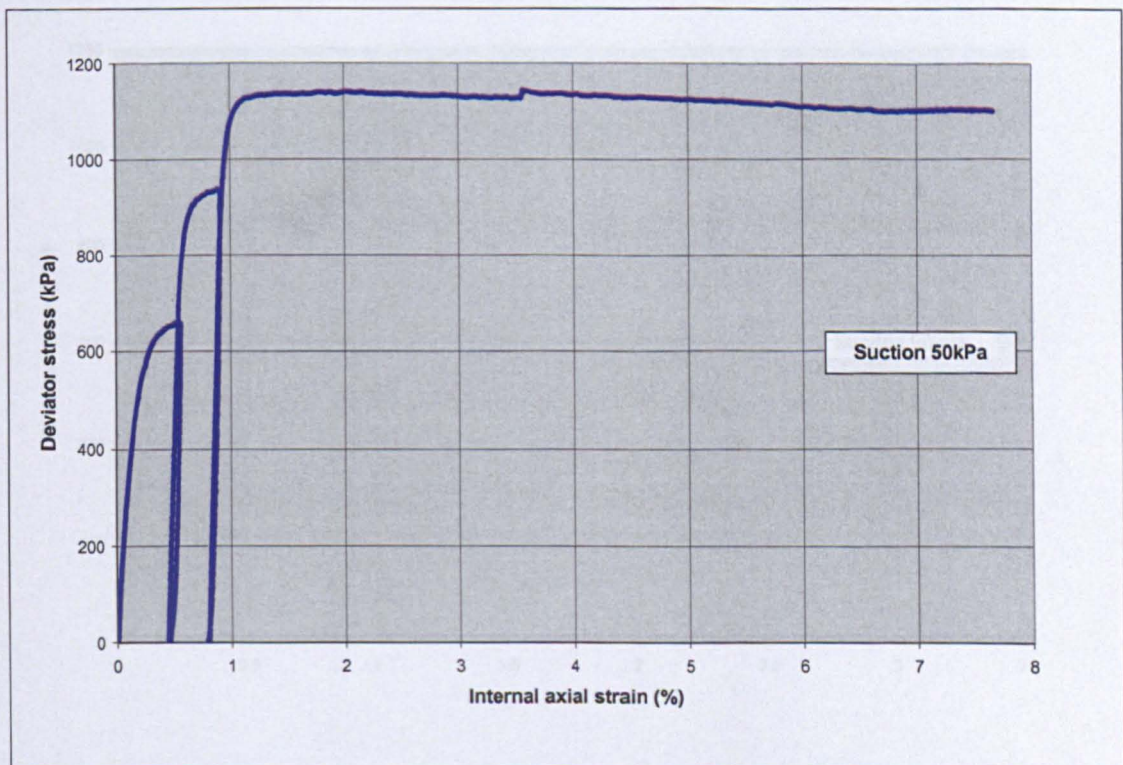


Figure 5.34 Graph of deviator stress versus internal axial strain during shearing for the multistage triaxial test on an unsaturated specimen at a suction of 50kPa (Test series C).

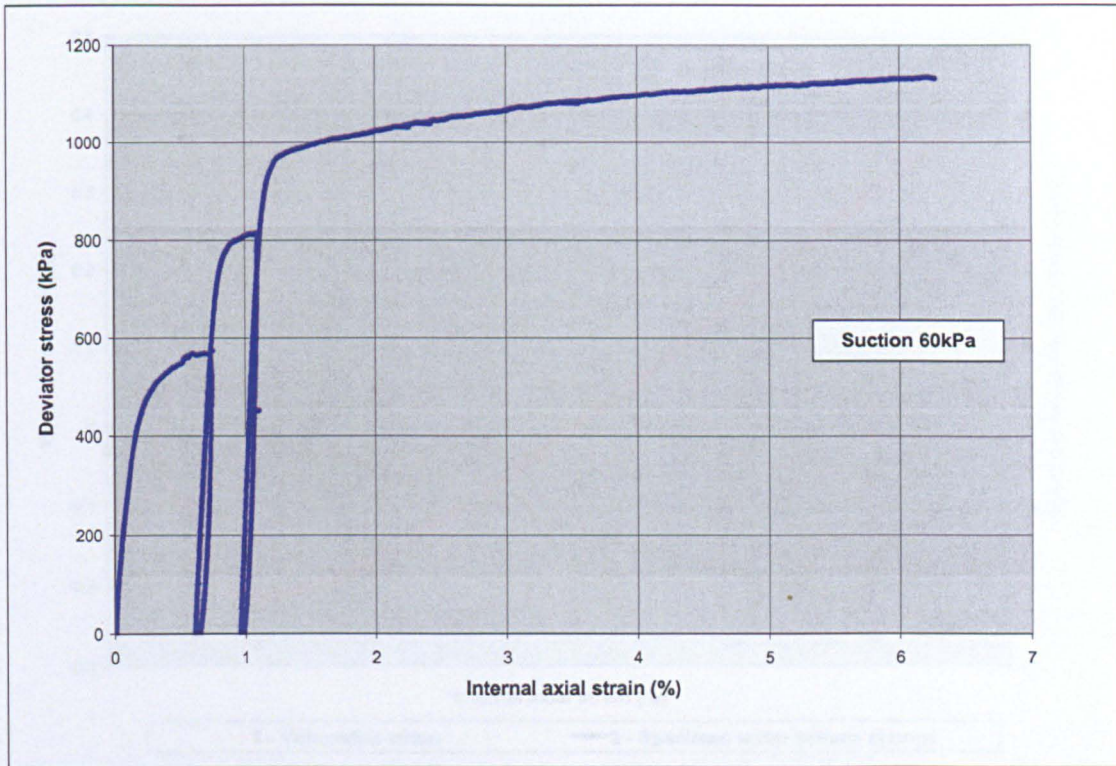


Figure 5.35 Graph of deviator stress versus internal axial strain during shearing for the multistage triaxial test on an unsaturated specimen at a suction of 60kPa (Test series C).

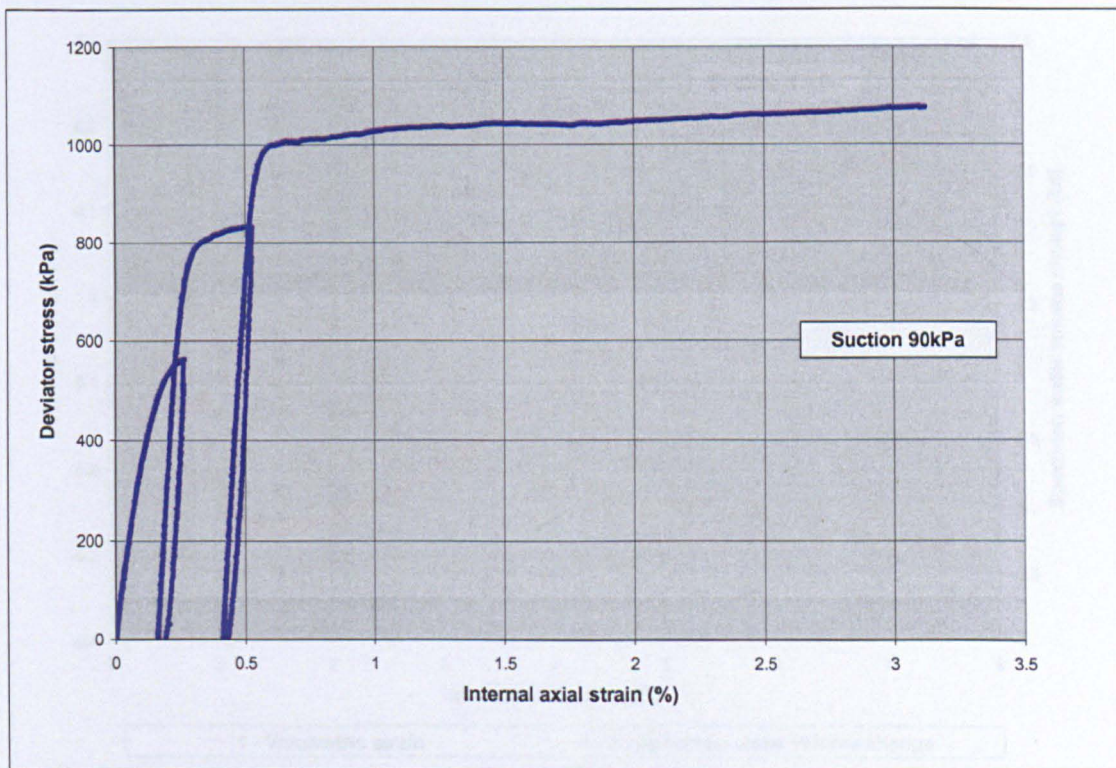


Figure 5.36 Graph of deviator stress versus internal axial strain during shearing for the multistage triaxial test on an unsaturated specimen at a suction of 90kPa (Test series C).

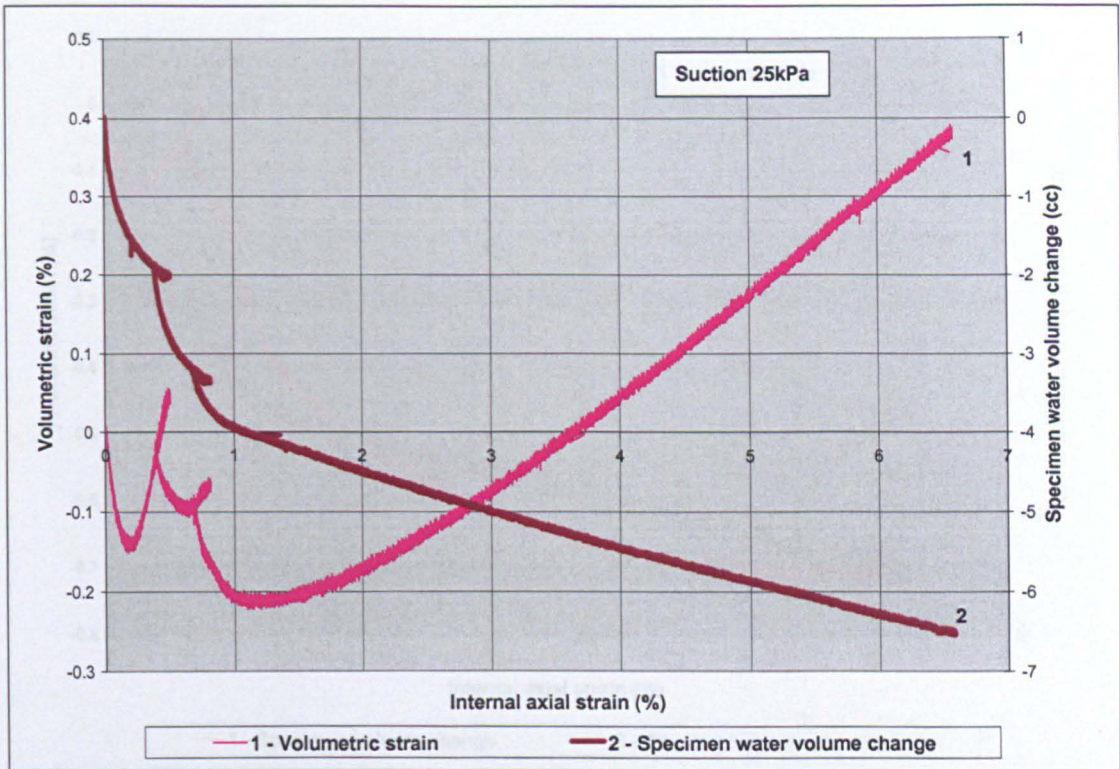


Figure 5.37 Graphs of volumetric strain and specimen water volume change versus internal axial strain during shearing for the multistage triaxial test on an unsaturated specimen at suction of 25kPa (Test series C).

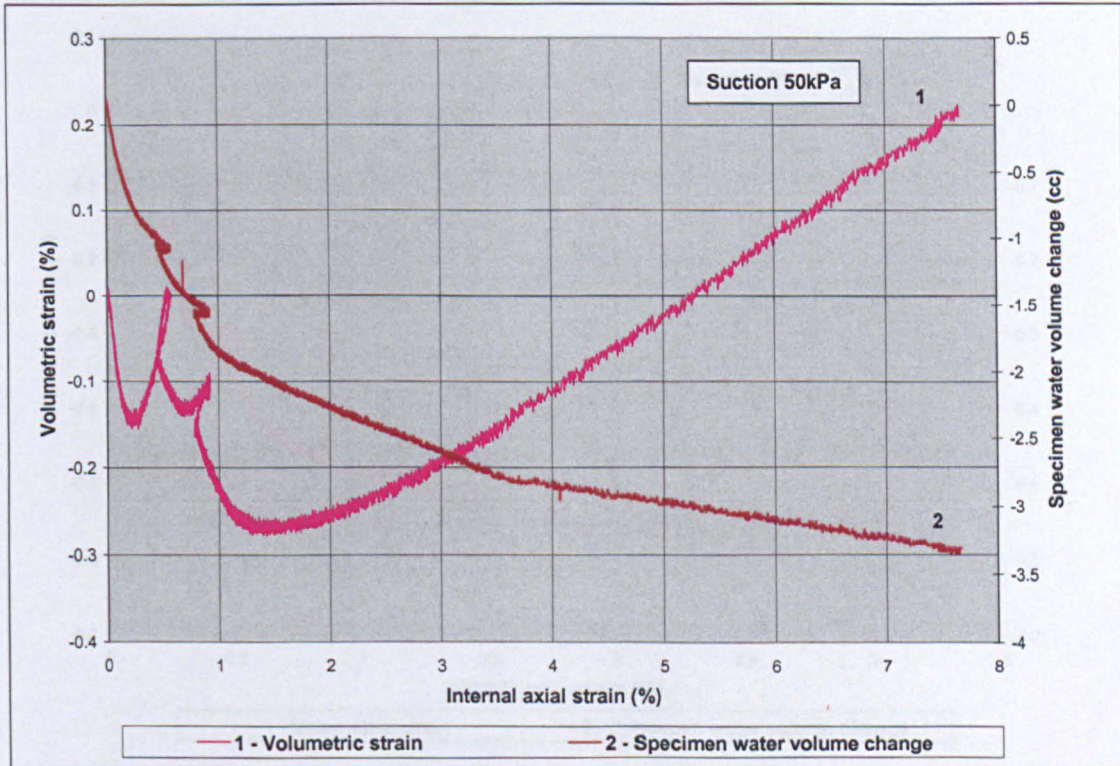


Figure 5.38 Graphs of volumetric strain and specimen water volume change versus internal axial strain during shearing for the multistage triaxial test on an unsaturated specimen at suction of 50kPa (Test series C).

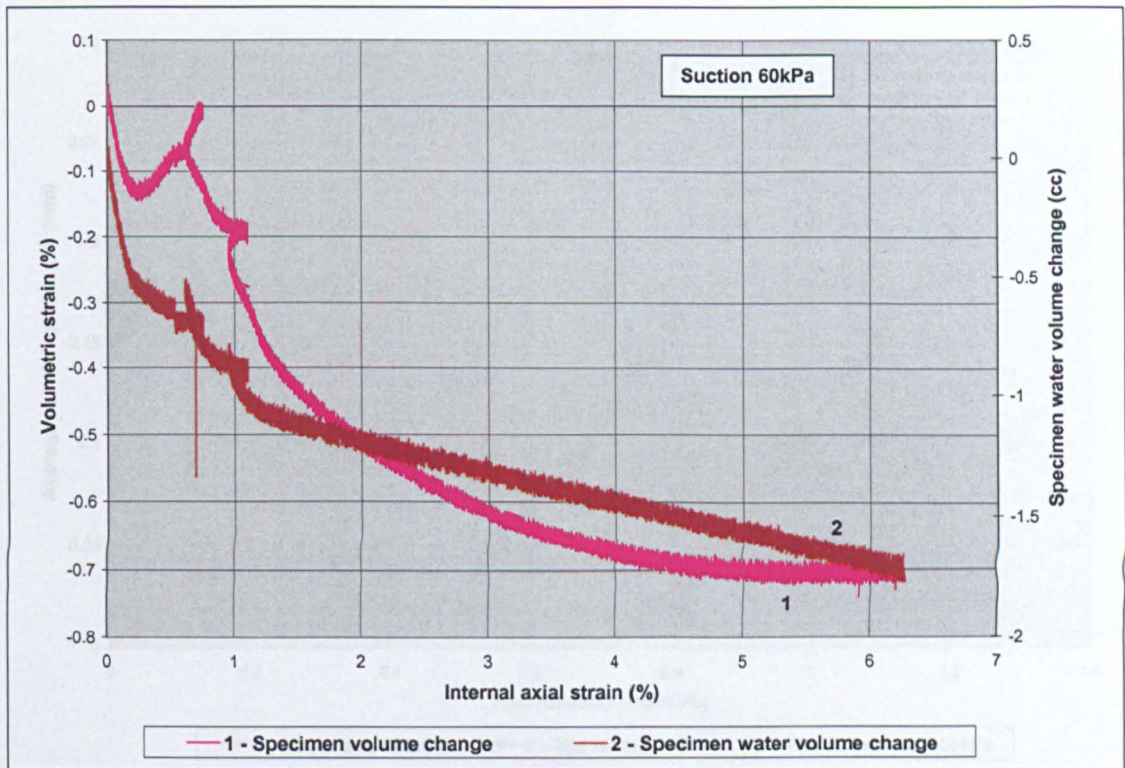


Figure 5.39 Graphs of volumetric strain and specimen water volume change versus internal axial strain during shearing for the multistage triaxial test on an unsaturated specimen at suction of 60kPa (Test series C).

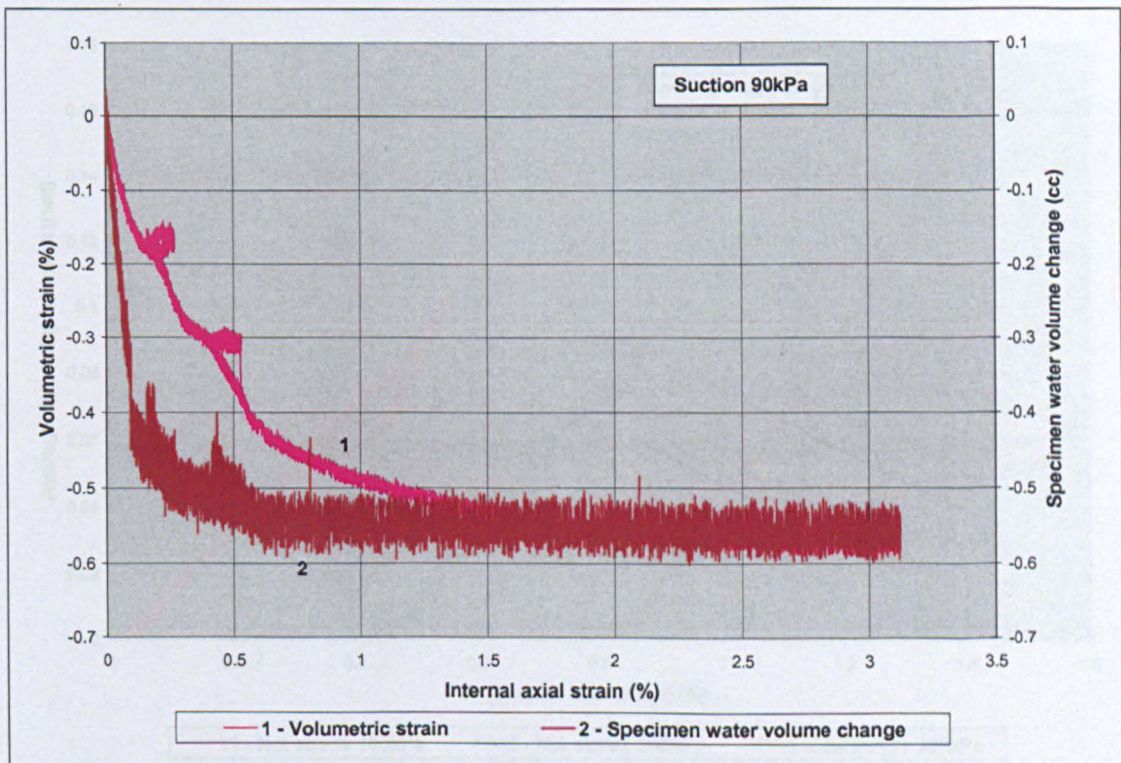


Figure 5.40 Graphs of volumetric strain and specimen water volume change versus internal axial strain during shearing for the multistage triaxial test on an unsaturated specimen at suction of 90kPa (Test series C).

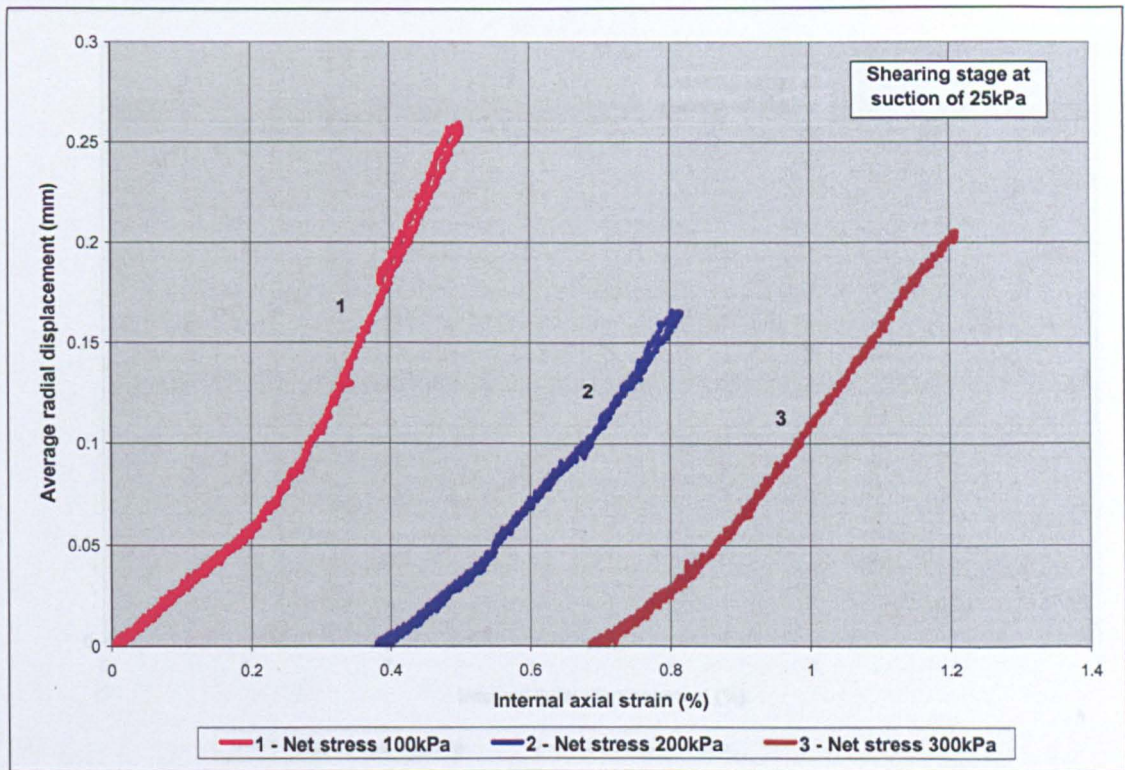


Figure 5.41 Graph of average radial contraction versus internal axial strain during shearing for the multistage triaxial test on an unsaturated specimen at suction of 25kPa (Test series C).

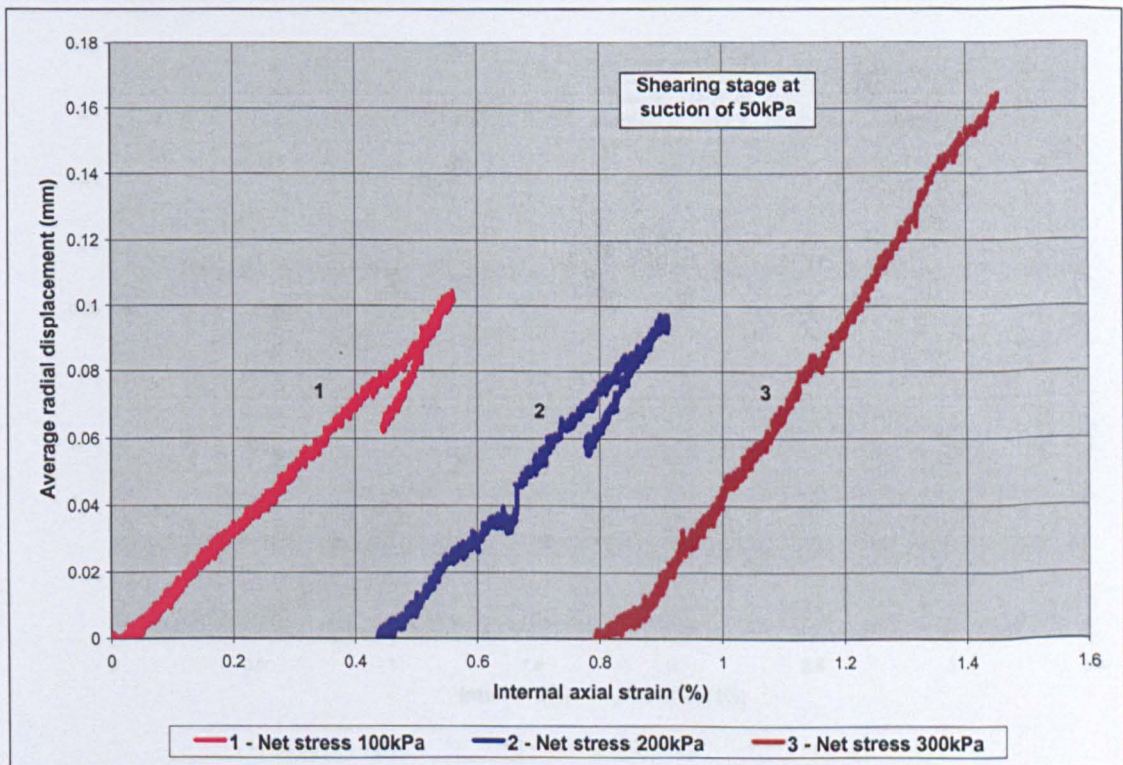


Figure 5.42 Graph of average radial contraction versus internal axial strain during shearing for the multistage triaxial test on an unsaturated specimen at suction of 50kPa (Test series C).

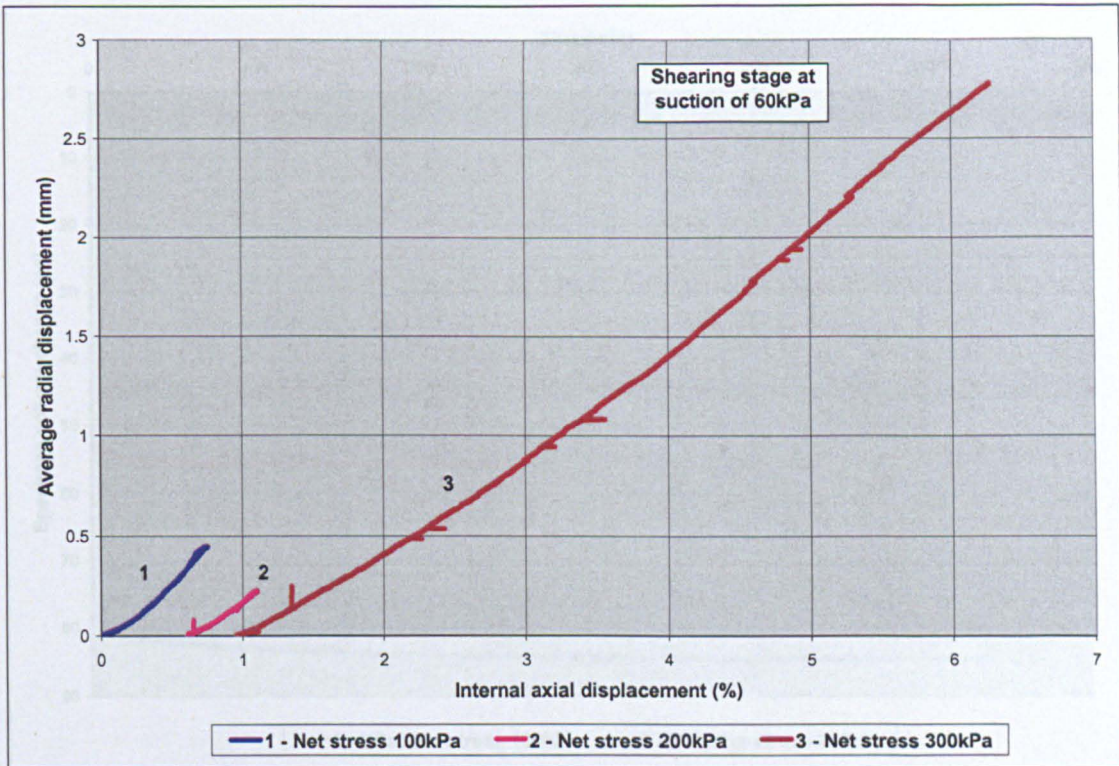


Figure 5.43 Graph of average radial contraction versus internal axial strain during shearing for the multistage triaxial test on an unsaturated specimen at suction of 60kPa (Test series C).

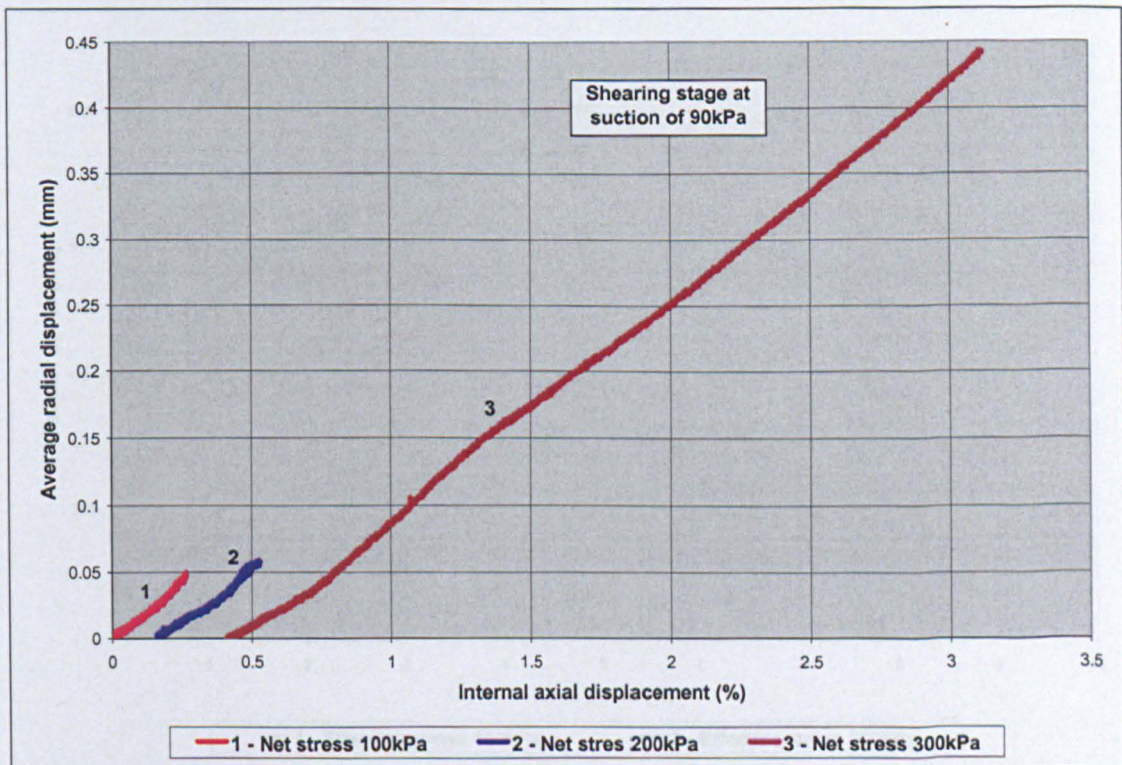


Figure 5.44 Graph of average radial contraction versus internal axial strain during shearing for the multistage triaxial test on an unsaturated specimen at suction of 90kPa (Test series C).



Figure 5.45 Consolidation curves at effective stresses of 100 and 200kPa for the specimens of minimum particle size of 5mm used in test series D.

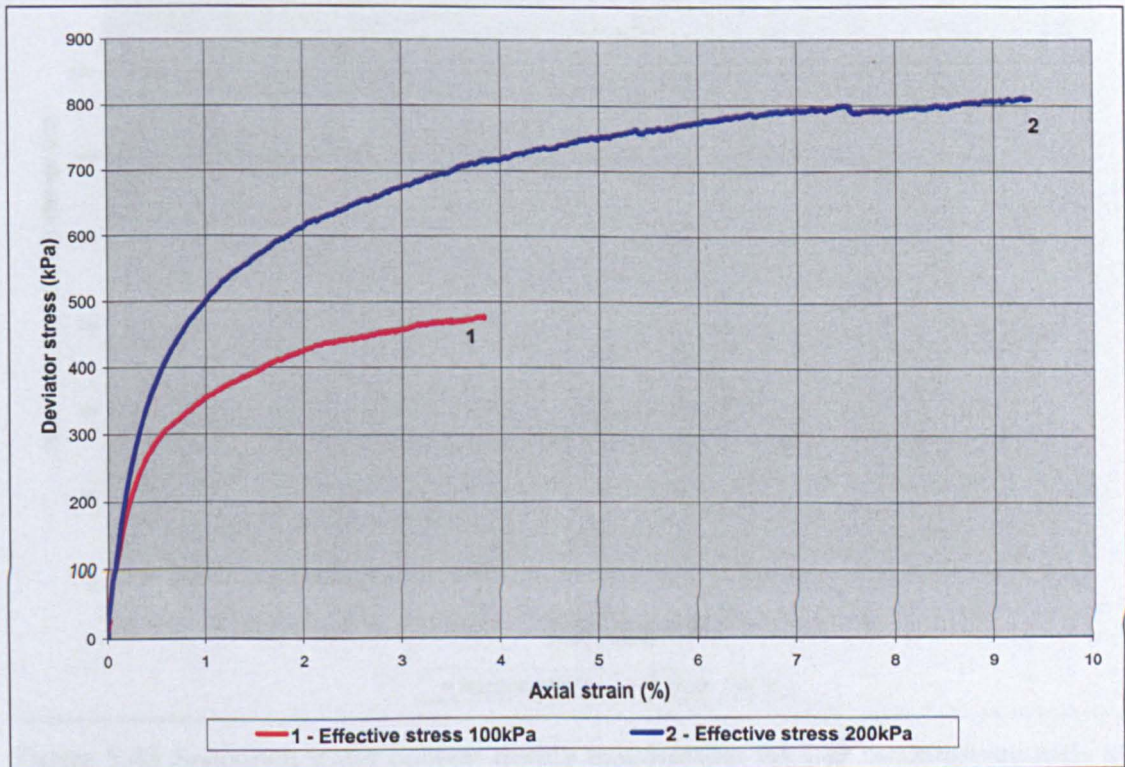


Figure 5.46 Graphs of deviator stress versus axial strain during the shearing stage for the specimens of minimum particle size of 5mm used in test series D.

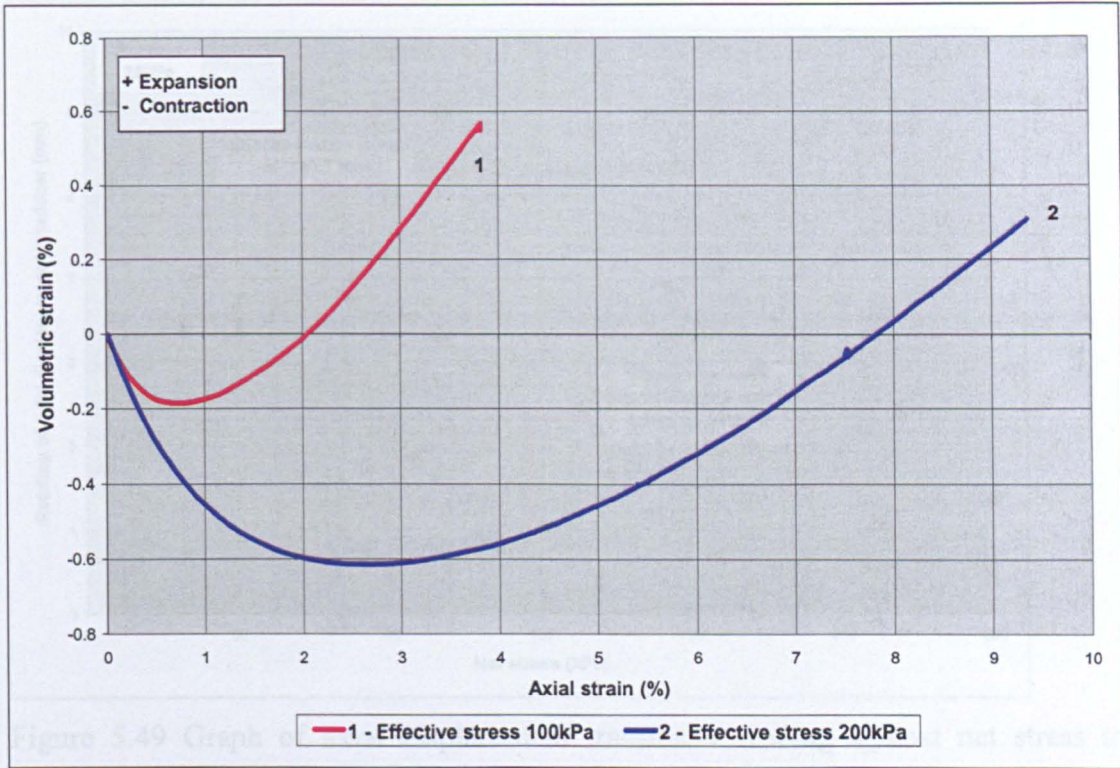


Figure 5.47 Graphs of volumetric strain versus axial strain during the shearing stage for the specimens of minimum particle size of 5mm used in test series D.

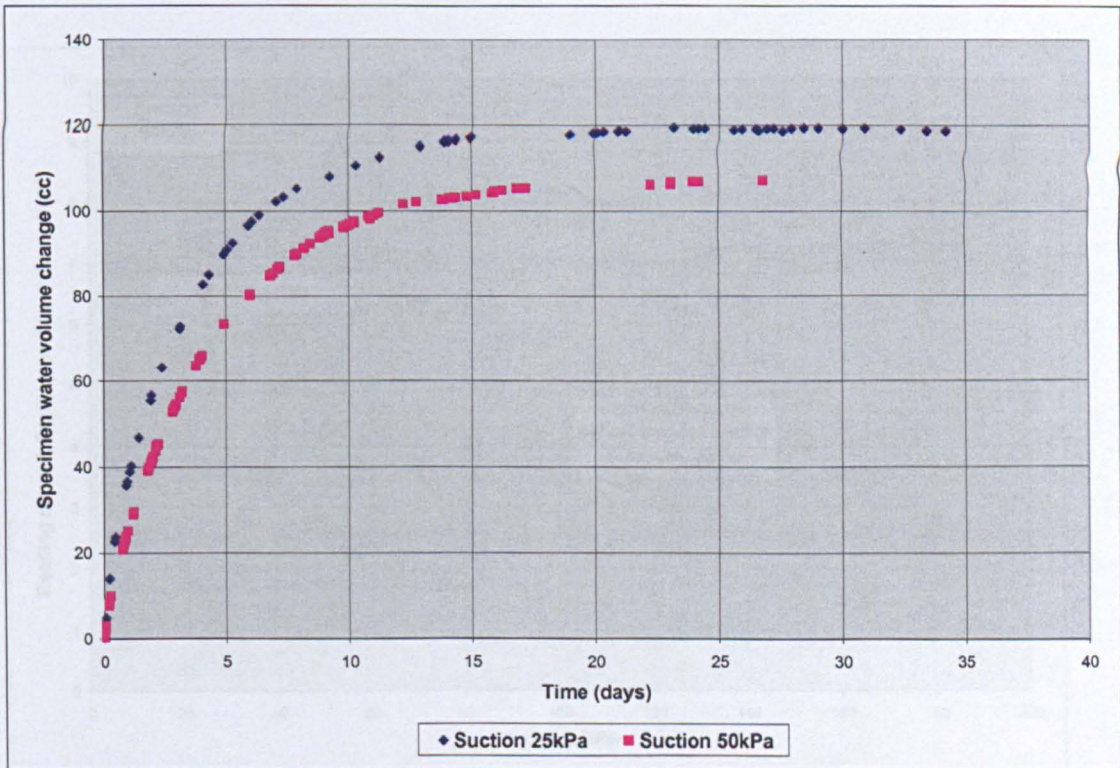


Figure 5.48 Specimen water content during equalisation for 1-D compression tests at suctions of 25 and 50kPa in test series E.

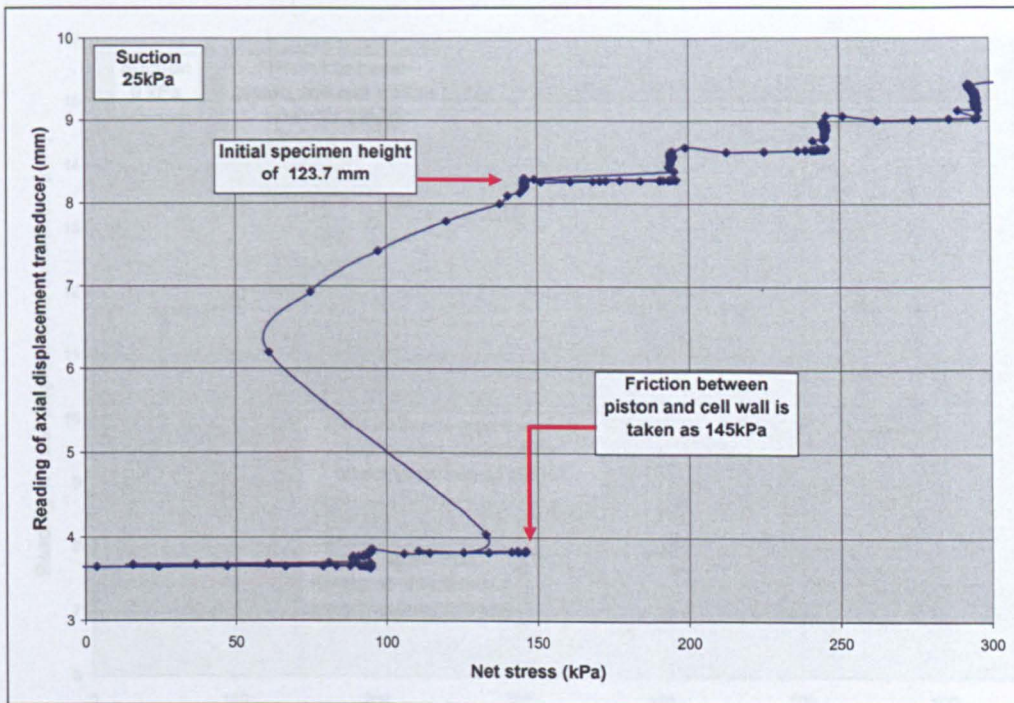


Figure 5.49 Graph of axial displacement transducer reading against net stress to determine the friction between the piston and the cell wall for the compression test at a suction of 25kPa in test series E.

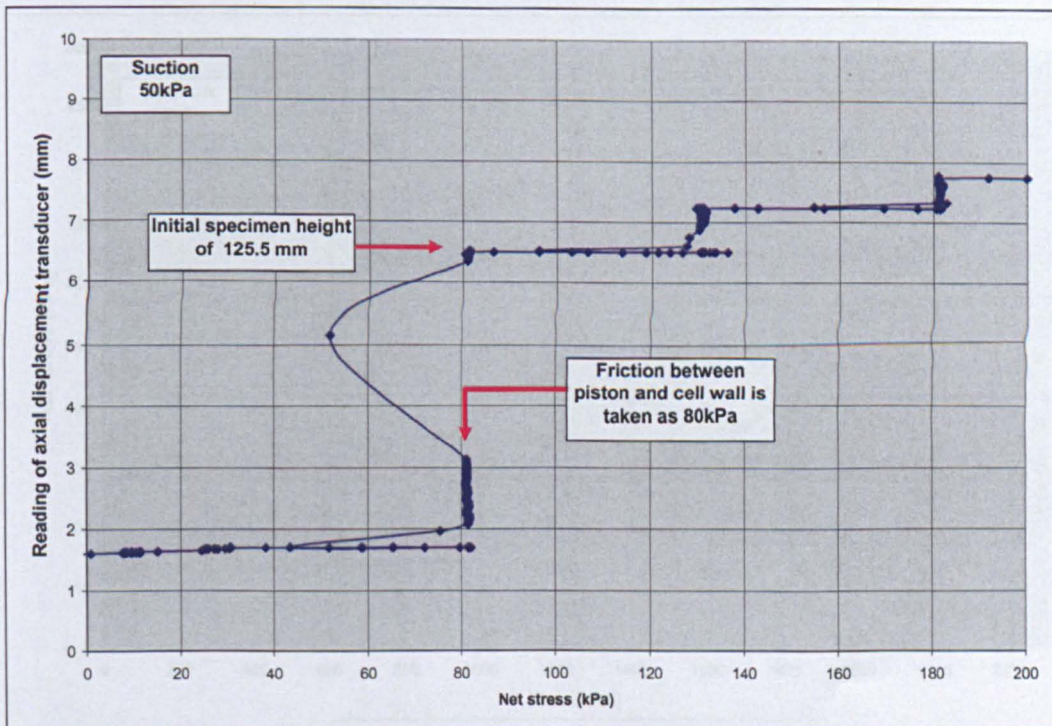


Figure 5.50 Graph of axial displacement transducer reading against net stress to determine the friction between the piston and the cell wall for the compression test at a suction of 50kPa in test series E.

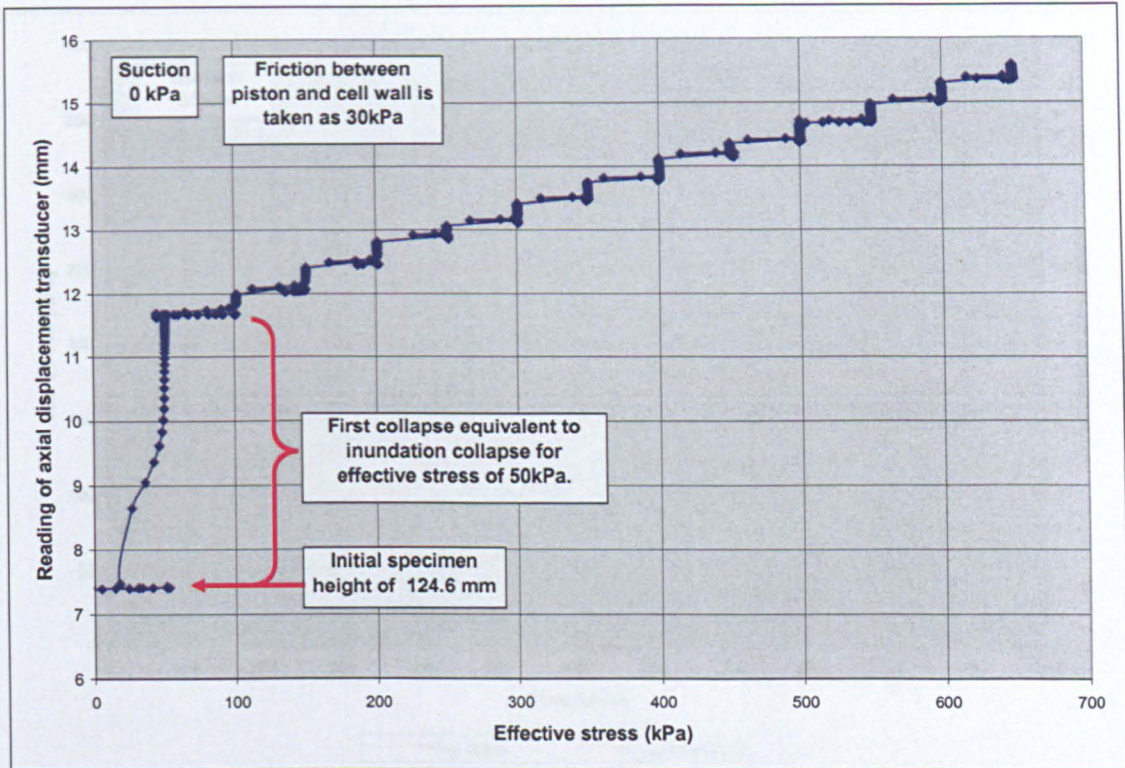


Figure 5.51 Graph of axial displacement transducer reading against effective stress for the compression test on saturated specimen in test series E.

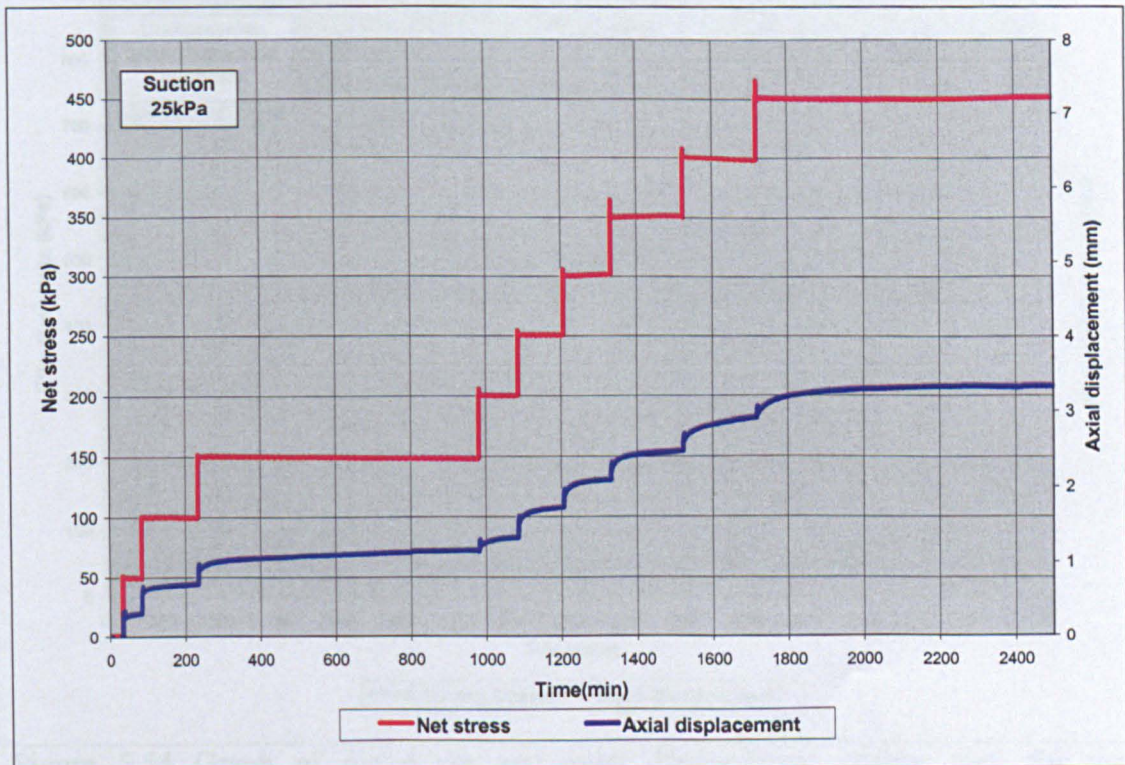


Figure 5.52 Graph of net stress and axial displacement against time for the compression test at a suction of 25kPa in test series E.

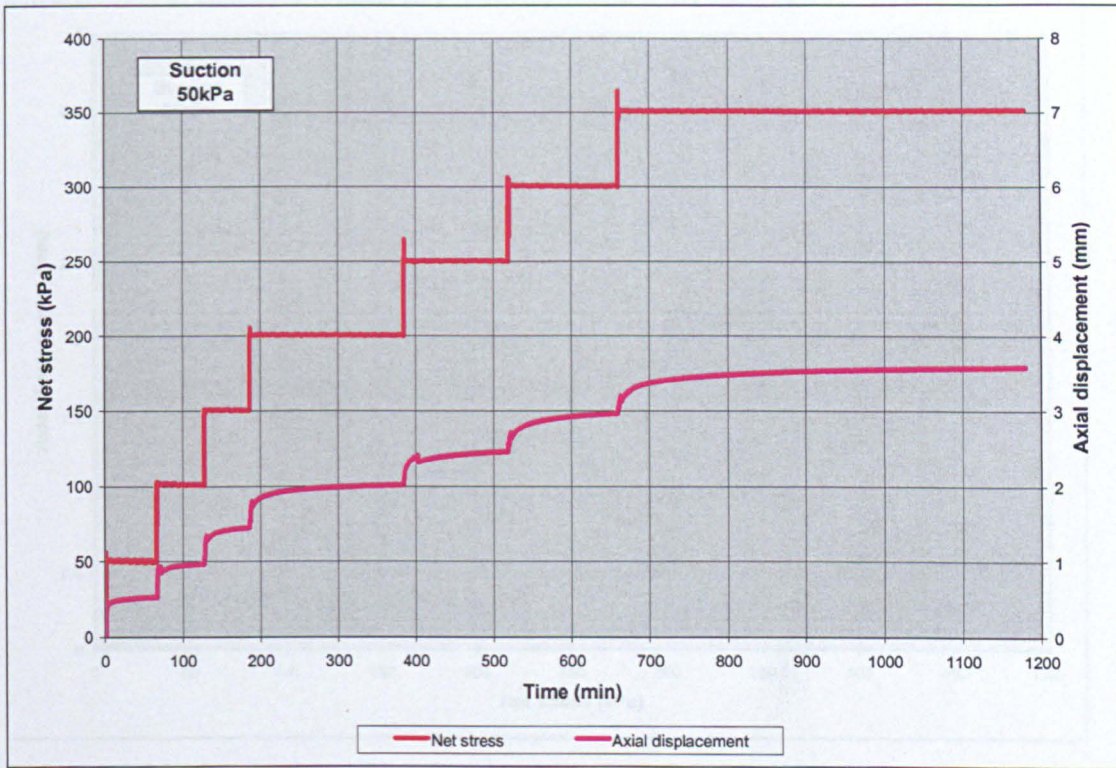


Figure 5.53 Graph of net stress and axial displacement against time for the compression test at a suction of 50kPa in test series E.

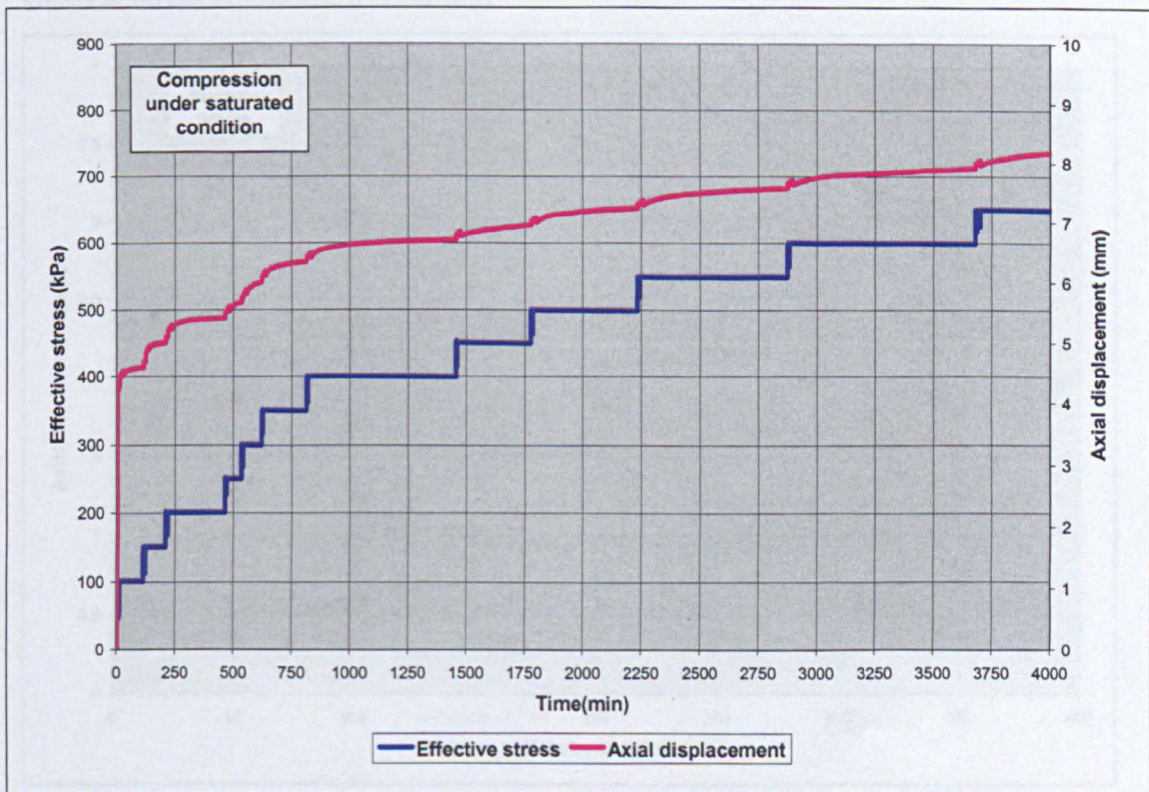


Figure 5.54 Graph of net stress and axial displacement against time for the compression test at saturation in test series E.

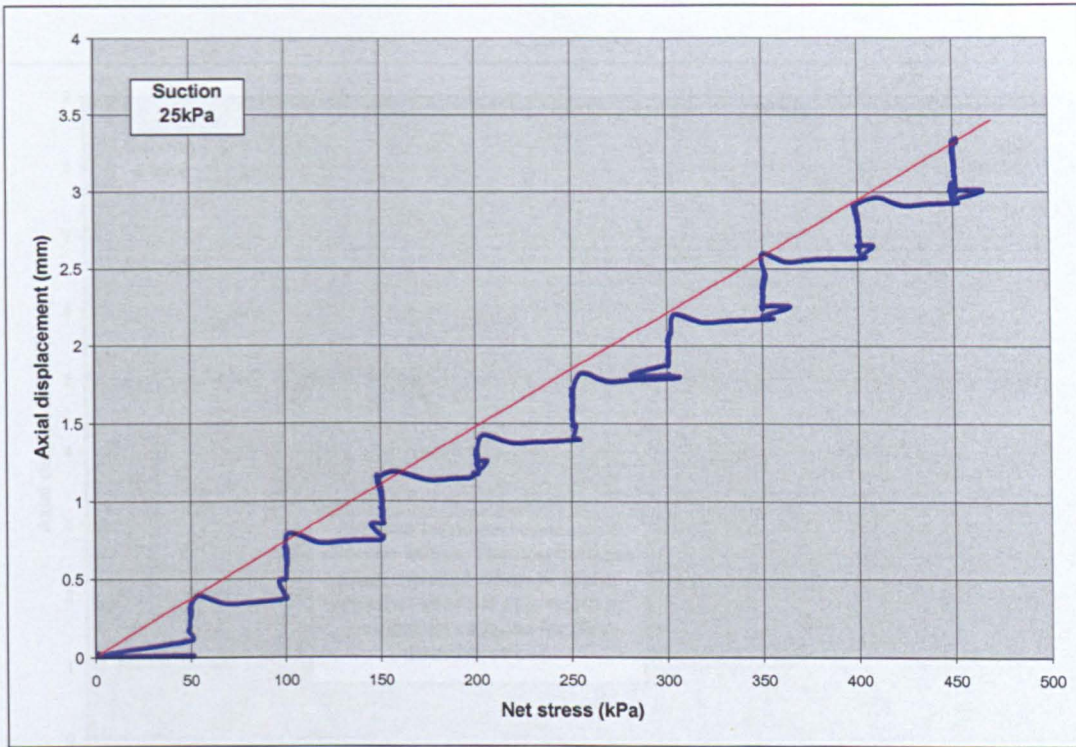


Figure 5.55 Stepped-graph of net stress against axial displacement for the compression test at a suction of 25kPa in test series E. The red line represents the states at stress equilibrium condition.

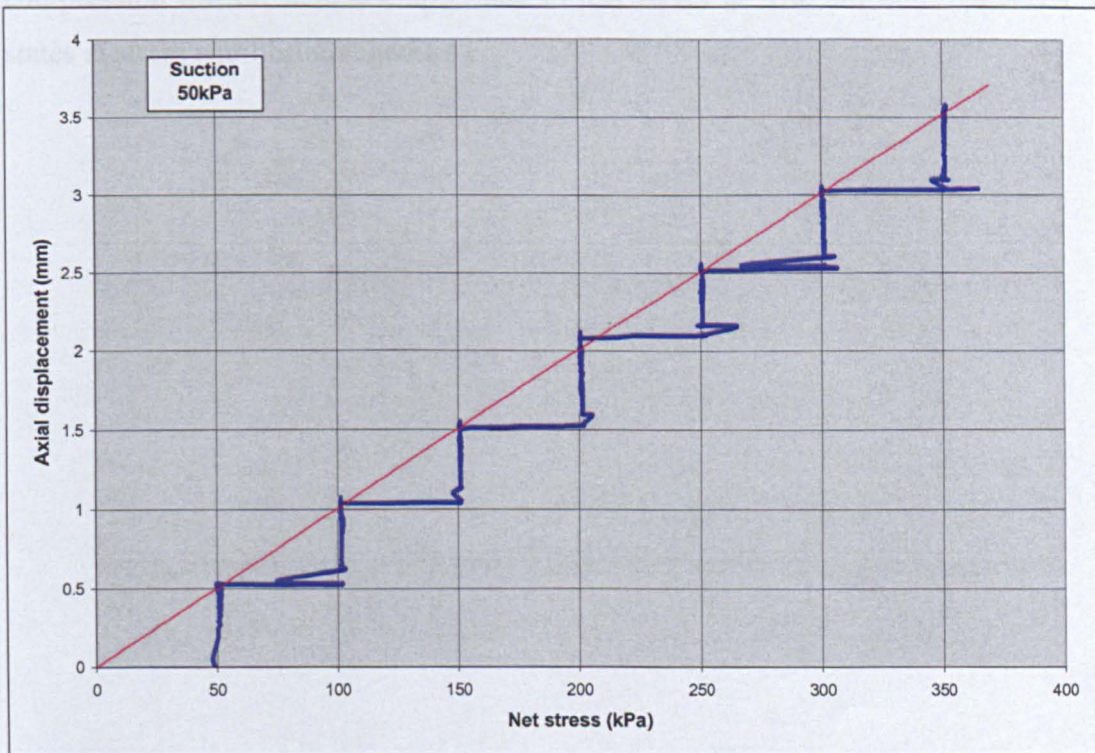


Figure 5.56 Stepped-graph of net stress against axial displacement for the compression test at a suction of 50kPa in test series E. The red line represents the states at stress equilibrium condition.

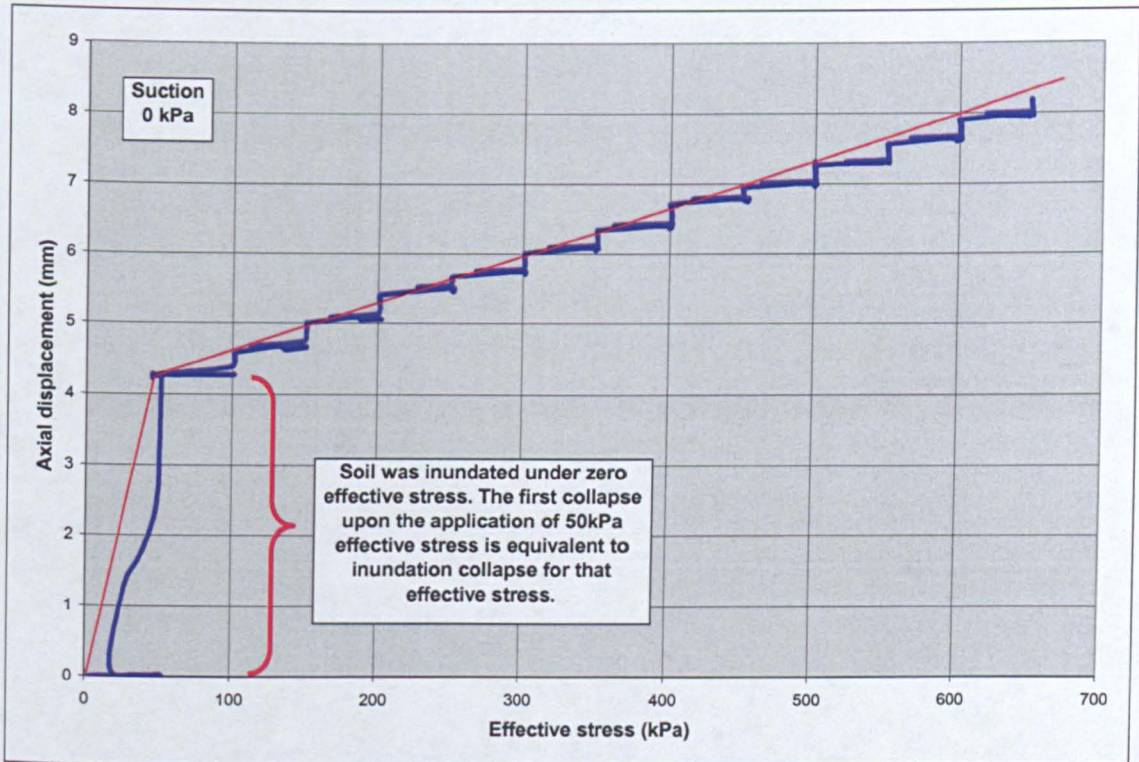


Figure 5.57 Stepped-graph of axial displacement versus effective stress for the compression test on saturated specimen in test series E. The red line represents the states at stress equilibrium condition.